Dissertation

submitted to the
Combined Faculties for the Natural Sciences
and for Mathematics
Ruperto-Carola University Heidelberg, Germany

for the degree of
Doctor of Natural Sciences

Put forward by
Gabriele Ulrike Schenk, born Schmitt
born in Bad Mergentheim
Oral examination: 22. November 2011

Soil-Atmosphere Coupling:
Looking from within the Soil towards the Surface

Referees: Prof. Dr. Kurt Roth
Prof. Dr. Dr. Hans-Georg Bock

Abstract The soil-atmosphere interaction is a key control of the thermal and hydraulic regime of both compartments. The goal of this work was to analyze the potential of temperature profile measurements to extract details of the coupling processes, since they are influenced by the heat transfer itself and by an energy sink due to the evaporation of water.
The surface is studied from two sides, the atmosphere and the soil. The former is accessible through remote sensing. The latter is difficult to observe, however. Hence, a method is developed to reconstruct the surface temperature from soil temperature profiles.
Conduction is the dominant heat transport process in soils. Therefore, reconstructing the surface temperature means back-projecting a diffusion process which is a well-known, but ill-posed problem. It is solved through a weighted linear regression in Fourier space and its applicability is demonstrated for heat conduction and evaporation experiments in the laboratory. Deviations between data and model hint at further processes which are subsequently identified. Combining the measured and reconstructed temperatures with soil water content measurements allows the quantification of all surface energy components for the laboratory experiments.
At the field scale, the temperature projection reveals a boundary layer between soil and atmosphere with distinct thermal properties. This results in an apparent decoupling of temperatures looking from above and from below the surface which highlights the challenge of quantifying the thermal dynamics of soils solely from remote sensing observations.

Kurzfassung Austauschprozesse an der Bodenoberfläche beeinflussen das thermische und hydraulische Regime im Boden und der bodennahen Atmosphäre entscheidend. Ziel dieser Arbeit ist es das Potential von Temperaturprofilmessungen zur Charakterisierung dieser Prozesse zu untersuchen, da sie direkt durch den Wärmetransport und den Energieentzug durch die Verdunstung von Wasser beeinflusst sind.
Die Bodenoberfläche wird dafür von beiden Seiten betrachtet, aus der Atmosphäre und von innerhalb des Bodens. Ersteres kann mittels Fernerkundung erfolgen, letzteres ist durch Messungen aber kaum realisierbar. Daher wird hier eine Methode zur Rekonstruktion der Oberflächentemperatur aus Profilen der Bodentemperatur entwickelt.
Wärmeleitung ist der dominante Transportprozess von Energie im Boden. Daher ist die Rekonstruktion gleichbedeutend mit der Rückprojektion eines Diffusionsprozesses, was ein bekannterweise mathematisch schlecht-gestelltes Problem ist. Die Lösung erfolgt mithilfe einer gewichteten linearen Regression im Fourier-Raum und ihre Anwendbarkeit wird für Wärmeleitungs- und Verdunstungsexperimente im Labor gezeigt. Abweichungen zwischen Messung und Rekonstruktion erlauben es, zusätzliche Prozesse im System zu identifizieren. Aus den gemessenen und rekonstruierten Temperaturen können darüber hinaus, in Kombination mit Wassergehaltsprofilen im Boden, die Energieflüsse an der Bodenoberfläche quantifiziert werden.
Auf der Feldskala lässt sich aus der systematischen Abweichung zwischen der Projektion und den gemessenen Oberflächentemperaturen folgern, dass die Bodenoberfläche als separate Schicht mit vom Boden und der Atmosphäre verschiedenen thermischen Eigenschaften betrachtet werden muss. Dies verdeutlicht die Herausforderung, die Wärmedynamik des Bodens allein aus Beobachtungen der Fernerkundung zu quantifizieren.

Contents

List of Figures

1 Introduction

For now we see only a reflection as in a mirror.
- 1. Corinthians 13, 12

Most of the objects surrounding us are non-transparent. Internal processes are just reflected at the outer surface and the complex conception behind is not directly observable from outside. As long as there are hidden details, these systems will always trigger an incitement in some of us to get to the bottom of things and to check our perception of what is behind.

One of these objects of interest is the Earth itself. There are many hidden processes below its surface and in particular the complex surface interaction between different compartments is fascinating and exciting in many respects and hence for a variety of disciplines.

1.1 Surface - a Characterization from Various Perspectives

Talking about the hidden side behind a surface requires first of all a definition of the term "surface". In the context of the Earth, we want to distinguish three perspectives:

- the system's perspective
- the model operational perspective
- and the sensor operational perspective

Looking from inside the soil, the surface is not just an interface, but a complex, three-dimensional structure where many crucial processes take place, for example the radiative energy entry, the partitioning of the surface energy and the evaporation of water. On the one hand, the transport of water and energy within the soil is channelized close to the surface, but on the other hand, the diffusive character of the soil processes yields a rapid spatial averaging in a shallow layer below the surface.
From the atmospheric side, the surface looks to some extent similar, as it is again a complex 3D-structure, but in addition the vegetation cover is a further significant component that has to be considered approaching the surface from that side. Besides, transport processes in the atmosphere are predominantly turbulent with characteristic time scales dependent on the size of the eddies. However, above a certain scale, this characteristic gets lost and at larger scales in time and space the processes are also dissipative.

From a model operational perspective, the surface is "just" the upper or lower boundary of the compartment of interest and its state has to be described by a certain value.

To be able to work with a continuous system representation, we have to define a *representative elementary volume* (REV) of several centimeters for the soil instead of a detailed pore space description and a representative fluid parcel of characteristic volume for the atmosphere. Therefore, the surface itself cannot be approached arbitrarily close from both sides, but just until the edge length of the characteristic length scale.

The only way to get specific information about the surface is to perform measurements. Direct measurements are often disturbing the surrounding and therefore bias the data. That is the reason to mostly use remote sensors to detect the surface processes non-invasively. In the end, the measured values will always comprise the three dimensional reality in a lower dimensional image. For example, an infra-red thermometer detects from above the surface a signal emitted by the upper 100 to 500 μm which is in addition always distorted to a certain extent by the air layer between soil surface and sensor. But finally, this type of data is the best we can get to be representative for the surface and hence will be treated as what we will call the "surface temperature information" in the following.

Therewith, the stage is set for this work which will in particular focus on the soil surface temperature information. In this project, a new method will be introduced to project back heat diffusion in soils and therewith to reconstruct the surface temperature information from measured soil temperatures. Furthermore, the potential of temperature information is analyzed to gain insights in the interaction processes between soil and atmosphere right at the soil surface. As this coupling is the key control between the water and energy cycle of the continents, various disciplines are working on an improved understanding and characterization of the exchange processes between the two compartments.
This work will contribute to that by looking from within the soil towards the surface and to project the knowledge gained below the surface upwards to infer information about the definite processes there which will be discussed in detail on the basis of experiments in the laboratory and in the field.

1.2 State of the Art

To provide an overview about what has already been done in this context, three main blocks will be distinguished. Firstly, a summary will be given about the methodological field of the reversion of diffusion processes. Besides the general mathematical context, two specific environmental applications will be presented: temperature reconstructions in the context of paleoclimate research and the reconstruction of the groundwater contaminant release history.
Secondly, a short overview of the analysis on soil temperatures will be given. And finally, the context will be further extended towards the atmosphere and the focus is shifted towards investigations and research interests in the coupling processes between the soil and the atmosphere.

1.2.1 Projecting back a Diffusion Process

Besides the fact that the reconstruction of the boundary condition for a diffusive process is a well-known, mathematically ill-posed problem, the type of problem is found in various contexts. Therefore, different disciplines are working to overcome the arising instabilities and limitations and try to estimate the related uncertainties.

Identifying an Unknown Source in a Diffusion Equation

As already stated before, the reconstruction of surface information is a mathematically-called *ill-posed* problem (*Hadamard*, 1902). Ill-posed means formally that the solution does not satisfy general conditions of existence, uniqueness or stability. The history to find stable solutions, at least for certain configurations, goes back more than 50 years and was raised in various fields of applications and a pure mathematical context.

Skaggs and Kabala (1994) give a short summary of methods to deal with this kind of problem. In many cases, the ill-posedness is impossible to overcome directly and special methods, such as Tikhonov regularization (*Tikhonov and Arsenin*, 1977), are needed to get a "best possible" solution. The Tikhonov regularization, for example, adds an additional smoothness constraint for the source function quantified by its second derivative. An intuitive discussion for the release history of a groundwater contaminant can be found in *Skaggs and Kabala* (1998).
These general methods do not solve the ill-posed problem directly in its general form, but transform it via additional constraints towards a related well-posed problem. Solutions of the related problem are in some sense close to the solution of the original problem.

Besides the more general approach of Tikhonov, there are numerous publications discussing the solvability of diffusion equations for unknown source functions of a certain type. To mention just a few, *Cannon and Esteva* (1986) specified the structural requirements of the source function for over-specified data-sets. For more general conditions, *Burykin and Denisov* (1997) discussed the determination of the source function where the source is defined by two unknown spatial functions with different, but known time dependency. Reconstructions in the context of the two-dimensional heat equation were proposed by *Ling et al.* (2006) under the restriction that the source function is a sum of some known functions. And only recently, *Qian and Li* (2011) presented a generalized Tikhonov regularization for identifying a completely unknown source which furthermore yields an error bound for the estimation. These are only a few examples to emphasize that the history of solving this type of ill-posed problems is still ongoing and for a variety of conditions it is still a question of open research.

Two Applications in Environmental Sciences

Paleoclimate Reconstruction These days, climate change is one of the major topics discussed intensively not only by environmental scientists, but also in the social disciplines and politics. It has an impact on nearly every sphere of society and therefore, it is of major interest to investigate the system Earth itself to characterize the complex

interaction between the compartments and evince as well reasons for a changing climate. Deviations in precipitation or differences in temperature are indicators for it. Changes are recorded by and reconstructed from "proxies" that are sensitive to these quantities. For example, the isotopic composition or growth rate of stalagmites *Hellstrom* (2006) or ice cores (*Dahl-Jensen et al.*, 1998) are analyzed to detect actual changes in temperature, but also to reconstruct former variations in the climate. Subsequently, process-based or empirical models are used to describe the system's evolution until todays direct measurements. Ideally, the model building reveals significant processes that caused former changes. At least, it should point to their origin and allow to estimate the impact of these factors. Finally, validating the models is a prerequisite to compare temperature reconstructions of various climate proxies and different locations and to be able to define a global temperature trend. In the end, a consistent image of the climate evolution is sought independent of the type of proxy that is used.
The characterization of the range of natural variations and the anthropogenic impact will result in implications about where we have to re-think our behavior in the future to minimize a further warming of our planet (*IPCC: Le Treut et al.*, 2007). Thus, it is a highly sensitive topic where the reliability of statements is extremely crucial.

Yet, all reconstruction approaches are challenged to extract most reliably the change in surface temperature from its indirect thermal signature in the corresponding record and to correlate the gained time-series, e. g. with known glacial periods, inter-glacial stages, and other cyclic events. Therefore, the main task is always to define the temporal resolution of the proxy, to ensure the stability of the reconstruction and to estimate the related uncertainty, independent of the type of proxy: entrapped ancient air bubbles in ice cores or tree rings, corals, lake or ocean sediments, stalagmites, old ground water or the like.

Groundwater Contaminant Release History In the context of soil science, the recovery of the release history of a groundwater contamination was probably the most famous of this type of problem. Especially in the 1990s, there were many contributions to the estimation of the spatial and temporal origin of a contaminant plume in case of groundwater pollution.
Given a concentration distribution at a certain time, the one-dimensional solute transport through a saturated homogeneous porous medium with constant transport parameters should be solved reversely in time. Following *Jury and Roth* (1990), the closed-form solution of the related differential convection-dispersion equation is given by

$$C(x,t) = \int_0^t C_{\mathrm{in}}(\tau)\; f_{\mathrm{r}}(x, t-\tau)\; \mathrm{d}\tau \tag{1.1}$$

where $C_{in}(\tau)$ is the resident concentration release history and f_{r} is the probability density function which describes the evolution of the concentration distribution in space and time. A comprehensive introduction to the concept of *transfer functions* in the context of solute and heat transport can be found in *Roth* (2006).

Skaggs and Kabala (1994) used in a deterministic approach exactly this model as the kernel in the Tikhonov regularization scheme to invert for the unknown incoming concentration C_{in}. Shortly afterwards, *Woodbury and Ulrych* (1996) proposed a probabilistic approach, denoted as *minimum relative entropy inversion*. Therewith, they derived a more reliable expression for the posterior density function and the expectation value of the linear inverse problem. Two years later, this was successfully extended to a three dimensional reconstruction procedure (*Woodbury et al.*, 1998). At the same time, a more general scheme was developed by *Snodgrass and Kitanidis* (1997) based on a geostatistical approach in a Bayesian framework. Here, no assumption about the nature and structure of the unknown source function has to be made, but the covariance of the unknown "state vector" is needed as a starting point. For the first time, their scheme allowed the validation and improvement of the underlying model in parallel, since the model parameter itself can be fitted to the data.

Altogether, the reversion of diffusion processes was analyzed trying to go back in time or space and even both in parallel. There are a variety of methods available that handle the ill-posed characteristics under certain conditions and presumptions, but a general solution for this type of problem was not yet found and will further challenge various disciplines.

1.2.2 Soil Temperature Analysis

In this work, the focus is in particular on soil temperatures. In the larger context, this information is of special interest from a remote sensing perspective, looking from the atmospheric side towards the soil, e. g. from satellites. For more than 20 years, there has been a huge effort to couple surface information, e. g. brightness temperatures or other active or passive radar data, directly to ground measurements and to extract even information about sub-surface processes. One approach is, for example, to combine remote measured temperatures with a coupled soil moisture and heat transfer model (*Entekhabi et al.* (1994), *Walker et al.* (2001), *Zhang et al.* (2006), *de Lannoy et al.* (2007)). By using these measurements at distinct times, e. g. a direct insertion procedure or statistical frameworks like the Kalman filter (*Kalman*, 1960) is used to adapt the model simulations of higher temporal resolution to the data and therewith to trace the evolution of soil temperature and water content changes in the best possible way.

Most of the mentioned reconstruction procedures and even the data assimilation tools in the field of remote sensing are based on linear models, in particular for the heat transport. The theoretical analysis of heat conduction in soils was started by *Carslaw and Jaeger* (1959) already more than 50 years ago, when they investigated analytically the underlying equations for various domain configurations. *Lettau* (1954) contributed also during that time, already considering non-homogeneous soils with depth-dependent thermal parameters. The general mathematics of solute diffusion was presented even more detailed by *Crank* (1975). There, a variety of solutions for diffusive transport is presented considering also non-constant diffusion coefficients in time and space for which strict analytical solutions do not exist.

In the direct context of soil sciences, *Horton et al.* (1983) compared six different methods to determine the apparent thermal diffusivity from soil temperature time-series in various depths. The finite-difference method of *Richtmeyer and Morton* (1967) and the fitting of six Fourier series to the data in time space (*Horton et al.*, 1983) provided the most reliable estimates about the soil thermal diffusivity. In a subsequent publication (*Horton and Wierenga*, 1983), they presented soil heat flux estimations based on an analytic expression of the surface temperature approximated by a Fourier series. It already turned out that the flux estimates compared better to data than the results from the temperature integral or calorimetric method, even for inhomogeneous soils. Therewith, the Fourier method already pronounced its robust character in analyzing a diffusive process.
Nassar and Horton (1989) followed that line by extracting changes in the thermal diffusivity with depth by fitting a cubic spline in the Fourier representation with one harmonic of soil temperature profiles and finally ended up by a multi-harmonic analysis for non-uniform soils (*Nassar and Horton*, 1990).

Parallel to the first extensions of analyzing soil temperatures with Fourier series, *Jury and Roth* (1990) developed an approach to describe the transport of solutes through soils by conduction and convection by a convolution integral of the initial solute concentration and a transfer function (Eq. (1.1)). *Roth and Boike* (2001) adapted this approach in the context of permafrost soils to project soil temperatures close to the surface deeper into the ground. This approach is in so far complementary to those based on Fourier analysis, as it describes the temporal evolution of a single δ-heat pulse and afterwards superposing a variety of them to end up with the complete temperature signal. In contrast, Fourier analysis is based on periodic base functions to describe the whole temperature signal and its evolution in depth by the modification of the different frequency components due to the diffusion process. Therefore, Fourier method with its continuous base functions extracts efficiently the characteristics of long time-series, but has deficiencies dealing with abrupt changes or discontinuities. Whereas using the transfer function approach allows to resolve distinct events in detail and would be the method of choice for non-periodic and short data-sets due to the sharp character of its base function.

Passerat de Silans et al. (1996) finally analyzed a soil temperature data-set of the HAPEX-Sahel experiment comparing the Fourier and Laplace approaches to characterize the soil thermal properties. Their recommendation which method to use under which condition agrees with the theoretical considerations above.

Altogether, analyzing soil temperature signals by Fourier methods is based on the amplitude and phase information comprised in the signal. But so far, all approaches used temperature signals in time domain and did not compare amplitude and phase changes for different frequency components separately, even the modulation of the signal with depth is frequency dependent. Thus, the starting point of the approach proposed in this work is to extract the amplitude and phase information with depth for all frequencies comprised in the time-series of soil temperatures by Fourier analysis. Estimating subse-

quently the thermal diffusivity in frequency domain will yield more reliable results, since the frequency-dependency is explicitly accounted for. Finally, the solid estimation of the thermal properties is a prerequisite and the basis for a stable reconstruction of the surface temperature information later on.

1.2.3 Soil-Atmosphere Coupling

The water and energy cycle between the soil and the atmosphere is coupled by the evaporation flux. Therefore, it is is one of the key processes in the environmental system Earth and its controls. Its impact is investigated in a wide range of disciplines such as hydrology, meteorology, and climatology, and their applications, e. g. agriculture (*Pielke Sr. et al.*, 2007), groundwater recharge (*de Vries and Simmers*, 2002), and water management (*Sorooshian et al.*, 2011).
It is usually possible to estimate the fluxes of interest within one compartment, the soil or the atmosphere, via direct flux measurements or by using empirical flux laws. But in many cases, this is elaborate or not sufficiently reliable. Besides, the boundary fluxes across the soil-atmosphere interface are needed especially for modeling applications. Yet, extracting the coupling is a challenging task, as measurements of a certain variable in different compartments face different problems due to the different characteristics of the transport regimes. For example, the soil water dynamics is a highly non-linear process and the atmosphere in addition exhibits turbulent regimes. This emphasizes even more the complexity of the processes approaching the soil-atmosphere boundary layer from both sides and hence the overall challenge to characterize the surrounding media sufficiently to finally approach a closed balance for the heat and water exchange at the soil surface.

The starting point in this work is that, close to the surface, the atmosphere and the soil are linked increasingly to each other. Thus, the analysis of near-surface data reveals information about the ongoing exchange processes between both compartments (*Zdunkowski et al.*, 1975). Furthermore, surface data in general has a crucial role, since an error in, for example, the surface temperature will directly result in an error of the corresponding sensible heat flux estimates (*Lüers and Bareiss*, 2010).

In this work, the focus is in particular on temperature data, since its potential to trace distinct processes is known and widely used. One example is the evaporation process. But even beyond, temperature signals are analyzed to extract information about groundwater discharge in streams (*Lowry et al.*, 2007) or to detect the snowpack thickness and many more. An overview on the wide range of applications in hydrology, especially of distributed temperature sensors (DTS) is given by *Selker et al.* (2006).
But this project was based on the idea to use the relative simple temperature measurements within the soil, and also in the atmosphere to infer information about processes occurring directly at the soil-atmosphere boundary. There, the evaporation of water from the surface and the transpiration from plants is of major interest and the potential and limitations to decode the thermal signature of these processes are analyzed.

Surface Energy Partitioning at the Field Scale

The energy partitioning at the soil surface as such is crucial, because, together with the precipitation, it drives the water and energy cycle of the Earth. For a long time, advanced model simulations are performed to study the impact of evapotranspiration and soil moisture on the coupling between the soil and the atmosphere covering all scales, from the field scale (*Camillo et al.*, 1983) to the regional (*Franks et al.*, 1997) and finally to the global scale (*Miralles et al.*, 2011). The model assumptions differ quite significantly in the complexity of the underlying structure reaching from heuristic bucket-models to physically-based process descriptions. But finally, all of them reach the point where the modeled system has to be parameterized. This yields a back-check of our prior knowledge about the system and discrepancies might gain new insights about the actual processes that are so far neglected in the conceptual model.

Even focusing only on the soil side and considering the coupling between the heat, water vapor and liquid water fluxes is a challenge and various studies (*Schelde et al.* (1998), *Bittelli et al.* (2008), *Saito et al.* (2006)), even considering the same scale, differ in the way they represent or parametrize the soil moisture dynamics and the link between the water and energy regime at the surface and within the soil.

Simplifying the system even further and regarding only one of the surface energy components is challenging, again due to the site specific calibration of the models, since further implications about the system's behavior might be based on these results.
Jimenez et al. (2011), for example, estimated separately the global ground heat flux, but in the end always the question arises about implications for the sensible and latent heat flux. At smaller scales, the ground heat flux as such is the crucial component, for example in permafrost regions (*Boike et al.* (2003), *Westermann et al.* (2009)). Conclusions based on flux estimates involve always implications for the complete system, since processes in the complex interplay of the Earth's compartments can never be separated.

Due to the system's complexity and always limited measurement abilities, a variety of approximation procedures for the different surface flux components were developed. Depending on the type of data and the computational effort, empirical or strongly simplified approaches try to capture the most dominant features based on a minimal set of parameters. Already before, we discussed different approaches inferring the soil heat flux from soil temperature measurements. From a soil scientist's perspective, this is based quite solidly and we usually have the necessary measurements in the right resolution. From an atmospheric perspective, this information in the soil is often not available. *Liebethal and Foken* (2007) reviewed, for example, six parametrization approaches to infer the ground heat flux from a most simple set of measurements, mainly from the air. The opposite is true, e. g. for the evaporation flux. Eddy-covariance measurements are used to directly observe the sensible and latent heat flux in the atmosphere (*Foken*, 2008). But since this method is quite elaborate, there are many empirical approaches to infer the evapotranspiration at the soil surface from more simple measurements. The most famous one is probably the FAO Penman-Monteith equation (*Allen et al.*, 2006) using atmospheric

measurements from weather stations. For the simplified approaches, the price to pay is the temporal resolution and the overall accuracy of the estimate. For the evaporation estimates, this means for example only information on a daily mean basis, as the measurement equipment and hence the underlying data-sets cannot resolve the turbulent characteristics of the fluxes.

Coming back to the value of the surface temperature information, it can be stated that, especially in the context of evaporation, it carries indirectly the thermal signature of the phase change and hence can be used to infer a direct correlation to the evaporation flux (*Monteith*, 1981). Many studies investigated that link for bare soil conditions (*Katul and Parlange* (1992), *Qiu et al.* (1998)), but as well for radiometric surface temperature measurements over vegetated surfaces (*Norman et al.* (1995), *Moran et al.* (1996), *Francois* (2002), *Qiu and Zhao* (2010)).
The field experiments performed in this project allow in particular to investigate the influence of the vegetation cover on the soil system itself, but furthermore on the surface fluxes and surface measurements from above. Two soil profiles were instrumented only a few meters apart from each other. For one, the surface was held bare during the complete experiments and one was covered by grass. The similar textural layering allows to study explicitly the impact of the plants during the seasons, and thus the relation between the evaporation and transpiration fluxes at the soil surface.

Investigations of the Evaporation Process in the Laboratory

Laboratory experiments allow a detailed analysis of the processes at the soil surface. Furthermore, the soil-atmosphere system is less complex compared to the field investigations due to the potential to control the boundary conditions. Therefore, radiative forcing by the sun, vegetation cover, and soil layering can be neglected in a first step and the focus is directly on the fundamental processes.

Evaporation experiments at the laboratory scale were first proposed by *Gardner and Miklich* (1962). Typically, they are used to investigate the soil hydraulic properties of an initially water saturated soil column, while the soil water can evaporate at the surface. In the 1990s, *Wendroth et al.* (1993) among others rediscovered the value of these measurements to infer these properties by numerical inversion, as the range of soil water potentials is quite wide. The evaporation experiment itself is the complementary approach to the *multi-step outflow* (MSO) experiments (*van Dam et al.*, 1994) which became a standard procedure for the characterization of the soil hydraulic properties in the laboratory. The final combination of both methods makes use of the advantages of each method, since it is based on the maximal pressure head range (*Schelle et al.*, 2010).
Schneider et al. (2006) proposed a more advanced set-up which allows the direct control of the water potential in the air above the soil surface. In particular, they found during the numerical simulations of their experiments (*Schneider-Zapp et al.*, 2010) that the thermal properties of the upper few millimeters of the soil surface are crucial for the resultant fluxes. Hence, they cannot be treated as an interface, but form a boundary layer with different hydraulic properties.

In the last three years, further laboratory experiments in *Hele-Shaw cells* (*Saffman and Taylor*, 1958) and cylindrical soil columns were performed to study the evaporation process itself in the soil and the coupling towards the atmosphere in even more detail. The influence of textural differences on the depth of the drying front (*Lehmann et al.*, 2008), of vertical heterogeneities (*Lehmann and Or*, 2009) and horizontal layering (*Shokri et al.*, 2010) were discussed for various soils to extract their impact on the resultant evaporation fluxes and their temporal evolution.

Most recently, researchers were as well focusing on the thermal signature of the evaporation process in the surface temperature. *Shahraeeni and Or* (2010) presented an inverse method to infer the evaporation flux under constant laboratory conditions from the surface temperature data measured by a thermal infra-red camera. Within this work, the experimental set-up was extended to be able to change the thermal conditions in air during the experiment and besides, temperature and water content profiles were measured within the soil to end up with a complete description of the thermal and hydraulic process in the soil, the air, and directly at the surface.

1.3 Outline

This work is partitioned in three parts: (i) developing a method to reconstruct the surface temperature from measured soil temperature profiles, (ii) a laboratory experiment to validate the method and investigate the soil-air interaction under controlled conditions, and (iii) a field experiment with different types of surface covers to extract the impact of vegetation and to analyze the applicability and limitations of simplified model assumptions under natural conditions.
Therefore, developing a new methodological approach for a certain class of mathematical problems was not the main focus of this project. Instead, the strength lies in the understanding of a measured reality on the background of a solid theoretical foundation. The processes in the two compartments, soil and atmosphere are linked at the soil surface and have in particular a considerable influence on the surface temperature. Testing initially simple model assumptions in systems with increasing complexity unveils step-by-step additional processes which have to be included in an extended representation and therefore a better characterization of the soil-atmosphere coupling.

The following overview defines the starting point of this work and outlines the further structure of this thesis.

Surface Temperature Reconstruction:

- Time series of soil temperature profiles can be analyzed robustly and efficiently by Fourier's method which, in addition, allows the thermal characterization of the soil.
- The new approach will analyze the spectral information of the temperature signals in frequency domain to overcome the bias due to superposed frequency components.

- Amplitude and phase information in frequency space allow to reconstruct their original value directly at the surface and therewith, the reconstruction of the temperature signal at the surface. This is equipollent with the stable reversion of the diffusive heat transfer in the soil.
- With the estimated thermal properties and the surface temperature reconstruction, the surface energy flux into the ground is estimated.

Laboratory Heat Transfer Experiments:

- Pure heat conduction and evaporation experiments in a sand column are performed under controlled conditions in a climate chamber.
- The new method to reconstruct the surface temperature from time-series of soil temperature profiles is validated.
- All coupling processes at the soil surface can be decoded from their thermal signature and will therefore be quantified from the measurements of the temperature profiles in the soil and the air above.
- The simplified model assumptions reveal the impact of additional processes during the experiments. Analyzing the deviations finally yields a complete image of the involved processes.

Coupling of Water and Energy Fluxes at the Field Scale:

- Two soil profiles were instrumented, one under a bare surface and one under grass.
- Due to the similar textural layering, the definite influence of the plants due to root water uptake and transpiration is extracted from the soil temperature and water content profiles.
- The complex interactions between the water and energy cycle of the soil and the atmosphere are studied.
- The performance of the surface temperature projection under field conditions is discussed.
- The simplified model assumptions again yield a deeper insight in the type of neglected processes at the field scale.

2 Theory

In the following section, the basic theoretical concepts for water and heat transport in soils and the atmosphere are introduced. The description of both types of transport processes is completed by their coupling through the vaporization of water. Finally, the coupling processes between the soil and the atmosphere will be described in detail, since they are the forcing at the interface between the two compartments.
For simplicity, we will restrict the transport equations to one dimension and hence state them for the vertical flux component, denoted by z.

2.1 Transport Processes in the Soil

2.1.1 Soil Water Flow

The theory related to the soil water flow will be described following *Roth* (2006). Starting point the conservation of a water volume

$$\partial_t \theta_\mathrm{w} + \partial_z j_\mathrm{w} = 0 \,, \tag{2.1}$$

expressing that a temporal change in the volumetric water content θ_w is equalized by a spatial change in the water flux j_w. At that point, only water in the liquid phase is considered and this flux can be described by the *Buckingham-Darcy law*

$$j_\mathrm{w} = -K_\mathrm{w}(\theta_\mathrm{w}) \partial_z \psi_\mathrm{w} \,, \tag{2.2}$$

which relates the soil water flux j_w to the gradient in the water potential ψ_w via the hydraulic conductivity function $K_\mathrm{w}(\theta)$. The latter is a hydraulic property of the underlying soil and depends itself on the hydraulic state of the soil. Furthermore, the water potential ψ_w can be replaced in first order by the sum of the *matric potential* ψ_m and the gravitational potential $\psi_\mathrm{g} = \rho_\mathrm{w} g z$. Thereby, g stands for the acceleration due to gravity, z for the coordinate in vertical direction and ρ_w denotes the mass density of water.
The matric potential is related to the capillary forces within the soil matrix and, assuming spherical pores, it can be derived from the *Young-Laplace equation* as

$$\psi_m = p_\mathrm{w} - p_\mathrm{a} = \frac{2\sigma_\mathrm{w}}{r_\mathrm{w}} \,. \tag{2.3}$$

It relates the surface tension of the water σ_w and the interfacial radius of the water meniscus r_w with the pressure difference between the pore water and the air above the water meniscus $p_\mathrm{w} - p_\mathrm{a}$.
For a stationary system,

$$\partial_t \theta_\mathrm{w} = \partial_z j_\mathrm{w} = 0 \tag{2.4}$$

and hence this implies that j_w is constant. From equation (2.2), we can further conclude that

$$\partial_z \psi_\mathrm{w} = \partial_z \psi_\mathrm{m} + \partial_z \psi_\mathrm{g} = \text{const.} \tag{2.5}$$

Since

$$\partial_z \psi_\mathrm{g} = \rho_\mathrm{w} g \ , \tag{2.6}$$

this yields that also

$$\partial_z \psi_\mathrm{m} = \text{const} \ . \tag{2.7}$$

Therefore, ψ_m is also a linear function of z in a stationary system.

Combining the conservation and flux equations above yields the so-called *Richards equation*:

$$\frac{\partial \theta_\mathrm{w}}{\partial t} = \partial_z \left[K_\mathrm{w}(\theta_\mathrm{w}) \partial_z \left[\psi_\mathrm{m} - \rho_\mathrm{w} g z \right] \right] \ . \tag{2.8}$$

This is non-linear differential equation, since the hydraulic conductivity itself depends on water content.
At this point, there are two unknowns in the actual equation, the water content θ_w and the matric potential ψ_m. Therefore, a second material property relating these two quantities is introduced, called the *soil water characteristic* $\theta_\mathrm{w}(\psi_\mathrm{m})$. Expressing in addition the hydraulic conductivity function no longer as a function of the water content, but also as a function of the matric potential yields finally the following equation describing water movement in soil:

$$\frac{\partial \theta_\mathrm{w}}{\partial \psi_\mathrm{m}} \frac{\partial \psi_\mathrm{m}}{\partial t} = \partial_z \left[K_\mathrm{w}(\psi_\mathrm{m}) \left[\partial_z \psi_\mathrm{m} - \rho_\mathrm{w} g \right] \right] \ . \tag{2.9}$$

The two material properties, $\theta_\mathrm{w}(\psi_\mathrm{m})$ and $K(\theta_\mathrm{w}(\psi_\mathrm{m}))$, are typically parametrized in terms of the *water saturation*

$$\Theta(\theta) = \frac{\theta - \theta_\mathrm{r}}{\theta_\mathrm{s} - \theta_\mathrm{r}} \ . \tag{2.10}$$

The functional expressions of the two most popular parameterizations for the soil water characteristic, the Brooks-Corey (*Brooks and Corey*, 1966) and the van Genuchten (*van Genuchten*, 1980), are given by:

Brooks-Corey:

$$\Theta(\psi_\mathrm{m}) = \begin{cases} \left[\psi_\mathrm{m} / \psi_0 \right]^{-\lambda} \ ; & \psi_\mathrm{m} < \psi_0 \ , \\ 1 \ ; & \psi_\mathrm{m} \geq \psi_0 \ , \end{cases}$$

where ψ_0 represents the air entry value of the largest pore and λ is a positive parameter. The major disadvantage regarding numerical simulations is the discontinuity for $\psi_\mathrm{m} = \psi_0$.

van Genuchten:

$$\Theta(\psi_\mathrm{m}) = \left[1 + \left[\alpha \psi_\mathrm{m} \right]^n \right]^{-1+1/n} \ , \tag{2.11}$$

with $\alpha < 0$ and $n > 1$. Here, α is the scaling factor for the matric potential and $1/\alpha$ correspond to the air entry value.

Furthermore, *Roth* (2006) showed that the two parameterizations approach each other for $\alpha\psi_{\mathrm{m}} \gg 1$ and

$$\frac{1}{\alpha} = \psi_0, \quad n - 1 = \lambda \; . \tag{2.12}$$

For the hydraulic conductivity function, the Mualem model (*Mualem*, 1976) is the one commonly used in practice. Both parameterizations for the soil water characteristics can be combined with it,which yields the following two expressions:

Mualem-Brooks-Corey:

$$K(\Theta) = K_{\mathrm{s}}\Theta^{\tau+2+2/\lambda} \tag{2.13}$$

with the saturated conductivity K_{s} and the parameter τ is typically set to 0.5.

Mualem-van Genuchten:

$$K(\Theta) = K_{\mathrm{s}}\Theta^{\tau}[1 - [1 - \Theta^{n/[n-1]}]^{1-1/n}]^2 \; . \tag{2.14}$$

The difference between the two parameterizations lays in the slope of the transition zone between water saturation and the unsaturated range. A combined visualization of these parameterizations can be found in *Roth* (2006) (Fig. 5.3). The final choice of the parameterization will be advised by the characteristics of the specific experiment, since the temporal evolution of the water content profiles exhibits considerably differences between the two expressions.
In this work, the hydraulic properties are estimated for the Mualem-van Genuchten parameterization from inverse modeling of a laboratory multi-step outflow experiment (*van Dam et al.*, 1994).

2.1.2 Soil Heat Transport

Heat transfer in general means the exchange of thermal energy between two systems. Three major mechanisms can be distinguished:

Diffusion: kinetic energy is directly exchanged on a microscopic scale.

Convection: energy is transported by fluid motion.

Radiation: energy is transported via electromagnetic waves between two objects.

For soils, we will in a first step consider heat transport purely to conduction. Again, the starting point for the process description is a conservation equation, now energy conservation:

$$\partial_t[C_{\mathrm{h}}T] + \partial_z j_{\mathrm{h}} = 0 \; . \tag{2.15}$$

Hence, a change in the amount of energy stored in a soil volume will cause or is the result of a spatial change of the heat flux in that volume, where C_{h} denotes the soil heat

capacity [J m^{-3} K^{-1}]. This can in turn be deduced by the weighted mean of all fractions of water, air and soil matrix in the respective soil volume:

$$C_{\mathrm{h}} = \sum_i \theta_i \rho_i c_i \ . \tag{2.16}$$

Therein, θ_i, ρ_i and c_i are the volume fraction, mass density [kg/m^{-3}] and the specific heat capacity [J $kg^{-1}K^{-1}$] of the different soil constituents i.
To describe the heat flux, it can again be related to a gradient, here a temperature gradient, which yields *Fourier's law*:

$$j_{\mathrm{h}} = -K_{\mathrm{h}} \partial_z T \tag{2.17}$$

with the thermal conductivity K_{h} [W m^{-2} K^{-1}].
For a constant heat capacity and thermal conductivity, the soil thermal diffusivity can be defined as

$$D_{\mathrm{h}} = \frac{K_{\mathrm{h}}}{C_{\mathrm{h}}} \tag{2.18}$$

and the combination of the conservation and flux equation yields a linear differential equation to describe pure heat conduction or heat diffusion in soils:

$$\partial_t T - D_{\mathrm{h}} \partial_{zz} T = 0 \ . \tag{2.19}$$

2.1.3 Coupling of Water and Energy Cycle in the Soil

For the coupling of the heat transport to the soil water cycle, two more transport processes have to be considered from an "energetic" perspective. Firstly, energy will be transported via convection due to the water flux in the system. Beside, we have now also to account for the phase change of water. Therefore, Fourier's law has to be extended by additional terms representing these two contributions:

$$j_{\mathrm{h}} = -K_{\mathrm{h}} \partial_z T + C_{\mathrm{h,w}} T j_{\mathrm{w}} + \lambda j_{\mathrm{v}} \tag{2.20}$$

with the liquid water flux j_{w} (Eq. (2.2)), the water vapor flux j_{v}, $C_{\mathrm{h,w}} = 4.22\,\mathrm{MJ\ m^{-3}K^{-1}}$ the heat capacity of water, and $\lambda = 2.45\,\mathrm{MJ/kg}$ the latent heat of vaporization.
The vapor flux itself can be defined by *Fick's law* of diffusion

$$j_{\mathrm{v}} = -D_{\mathrm{v}} \frac{\partial e_{\mathrm{s}}}{\partial z} \tag{2.21}$$

with the vapor diffusivity D_{v} [m^2/s] and the soil water vapor pressure e_{s} [kPa]. Its relation to the soil matric or pressure potential ψ_{m} (Eq. (2.3)) is obtained from *Kelvin's equation*:

$$\frac{e_{\mathrm{s}}(\psi_{\mathrm{m}})}{e_0(T)} = \exp\left(\frac{m_{\mathrm{w}} \psi_{\mathrm{m}}}{\rho_{\mathrm{w}} R T_{\mathrm{s}}}\right) \tag{2.22}$$

with $m_{\mathrm{w}} = 0.018\,\mathrm{kg/mol}$ the molecular weight of water, the universal gas constant $R = 8.31\,\mathrm{J\ mol^{-1}K^{-1}}$, the soil temperature T_{s} [K] and the saturated water vapor pressure e_0 [kPa] given by the *Magnus' formula* (*Buck*, 1981):

$$e_0(T) = 0.611 \cdot \exp\left(\frac{17.27\ T}{T + 237.3}\right) \ , \tag{2.23}$$

but this time the temperature T has to be given in $°C$.

Form this, it can be recognized that the water vapor pressure e_s is not only a function of the matric potential, but also of the temperature. Thus, the water vapor flux can be written as

$$j_\mathrm{v} = -D_\mathrm{v}\left[\frac{\partial e_\mathrm{s}}{\partial T}\frac{\partial T}{\partial z} + \frac{\partial e_\mathrm{s}}{\partial \psi_\mathrm{m}}\frac{\partial \psi_\mathrm{m}}{\partial z}\right] , \tag{2.24}$$

$$= j_\mathrm{v}^T + j_\mathrm{v}^i \tag{2.25}$$

and hence as the sum of a thermal and an isothermal vapor flux component.

Analogue to the additional components added to Fourier's law to account for conductive heat transport and the energy needed for phase change of water, we have to extend the Buckingham-Darcy flux law for the liquid water flux in the soil to account for the water vapor component:

$$j_\mathrm{w} = -K_\mathrm{w}(\theta_\mathrm{w})\partial_z\psi_\mathrm{w} + j_\mathrm{v} . \tag{2.26}$$

Eventually, we end up with a set of two differential equations coupled by the fluxes of liquid water and water vapor which have to be solved in parallel to model explicitly the link between the water and energy transport in soils.

2.1.4 Soil Water Evaporation

We want to close this section with a more phenomenological description of the evaporation process within soils and at their surface following *Lehmann et al.* (2008). Conceptually, the temporal evolution of the evaporation flux is shown in Figure 2.1 assuming an initially completely water saturated soil column and an unlimited potential of the air to take up the evaporated water. During the experiment, the soil surface is free to evaporate water and hence, the water table will continuously decrease within the column.

The high and nearly constant drying rate in the beginning is denoted as *stage 1 evaporation*. In this period, the soil hydraulic properties limit the evaporation flux, since they control the liquid water flow in the capillaries towards the surface. Furthermore, the flux is high as long as liquid films directly reach the soil surface where the phase changes occurs. Therefore, stage 1 evaporation will last longer for fine textured porous media than for coarse grained ones.
The pore size distribution is in additional characteristic for the depth of the evaporation front or film region at the end of stage 1 which is called the *characteristic length* of the soil.

Once, the water table falls below a certain depth, the liquid films in the pore space do not reach the soil surface anymore. Thus, evaporation of water occurs no longer at the soil surface, but within the soil and the water vapor has to be transported by diffusion towards the surface. The size of the flux is now limited by the vapor diffusion coefficient of the soil and the transport process is less efficient compared to the surface evaporation. The drop of the evaporation flux characterizes the beginning of *stage 2 evaporation* and

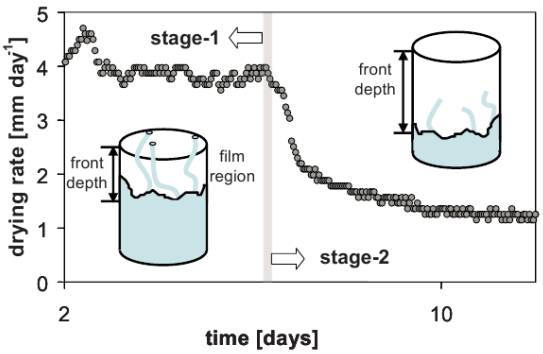

Figure 2.1: Conceptual diagram of evaporation stages (*Lehmann et al.*, 2008). The high drying rate during stage 1 evaporation stays constant as long as the capillary forces supply liquid water directly at the soil surface where the phase changes takes place. Afterwards, the rate decreases, since the liquid films do no longer reach the surface and the water is vaporized within the soil and transported by vapor diffusion towards the surface.

reflects the diffusion length of the vapor transport.

Textural heterogeneities introduce an additional scaling of the evaporation flux. Dependent on the the hydraulic properties, horizontal layers can extend or limit stage 1 evaporation from the upper soil layer, depending on the ratio between layer thickness, characteristic lengths, and the water table depth (*Shokri et al.*, 2010).
Vertical textural contrasts can enhance the evaporative losses of the soil due to the fact that lateral flow is induced in the soil system (*Lehmann and Or*, 2009). In general, the evaporation flux from larger pores is higher. Yet, they will also be drained earlier compared to finer pores, since capillary forces are proportional to the inverse pore radius (Eq. 2.3) and hence lower for larger pores. Vertical heterogeneity allows now a horizontal water flux from finer towards the larger pores which stabilizes, at least for some time, the water level in the larger pores and results in an elongation of stage 1 compared to a homogeneous profile of the coarser soil.
Altogether, patches of different texture also reveal different evaporation fluxes and the energy sink due to the phase change scales with the size of the evaporation flux. This can finally be used to distinguish different flow regimes from their thermal signature at the soil surface (*Monteith* (1981), followed by studies on various scales (compare Sec. 1.2.3).

2.2 Transport Processes in the Atmosphere

The atmosphere is a fluid with a turbulent flow character. Therefore, the term diffusion, as used until now, has to extended to be able to describe processes within a similar notation despite of the different nature of the underlying transport process. In the atmosphere, the turbulent mixing or the mixing due to eddy motion is denoted by "eddy diffusion". Molecular diffusion in the original sense takes only place in the lower few millimeter above the soil surface, but further up the atmosphere exhibits layers that are characterized by the increasing size of the eddies.

Before, taking a closer look at the explicit representation of the transport processes, we first introduce the *Rayleigh number* as an criterion to characterize the transition from a diffusive to a convection or turbulent flow regime. Following *Niemela et al.* (2000), the Rayleigh number indicates the dynamical state of a fluid and can be viewed as the ratio of the convective forces and the product of thermal and momentum diffusivities. It can be calculated by

$$Ra_x = \frac{g\beta}{\nu D_\mathrm{h}}(T_\mathrm{surface} - T_\mathrm{air})x^3 \ , \tag{2.27}$$

where $g = 9.81\,\mathrm{m/s^2}$ is again the gravitational acceleration, ν [Pa s] the kinematic viscosity, and thermal expansion coefficient β can be approximated as $0.003\,\mathrm{K}^{-1}$ for air. x is the characteristic length of the system. The crucial point is the estimated Rayleigh number with the so-called "critical Rayleigh number" which is given by

$$Ra_\mathrm{crit} = \frac{\pi^4(1+a^2)^3}{a^2} \ . \tag{2.28}$$

Therein, a is the aspect ratio which is again characteristic for the underlying system, since it denotes the ratio of the convection roll height to its width.

Compared to molecular diffusion, turbulent transport implies not only that it is much more efficient, but furthermore the transport of momentum, heat and gases in air is characterized by the same effective diffusion parameter. Thus, their transport behavior differs only on a molecular scale, not in the macroscopic, convective dominated regime which applies for the atmosphere most of the time.

2.2.1 Basic Equations of Motion

In principle, the fluid motion in the atmosphere can be described by the *Navier-Stokes equation* for the wind or momentum transport, the heat transfer and the transfer of trace gases. But as turbulent motion has to be included, all variables have to be regarded as a mean part $\overline{x}$ and a fluctuating part x' denoted as the *Reynold's decomposition*:

$$x = \overline{x} + x' \ . \tag{2.29}$$

Finally, this yields a system of equations with more unknown parameters than equations. Thus, simplifications and assumptions, for example about the covariance terms,

will always be needed to determine a solution. In addition, we seek an estimate of the atmospheric fluxes with reasonable effort and hence, we will only consider a first-order closure here following *Foken* (2008) where a further detailed discussion of the system can be found.

The starting point for the *first-order* or *local closure* is, analogue to the soil system, the assumption that the vertical flux is proportional to the vertical gradient of the relevant state variable ξ. But according to the underlying eddy diffusion, the proportionality factor is called the "eddy diffusion coefficient" D_a. Therefore, the local closure is calculated from

$$\overline{u_i'\xi'} = -D_\mathrm{a}\frac{\partial \xi}{\partial z} \tag{2.30}$$

with u_i the horizontal wind component.

Usually, only the diffusion coefficient for momentum is distinguished from those for sensible heat, water vapor or other trace gases. They are related via the turbulent *Prandtl number* of ~ 0.8 for air:

$$D_\mathrm{a,m} = Pr_\mathrm{t} D_\mathrm{a,H/E}\ . \tag{2.31}$$

This finally yields for the momentum, the sensible heat and water vapor flux:

$$\overline{u'w'} = D_\mathrm{a,m}\frac{\partial \overline{u}}{\partial z}\ , \tag{2.32}$$

$$\overline{w'T_\mathrm{a}'} = D_\mathrm{a,H}\frac{\partial \overline{T_\mathrm{a}}}{\partial z}\ , \tag{2.33}$$

$$\overline{w'q_\mathrm{a}'} = D_\mathrm{a,E}\frac{\partial \overline{q_\mathrm{a}}}{\partial z} \tag{2.34}$$

with the vertical wind component w, the air temperature T_a and q_a the specific humidity in air.

2.2.2 Parameterization of Turbulent Diffusion Coefficients

For neutral stratification in the surface layer, the turbulent diffusion coefficient of momentum is given by

$$D_\mathrm{a,m} = \kappa z u_* \tag{2.35}$$

with the Karman constant $\kappa = 0.4$, the vertical height z [m] and the friction velocity u_* [m/s]. The latter can be calculated from the logarithmic wind profile by using

$$u(z) - u(z_0) = \frac{u_*}{\kappa}\ln\frac{z}{z_0} \tag{2.36}$$

with the height z_0 where the extrapolated wind profile $u(z_0)$ is zero.
This finally yields for the three fluxes

$$u_* = \kappa z\frac{\partial u}{\partial z} = \kappa\frac{\partial u}{\partial \ln z}\ , \tag{2.37}$$

$$\overline{w'T_\mathrm{a}'} = -\alpha_0\kappa u_*\frac{\partial T_\mathrm{a}}{\partial \ln z}\ , \tag{2.38}$$

$$\overline{w'q_\mathrm{a}'} = -\alpha_{0,\mathrm{E}}\kappa u_*\frac{\partial q_\mathrm{a}}{\partial \ln z} \tag{2.39}$$

with the coefficients $\alpha_0 = \alpha_{0,\mathrm{E}} = 1/Pr_\mathrm{t} \approx 1.25$.

Transferring these equations to kinematic units of $\mathrm{W/m^2}$, the sensible heat flux H in air can be calculated as

$$H = c_{\mathrm{p,a}} \rho_\mathrm{a} \overline{w' T'_\mathrm{a}} \tag{2.40}$$

with $c_{\mathrm{p,a}}$ the specific heat of air for constant pressure and ρ_a the air density.
For the latent heat of evaporation E, this yields analogous

$$E = \rho_\mathrm{a} \lambda \overline{w' q'_\mathrm{a}} \,, \tag{2.41}$$

$$= \rho_\mathrm{a} \, \lambda \, \frac{0.622}{p_\mathrm{a}} \, \overline{w' \, e'_\mathrm{a}} \,, \tag{2.42}$$

where e_a [kPa] denotes the water vapor pressure in air and p_a [kPa] the barometric air pressure.
For completion, the relation between the water vapor pressure in air and the typically measured relative humidity rh [%] is given by

$$rh = 100 \cdot \frac{e_\mathrm{a}}{e_0(T_\mathrm{a})} \tag{2.43}$$

and $e_0(T)$ is again obtained from equation (2.23).

Strictly speaking, these flux equations are only valid in dynamic sub-layers where the influence of thermal stratification can be neglected. This is usually not the case during the day, but can be assumed for calculations on a daily mean basis. However, *Monin and Obukhov* (1954) extended these equations to non-neutral conditions by characterizing a characteristic length to relate the dynamic, thermal and buoyancy processes with the height of the sub-layer. A review of this approach can be found in *Foken* (2006).

2.3 Soil-Atmosphere Coupling

The Earth's surface is the main energy transfer area (*Foken*, 2008) and the water and energy cycle in the soil and the atmosphere are linked by the exchange processes occurring there. After discussing the transport processes separately for both compartments, the focus of this last section is on their coupling from a field scale perspective.

2.3.1 Energy Balance at the Earth's Surface

A cross-section through the soil-atmosphere continuum is sketched in Figure 2.2. The net energy entry R_n is partitioned at the soil surface into the ground heat flux G, the sensible heat flux H in air and the portion ET that is used to evaporate water from the soil surface or the plant leaves. Writing this as an energy conservation equation at the surface yields

$$R_\mathrm{n} + H + G + ET \ + \Delta Q = 0 \,, \tag{2.44}$$

where ΔQ represents further the energy storage in the air, the plants and the soil. Following *Foken* (2008), we will stick to the convention that radiation and energy fluxes are positive, if they transport energy away from the soil surface (into the atmosphere or the ground), otherwise they are negative.

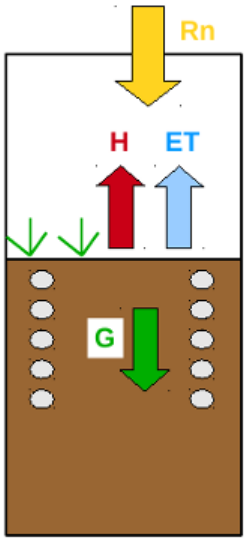

Figure 2.2: Surface Energy Balance. The incoming net radiation $R_\mathrm{n}$is balanced by the sensible heat fluxes of the ground G and in the air H and the energy ET removed due to the evaporation of water from the soil surface and the plant leaves. The dots indicate the typical instrumentation of water content and soil temperature profile measurements.

The ground heat flux (Eq. (2.17)) as well as the sensible heat flux in the atmosphere (Eq. (2.40)) and the evaporation flux from the soil surface (atmospheric perspective: Eq. (2.42), perspective from the soil side: Eq. (2.25)) are already defined within the process descriptions in the respective compartment above. Only the net radiation has not yet been introduced in detail which will be done in the following paragraph.

Net Radiation

The radiation in the atmosphere is divided in to shortwave (solar) and longwave (heat) radiation (e. g. *Foken* (2008)). The wavelength of the longwave radiation is defined above the visible red and has a wavelength larger than $1\,\mu$m. The net radiation entry R_n at the surface is the sum of all the in- and outgoing radiation entries and can be written as

$$R_\mathrm{n} = S\uparrow + S\downarrow + L\uparrow + L\downarrow \ . \tag{2.45}$$

The surface albedo is defined as the ratio between the incoming and outgoing shortwave components:

$$a = \frac{S\uparrow}{S\downarrow} \ . \tag{2.46}$$

Furthermore, the outgoing long-wave radiation fluxes can be determined according to *Stefan-Boltzmann law*:

$$L\uparrow = \epsilon_\mathrm{IR}\sigma_\mathrm{SB}T_0^4 \ , \tag{2.47}$$

where the Stefan-Boltzmann constant is given by $\sigma_\mathrm{SB} = 5.67 \times 10^8\,\mathrm{W\,m^{-2}\,K^{-4}}$ and the emissivity for different land covers ranges from 0.986 for thick green grass to 0.949 for dry fine sand (*Geiger et al.*, 1995).
For the calculations in this work, a mean value of $\epsilon = 0.96 \pm 0.04$ is used for all types of surface cover and the error in the actual emissivity of the soil surface is assigned to the overall measurement uncertainty.

Potential Evapotranspiration

Direct measurements of the evaporation flux can not be easily achieved. Water content measurements in the soil need to be scaled by the hydraulic properties to calculate the fluxes. Yet at that point, the characterization of the soil system is further challenged due to the non-linear nature of the soil water dynamics and hence, close to the surface the gradients might be rather steep.
Looking from the atmosphere, this task is comparably hard, since its transport regime is turbulent and a closure of the equations is hardly achieved, even by advanced eddy-covariance measurements (*Foken*, 2008).

Therefore, *Allen et al.* (2006) proposed an approach to estimate the *potential evapotranspiration* rate λET_0 from a grass surface under reference conditions, meaning a defined grass height and unlimited water availability at the surface. This rate combines therewith tow separate processes: (i) the evaporation of the water from the soil surface, and (ii) the transpiration from the plant leaves. Considering the principal weather parameters that

influence the evapotranspiration rate yields an estimate for the evaporation power of the atmosphere under these conditions over the standardized vegetated surface. Afterwards, this upper limit has to be scaled by site specific characteristics to end up with an actual estimate.

The considered atmospheric measurements are the net radiation, the air temperature, humidity and wind speed. From this, the potential evapotranspiration rate can be calculated from the *FAO Penman-Monteith* equation given by

$$\lambda ET_{0,\mathrm{PM}} = \frac{\Delta(R_\mathrm{n} - G) + \rho_\mathrm{a} c_\mathrm{p} \frac{(e_0(T_\mathrm{a}) - e_\mathrm{a}(T_\mathrm{a}))}{r_\mathrm{a}}}{\Delta + \gamma \left(1 + \frac{r_\mathrm{s}}{r_\mathrm{a}}\right)} \,. \tag{2.48}$$

Most of the quantities were already introduced before, despite of the psychrometric constant γ and Δ which denotes the slope of the saturated water vapor pressure curve, given by the Magnus' formula (Eq. (2.23)).

The expression itself can be deduced from the surface energy balance combined with the flux formulas for the sensible heat flux H (Eq. (2.40)) and the latent heat flux E (Eq. (2.42)). The exact derivation can be found in the appendix A.2.

Looking from the atmospheric side, a direct calculation of the evaporation flux at the soil surface is not possible due to the missing information about the water vapor pressure directly at the soil surface. Actually, this would be the correct quantity to be considered in the water vapor pressure deficit in the numerator of equation (2.48). As the soil moisture directly at the surface is also unknown, the approximation to assume a saturated soil surface was made. Since the soil surface temperature is usually not known either, an even further simplification was necessary. Finally, the water vapor pressure deficit is calculated purely for within the atmosphere, not considering directly the state of the soil at all. As already mentioned, its impact will than afterwards be included by various scaling factors due to the actual vegetation cover and the hydraulic state of the upper soil layer to end up with a reliable estimate for the actual evaporation flux (*Allen et al.*, 2006).

Potential Partitioning in Evaporation and Transpiration

From the Penman-Monteith equation, a flux estimate is calculated which is the sum of the potential evaporation and the potential transpiration of a reference grass surface. *Campbell and Norman* (1998) proposed the ratio τ which allows to estimate the separation into the two distinct components:

$$E_0 = \tau ET_0 \,, \tag{2.49}$$

$$T_0 = (1 - \tau) ET_0 \,. \tag{2.50}$$

Therein, τ is defined as the fraction of incident radiation τ [-] that reaches the soil surface and is not intercepted by the canopy. This in turn can be estimated from

$$\tau = \exp(-kL) \,, \tag{2.51}$$

where k [-] is the extinction coefficient which can be assumed to be constantly 0.398 (*Ritchie*, 1972) and the leaf area index L which can be empirically calculated for grassland according to *Menzel* (1997) as

$$L = -1.552 + 51.188 h_{\mathrm{g}} - 74.967 h_{\mathrm{g}}^2 \tag{2.52}$$

with the grass height h_{g} [m] which is assumed to be 0.12 m for the reference grass.

But again, this separation yields also the upper limit for each component and the actual values will be considerably smaller, especially for an unsaturated soil surface and hence, a dry upper soil layer.

2.3.2 Exchange Processes between Soil and Atmosphere

In the following, three steady-state scenarios of the coupling processes between soil and atmosphere will be discussed, thereby increasing the system's complexity stepwise from no-flow conditions in the beginning. The key controls in the system are the water vapor pressure and the temperature. Therefore, we will analyze profiles of them in the soil and the air above, as well as directly across the boundary layer at the soil surface.
Starting from thermal and hydraulic equilibrium, the influence of a constant water vapor gradient between the soil surface and the air will be discussed which induces an evaporation flux. This situation corresponds to the steady-state or the mean state during the laboratory evaporation experiments later on. Afterwards, an additional energy entry, e. g. by net radiation, is added at the surface as found under field conditions. Yet, the system's state is still considered to be stationary an hence, wind and cyclic changes in net radiation, that cause cyclic temperature and relative humidity variations, are neglected in first order.

No-Flow Condition

The no-flow conditions in Figure 2.3 set the starting point for our analysis. The hydraulic regime on the left side of the graphics is represented by the water vapor pressure in air and the matric potential in the soil, both denoted by ψ. The thermal regime is illustrated by the temperature profiles on the right side. We distinguish three layers: the soil on the bottom, the air above, and in-between a boundary layer or transition zone where the final exchange processes take place. Each layer is characterized by its thermal and hydraulic conductivity, K_{h} and K_{w}, respectively. The index corresponds to the transported quantities, heat and water. As already mentioned above, the hydraulic conductivity in the soil is a function of the matric potential (Eq. (2.14)) which results in a non-linear soil water dynamics. In contrast, the thermal regime in both compartments is linear, at least in a first-order approximation of the transport processes in the atmosphere (Eq. (2.39)).

No-flow conditions denote the state for which the system is in hydraulic and thermal equilibrium, meaning no fluxes occur between the different layers. As we consider the fluxes to be proportional to the gradients in the respective quantity, all temperatures in the system are equal. The same is true for the water vapor pressure between the upper

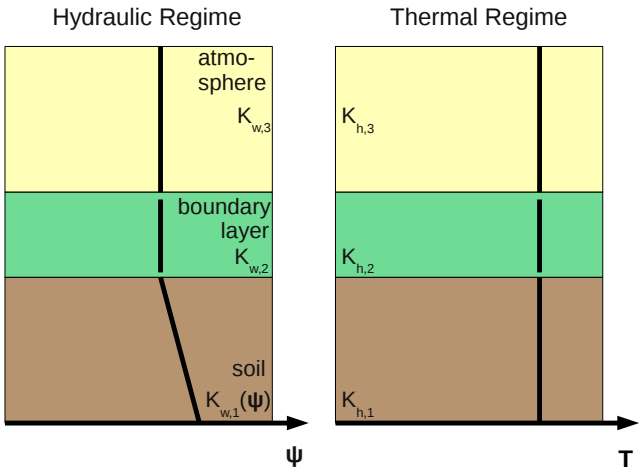

Figure 2.3: No-flow conditions in the soil-atmosphere continuum. *left:* Water potential distribution. In air represented by the water vapor pressure, in the soil by the matric potential, both denoted by ψ. *right:* Temperature profile. As there are no gradients in temperature and water potential, there is no transport of heat and water across the soil-atmosphere transition zone. The linear decrease in the matric potential is finally balanced by the opposite gradient in the gravitational potential. The sum of both is the final water potential.

part of the soil layer, the boundary layer, and air above. Only in the soil, where the matric potential is plotted, we find a linear decrease from the bottom of the soil layer towards the top. The reason for this is that the water flux is proportional to the gradient in the water potential (Eq. (2.2)) which is the sum of the matric and the gravitational one. Since the hydraulic steady-state or no-flow condition in the soil implies

$$\partial_z(\psi_\mathrm{m} + \psi_\mathrm{g}) = 0 \tag{2.53}$$

and the the gravitational potential is linear in the depth z, this yields that the matric potential is also linear, but in the opposite direction.

Surface Evaporation without Radiative Forcing

A gradient in the water vapor pressure between the air (Eq. (2.43)) and the top of the boundary layer (Eq. (2.22)) is also called a water vapor pressure deficit in air. This results in an evaporation flux E from the soil surface (Eq. (2.42)). The water is supplied by the corresponding soil water flux towards the surface. For a fixed water table, the gradients close to the surface become increasingly steep, while the soil gets drier. The phase change removes energy from the surface layer and causes a decrease in the surface temperature. The energy sink is balanced by a sensible heat flux from the ground G (Eq. (2.17)) and the air H (Eq. (2.40)) according to the temperature gradients towards the surface and

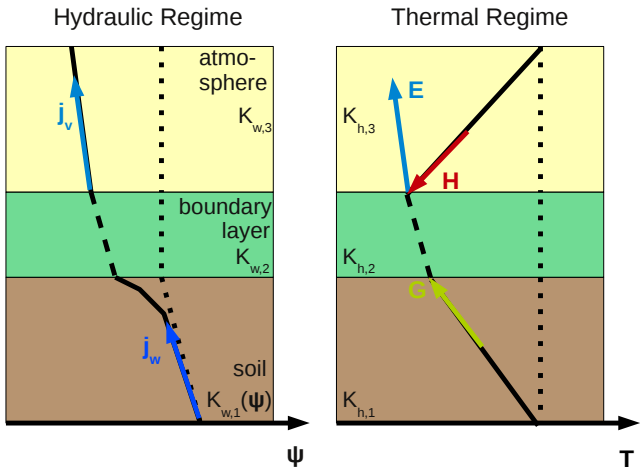

Figure 2.4: Thermal and hydraulic regime in the soil and the atmosphere during surface evaporation. *left:* Water potential distribution. In air represented by the water vapor pressure, in the soil by the matric potential, both denoted by ψ. *right:* Temperature profile. *Dotted lines* indicate the initial equilibrium state. Due to a water vapor pressure gradient in air, water evaporates from the soil surface. The evaporation flux j_v is supplied by a corresponding water flux j_w from within the soil. The phase change causes an energy sink $E = j_\mathrm{v}\lambda\rho_\mathrm{w}$ at the surface which is balanced by a ground heat flux G and a sensible heat flux H in air.

the respective thermal properties of the different compartments.

In particular during stage 1 evaporation, when the evaporation flux is almost constant for constant air temperature and water vapor pressure, the conditions sketched above are similar to those we finally find during the evaporation experiments in the laboratory. Therefore, we will come back to this scenario in chapter 4. Characterizing the thermal and hydraulic properties of all compartments according to the experimental set-up and using the transport equations from the sections before should finally yield a complete quantitative description of the coupled system.

With respect to the reconstruction of surface information from measurements within the soil, the boundary layer is the crucial. *Schneider-Zapp et al.* (2010) stated for laboratory evaporation experiments under similar conditions as sketched in Figure 2.4 that the soil surface cannot be regarded as an interface, but forms a layer with distinct material properties. Yet, a projection from, e. g. the topmost measurement, within the soil towards the surface must assume constant thermal properties up to the lower end of the atmosphere. If this is not the case, the projection will not agree with the measured surface temperature gained for example from an infrared thermometer looking from above onto the surface. In particular for vegetated surfaces, where the sensor detects a mean signal

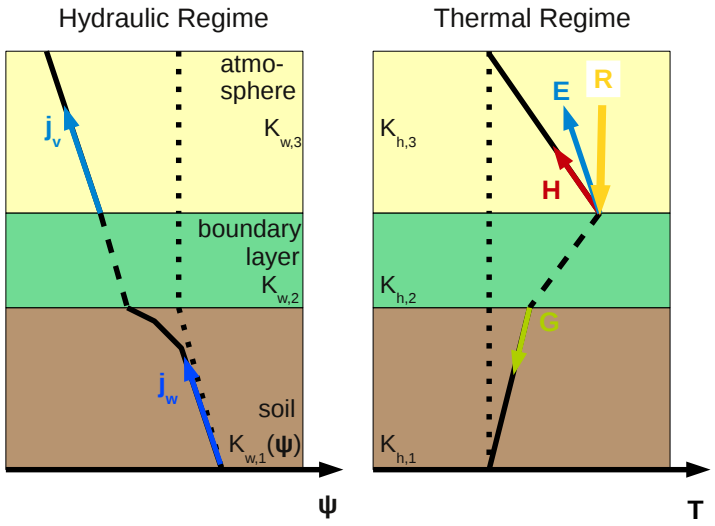

Figure 2.5: Thermal and hydraulic regime in the soil and the atmosphere for surface evaporation and an additional net energy entry. *left:* Water potential distribution. In air represented by the water vapor pressure, in the soil by the matric potential, both denoted by ψ. *right:* Temperature profile. *Dotted lines* indicate the initial equilibrium state. The additional net energy entry R at the surface exceeds the energy removal due to evaporation. Therefore, the sensible heat fluxes G and H change direction and heat is transported into the soil and the air. All temperatures will increase and this has a back-coupling effect on the water vapor pressure deficit between the soil surface and the air which will finally result in an enlarged evaporation flux j_v compared to the scenario before, except the water could not be supplied by the soil.

emitted from the plants and the soil in between, there might be a discrepancy between the reconstructed and measured surface temperature according to the difference in the thermal properties of the different layers.

Surface Evaporation with Radiative Forcing

Under field conditions, the coupling processes are even more complex due to the additional heat entry by radiation. In the last scenario, we consider the net radiation R to provide more energy at the surface than actually removed by the evaporation process (Fig. 2.5). Due to the additional energy entry the temperature at the surface is now higher than in the air above and the soil below. Therefore, the direction of the sensible heat fluxes. H and G, change and both compartments are warmed by the heat that is transported away from the surface. The higher temperatures themselves have a back-coupling effect on the evaporation flux which will increase as the water vapor pressure deficit between the surface and the atmosphere is increased. This is of course only possible, if at the same time the soil can provide the requested water to the surface layer.

Otherwise, the evaporation flux cannot enlarge and the energy will cause a further rise in the surrounding temperatures.

Altogether, the two evaporation scenarios reveal the key controls of the surface coupling between the hydraulic and thermal regime. A water vapor pressure deficit $e_a - e_{surf}(\psi_m, T_{surf})$ between the air and the surface results in an evaporation flux from the surface under the prerequisite that water can be supplied from deeper down in the soil. Yet, the water vapor pressure deficit is a function of the temperature due to Kelvin's equation (2.22). Furthermore, the energy sink due to the phase change results in a temperature decrease. A stationary system will exhibit a balance between the evaporation flux at the surface, its water vapor pressure and temperature. In addition, the energy removed from the surface has to be supplied from the surrounding and hence the sensible heat fluxes have to be also consistent with their temperature gradients in the soil and the atmosphere.

For natural forcing, the water vapor pressure in air is changing due to the convective or turbulent vapor transport by the wind. Besides, the energy supply and therewith all temperatures change on a daily and yearly cycle, and on scales in between due to the actual weather conditions. In combination with the non-linearity of the soil water dynamics, an exact description of the system with a closed energy balance at the surface is hardly achievable. Even with measurements that resolve turbulence, the thermal and hydraulic characterization of the soil, the atmosphere and the related surface layer will always be a challenge.

3 Soil Temperature Projection Method

In the following chapter, a method will be introduced to infer information about the surface temperature from soil measured temperature profiles. This means a reversion of the heat diffusion process in soils which is the main energy transport mechanism. The motivation is a better characterization of the surface energy partitioning and the corresponding surface fluxes. For this purpose, a new method was developed to project the information from within the soil upwards to reconstruct the temperature signal directly at the surface.

From a mathematical perspective, the problem is ill-posed and already for a long time structurally investigated by various disciplines in distinct contexts (Sec. 1.2.1). In the following, a new approach is introduced and main steps and criteria for a stable and reliable reconstruction will be discussed on the basis of a synthetic data-set. Its application and performance for laboratory and field measured data-sets is postponed to the later chapters.

3.1 Frequency Analysis of Soil Temperature Profiles

An intuitive analysis of heat conduction in soils is given for a simple surface temperature signal, superposed of two sine-functions given by

$$T(0,t) = 20 + 5\,\sin(2\pi f_1 t) + 2\,\sin(2\pi f_2 t)\;, \tag{3.1}$$

where t is the time in hours and the frequencies are exemplary chosen as $f_1 = (24\,\mathrm{h})^{-1}$ and $f_2 = (6\,\mathrm{h})^{-1}$. A section of the modeled soil temperatures at various depths is shown in Figure 3.1. As already mentioned, the underlying numerical model assumes pure heat conduction in a homogeneous soil profile with constant thermal diffusivity and the forcing at the soil surface is given be equation (3.1).
Comparing the extrema with depth, the amplitude decreases and an increasing phase shift can be noticed. The fact that the 24 h-cycle is still resolvable below a depth of 30 cm whereas this pertains not for the 6 h-cycle suggests that the amplitude damping is frequency-dependent.

Following *Carslaw and Jaeger* (1959), an analytical solution of the heat diffusion equation (2.19) can be deduced for a periodic temperature forcing at the surface

$$T(0,t) = \int_0^\infty \alpha(\omega,0)\,\sin(\omega\,t + \phi(\omega,0))\;\mathrm{d}\omega\;, \tag{3.2}$$

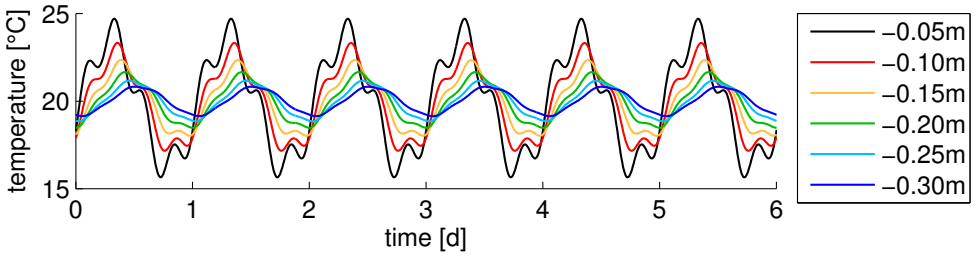

Figure 3.1: Section of synthetic soil temperatures in different depths for pure heat conduction in a homogeneous soil profile and a superposition of two sine-functions (Eq. (3.1) as surface forcing. With depth, the temperature amplitudes decrease and the variations are increasingly phase shifted.

where $\alpha(\omega, 0)$ and $\phi(\omega, 0)$ denote the amplitude and phase of frequency ω at the surface. Hence, we end up with an expression for the temperature signal in a certain depth z

$$T(z,t) = \int_0^\infty \alpha(\omega,0)\exp(-kz)\,\sin(\omega\,t + [\phi(\omega,0) - kz])\,\mathrm{d}\omega\,, \tag{3.3}$$

where

$$k = \sqrt{\omega/(2D_\mathrm{h})} \tag{3.4}$$

describes the projection factor [1/m] dependent on frequency and the soil thermal diffusivity D_h. The analytic expression (3.3) shows that the damping of the amplitudes is exponential with depth, since $\alpha(\omega, 0)$ is scaled by $\exp(-kz)$. Furthermore, the linear increase of the phase shift is stated by the addition summand in the sine-argument.

Starting from equation (3.4), we can further define the penetration depth d_p of a certain frequency component via

$$d_\mathrm{p}(\omega) = -\frac{1}{k(\omega)} \cdot \ln\left(\frac{\alpha_\mathrm{crit}}{\alpha(\omega,0)}\right), \tag{3.5}$$

where α_crit is the critical amplitude that can be resolved within the system. In our experiments, the sensors have a typical resolution of $\pm 0.2\,^\circ\mathrm{C}$. Therefore, this value is used for approximations, if nothing different is stated.

Transforming soil temperatures of various depths to Fourier space yields spectra of the amplitude and phase information over frequency for each depth. Figure 3.2 shows some amplitude spectra corresponding to the soil temperatures in Figure 3.1. In both figures, the color coding corresponds to the same depth. The dashed lines indicate the amplitude damping over frequency and depth. At the surface, the amplitude of the daily cycle was $5\,^\circ\mathrm{C}$ (Eq. 3.1). Hence, the loss of information is much stronger for high frequency components and only lower frequencies can be resolved at greater depths.
The final goal is to reconstruct surface temperatures from profile measurements within

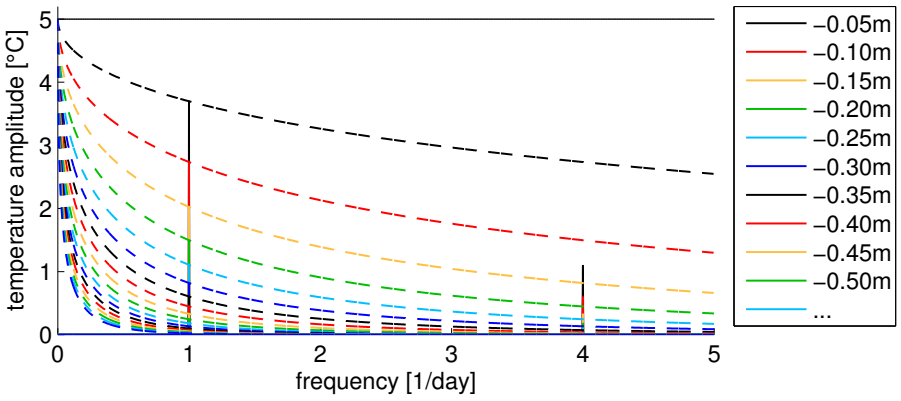

Figure 3.2: Amplitude spectrum of synthetic soil temperature profile (Fig. 3.1). *Solid lines:* Amplitude spectra from Fourier analysis. *Dashed lines:* Exponential decrease of information content with depth and frequency for an amplitude of 5 °C at the soil surface. To reconstruct the temperature signal at the surface, the amplitude spectrum in a certain depth has to be increased exponentially to revert the loss of information.

the soil. Hence, the unstable nature of the mathematical problem becomes already evident due to the frequency-dependent scaling factors of the amplitudes. The information in the soil has to be increased exponentially to reproduce the original surface amplitude. But, spectral noise might as well been amplified by the same factor. Therefore, we have to establish a selection criterion to distinguish between signal and noise components in frequency space in order to succeed in a stable reversion of the heat diffusion process and the reconstruction the surface temperature signal. In the following paragraphs, the projection method proposed here will be explained based on synthetic data. Its applicability and performance for measured data-sets will be discussed later in the context of laboratory experiments (Sec. 4.2.2 and 4.3.3) and measurements at the field scale (Sec. 5.4)

In this section, the surface temperature reconstruction will be introduced and demonstrated for a synthetic data-set of one year. It was generated by the *COMSOL* (2008) *Multiphysics* diffusion module, assuming a homogeneous soil profile with a constant thermal diffusivity $D_\mathrm{h} = 1.0 \times 10^{-6}\,\mathrm{m^2/s}$. Only a 1.5 m-deep profile will be analyzed in the following. But to avoid disturbances from the lower boundary, the bottom of the simulated profile was set to a depth of 10 m. At the lower boundary, the mean surface temperature was used as a constant Dirichlet boundary condition in order to introduce no net soil heat flux into the profile. In order to achieve the most reliable frequency composition of the temperature signals, we used a measured soil temperature time-series from one of our field sites as an upper boundary condition.
The simulation result is shown in Figure 3.3. Again, the fast temperature variations at the surface are damped away within the upper 0.5 m and only the long-term fluctuations,

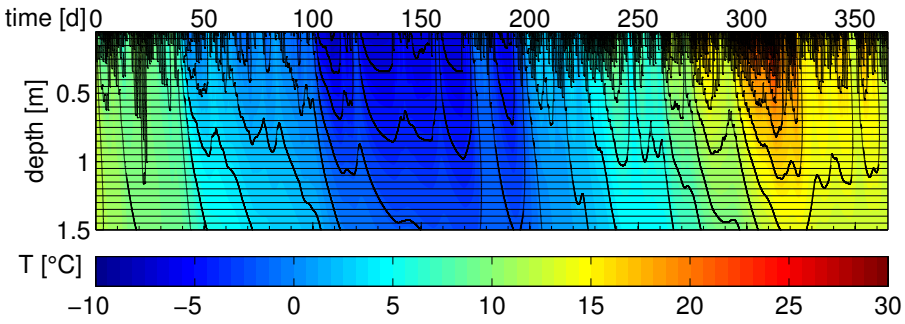

Figure 3.3: Synthetic soil temperature data of one year. Heat is purely transported by conduction and the soil profile is assumed to be homogeneous with $D_\mathrm{h} = 1.0 \times 10^{-6}\,\mathrm{m}^2/\mathrm{s}$. At the upper boundary, the forcing was set to a field-measured soil temperature time-series.

such as seasonal variations, penetrate to deeper soil levels. We should be aware that this data-set contains no "non-conductive" processes like advective energy transport from rain events or additional energy entries or removals due to phase changes, like freezing, thawing, or the evaporation of water.

The first step is to transform this data-set into Fourier space. Therefore, each temperature time-series is centered and the subsequent *Fast Fourier Transformation* (FFT) yields spectral information of all frequencies comprised in the temperature signal. Due to the amount of entries in the amplitude spectra (Fig. 3.4(a)), the challenge is to distinguish those that are significant for the signal's characteristics from those being noise, e. g. due to numerical diffusion.
For real experimental data, a good starting point is the noise level in our temperature probes. As their resolution in time domain is assumed to be $\pm 0.2\,^\circ\mathrm{C}$, we apply this criterion here as a first guess.
The next step is to translate this noise handle to Fourier space or to find a similar measure. At this point, our heuristic approach is to sort the amplitude spectrum of the uppermost sensor in decreasing order. An example is shown in Figure 3.4(b). One remark concerning the unit of the amplitude spectra: In the context of this work, we do not retain the convention of plotting power spectra [$^\circ\mathrm{C}^2$]. Instead, the amplitudes in frequency space are considered in units of temperature [°C] by normalizing the original Fourier components by the number of frequency entries and taking the angle and the absolute value of these values for the further analysis. This allows the direct usage of the noise level estimated in time space. Hence, the resolution of the temperature data can be treated as a threshold to distinguish in the spectrum noise from significant information.
A first, naive approach was to denote all frequencies with amplitude components below $0.2\,^\circ\mathrm{C}$ as noise. However, this proved to be too restrictive and resulted in a loss of too many characteristic features of the signal. Instead, the final procedure is to first sort the amplitude spectrum in decreasing order and afterwards to sum up all amplitudes starting

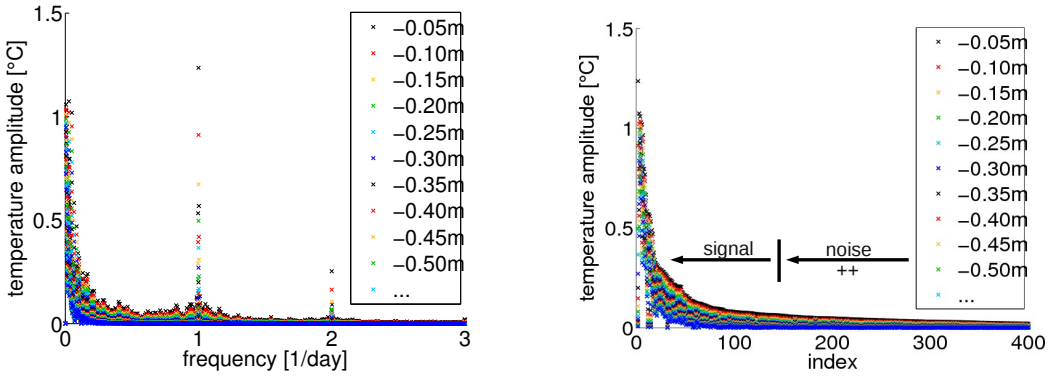

(a) Amplitude spectra of synthetic soil temperature profile of one year.

(b) Sorted spectra divided in components which are significant and those denoted to be noise.

Figure 3.4: The amplitude entries in the spectrum of the uppermost sensor are sorted in decreasing order. Starting from the smallest, these amplitude entries are summed up, until a preset noise level is reached. This yields a criterion to distinguish between signal and noise components.

from the smallest until a certain threshold of the pre-defined noise level in time domain is reached. This procedure was deemed to be a good measure to skip all frequency components too small to provide valuable information about the signal. At the same time, it allows many small scale structures to still be present in the remaining spectrum. This criterion was established as most appropriate for our application. It seems to have the right degree of accuracy to capture all significant temperature features resolved by the measurements, where the absolute accuracy of our sensors is assumed to be $\pm 0.5\,^{\circ}\mathrm{C}$ and their resolution $\pm 0.2\,^{\circ}\mathrm{C}$. The concrete impact of this criterion is demonstrated in more detail for the laboratory data-sets in the following chapter.

3.2 Estimation of the Soil Thermal Diffusivity

Once decided which frequency components are significant for the corresponding temperature signal, the corresponding profile information is used to estimate the projection factor k and therewith determine the soil thermal diffusivity D_h of the underlying soil.
Equation (3.3) describes the exponential decay of the amplitude with depth and the linear shift of the phase proportional to the factor $k = \sqrt{\pi f / D_\mathrm{h}}$. Hence, extracting the phase and amplitude information of the temperature time-series in each depth by Fourier analysis allows us to estimate the projection factor k, as the absolute values of phase and amplitude for all frequencies and all depths are obtained. In conclusion, we can perform a linear regression on the profile information, the phase and the natural logarithm of the amplitude of all significant frequency components.

All frequency information, declared as significant in the sorted amplitude spectrum, is used in the linear regression procedure. Hence, the fitting data consists of frequency scaled phase and log-amplitude values from the essential part of the spectra

$$\left\{ \frac{\log(\alpha(f_i, z_j))}{\sqrt{\pi f_i}},\ \frac{\phi(f_i, z_j)}{\sqrt{\pi f_i}} \right\},\ i = 1,\ \ldots,\ N,\ j = 1,\ \ldots,\ M\ , \tag{3.6}$$

where N is the number of significant frequency entries and M the number of measurement depths in the profile.
We assume the information content of the data to decrease with depth proportional to

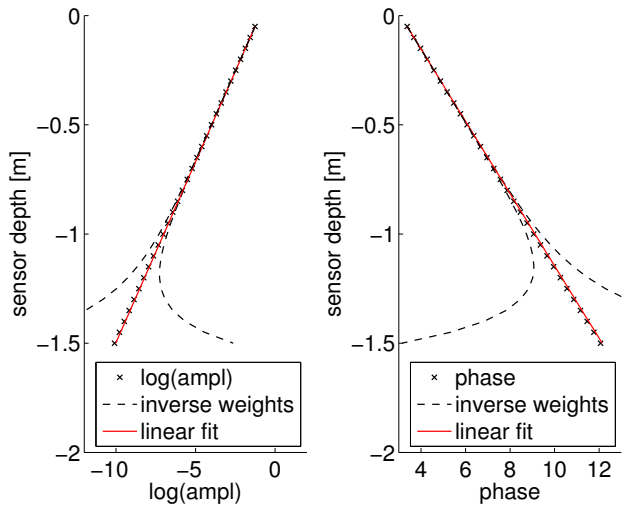

Figure 3.5: Estimation of thermal diffusivity from synthetic soil temperature profile of one year. Noise level was set to 0.2 °C. Fit results are exemplary for profile information of the daily cycle. *left:* Linear fit (*red*) of log-amplitude data (*crosses*). *right:* Linear fit (*red*) of phase profile data (*crosses*). *Dashed lines* indicate inverse weights used within regression procedure, reflecting information loss with depth.

the increase of the damping factor of the amplitude. As a consequence, we will use a weighted form of the linear regression scheme to take this loss into account. Thus, the weights for each frequency and measurement depth are implemented as the exponential scaling factor of the amplitude

$$w(f_i, z_j) = \exp(-k_\mathrm{w}(f_i) z_j), \tag{3.7}$$

where $k_\mathrm{w}(f_i) = \sqrt{\pi f_i / D_\mathrm{h,ts}}$ defines a representative projection factor for each frequency with a fixed thermal diffusivity $D_\mathrm{h,ts} = 1.0 \times 10^{-6}\,\mathrm{m^2/s}$ in the order of magnitude of a typical soil. For the daily cycle comprised in the synthetic data-set, the log-amplitude and phase profiles are plotted as crosses in Figure 3.5. The red line indicates the fit derived by the linear regression and the dashed lines illustrate the inverse weights with depth.

From the spectrum (Fig. 3.4(a)), the amplitude of the daily cycle can roughly be determined as 1.3 °C. Therefore, the penetration depth $d_\mathrm{p,day}$ of the daily cycle can be estimated by

$$d_\mathrm{p,day} = -k_\mathrm{p}^{-1}(86400^{-1}\,\mathrm{Hz}) \cdot \ln\left(\frac{0.2\,^\circ\mathrm{C}}{1.3\,^\circ\mathrm{C}}\right) \approx 0.31\,\mathrm{m}, \tag{3.8}$$

and we would expect to have a significant amplitude entry for the daily cycle in the spectra of the upper part of the profile. Below, noise dominates the amplitude values, whereas the situation for higher frequency components is even more problematic, as they are already damped away to a greater degree. Substantial information about fast temperature fluctuations can therefore only be extracted from more shallow parts of the soil profile.
As we have investigated so far synthetic data only, the increase in phase and logarithmic decay of the amplitude for the daily cycle shown in Figure 3.5 is almost perfectly linear over the whole profile. Hence, the linear fit describes the complete data adequately. However, we could not resolve log-amplitudes below −1.6 m in real experimental data, which corresponds to temperature amplitudes below the convenient sensor resolution of 0.2 °C. In general, it turned out that the frequency analysis is able to extract information even with amplitudes below an objectively chosen noise level of the data-set itself. Therefore, two assumptions have to be fulfilled. Firstly, the data-set itself has to be long enough, so that the respective frequency can be detected reliably. And secondly, this works only for frequencies which are solid and omnipresent in the data, without abrupt changes in phase for example. This implies that these fluctuations are caused by “fundamental reasons”, e. g. the Earth’s rotation, which causes the daily and yearly cycle. For changes in weather conditions on medium or even smaller time scales, which happen abrupt or introduce frequencies which have no stable phase relation, this is not not the case. But for the fundamental harmonics in the system, their steady impact is in a sense “locked-in“ and thus seems to be detectable even with amplitudes below the noise level.

The uncertainty bounds and thus the weights for the regression scheme are chosen very “defensively”. For the daily cycle in the synthetic data, Figure 3.5 reveals that the weights seem to influence the profile information only below 0.8 m significantly, whereas

the penetration depth was estimated above as $\sim 0.3\,\mathrm{m}$. Hence, these reduce the influence of data points which are clearly below the underlying noise level only. From our experience so far, this seems to be restrictive enough to keep the whole estimation procedure and later on the surface temperature reconstruction stable, also for real data-sets. This in turn prevents us to interfere the procedure with harder restrictions.

In the final step, the projection factor k estimated by the weighted linear regression can be used to derive the soil thermal diffusivity D_h through the following expression

$$D_\mathrm{h} = \left(\frac{\pi\, f}{k}\right)^2 . \tag{3.9}$$

For the complete synthetic data-set of one year, this yields a value of $0.999 \times 10^{-6}\,\mathrm{m}^2/\mathrm{s}$, which is negligible $0.1\,\%$ off the true value and thus indicates a very good performance of the overall regression.

For the estimation of the thermal diffusivity, the influence of the separation criterion between signal and noise components seems to be negligible. For a threshold of $0.2\,^\circ\mathrm{C}$ nearly 5000 frequency entries are considered for the fitting routine. If this noise level is divided by two, the linear regression will be based on more than 8000 frequency components. If it is chosen ten times larger, only 800 will be considered. But finally the estimated D_h changes only on the fourth decimal. The implications of different frequency contents on the reconstructed surface signal are however not negligible and will therefore be discussed again in the next paragraph.

In the following, two additional points will be emphasized in the context of estimating the projection factor and hence the thermal diffusivity. Even if the profile information is weighted to account for the decreasing information content, both types of data, phase and amplitude, have to be considered in the fit. The estimated parameters become notably worse by using for example only the amplitude information. This results in an up to ten percent larger deviation from the true value. The same effect is detected, if only one frequency component, e. g. the daily cycle which will be significant for most real data-sets, is considered in the regression procedure. Once the spectral entries are defined as noise or signal components, the procedure is stabilized by the fact that many independent frequencies are considered within the fit. All these components contain valuable information, which, of course, has to be weighted, but in the end improves the reliability and reduces the uncertainty of the final parameter k or D_h.

The quality of the fit can finally not easily be specified by standard statistical means as part of the data was log-transformed beforehand. Thus, measures, e. g. to estimate confidence limits, cannot be easily applied to characterize the quality of k, and moreover that of D_h. As the thermal diffusivity is the quadratically inverse of k (Eq. (3.9)), the underlying statistics become too complex and were not further pursued in this work. Ignoring the log-transformation of the amplitude data in the fit, one could think that it might be possible to transform the straight-forward-estimate for the confidence limits of k directly to an confidence interval for D_h ending up with an appropriate measure. But especially for the measured data-sets, their order of magnitude was two or even three times

smaller compared to the estimated value. Comparing those fits and the corresponding data just by eye, we would state the real accuracy to be significantly worse. Hence, the detailed analysis of the synthetic test case presented in this chapter serves for the moment as the only way to evaluate the performance and limits of the method presented here.

3.3 Reconstruction of the Surface Temperature

The linear regression of the spectral profile data allows in a next step to extrapolate this information towards the soil surface. The linear fit of the log-amplitude and phase profiles for each frequency is therefore extended at the upper end towards $z = 0$. This yields estimated surface spectra for phase and amplitude. Afterwards, these estimates are transformed back for all frequencies to the time domain which provides ideally a reconstruction of the original surface temperature signal from the time-series measured within the soil. This sounds rather simple, but we should keep in mind that projecting back a diffusion process is an ill-posed mathematical problem. Until this step, we had to come up with the essential idea how to distinguish between signal and noise components in Fourier space to have a reliable frequency basis for further analysis steps (see Section 3.1). In addition, a criterion was necessary to account for the decreasing information content with depth, but at the same time considering enough information to get the linear fit stable and hence a reliable estimate of the projection factor k (see Section 3.2). Finally, all these considerations led to a procedure that indeed allows the stable reconstruction of the surface temperature signal for pure diffusive heat transport in soils which was the driving force of the analyzed soil temperature signals.

In the upper part of Figure 3.6(a), the actual and reconstructed surface temperature for the synthetic data-set of one year are drawn. Below, the corresponding residual between data and projection is illustrated. By eye, the projection result overlays almost perfectly the surface temperature data. Between day 100 and day 160, deviations are minimal, since the corresponding amplitudes in the temperature signal are smallest. The root-mean-squared error (rmse) of 0.02 °C. This is an order of magnitude below the assumed noise level to distinguish between signal and noise components. Therefore, all significant frequency components of actual surface temperature signal are incorporated with right proportion and the overall residual looks mainly like white noise. However, we should note from the residual in Figure 3.6(b) calculated for the hourly mean values of the true and reconstructed time-series that the noise level is to some extent caused by a slight error in the reversion of the phase shift. The deviations are only half size, if we compare the mean temperature signals on a larger interval compared to the measured. As we will never fit the projection factor k and D_h completely correct, the reconstruction will not be judged in the further analysis on the same time resolution as it is calculated, but on a slightly coarser one.

But why is there an error for a completely modeled data-set at all? Firstly, there is always a certain amount of noise comprised in a data-set describing a diffusion process, even in a synthetically generated. And second, by extrapolating the frequency infor-

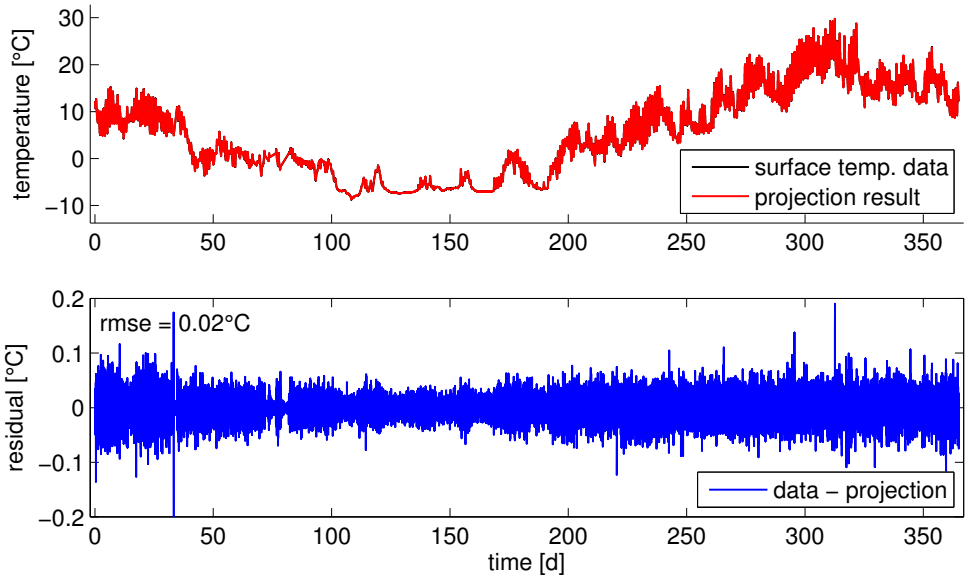

(a) Results for original data interval (10 min).

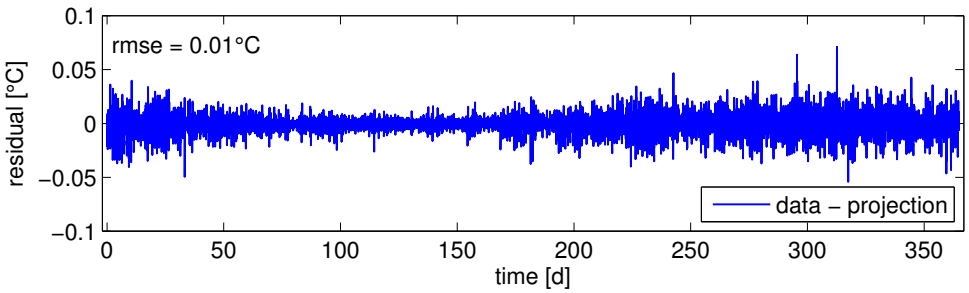

(b) Residual for hourly mean values.

Figure 3.6: Projection result for synthetic soil temperatures of one year. Noise level was set to 0.2 °C. *top:* Reconstructed (red) and actual (black) surface temperature. *middle & bottom:* Residual: difference between data and projection. The root-mean-squared error (rmse) is considerably smaller than the preset noise level and all significant features of the surface temperature are well reconstructed.

mation contained in the soil profile temperature data, we revert a diffusion process and therefore somehow "generate" information. Parts of the frequency information in the surface temperature signal immediately is lost due to diffusion while entering the soil. In particular for high frequencies, the signal-to-noise ratio gets increasingly worse with depth and we cannot measure arbitrarily close to the surface. In addition, amplitudes of such fluctuations are typically very small in real temperature data. Thus, small-scale variations will hardly be reconstructable, because the information about their phase and amplitude vanishes within the upper few centimeters of the profile. Therefore, the numerical noise contained in the signal is more emphasized, while the "true" signal is damped with depth. This is tried to be balanced by the usage of a weighted linear regression scheme to fit the spectral profiles. But in the end, noise will always be projected back to some extent which explains the omnipresent deviations between the reconstruction and the actual surface temperature, even for the synthetic data.

Altogether, the whole regression and extrapolation procedure is stabilized by considering various independent frequencies, since the inherent noise in the different depths is uncorrelated. Low frequencies penetrate deeper into the ground and devise a significant thermal signature in the temperature data at various depths. In contrast, high frequencies vanish in the upper part of the profile, but are important to match the original temperature signal at the surface. As a consequence, a systematic bias in the projection will result in an obvious structure in the residual and non-negligible amplitude entries.

3.4 Limitations for Finite Data-Sets

Fourier theory always assumes an infinite data basis which never holds for real data-sets. Particularly, the lowest frequency resolvable by the Fourier method is determined by the total length of the data-set. Analyzing the diffusion process in soils showed that high frequency components are damped away close to the surface and only low frequency components are contained in signals deeper down in the profile.
The latter suggests the definition of a *cut-off depth* for which the lowest frequency resolvable in a certain data-set is transformed into a corresponding depth. Above this depth, the lowest frequency should be significantly detectable in the temperature signal. Hence, the signal-to-noise-ratio $\alpha(f_{\min}, z)/\alpha(f_{\min}, 0)$ is set to one and following equation (3.5) the cut-off depth can be calculated by

$$d_{\text{cut-off}} = \frac{1}{k(f_{\min})} = \sqrt{\frac{D_{\text{h,ts}}}{\pi f_{\min}}}. \tag{3.10}$$

Therein, $f_{\min} = 1/T_{\max}$ [Hz] denotes the minimal resolvable frequency of a data-set of length $T_{\max}$ [s] and $D_{\text{h,ts}}$ is set again to be $1.0 \times 10^{-6}\,\text{m}^2/\text{s}$ to have the right order of magnitude for a typical soil. In further analysis, the investigated profiles will always be cut at $d_{\text{cut-off}}$ to get unbiased results from the regression and projection of the data.

3.4.1 Estimation of the Soil Thermal Diffusivity

Considering profile information in which all resolvable frequencies are already damped below the sensor's resolution would obviously induce a bias in the estimated thermal diffusivity due to the noise signals from below $d_{\text{cut-off}}$. Therefore, taking only the first 30 days of the synthetic data and performing a linear regression on the complete profile information yields a thermal diffusivity of $1.5 \times 10^{-6}\,\mathrm{m^2/s}$. Figure 3.7(a) reveals a nearly constant amplitude for the daily cycle below a depth of 0.8 m as an indicator for white noise.

Following equation (3.10), we can estimate the cut-off depth exemplary for the 30 d data-set. This yields a cut-off depth $d_{\text{cut-off},30d} = 0.87\,\mathrm{m}$ for the lowest resolvable frequency in this data-set, and thus, all other meaning frequencies are damped away in even more shallow parts above. This suggests to neglect the lower part of the profile data and to use only the upper meter to estimate the thermal diffusivity (Fig. 3.7(b)). The estimation of $1.003 \times 10^{-6}\,\mathrm{m^2/s}$ for D_{h} is then less than 0.5% off the correct value. Reducing the profile length any further will however not improve the quality of the estimated thermal diffusivity. Therefore we can conclude, that profiles, optimal for the regression procedure, might to some extent be larger than the cut-off depth, since shorter ones might lack of valuable information.

Referring to short data-sets in general, we can draw the conclusion that the lowest frequency resolvable from the data is determined by the total length of the underlying data-set. However, low frequency profile information stabilizes the regression scheme, as

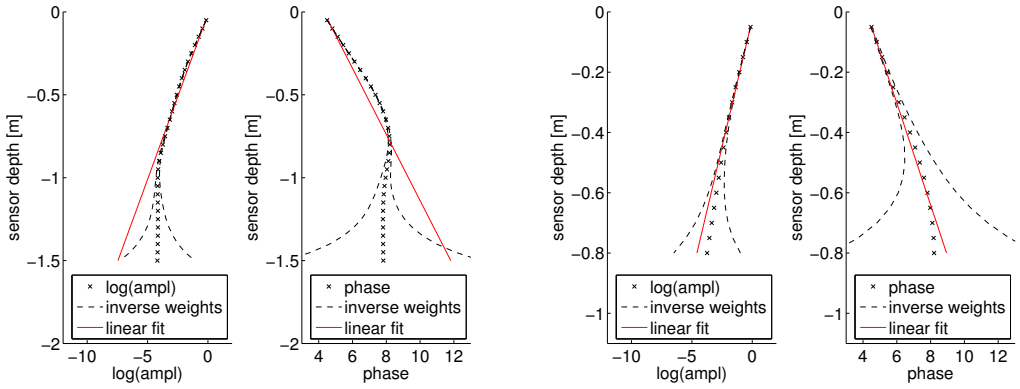

(a) Complete profile information used within fit routine.

(b) Only temperature data in upper meter of profile considered for estimation.

Figure 3.7: Estimation of thermal diffusivity of the first 30 days of the synthetic soil temperature profiles. Noise level was set to 0.2 °C. Fit results are shown exemplary for profile information of the daily cycle. *left:* Linear fit (*red*) of log-amplitude data (*crosses*). *right:* Linear fit (*red*) of phase profile data (*crosses*). *Dashed lines* indicate inverse weights used within regression procedure, reflecting information loss with depth.

the higher frequencies are damped away close to the surface. Altogether, our estimation procedure is in two ways problematic for short data-sets. That is why, for limited data-sets and depending on the depth of the deepest sensor, we suggest to skip the lower part of the profile in regard to the estimated cut-off depth, since the information comprised in the data is limited to higher frequencies and the information of these frequencies will not reach deep down into the ground. As the information about lower frequencies is also limited, deeper sensors will mainly detect noise, which results in a bias of the regression procedure.
Unresolved low frequencies could further influence the estimation procedure as the analysis of different parts of the data-set might yield different amplitudes for a certain frequency. In the first 30-day-section of the data-set, the amplitude of the daily cycle is by a factor of two smaller than, for example, within the 30-day-section starting at day 300. Without reducing the profile depth, the estimated D_h from the later interval of the data is $0.987 \times 10^{-6}\,\mathrm{m}^2/\mathrm{s}$ and therewith only less than 2 % off the true value. In this case, by chance, the information content of the significant frequencies suffices to fit D_h with acceptable accuracy.

Altogether it deems right that more information improves the regression and parameter estimates are more reliable. Yet, we have to keep in mind that the signal-to-noise ratio worsens with depth, particularly for high frequencies. Furthermore, the complete procedure could get de-stabilized and biased, if not enough low frequency information is extractable. Hence, the lower part of the profile information below a specific depth might have to be skipped.

3.4.2 Surface Temperature Reconstruction

Particularly for short data-sets, we have already seen that the exponential weights are not strong enough to prevent a bias in the estimated soil thermal properties and the profile information can only be used until a certain depth. Projecting only these first 30 days of the synthetic data-set reveals a further limitation of the method (Fig. 3.8). The deviations are in the order of 0.4 °C, even though the thermal diffusivity was reliably well estimated. However, this slight misfit causes a structure in the residual due to the daily cycle. Therefore, a further reduction of the noise level and thus using more frequencies to reconstruct the surface signal does not improve the projection result.

The largest deviations are found at both ends of the data interval, again an artifact of the underlying Fourier method. As already mentioned before, the Fourier analysis is based on the assumption of an infinite data basis. Yet, the temperatures at the beginning and the end are not equal or at least similar. Thus, the algorithm of the discrete Fourier transformation has to deal with a discontinuity, since the data stream is internally thought to be periodical. As a consequence, the discrepancy between reconstruction and model is largest at the ends which have to be disregarded in the interpretation.

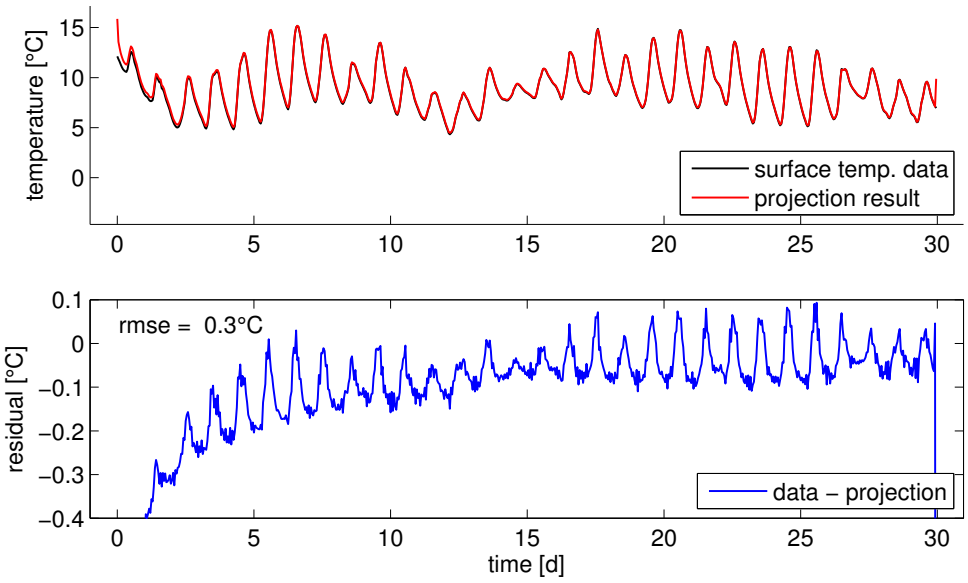

Figure 3.8: Projection results from soil temperatures of the first 30 days and the upper meter of the synthetic soil temperature profile. Noise level was set to 0.2 °C. *top:* Reconstructed (red) and actual (black) surface temperature. *bottom:* Residual: difference between actual and projected surface temperature. Particularly at the left and right edge, increasing artifacts due to Fourier analysis of finite data-sets are observed.

3.5 Influence of Thermal Layers

We want to close this section with a concluding theoretical investigation of the influence of soil layers with distinct thermal properties on the spectral profile information and the surface temperature reconstruction. Therefore, two soil temperature profiles for a time period of one year were generated with a layer boundary 20 cm below the surface. For the first scenario, the diffusivity of the upper layer was set to a value of $2 \times 10^{-7}\,\mathrm{m}^2/\mathrm{s}$ and the lower to $1.0 \times 10^{-6}\,\mathrm{m}^2/\mathrm{s}$ and the one for the other simulation vice versa. As an upper boundary, we again used a measured soil temperature time-series from one of our field sites. In total the simulated profile has a depth of 1.3 m and this time we used there also a measured time-series measured in the field as lower Dirichlet condition. The simulated temperature profiles and the extracted frequency information over depth are illustrated in Figure 3.9.

3.5.1 Estimation of the Soil Thermal Diffusivity

From the warm period around day 50, we could conclude without prior knowledge which scenario we are looking at. The upper 20 cm reveal a lower thermal diffusivity in this layer for the data-set in Figure 3.9(a), since the damping is much stronger compared to

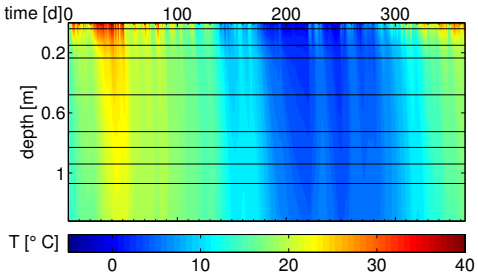

(a) Layer with lower thermal diffusivity overlying a profile with a higher one.

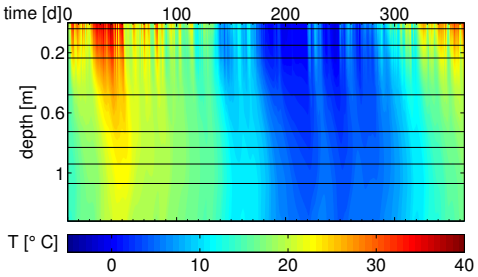

(b) Layer with higher thermal diffusivity overlying a profile with a lower one.

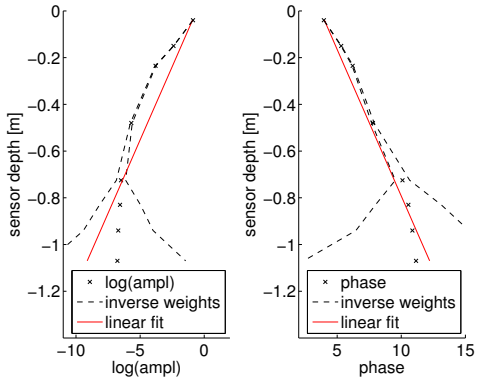

(c) Linear fit of spectral profile information in Figure 3.9(a).

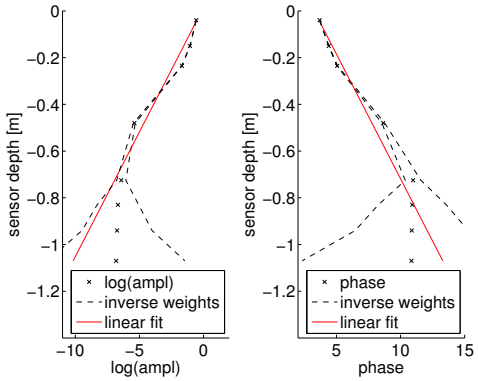

(d) Linear fit of spectral profile information in Figure 3.9(b).

Figure 3.9: Influence of thermal layering on the soil temperature profile and its spectral information. The layer boundary is at 0.2 m.

the data-set in Figure 3.9(b). Whereas in the left scenario, even the smaller temperature amplitudes at and below 20 cm penetrate nearly as deep as those in the right indicating a higher thermal diffusivity in the lower part of the left profile compared to the right. In addition, the phase shift in the lower part is considerably larger for the right data-set. This is indicated by temperature changes which are more shifted to the right and hence point also to a lower D_h there.

The thermal layers are verified by the amplitude and phase information of the temperature profiles presented below the corresponding data-set (Fig. 3.9(c) and Fig. 3.9(d)). The change from a flat slope to a steeper one below a depth of 20 cm corresponds to a change from a stronger to a weaker damping. Therefore, a layer with a lower thermal diffusivity overlies one with a higher ones In the second fit, the change in the slope along the profile is vice versa, since the thermal properties of the layers are exchanged.

For the estimated values of the thermal diffusivity, an analysis of the complete profile information approximates a kind of an effective value for both layers. For the layer with the lower D_h overlying one with an higher value, the linear regression yields a

value of $5.7 \times 10^{-7}\,\mathrm{m}^2/\mathrm{s}$. The estimate for the other scenario is with $4.1 \times 10^{-7}\,\mathrm{m}^2/\mathrm{s}$ slightly smaller, since the main part of the profile influences the overall modulation of the temperature signal with depth. An analysis of only the upper two temperature time-series yields with $1.9 \times 10^{-7}\,\mathrm{m}^2/\mathrm{s}$ still a slight underestimation of the true thermal diffusivity for the upper layer and analogous an overestimation with $1.1 \times 10^{-6}\,\mathrm{m}^2/\mathrm{s}$ for the profile with the higher diffusive upper layer. This points out that soil temperatures in both layers are influenced by the thermal properties of their surrounding. Therefore, an estimation of the thermal properties in a layered system will always be biased to some extent.

3.5.2 Surface Temperature Reconstruction

The deviations between the reconstructed and actual surface temperature for an effective thermal diffusivity estimated for the complete soil profiles are shown in Figure 3.10 and 3.11(a). An underestimated thermal diffusivity of the upper layer results in an overestimation of the projected surface temperature (Fig. 3.10). Furthermore, the residual is not centered around zero, but indicates a shift towards the minima, meaning that the temperature maxima are reconstructed worse than the minima.
For the opposite layering, the thermal diffusivity was overestimated which causes an underestimated projected surface temperature, again pointing out that the minima are

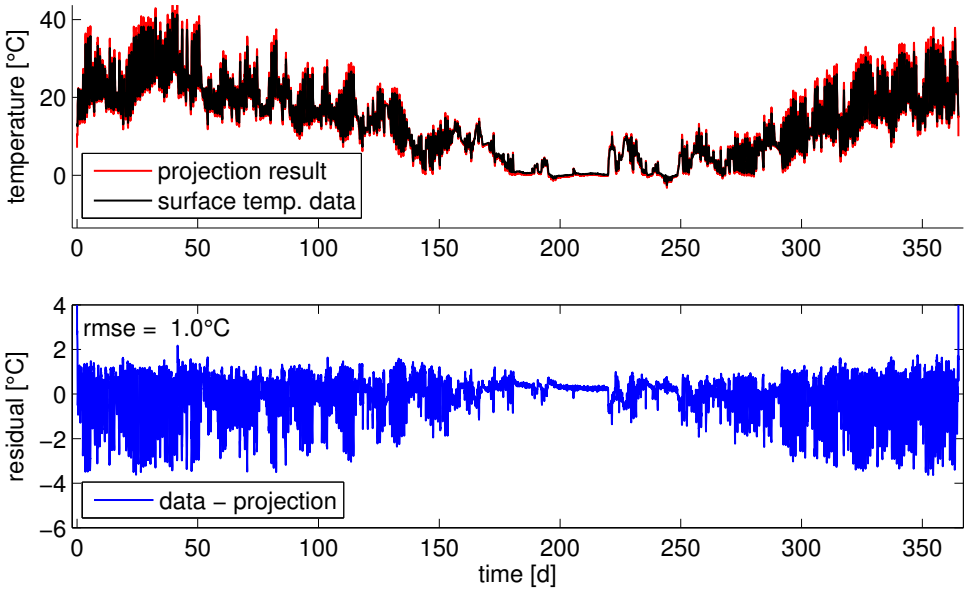

Figure 3.10: Projection results for soil temperature profile with thermal layers. A layer with higher thermal diffusivity overlies a profile with a lower D_h. Noise level was set to 0.5 °C. *top:* Reconstructed (red) and actual (black) surface temperature. *bottom:* Residual: difference between actual and projected surface temperature. Projection factor estimated from whole profile information results in an overestimation.

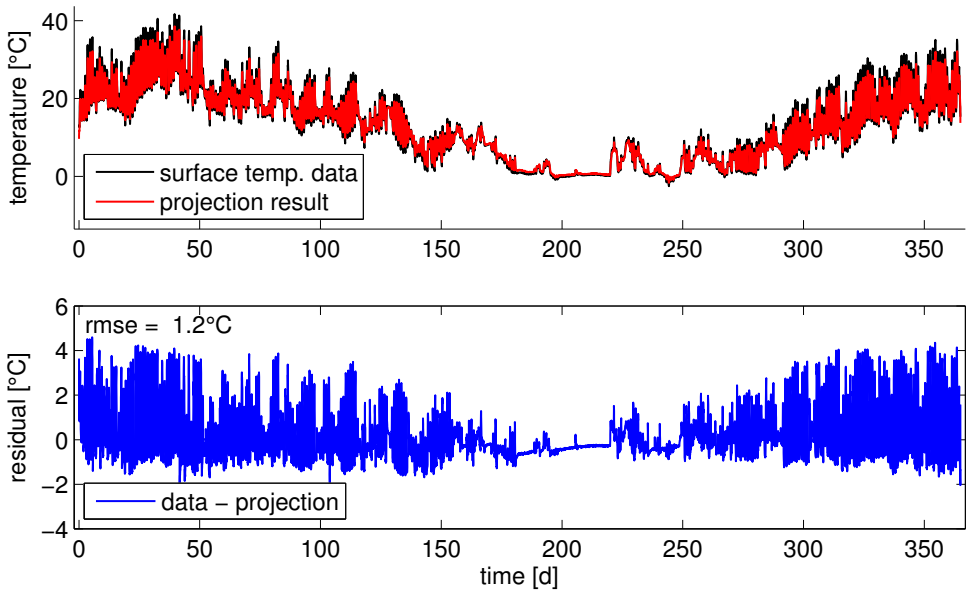

(a) Projection factor estimated from whole profile information results in an underestimation.

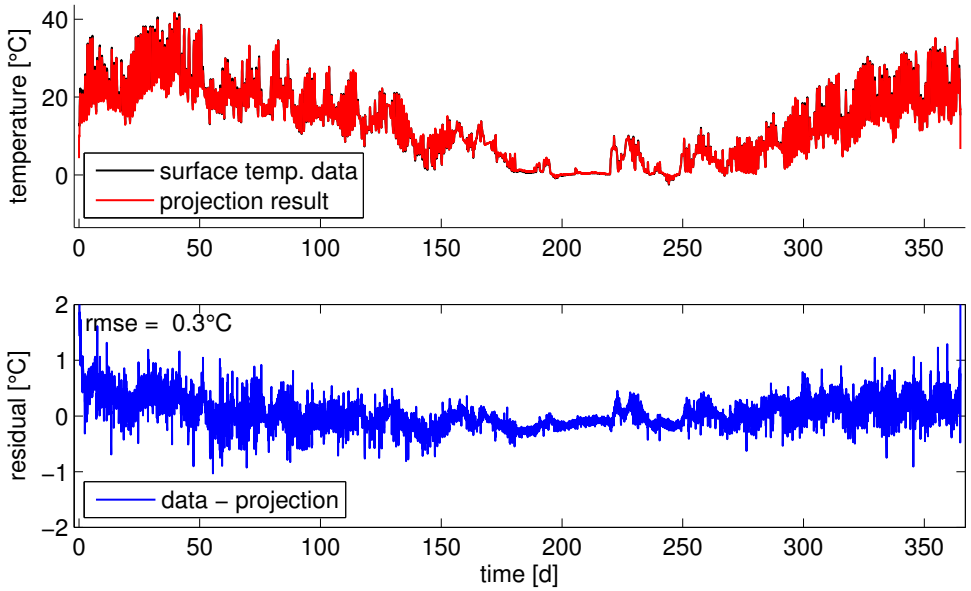

(b) Projection factor estimated from upper two sensors.

Figure 3.11: Projection results for soil temperature profile with thermal layers. A layer with lower thermal diffusivity overlies a profile with a higher D_h. Noise level was set to 0.5 °C. *top:* Reconstructed (red) and actual (black) surface temperature. *bottom:* Residual: difference between actual and projected surface temperature.

better reconstructed compared to the maxima (Fig. 3.11(a)).

In the end, a reasonable reconstruction of the surface temperature can be achieved, if the estimation procedure is based only on temperature data of the top few sensors which correspond to the upper soil layer. They allow to estimate the distinct slope at the top of the amplitude and phase profiles (Fig. 3.11(b)). As already discussed for the linear fit (Fig. 3.9(c) and 3.9(d)), the estimated D_h is biased by the lower part of profile. As a consequence, the surface temperature is still slightly underestimated and the root-mean-squared error of 0.3 °C is worse compared to the analysis of the homogeneous, synthetic soil temperature profile in the beginning of this chapter.

3.6 Summary

The outlined results can be summed up as follows:

1. Fourier analyzing soil temperature profiles extracts the linear relation between the log-amplitude and phase information with depth. Its slope comprises information about the thermal diffusivity of the soil which can be determined by a weighted linear regression.

2. An extrapolation of the spectral information towards the surface yields an estimate for the spectral information of the temperature right at the surface. To get the reconstruction in time-domain stable, a heuristic noise level is needed to define the various frequency components as signal or noise. Only those components denoted to be significant will be considered within the inverse Fourier transformation and therewith as a part of the reconstructed surface temperature.

3. The projection result from within the soil towards the surface will always be imperfect, as the temperature signals in a certain depth will never capture all original components. The damping of the amplitudes is frequency-dependent and temperatures cannot be measured arbitrarily close to the surface. In combination with the noise level setting, we will always miss high frequency components and enhance noise components by the extrapolation. This will always induce some noise in the final reconstruction.

4. The Fourier analysis is based on the assumption of an infinite data basis never fulfilled by real data-sets. Particularly, when the temperatures at the beginning and the end of the data-set are not on the same level, this causes already artifacts in the representation of the signals by the Fourier series and hence also in the reconstruction. Furthermore, the length of the data-set determines the minimal resolvable frequency. In the considered time interval, its penetration depth can be estimated and from deeper down, no data should be considered in the regression procedure, since no valuable information can be extracted therefrom.

5. Soil layers with distinct thermal properties will result in a changing relation of the phase shift and amplitude damping with depth. The log-amplitude and phase

profiles reveal a different slope within different layers. Due to the analytical kernel underlying this projection procedure, temperatures can only be reconstructed within homogeneous layers for which at least two temperature time-series are available.

In the light of these results, the temperature projection will be applied in the following chapters to soil temperature profiles from laboratory heat conduction and evaporation experiments as well as from field scale experiments with different vegetation cover. Therewith, its performance to studied to extract information about the surface temperature from measurements within real soils.

4 Heat Transport at the Laboratory Scale

A laboratory experiment was conducted for an in-depth study of the interaction between soil and atmosphere. Therefore, soil water content and temperature profiles in the soil and in the air above are measured with high spatial and temporal resolution in a laboratory sand column. The whole set-up was placed in a climate chamber in order to control the temperature forcing at the soil surface.

In a first step, pure heat conduction experiments were performed with a completely dry and wet sand. Therewith, the performance of the temperature projection method for measured data can be tested. Afterwards, the soil surface of the wet sand was left open to evaporate water. This allows to analyze the evaporation process for different types of air temperature forcing. One was constant over time and the second one had periodical variations. Again, the results of the surface temperature reconstruction will be investigated in the presence of an additional surface process. Furthermore, the soil-atmosphere coupling under the laboratory conditions is studied in detail.

4.1 Sand Column Experiment in a Climate Chamber

The sand column experiment was set up in a climate chamber ($\sim 2.5 \times 2.5 \times 2.2\,\mathrm{m}^3$), in which the air temperature can automatically be controlled and therefore different types of temperature forcing at the soil surface can be realized. Compared to field measurements, the laboratory conditions are less complex, since the soil texture is considered to be homogeneous over the profile and there is no radiative forcing at the soil surface.

In former experiments, *Gergely* (2007) and *Boll* (2009) used a similar set-up to study the dynamics of permafrost. *Bergmann* (2010) and *Ehrmann* (2011) adapted the main features of the set-up for evaporation experiments. Therewith, they contributed essentially to the experimental data presented here and the data is discussed in a first step there.
In the following section, the experimental set-up will just be outlined. The resultant data will then be discussed and evaluated in detail in section 4.2 and 4.3.

4.1.1 Experimental Set-Up

The images summarized in Figure 4.1 give an impression about the realization of the laboratory set-up in the climate chamber. On the left, the makrolon® soil column is shown which was filled with sand up to the top sensor for the experiments. Finally, the experiment had to be isolated to reduce the heat flux from the side. Therefore, three layers of mineral wool mats were added, each of them 10 cm thick. In the end, a space

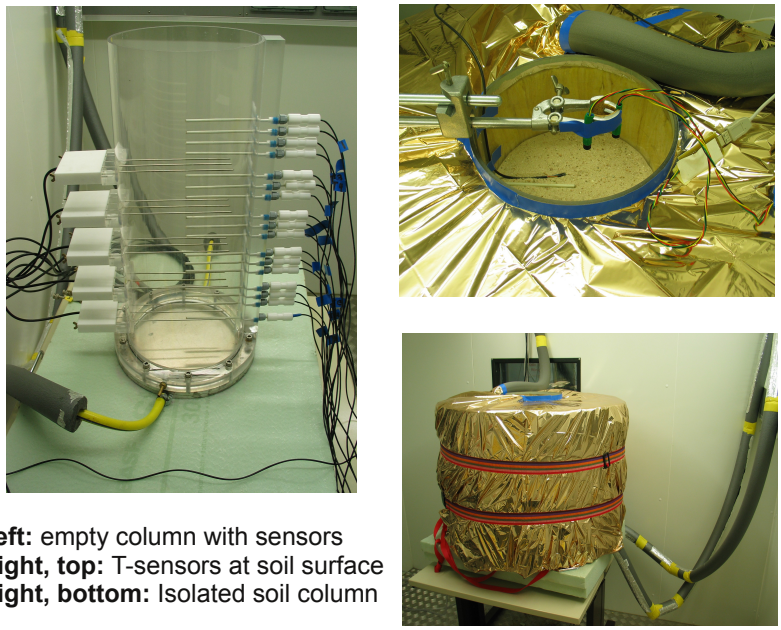

Figure 4.1: Experimental set-up in the climate chamber.

blanket was put as top layer around the whole set-up to prevent heat fluxes through the insulation as much as possible and to be able to use a theoretical 1D representation of the system later on. To force temperature changes in the system, the surrounding air temperature was periodically modulated for most of the experimental scenarios. At the bottom of the soil column, the temperature was stabilized at the mean air temperature by a tempered plate connected to a cooling unit (WKL603, LAUDA, Lauda, Germany). For the first heat conduction experiment, the sand was completely dry and the climate chamber forces the periodical changes in the air temperature. Afterwards, the sand column was completely saturated with water to change the thermal properties of the sand, but the surface was covered by a plastic foil to prevent evaporation during the second run. Later, two evaporation experiments were performed for different types of air temperature forcing. For the first, the air temperature was held constant at 28 °C and subsequently, the air temperature was again modulated periodically to get an insight in the increasingly complex interaction between the soil and the air above.

A theoretical sketch of the complete experiment is given in Figure 4.2. In the soil, 17 pt100 temperature probes are installed at an interval of 2 cm, except for the positions where five *time domain reflectometry* (TDR) probes are located. In order to detect changes in the soil water content in a high temporal and spatial resolution, the spacing between the TDRs is 8 cm and they are read-out in 10 min intervals. Soil temperatures are sampled in 2 min intervals. Above the soil level, the surface temperature was measured by a infra-red sensitive thermopile (MLX90614, Melexis Microeletronic Systems,

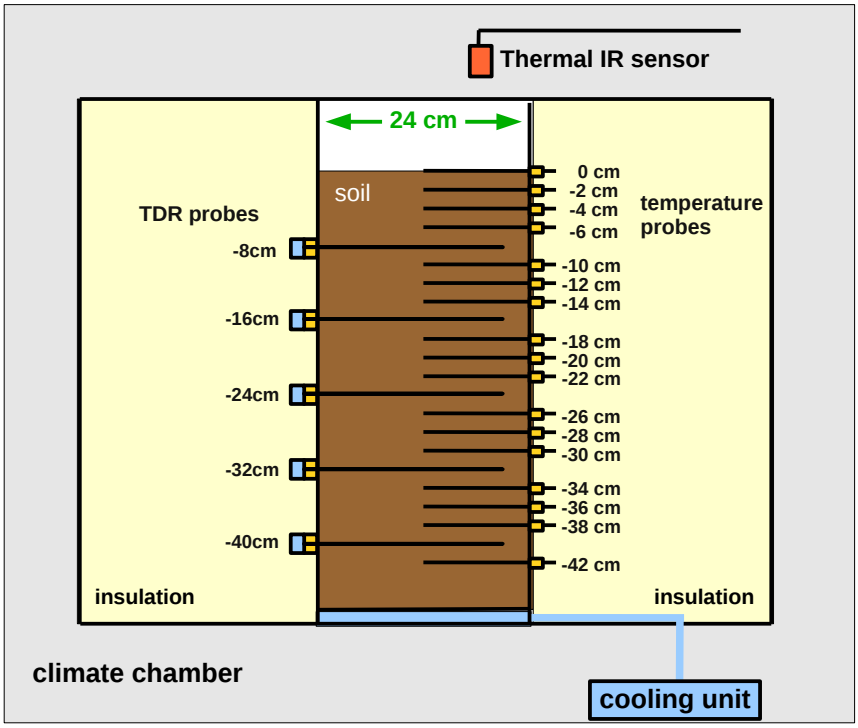

Figure 4.2: Sketch of soil column for evaporation experiment in climate chamber. Water content and temperature measurements were performed within and above the soil, as well as directly at the soil surface (adopted from *Bergmann* (2010)). The soil column is isolated by 30 cm of mineral wool. At the bottom, the temperatures can be stabilized by a cooling unit.

Ieper, Belgium). For technical reasons, the measurement frequency was 1 Hz, and the values were averaged to the 10 min interval of the soil temperature probes afterwards. In addition, the relative humidity was capacitatively measured (Vaisala HMP45C, Campbell Scientific, Logan, UT) to detect changes caused by the automatic control of the climate chamber.

For the last run, slight changes in the set-up had to be made. The filling height of the sand column was reduced from 47 cm to 37 cm. Therefore, the uppermost TDR probe had to be skipped and as a result, the upper four temperature probes installed in the soil column are now facing the air. This also implicated a modification of the air temperature forcing in air to reduce the penetration depths of the temperature signal in the soil.

4.1.2 Measurement Principles

All measurements were automatically logged via a data logger (CR1000, Campbell Scientific, Logan, UT), except for the infra-red sensors and the balance which were read-out separately by desktop computer via a self-written script. The main measurement principles will be summarized in the following.

Pt100 Soil Temperature Probes

The platinum resistance in the pt100 probes is temperature dependent. Via a 4-wire half bridge, the sensor detects changes in resistivity relatively to a reference resistance of 100 Ω. The resistance is located in a carbon fiber tube to ensure a stable installation (Fig. 4.3(a)). The temperature probes have an operation range from −40 °C to +60 °C. The dependency between resistivity and temperature is given via a quadratic relation for temperatures above 0 °C

$$R(T) = R_0 \cdot (1 \ + \ 3.90802 \cdot 10^{-3} \cdot T \ - \ 5.802 \cdot 10^{-7} \cdot T^2). \tag{4.1}$$

R_0 denotes the resistivity at 0 °C, which is close to 100 Ω and is precisely determined by a calibration in advance. Therewith, the absolute accuracy among the soil temperature probes in this experiment should be higher than the typical value of ±0.5 °C. Their resolution is specified as ±0.2 °C.

Soil Water Content from TDR

To measure the water content in soils, the TDR method is based on the dependence of the propagation velocity v of an electromagnetic pulse on the electrical permittivity ϵ of the surrounding medium.
The three rods of the TDR serve as a wave guide for the pulse (Fig. 4.3(b)). The travel time t_s of the signal in the soil along the TDR probe can be estimated from its reflections which is proportional to the electrical permittivity ϵ of the surrounding soil. A

(a) 4-wire pt100 temperature sensor

(b) TDR probes to measure water content

Figure 4.3: Sensors to measure soil temperature and water content (self-built, IUP Workshop)

comprehensive derivation of the exact procedure, including calibration requirements, can be found in the appendix of *Ludin* (2010). The permittivity can then be further linked to the volumetric soil water content θ by the *complex refraction index model* (CRIM) following *Roth et al.* (1990)

$$\theta = \frac{\sqrt{\epsilon} - \sqrt{\epsilon_{\text{quarz}}} - \phi(\sqrt{\epsilon_{\text{air}}} - \sqrt{\epsilon_{\text{quarz}}})}{\sqrt{\epsilon_{\text{water}}} - \sqrt{\epsilon_{\text{quarz}}}}, \tag{4.2}$$

with the porosity ϕ of the soil. Therein, soils are considered mainly as a mixture of a solid (quarz sand), aqueous (water) and gaseous (air) phase, for which the overall permittivity can be described as a composition of the dielectric numbers of its constituents weighted by its volume fraction.

Surface Temperature Measured by Thermal Infrared Sensors

Thermal infrared thermometers allow a non-invasive measurement of the surface temperature by detecting the thermal radiation emitted by an object. The most simple realization consists of a thermocouple to measure the absolute temperature of the sensor itself and, in addition, a thermopile to detect the incoming net heat flux $j_{\text{h,net}}$ from which the temperature difference between the observed surface and the sensor can be deduced. Finally, the object temperature is calculated from

$$j_{\text{h,net}} = \sigma_{\text{SB}} T_{\text{sens}}^4 - \epsilon_{\text{obj}} \sigma_{\text{SB}} T_{\text{obj}}^4 \, , \tag{4.3}$$

where σ_{SB} is again the Stefan-Boltzman constant and T_{sens} and T_{obj} denote the temperature of the sensor and the object, respectively.

At that point, the evaluation procedure assumes the observed surface to belong to a "black body" with emissivity $\epsilon = 1$. This means that it perfectly absorbs radiation at all wavelengths and, in turn, is a perfect emitter of thermal radiation which is only approximately the case for real objects.
In particular, the soil's emissivity differs between 0.96 ± 0.04 for different types of vegetation cover (*Geiger et al.*, 1995). Therefore, a final correction of the measured infrared temperatures is necessary to account for the scattered thermal radiation of the surrounding by

$$T_{\text{obj}}^4 = \frac{\sigma_{\text{SB}} T_{\text{sens}}^4 - (1 - \epsilon_{\text{obj}}) \sigma_{\text{SB}} T_{\text{sur}}^4}{\sigma_{\text{SB}} \epsilon_{\text{obj}}} \, . \tag{4.4}$$

Therein ϵ_{obj} is the actual emissivity of the observed object and T_{sur} the temperature of the sensor's surrounding, e. g. the air. Under laboratory conditions, this is less crucial, but in the field the thermal radiation from the upper atmosphere is partly reflected at the soil surface. This affects the measured temperatures considerably and results in a systematical underestimation of the true temperatures (*Bauser*, 2011).

4.2 Pure Heat Conduction Experiments

In this section, we will discuss laboratory experiments which fulfill the assumption of pure heat conduction (Equ. (2.19)). The surrounding air temperature T_{air} $[°C]$ was automatically modulated following a superposition of two sine-functions given by

$$T_{\text{air}}(t) = 22 + 5\,\sin(2\pi f_1 t) + 2\,\sin(2\pi f_2 t), \tag{4.5}$$

where t denotes the time in hours and f_1 and f_2 were set to $(24\,\text{h})^{-1}$ and $(6\,\text{h})^{-1}$ respectively. In Figure 4.4 the resultant realization and its amplitude decomposition is shown. There is a lack of nearly 1.5 h between the forcing and the realization due to the fact that the climate chamber does not contain air only, but more experimental equipment. Hence, it needs some time to heat up and cool down the entire chamber. Furthermore, the actual mean air temperature of 22.7 °C is slightly higher than the assumed value. In addition, the frequency decomposition in Figure 4.4(b) shows smaller amplitudes, particularly for the low frequency component, compared to the preset 5 °C and 2 °C. Furthermore, the control of the climate chamber introduced additional frequencies in the close surrounding of the main components and the low frequency part of the spectrum indicates small variations during different cycles. In conclusion however, the forcing is of low complexity which allows a detailed analysis of the soil thermal processes and a first performance test of the temperature projection method on a measured data-set.

4.2.1 Experimental Results

In the first experiment, the sand was completely dry. The air temperature was periodically modulated (Eq. (4.5)) for two weeks. The resultant soil temperature profiles are shown in Figure 4.5.

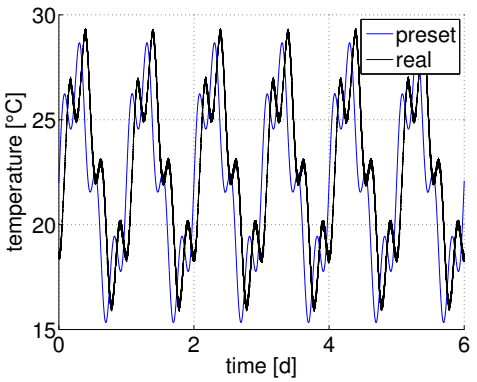

(a) Air temperature forcing during heat conduction experiments.

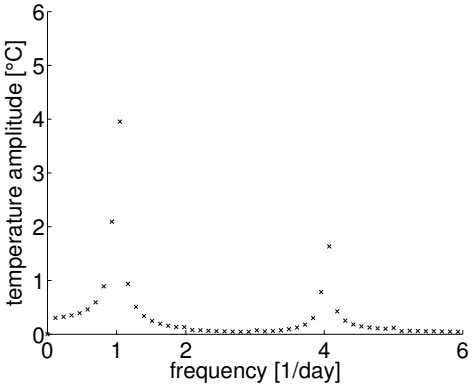

(b) Amplitude spectrum of air temperature forcing.

Figure 4.4: Laboratory air temperature forcing during the pure heat conduction experiments and the corresponding amplitude spectrum. Automatic control of climate chamber was preset to a superposition of two sine-functions (Eq. (4.5)).

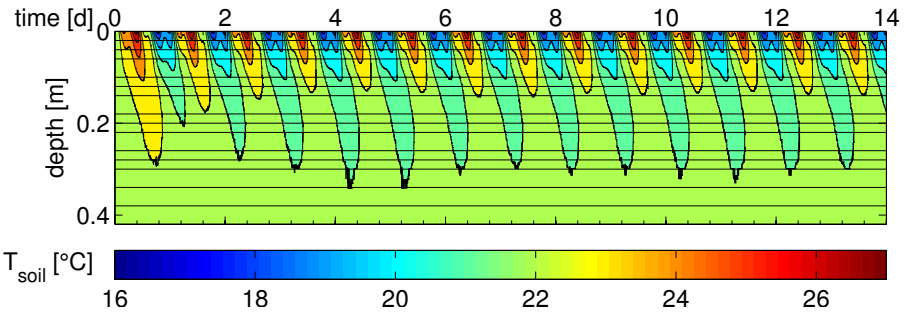

Figure 4.5: Soil temperature profile of dry sand experiment. *Horizontal black lines* indicate sensor positions. *Contour lines* are plotted in 1 °C intervals. Heat is only transported by diffusion.

The experiment started from thermal equilibrium. The complete climate chamber, including the experimental set-up, was at 22 °C. As a consequence, a lot of energy is stored in the soil at the beginning of the experiment due to the more than three orders of magnitude larger heat capacity of quarz sand compared to air. During the first three days, the soil adapts only slowly to the periodic forcing during the first three days. Subsequently, the temperature cycles penetrate more uniform into the soil. The damping of the amplitude with depth can clearly be seen in the data, as well as the phase shift of the extrema. There is an obvious asymmetry between the warming an cooling cycles. The rise in temperature does not seem to penetrate as deep into the soil as the corresponding decrease. This can be deduced from the air temperature forcing as indicated in Figure 4.4(a). The gradients in the cooling cycles are much steeper than those of the temperature increase due to the superposition of the two sine-functions. The interference between the 6 h- and the 24 h-cycle results in a more "direct" decrease in temperature from the maximum to the minimum in comparison to the reverse way. Therefore, the forcing of the cooling cycles to penetrate into the soil is stronger compared to that of the warming cycle, as the heat flux is proportional to the temperature gradient (Eq. (2.17)). This explains the asymmetric penetration depth between the two periods.

For the second experiment, the sand column was completely saturated with water and the surface was covered by a plastic foil to prevent evaporation. The air temperature forcing was kept the same as before, soil temperatures were measured for 12 days (Fig. 4.6).
At first, the experiment was again in thermal equilibrium. During the first two days, it had to adapt to the periodic forcing. Later on, temperature cycles entering the soil were more uniform. The asymmetry in the forcing can again be identified by different penetration depths for warming and cooling cycles. In addition, it is apparent that the temperature fluctuations are not as large as in dry sand. The temperature variations, especially close to the soil surface, were smaller than for dry sand. The reason for this is the increased heat capacity of the soil column due to the added water. The heat capacity

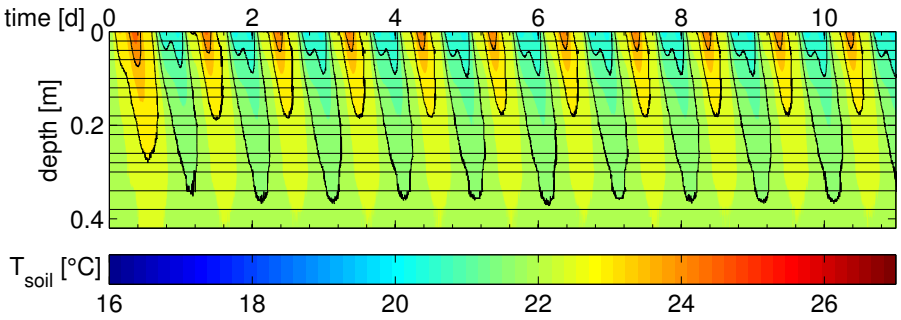

Figure 4.6: Soil temperature profile for wet sand experiment. *Horizontal black lines* indicate sensor positions. *Contour lines* are plotted in 1 °C intervals. Water is prevented to evaporate by a plastic foil at the soil surface. Hence, heat transport in the soil is purely conductive and the soil thermal properties are constant in time.

of air is three orders of magnitudes smaller than that of water. Hence, the energy needed to change the soil temperature for air filled pores is much less than that needed for the same change in a water-saturated soil. As the forcing at the soil surface is the same in both experiments, the surface temperature varies less for the water-saturated soil column. However, the temperature fluctuations in the soil (indicated by the contour lines) seem to penetrate deeper into the ground compared to dry sand. Thus, even though the heat capacity has been drastically increased by 60 % through the amount of water added to the sand: $C_{\mathrm{h,dry}} = 1.7 \times 10^6\,\mathrm{Jkg^{-1}m^{-3}}$ and $C_{\mathrm{h,wet}} = 2.7 \times 10^6\,\mathrm{Jkg^{-1}m^{-3}}$, the thermal conductivity is enlarged by about a factor of four (*Sepaskhah and Boersma*, 1979). This implies an overall higher thermal diffusivity for wet compared to dry sand, since it is defined by the quotient of heat conductivity and capacity (Eq. (3.9)).
The idea behind these two experiments was to characterize the upper and lower bounds of the soil thermal properties for the sand used in this experiments. The estimation of the thermal diffusivity will be discussed in the following section. The next experimental step (Sec. 4.3) will then enhance the complexity of the system and the evaporation of water at the soil surface will be added.

The observations from the pure heat conduction experiments are summarized in the temperature profiles of one temperature cycle shown in Figure 4.7. For the same air temperature variation, the surface temperature fluctuations are more than 3 °C larger for the dry soil, but influence deeper soil temperatures below 20 cm only for the cooling cycle. Whereas for the wet sand, the surface temperature changes only in a small range, but due to its higher thermal diffusivity this information reaches nearly the bottom of the soil column.
As it is an independently working unit, one remark concerning the heat plate which stabilizes the temperature at the bottom of the soil column to the mean air temperature. We have a small offset between the temperature measured internally by the instrument and

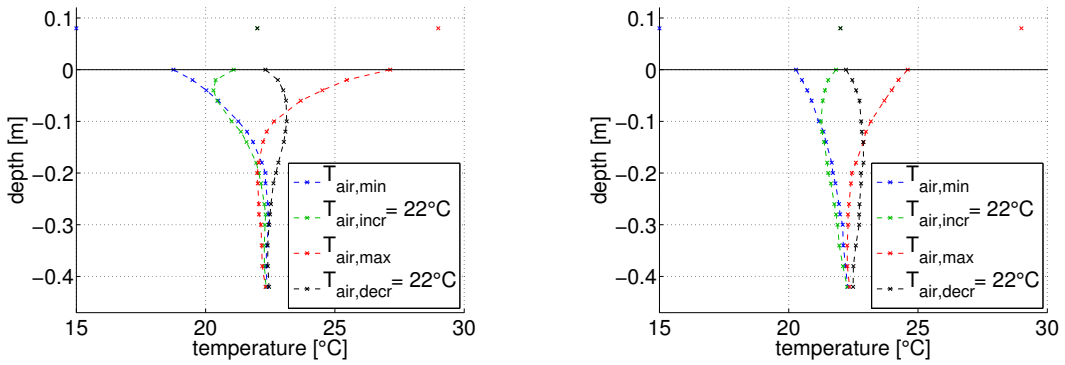

(a) Dry sand.

(b) Water saturated sand.

Figure 4.7: Temperature profiles during one air temperature cycle for the pure heat conduction experiments corresponding to Figures 4.5 and 4.6 respectively. Surface temperature variations and penetration depths differ due to the added water, since the soil thermal properties depend on water content.

soil temperatures measured by the pt100 temperature probes. The offset and fluctuations due to this system should be smaller than $\pm 0.5\,^{\circ}\mathrm{C}$ and are negligible therewith. Yet, we have to focus once more on its influence on the temperature variation in the soil column, as an infinite lower end of the soil profile is assumed from theory.

Influence of Bottom Heat Plate

Part of the following analysis is based on the analytic solution of the heat conduction equation (2.19) for periodic forcing, consequently the next paragraph investigates the underlying assumption of an infinite lower end for the experimental set-up. As we would like to validate our projection method (Sec. 3) for real measured data, this is necessary to prevent a later bias in the reconstructed surface temperatures.

This investigation is heuristic as we know neither the true material properties of the applied sand nor the analytic expression for the resultant surface temperatures of the dry and wet sand experiments. Hence, this concept tries to characterize the influence of the finite soil column with fixed temperature at the bottom by comparison with a simulation of a much deeper soil column. As theory assumes an infinite lower end of the profile, we simulated two soil temperature profiles with constant thermal diffusivity and different profile depths. The soil column in the climate chamber experiments is 0.47 m deep. Therefore, the simulations were performed for such a profile depth and for 1.47 m. The thermal diffusivity was set to $10^{-6}\,\mathrm{m}^2/\mathrm{s}$ which is in the upper range of the expected values for real soils. As upper boundary condition at the surface, the temperature measurements of the real experiments were used. The lower end was kept constant at mean surface temperature. Hence we end up with an upper estimate of the impact for both measured forcings.

Figure 4.8 shows the temperature difference between the long and the short profile simulations at the lower ten sensors. As expected, the closer the sensor are to the heat plate,

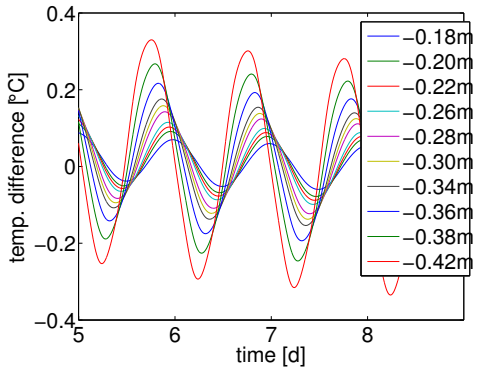

(a) Temperature difference at the bottom of the soil column for surface temperature forcing measured during the dry sand experiment.

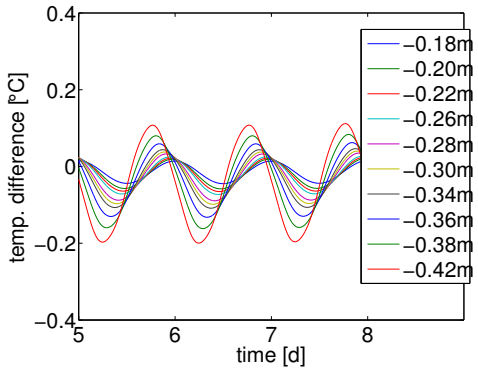

(b) Temperature difference at the bottom of the soil column for surface temperature forcing measured during the wet experiment.

Figure 4.8: From heuristic numerical test, four-day cut-out of the temperature difference at the lower soil temperature probes due to the temperature stabilization by the bottom heat plate. Its impact at the lowest three sensors might be significant for the dry sand surface temperature variations, while it seems to be negligible for the wet sand temperature fluctuations.

the larger the effect of the temperature stabilization is on the soil temperature amplitude at that level. Since the increasing temperature difference before day 6 corresponds to a cooling cycle and the decrease after day 6 to a temperature rise, the amplitudes in a finite profile are much more damped away than in the corresponding infinite profile at the same depth. For the larger temperature variations at the surface of the dry sand, the temperature stabilization at the bottom of the soil column might significantly influence the soil temperature signals as the deviation at the lower three sensors is estimated larger than $\pm 0.2\,^{\circ}\mathrm{C}$. For the stronger damped temperature fluctuations in the wet sand, the influence on the whole profile seems to be smaller than $\pm 0.2\,^{\circ}\mathrm{C}$ which would be the resolution of the soil temperature probes in the real experiments. The whole procedure is based on a rough estimate of the thermal diffusivity. As a precaution, only sensors above 0.36 m will be used for further analysis based on the analytic solution of the heat diffusion equation. The ones below that depth might be biased by the bottom heat plate.

4.2.2 Soil Temperature Projection

The temperature profiles measured in dry and completely wet sand enables us to find the upper and lower bound of the thermal diffusivity for the sand used in the laboratory experiments. Furthermore, we seek to validate the surface reconstruction method by the experimental data.

In Section 3.2, an estimation procedure was introduced based on the frequency analysis of time-series of temperature profiles. In a first step, we will apply this method to the lab-measured data-sets discussed in the previous section. Based on that, the surface temperature will be reconstructed and compared to the measured data. As the assumptions of an infinite data-set in space and time is not fulfilled for real experiments, the accuracy

of the method might be limited for the analytical method. Thus, we will eventually check back the estimated soil thermal diffusivities by running an inversion procedure based on a numerical heat diffusion model.

Estimation of the Soil Thermal Diffusivity

The estimation procedure presented in the previous chapter is based on the Fourier analysis of soil temperature profiles. The exponential damping of the amplitude and the linear increase of the phase shift win proportion to depth is known from theory. Both changes are proportional to the projection factor k (Eq. (3.4)) which depends on frequency and the soil thermal diffusivity of the corresponding soil. Hence, analyzing the amplitude and phase information in several depth allows an estimate of D_h.

The amplitude spectra of the experiments in dry and wet sand obtained from Fourier analysis of the soil temperature profiles are shown in Figure 4.9. The first two days of the data-set were skipped due to thermal equilibrium condition in the beginning, since the system needed to overcome the initial condition first. The underlying data-sets are about ten days long,. Hence, the lowest resolvable frequency and at the same time the resolution of the spectral lines is given by $f = (10\,\mathrm{d})^{-1} = 1.2 \times 10^{-6}\,\mathrm{Hz}$. The two significant peaks refer to the two frequencies (daily and 6 h-cycle) contained in the external air temperature signal. The magnitude of a particular entry reflects the original amplitude of the corresponding signal in that depth. As mentioned above, the temperature signal entering the soil at the surface is less damped in the dry sand. Thus, the amplitudes in the dry sand spectra are larger than the corresponding ones in wet sand. Furthermore, the noise level of the dry sand data is also higher than that of in the wet sand spectra which can be deduced from the entries next to both peaks.

For the estimation of the projection factor k, and thus D_h, we will not only use the am-

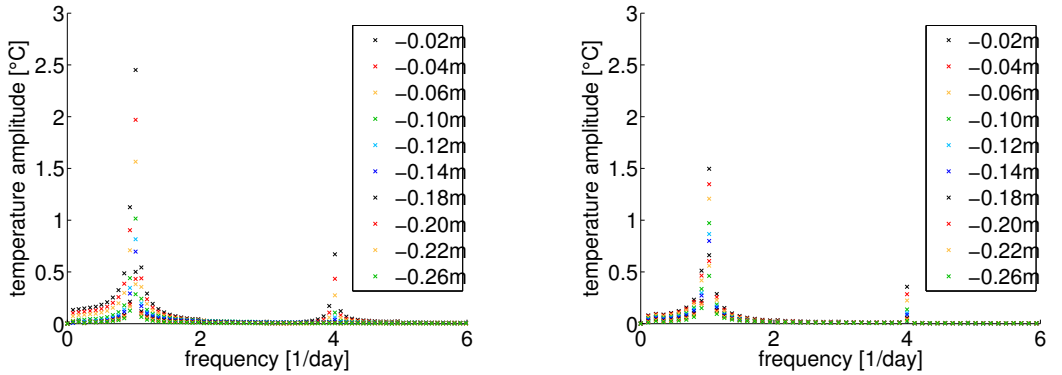

(a) Soil temperature amplitudes in dry sand.

(b) Soil temperature amplitudes in wet sand.

Figure 4.9: Amplitude spectra of dry and wet sand temperature profiles corresponding to Figure 4.5 and 4.6 respectively. The two peaks indicate the two main frequencies superposed as external air temperature forcing

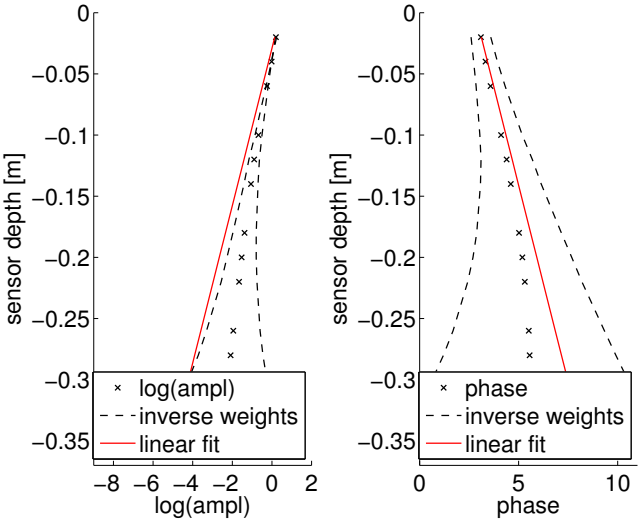

(a) Frequencies considered for linear fit were chosen through noise level criterion.

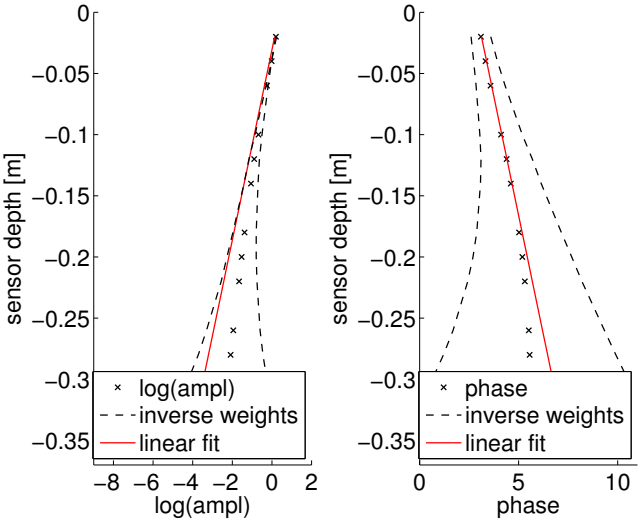

(b) Low frequency entries excluded from linear regression procedure.

Figure 4.10: Estimation of thermal diffusivity for the soil temperature profiles of the dry sand experiment. Fit results are shown exemplary for profile information of the daily cycle *left:* Linear fit (*red*) of log-amplitude data (*crosses*). *right:* Linear fit (*red*) of phase profile data (*crosses*). *Dashed lines* indicate inverse weights used within regression procedure, reflecting information loss with depth.

plitude spectra, but the analogous phase spectra in each depth likewise. For the data-sets of about ten days, the cut-off depth can be calculated as 0.52 m (Eq. (3.10)). Hence, the whole profile information could be used. However, as assumed in the previous section, soil temperatures deeper down the column might be influenced by the bottom heat plate. As a consequence, the four deepest sensors will be skipped for the following analysis.
Fourier analysis of the soil temperature profiles within the dry sand yields Figure 4.10 for the daily cycle. For the linear fit in Figure 4.10(a), the noise level was set to 0.2 °C. This determined the number of frequencies denoted as significant for the signal. It should be emphasized that no additional information was provided to the regression procedure, e. g. only two significant frequencies are comprised in the data. We only applied the typical threshold to see how this method works on a general level. This results in 1751 frequency entries considered in the linear fit of the profile information which we would expect to bias the final estimate. At eye-sight, the fitted projection factor seems to be too small to describe the amplitude damping and the increasing phase shift, although their change over depth seem to be close to linear. This indicates the influence of other, less significant or negligible frequency components. Increasing the noise level to 0.5 °C drastically reduces the number of frequencies denoted to be significant to 229, however changes the estimated D_h only by 2 %. This finally yields an estimated thermal diffusivity of $1.5 \times 10^{-7}\,\mathrm{m^2/s}$ for the dry sand.

Figure 4.9(a) highlights some frequency components around the daily peak as well above most of the other frequency entries. They agree with the lower frequency components also present in the frequency decomposition of the air temperature (Fig. 4.4(b)). Additionally, low-frequencies are generally less damped with depth compared to higher ones and hence, they induce a bias in the estimation of the thermal diffusivity. Since the linear regression works on the information about amplitude and phase modulation with depth, a further criterion is needed to skip those frequency components which are not considerably influenced over the considered profile depth. A change less than 20 % proved to be an appropriate threshold. Hence, all frequencies for which the corresponding amplitudes are damped less than this percentage are neglected. This yields the following definition for the *cut-off frequency* at the lower end of the frequency spectrum:

$$f_\text{cut-off} = \left(\frac{|\ln(0.2)\ |}{z_\mathrm{p}} \right)^2 \cdot \frac{\pi}{D_\mathrm{h,ts}} \tag{4.6}$$

with the profile depth z_p and an exemplary thermal diffusivity of $D_\mathrm{h,ts} = 1.0 \times 10^{-6}\,\mathrm{m^2/s}$ as correct order of magnitude for typical soils. The resulting fit applying this additional criterion has significantly improved as shown in Figure 4.10(b). Close to the surface, the slope of the fit and the profile data are in agreement, deeper down however the deviations are increasingly larger. This points to a discrepancy between the data-set and the model description assuming pure heat conduction in 1D. As we are mainly interested in good representation close to the surface, we can neglect this fact, as the weights ensure the focus on the near surface data. Finally, this yields an estimated thermal diffusivity of $2.3 \times 10^{-7}\,\mathrm{m^2/s}$ for the dry sand.

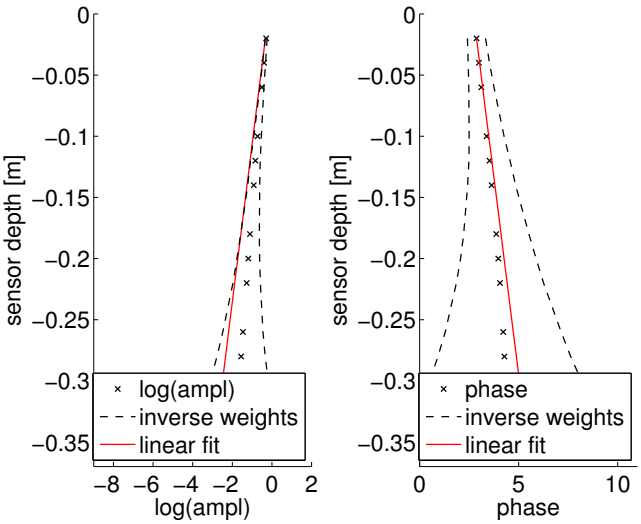

Figure 4.11: Estimation of thermal diffusivity from lab-measured soil temperature profiles of the wet sand experiment. Fit results are shown exemplary for profile information of the daily cycle. *left:* Linear fit (*red*) of log-amplitude data (*crosses*). *right:* Linear fit (*red*) of phase profile data (*crosses*). *Dashed lines* indicate inverse weights used within regression procedure, reflecting information loss with depth.

Not considering the cut of frequencies below the defined level, the fit of the profile information for wet sand shows the same characteristic bias, although to a slighter extent as the absolute amplitudes are notably smaller. The final fit with regard to the low frequency cut-off is shown in Figure 4.11. Again, the fit represents the profile information close to the surface well, however the data deeper down suggests a steeper slope. Altogether, the corresponding effective thermal diffusivity for the wet sand profile was estimated to $6.2 \times 10^{-7}\,\mathrm{m^2/s}$. As already expected from greater penetration depths of the signal, the value is about three times larger than that for dry sand. Hence, we can define the range of thermal properties of the sand used in the laboratory experiments of this work.

To conclude the analysis of the spectral profile information, an additional remark on the accuracy of the estimated D_h is needed. As already mentioned, the underlying statistics for the linear regression procedure here is too complicated to use straight-forward measures to characterize the uncertainty in the estimated parameters. The amplitude data is log-transformed, however not the phase profile. To ignore all these restrictions and transform nevertheless the edges of the confidence interval for the projection factor k "brute-force" via relation (3.9) would yield an uncertainty in the order of $10^{-10}\,\mathrm{m^2/s}$. In light of the deviations in the lower soil profile, the weights' balance seems to be too small to be reliable. Therefore, a solid statistical analysis beyond the scope of this work is needed and we will not refer back to this estimation for further analysis.

Surface Temperature Reconstruction

With the estimated projection factor k, the surface temperature can be reconstructed following the procedure described in Section 3.3. Using a noise level of 0.2 °C results in the above mentioned 1751 frequency entries in the spectra deemed to be significant. Originally, only two frequencies were set for the air temperature signal, however its realization revealed many more (Fig. 4.15(b)). Yet, more than a thousand points hint at a too weak criterion to select the frequencies considered in the projection. As a consequence, high frequency noise overlays the correct temperature variation of the reconstruction in Figure 4.12. The *root mean squared error* (rmse) of nearly 0.4 °C is still in the range of the sensor accuracy. However, an increase in noise level should yield a better reconstruction. For a noise level of 0.5 °C, the projection results are shown in Figure 4.13. Indeed, the high frequency noise is absent and the reconstruction fits the data much better. Yet, the remaining low frequency structure in the residual is now clearly visible. It indicates an underestimation of the amplitudes of both extremes, the minima and the maxima as well as a slight error in phase shift. Both suggest a structural error in the projection factor and the thermal diffusivity respectively. As the correct amplitudes are slightly smaller, the estimated D_h seems to be too large, since the projection factor is proportional to its inverse (Eq. (3.4)). We will however come back to this after the results of the wet sand experiment, since the deviations in the lower part of the profile indicate an even larger value and hence point to the opposite direction.

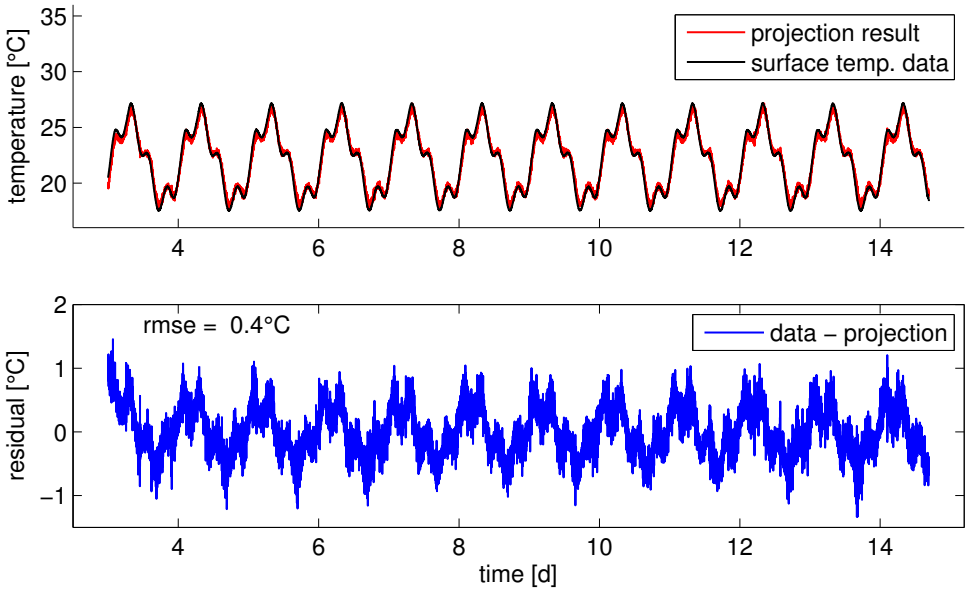

Figure 4.12: Projection results of the dry sand experiment. Noise level was set to 0.2 °C. *top:* Reconstructed (red) and measured (black) surface temperature. *bottom:* Residual: difference between data and projection result.

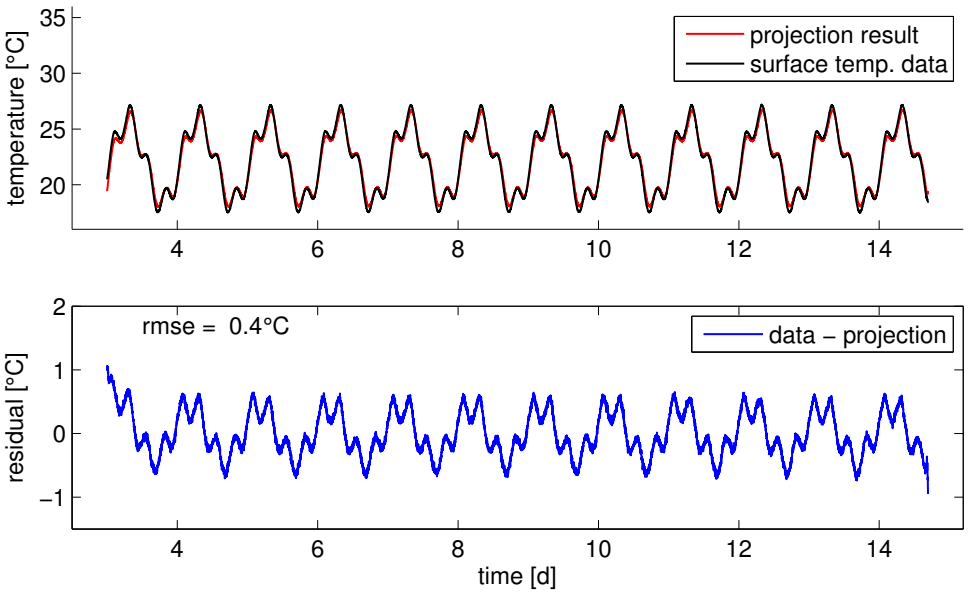

Figure 4.13: Projection results of the dry sand experiment. Noise level was set to 0.5 °C. *top:* Reconstructed (red) and measured (black) surface temperature. *bottom:* Residual: difference between data and projection result.

The reconstruction from the wet sand temperature profiles yields Figure 4.14. The root mean squared error is significantly smaller compared to the dry sand projection, even for the low noise level of 0.2 °C. The original surface temperature signal entering the soil is more damped and thus more smooth as that in dry sand. This was already explained before by the larger heat capacity of wet sand. Therefore, the overall amplitudes of the signal are smaller and noise is more suppressed. This results in less or at least smaller noise components in the spectrum. Most of them are sorted out, even by the weaker noise selection criterion. Furthermore, the reconstruction fits the data to a greater extend and the remaining white noise is well below the sensor resolution. Yet, the low-frequency structure underlying the high-frequency components reveals as well a biased projection factor and hence an error in the estimated thermal diffusivity. Apart from this, the residual look like pure white noise without any characteristic feature.

After pointing out all the details about special criteria for the application to real data-set and the resulting deviations between data and reconstruction, we should address the ill-posed character of the underlying problem, even for a measured data-set. From this point of view, both results, for dry and wet sand, emphasize the good performance of the method. Without additional knowledge of the functional form of the surface temperature signal and the frequencies comprised in it, our approach yields a reconstruction within and even below the accuracy of the sensors. Hence, we can conclude that our method is capable of reverting the heat diffusion process in a stable way considering all frequency

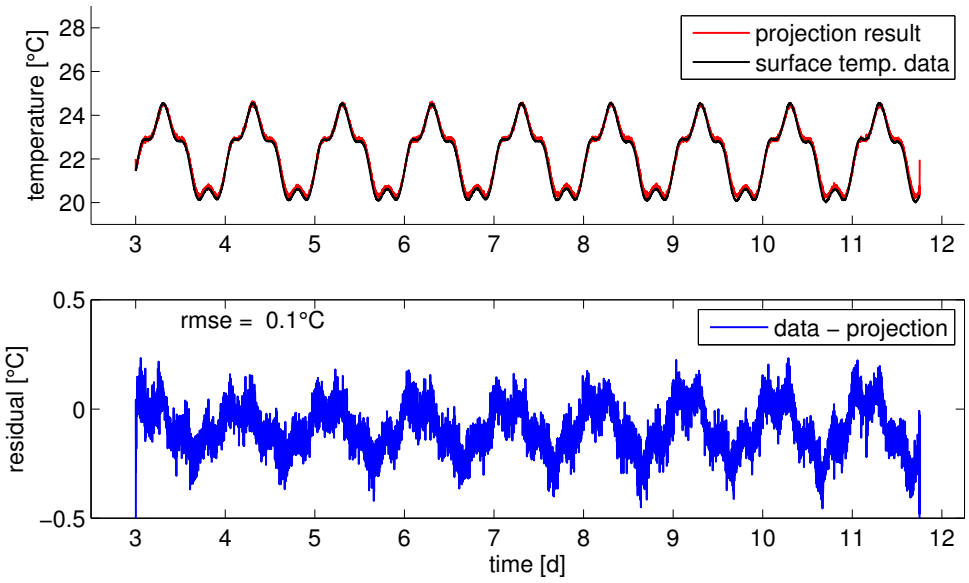

Figure 4.14: Projection results of the wet sand experiment. Noise level was set to 0.2 °C. *top:* Reconstructed (red) and measured (black) surface temperature. *bottom:* Residual: difference between data and projection result.

components that are well resolved in time-series of soil temperature profile. Looking at the results for the experiments above, this applies not only to synthetic data-sets, but to experimentally measured likewise.

Structure in Residuals of Projection

Looking at the structure in the projection residuals, we will close this section analyzing their frequency decomposition for the dry sand experiment (Fig. 4.13). At eye-sight, the deviations already suggest the same frequency components as the air temperature forcing. The amplitude spectra of the measured air temperature and the residual is shown exemplary for the dry sand experiment in Figure 4.15. It reveals a coupling between the outer air temperature forcing and the misfit of the surface temperature reconstruction. From the residuals, we have seen that the thermal diffusivity seems to be overestimated. However, the deeper profile information in Figure 4.10 and 4.11 hints at an underestimation. To resolve this apparent contradiction, we will take a closer look at the estimated D_h through the corresponding numerical heat conduction model in the following section.

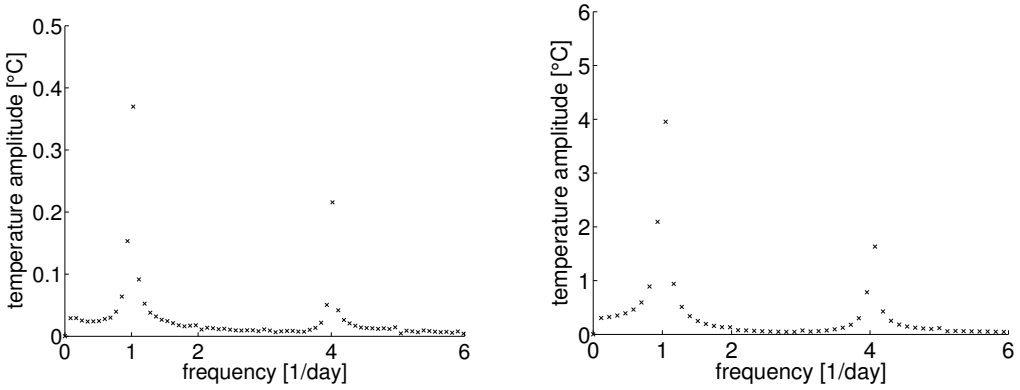

(a) Amplitudes in projection residual of dry sand experiment.

(b) Amplitudes in air temperature forcing during dry sand experiment.

Figure 4.15: Amplitude spectra of projection residual of dry sand experiment reveals the same frequency decomposition as the air temperature forcing.

4.2.3 Numerical Validation of Estimated Thermal Diffusivities

The projection results indicate that the thermal diffusivity estimated by the linear regression procedure does not completely fit to the true thermal properties of the dry and wet sand. However, as it is not possible to calculate directly an accuracy measure for the estimated values due to the complex underlying statistics, we try to validate them by comparing a numerical forward simulation based on the respective value for D_h to the measured data. In addition, we will infer an independent estimation from inversion of the numerical model.

The numerical forward model is the same as used for the generation of the synthetic data in Section 3. Pure heat conduction in 1D is considered and the sand column is assumed to be homogeneous with constant thermal diffusivity. The upper and lower boundaries are set to the temperature measurements at the surface and at 0.42 m. In the beginning, the system is in thermal equilibrium.

Estimated Soil Thermal Diffusivity from Profiles of Frequency Information

The residual between data and model for the estimated thermal diffusivity for the dry sand from the temperature projection method is shown in Figure 4.16(a). The deviations up to $\pm 0.6\,^\circ\mathrm{C}$ are of characteristic shape, since they trace the contour lines of the temperature data. The cooling periods in the data are systematically cooler, the warming phases respectively warmer than predicted by the simulation. In addition, the predicted penetration depth is too shallow. Therefore, the estimated value of $2.3 \times 10^{-7}\,\mathrm{m}^2/\mathrm{s}$ might be an underestimation of the actual thermal diffusivity. The lower part in the linear fit of the amplitude and phase profiles in Figure 4.10 supports this assumption. Since we are focusing on the near surface information in the context of the surface temperature reconstruction, we forced the regression through the weights to emphasize the upper part

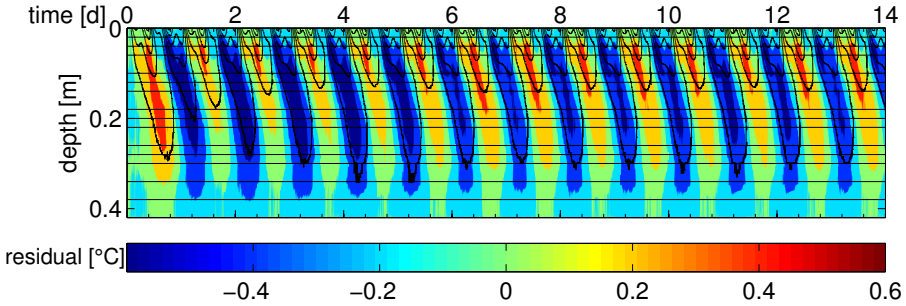

(a) Dry sand experiment.

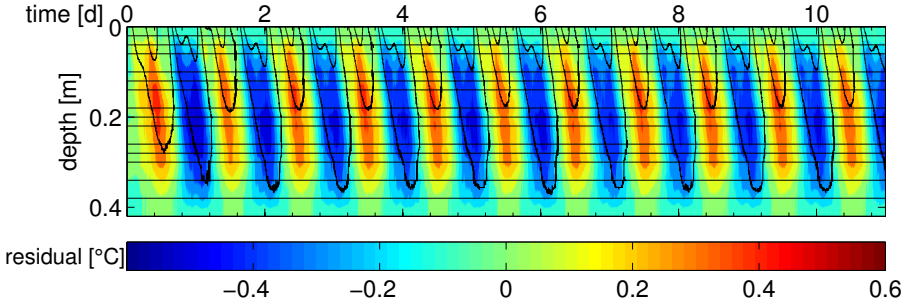

(b) Wet sand experiment.

Figure 4.16: Soil temperature residuals (data - model) for estimated thermal diffusivities of the dry and the wet sand from frequency information. Horizontal black lines indicate sensor positions. *Contour lines* refer to the corresponding measured soil temperature profiles (Fig. 4.5 & 4.6). Although the deviations are in the same order of magnitude as the accuracy of the sensors, their shape indicate an underestimation of the correct D_{h}.

of the profile. We have already seen that using this thermal diffusivity in the projection introduces a bias of the same size and structure as the residual for the corresponding numerical forward simulation. However, we can conclude that D_{h} is too large. These two trends contradict each other. Therefore, we attempted to gain deeper insight in the underlying data-set from the numerical inversion in the following.

For completion, the residual for the wet sand experiment (Fig. 4.16(b)) evinces the same structure. The deviations fit the contour lines of the temperature data. The overall temperature amplitudes are smaller compared to the dry sand and hence the underestimated thermal diffusivity results also in a smaller error. However, once more, we would expect the true value to be significantly larger than the $6.3 \times 10^{-7}\,\mathrm{m}^2/\mathrm{s}$ obtained by the linear regression.

Numerical Inversion to Estimate the Soil Thermal Diffusivity

In the following, we use an optimization algorithm around the above mentioned numerical forward model. With the *Levenberg-Marquardt* algorithm (*Marquardt*, 1963), the thermal

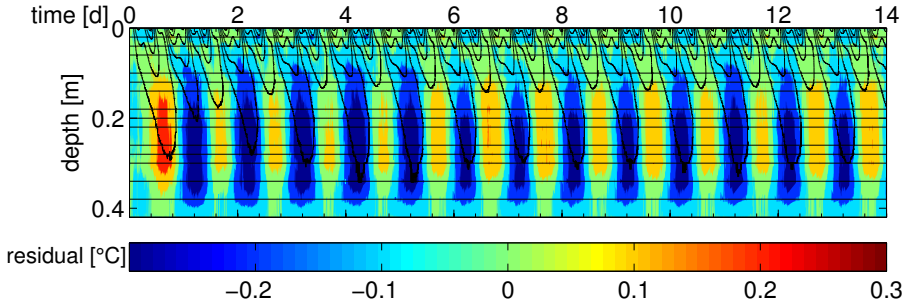

(a) Dry sand experiment.

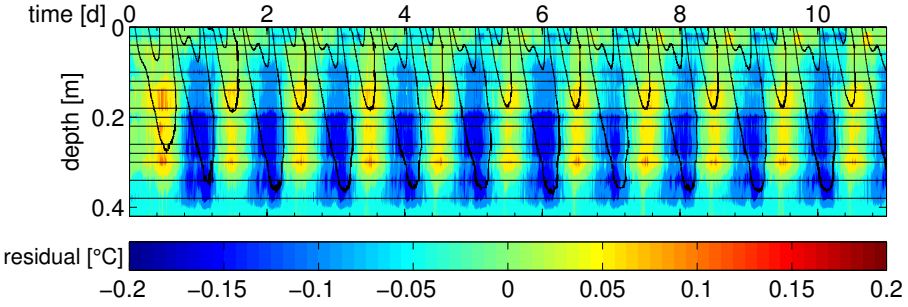

(b) Wet sand experiment.

Figure 4.17: Soil temperature residuals (data-model) for estimated thermal diffusivities of the dry and the wet sand from numerical inversion. *Horizontal black lines* indicate sensor positions. *Contour lines* refer to the corresponding measured soil temperature profiles (Fig. 4.5 & 4.6). The shape of the deviations indicates heat fluxes from the sides which are not represented in the model.

diffusivity is estimated inversely from the soil temperature data-sets of the dry and wet sand experiments.

The residual in Figure 4.17(a) shows that the deviations for the dry sand are only half as big as in Figure 4.16(a). This is a result of the larger estimate of $9.6 \times 10^{-7}\,\mathrm{m}^2/\mathrm{s}$ for the thermal diffusivity which is about a factor of 1.5 larger than the value estimated via the linear fit of the frequency information profiles. We can see that the representation of the overall soil temperature profiles has already improved considerably. Yet, the reconstruction of the surface information would get worse with this D_h. Therefore, the effective thermal parameter for the experiments here seems to be dependent on the focus we set during the parameter estimation. For the linear regression, the weights emphasize the upper part of the profile and the numerical model optimizes for the more for overall fit of the temperature profiles. Therefore, this discrepancy in the two estimates and the remaining deviations between data and model raises the question why the model does not fit the data to a greater degree?
The experiment was designed so that, especially for the dry sand, the soil temperature changes only due to heat conduction. Nevertheless, our model assumptions fail at some

point. Comparing the structure of the residual for the D_h of the linear regression (Fig. 4.16(a)) to this residual, a structural difference can be found. For example, the maximal deviation is no longer in the upper 20 cm, but in the lower part of the soil column. Furthermore, these deviations occur before the temperature variation (indicated by the contour lines) reaches that depth. Therefore, the error is largest, when the air temperature outside the sand column takes its maximum or minimum which is verified by the frequency analysis of the residuals.

Naturally, the same phenomenon is found when looking at the residual of the numerically estimated D_h for the wet sand (Fig. 4.17(b)). Again, the effect is not as pronounced as for the dry sand because of the overall smaller temperature amplitudes in the soil. Strictly speaking, it is even below the assumed noise level of the sensors and therefore reasonable. Yet, the structure exhibits the same neglected process which is, from the point of process understanding, not yet satisfying.

Following *Gergely* (2007), the heat flux per column height through the insulation can be estimated for steady state conditions via

$$\frac{j_h}{h} = -K_{h,ins} \cdot 2\pi r \, \frac{\partial T}{\partial r} \tag{4.7}$$

$$= -K_{h,ins} \cdot 2\pi \, \frac{T_{out} - T_{in}}{\ln \frac{r_{in}}{r_{out}}} \tag{4.8}$$

where $K_{h,ins} = 0.04\,\mathrm{J\,m^{-1}s^{-1}K^{-1}}$ is the heat conductivity of the insulation, r_{in} and r_{out} are the inner and outer radius of the insulation. T_{in} and T_{out} indicate the temperature at its inner and outer side. This points to maximal heat fluxes from the side for minimal and maximal air temperatures. Furthermore, the flux will be largest at the temperature stabilized bottom of the soil column where the temperature gradient towards the outside forcing is largest. Hence, the structure of the residual is an indication of the two dimensional character of the heat flow in the experiment which is neglected by the simplified 1D representation. A numerical test simulation in 2D should give further information about the impact of heat flow through the insulation at the sides and hence will be presented in the following paragraph.

Theoretical Analysis of the Influence of Lateral Soil Heat Fluxes

As the residuals already suggested a significant influence of heat fluxes from the side boundaries, we will close this section with a short analysis of a two dimensional system considering these fluxes. The model domain is sketched out in Figure 4.18. The experimental set-up can be assumed as rotational symmetric. A change of the reference system to cylindrical coordinates (Eq. (A.4)) in the appendix) allows a simplified representation of the system based on that special type of symmetry. For the full 2D simulations, a particular module is available in the *COMSOL* (2008) *Multiphysics* simulation toolkit. Hence, the model domain is shown on the right side of the sketch above. It is sized similarly to the laboratory experiments discussed before: a soil column with radius 0.12 m and a 0.42 m thick insulation, both 0.42 m high. Initially, the whole experiment is in

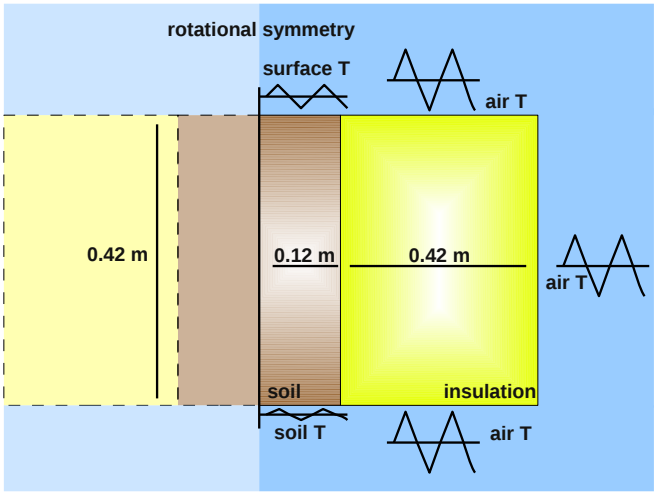

Figure 4.18: Sketch of model domain for 2D test simulation. Due to the rotational symmetry of the set-up, it is most efficient to solve the heat conduction equation in cylindrical coordinates.

thermal equilibrium at 22 °C. The measured temperature time-series of the surface, the air and the deepest soil temperature probe during the dry sand experiment are used as Dirichlet boundary conditions at the top, the sides and the bottom. On the left side, a preset boundary condition is applied to take the special symmetry into account. With this 2D module, two types of simulations were conducted to be able to extract the influence of the fluxes through the insulation. The thermal conductivity of the insulation is given by the fabricator as $K_{\mathrm{h,ins}} = 0.04\,\mathrm{J\,m^{-1}s^{-1}}K^{-1}$ and the heat capacity for the mineral wool as $C_{\mathrm{h,ins}} = 1.2 \times 10^5\,\mathrm{J\,K^{-1}m^{-3}}$. This finally yields a thermal diffusivity of $D_{\mathrm{h,ins}} = 3.5 \times 10^{-7}\,\mathrm{m^2/s}$. For the soil column, we took the estimated thermal diffusivity $D_{\mathrm{h,soil}} = 2.3 \times 10^{-7}\,\mathrm{m^2/s}$ of the dry sand experiment, as the impact there seems to be larger than for wet sand. In order to illustrate the influence of the side fluxes, we simulated two comparable scenarios: in the first one, the 2D model was calculated as described, in the second one the right boundary of the soil column was set to no-flow condition. The resultant temperature difference over time in the middle of the soil column, which corresponds to the left edge of the model domain, and is shown in Figure 4.19.

The difference between the simulation taking into account lateral fluxes through the insulation compared to a no-flow boundary at the sides shows the same characteristics as the residuals between the measured data and the 1D simulations above (Fig. 4.17(a) and 4.17(b)). In general, the heat flux through the insulation amplifies the trend in the soil heat flux. Again, the deviations do not trace the contours of the temperature variations, but follow close to instantaneously the changes in the outer air temperature. Additionally, the deviations are largest at the bottom of the soil column. As the bottom of the soil column is temperature stabilized and temperature amplitudes are already significantly damped below 20 cm, temperature gradients and consequently the fluxes

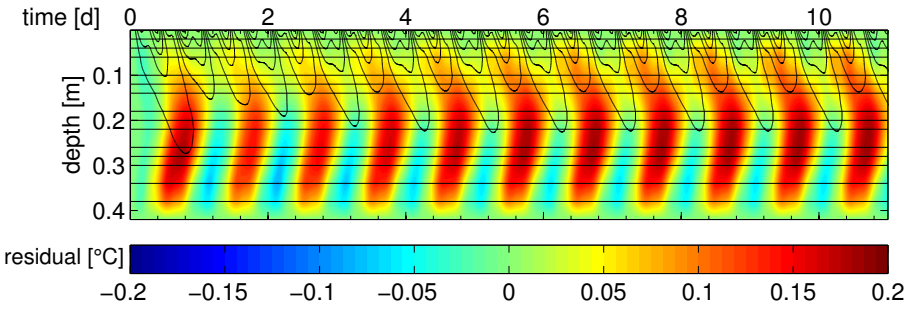

Figure 4.19: Soil temperature difference in the middle of the soil column for 2D simulations with and without heat fluxes through the side boundary.

from and towards the insulation are largest at this point. Hence, the lower part of the profile suggests a larger thermal diffusivity. This results in a compensation of the additional heat entry and removal from the side in an one-dimensional model representation.

For a higher soil thermal diffusivity, as e. g. for the wet sand, the effect of the side fluxes on the soil temperatures is smaller. The heat fluxes are continuous throughout the side boundaries. However, due to the larger thermal conductivity the corresponding temperature gradients will be smaller. Altogether, we can conclude that we ascribed the misfit of the 1D model. In addition, an effective D_h will overestimate the actual one, as it will be biased by the net impact of the heat fluxes from the side, if not explicitly represented.

A further attempt to estimate the correct D_h from an inversion based on the two-dimensional model did not succeed. On the one hand, the estimated value is sensitive to the thermal properties denoted to the insulation, but the roughly estimated values do not yield a significant change in the final soil thermal diffusivity estimates for the dry and wet sand. On the other hand, an estimation of both thermal parameters, for the soil and the insulation, did not converge. The measured soil temperatures in the middle of the soil column are not sensitive enough to improve the value of the insulation. We have no additional temperature measurements within the insulation itself which could provide further insight to the complete system. Therefore, the analysis concerning side fluxes from the insulation shows the qualitative effect which is consistent with the findings in the real data-sets, however it cannot be quantified any further at that point.

Let us turn back to the implications of the lateral heat fluxes on the frequency analysis of soil temperature profiles and the reconstruction of the surface temperature information. We have seen that the lateral heat fluxes enhance the temperature variations in the soil, the cooling and warming. Analyzing the frequency information with depth of the 2D simulation yields at first glance an identical profile and a similar quality of the fit (Fig. 4.20). With $2.4 \times 10^{-7}\,\mathrm{m}^2/\mathrm{s}$ the estimated thermal diffusivity for the data-set

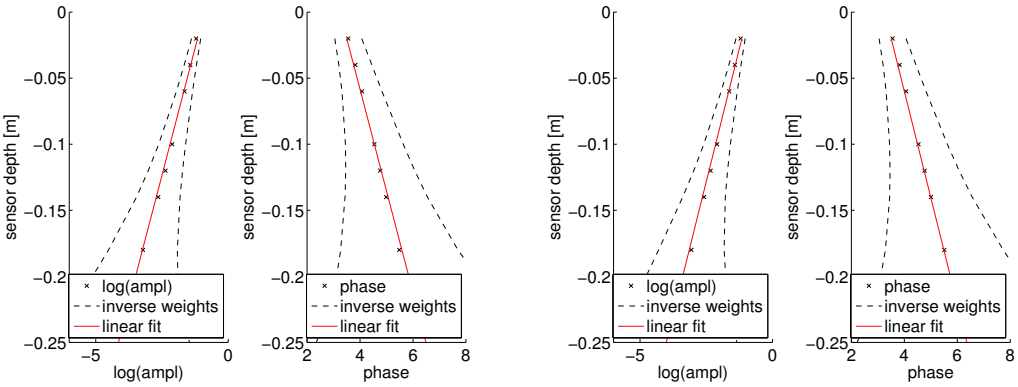

(a) No heat entry or removal from the side.

(b) With lateral heat flux..

Figure 4.20: Estimation of thermal diffusivity from simulated 2D soil temperature profiles. Fit results are exemplary for profile information of the daily cycle. *left:* Linear fit (*red*) of amplitude data (*crosses*). *right:* Linear fit (*red*) of phase profile data (*crosses*). *Dashed lines* indicate inverse weights used within regression procedure, reflecting information loss with depth.

with no-flow conditions at the side boundary is slightly too high (Fig. 4.20(a)). The same evaluation on the data-set with lateral fluxes results with $2.8 \times 10^{-7}\,\mathrm{m}^2/\mathrm{s}$ in an even stronger overestimation (Fig. 4.20(b)) which is a bias caused by the additional heat flux from the side. Additionally, the phase information below 0.1 m suggest a slightly different slope. From the temperature difference between the two models, we have concluded that no large deviations are to expect, yet the following trend becomes evident: In the presence of lateral heat fluxes which induce an amplifying trend in the soil temperature changes, we would expect any estimation procedure based on an one-dimensional model representation to compensate this through an increase in the thermal diffusivity value.

Furthermore, the reconstruction of the surface temperature in Figure 4.21 reveals the same residual structure due to the error in the estimated D_h as the projection of the experimental data. This structure indicates the misfit and hence a structural error in the underlying model settings. Therefore, the residuals for the dry and wet sand experiments are a consequence of the heat fluxes through the insulation, as they lead to a higher thermal diffusivity estimate from the profile data in a one dimensional system representation.

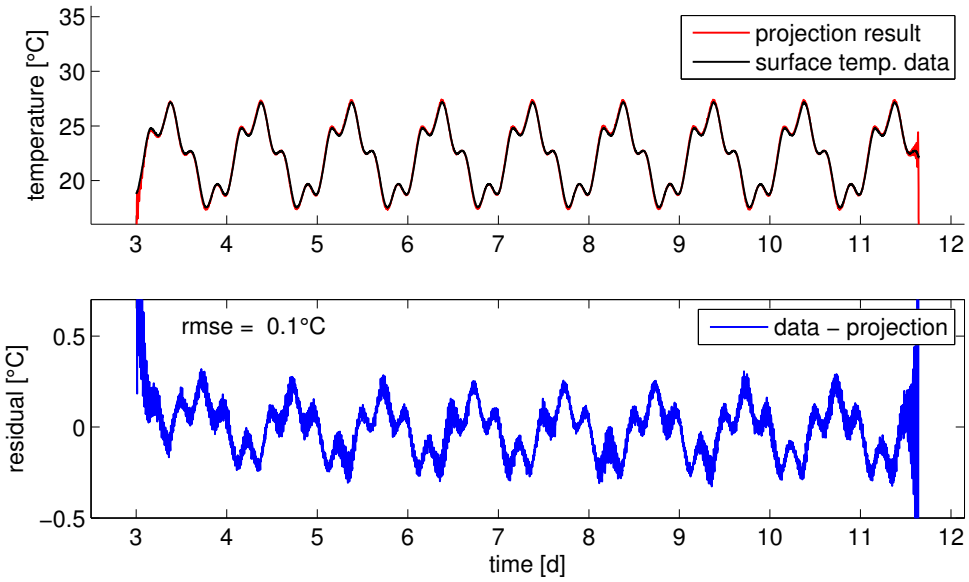

Figure 4.21: Projection results for synthetic soil temperature profile with lateral heat fluxes. Noise level was set to 1 °C. *top:* Reconstructed (red) and actual (black) surface temperature. *bottom:* Residual: difference between actual and projected surface temperature.

4.3 Evaporation Experiments

After the pure heat conduction experiments as outlined in the last section, we increased the level of complexity in the system by the evaporation of the water at the surface. In the first experiment, the air temperature was held constantly at 28 °C. Afterwards, a second evaporation experiment was performed again with periodically modulated temperatures.

4.3.1 Experimental Results

Constant Air Temperature

For the first evaporation experiment, the same soil column was used as in the pure heat conduction experiments. The only modification compared to the set-up in Figure 4.1 was a balance (CH1NE, Sartorius AG, Göttingen, Germany) which was put under the insulated soil column. The balance has an accuracy of 0.1 g, but due to the fan of the temperature control of the climate chamber the final resolution of the weight measurement is not better than 1 g. Nevertheless, the balance unit allows the detection of the water loss by evaporation and with that the calculation of the corresponding evaporation flux.

We start to analyze the experiment with constant air temperature from a thermal perspective and hence, with the resultant soil temperature profile which is shown in Figure 4.22. Initially, the soil column was water saturated and no water was evaporating its surface. The whole experimental set-up was in thermal equilibrium at 28 °C and the air temperature was kept constant at that level all the time. Therefore, the low temperatures at the soil surface reflect the increasing cooling due to evaporation. The energy needed for the phase change is removed from the surrounding air and soil. Hence, temperatures at and close to the surface decline by 5 °C in the first ten days. In the second part of the

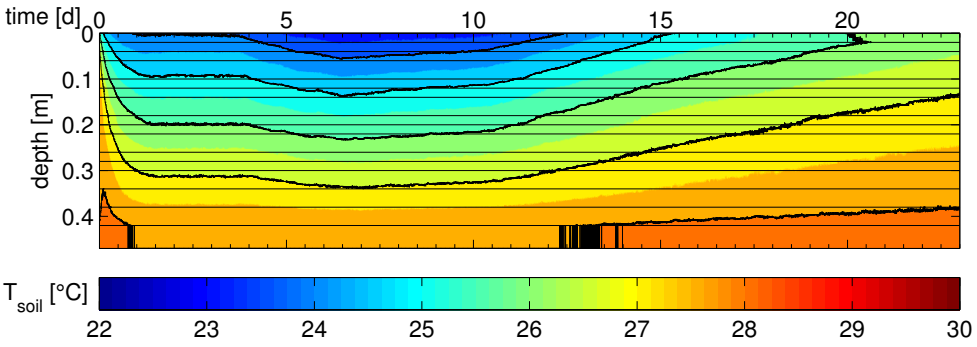

Figure 4.22: Soil temperature profile for evaporation experiment with constant air temperature. The evaporative cooling results in surface temperatures up to 5 °C below the air temperature of 28 °C. Around day 10, the surface temperature rises, since the evaporation flux decreases due to the limited water availability at the surface.

experiment, the energy removal at the surface seems to decrease which causes the soil temperatures to rise again. This can be explained by the limited availability of water at the surface after some time. As long as the water is sucked up to the surface through the capillary forces and the phase change occurs at the top of the soil column, the evaporation flux and hence the energy sink is high. No water reservoir was connected to the soil column to stabilize the water table at a certain height within the sand. Hence, the evaporation caused the water level to sink continuously. Below a certain depth, the capillary forces cannot transport the water within the pores towards the surface. Therefore, the water evaporates within the soil and is transported as vapor upwards. This transport mechanism is a lot slower. Therefore, the evaporation flux and the energy sink drops down.
These two phases of the experiment are distinguished as stage 1 and stage 2 evaporation (*Scherer* (1990), *Yiotis et al.* (2004)). Stage 1 characterizes the evaporation flux limited by the soil hydraulic properties, whereas the vapor transport within the soil is the crucial process restricting the evaporation flux in stage 2.

Further system variables measured during this evaporation experiment are shown in Figure 4.23. The weight loss of the soil column and the resulting evaporation flux are outlined in Figure 4.23(a) and 4.23(b) respectively. As the balance has an accuracy of approximately 1 g and was measured with a rate of 1 Hz, its resolution is high enough to detect even small weight changes. The calculated flux in mm/h indicates a noise level of about 0.1 mm/h of the set-up, as we can see no physical explanation for small scale fluctuations of this size. Altogether, these figures verify that the evaporation flux was higher during the first ten days, and afterwards decreased by more than a factor two.

Even more details about the progress of the soil temperature profiles and the evaporation flux can be explained by the remaining system variables, the relative humidity (Fig. 4.23(c)) and the soil water content (Fig. 4.23(d)). For example, the higher surface temperatures until day 5 correspond to a lower evaporation flux during that time and correlate with a higher relative humidity (Fig. 4.23(c)). We know from previous experiments that the temperature regulation of the climate chamber is associated to a decrease in relative humidity while operating the system. As the potential evaporation is proportional to the water vapor pressure deficit and the relative humidity accounts for the actual water vapor pressure in the air, both quantities are directly linked and mutually affect each other. Therefore, a ten percent higher relative humidity has a significant impact on the amount of water evaporating from the surface. It was already mentioned in section 4.1.1 that the climate chamber can only modulate the air temperature, not the relative humidity. However, as the air supply of the laboratory is connected to the ambient air, the relative humidity reflects weather changes outside the building, hence influencing the detailed evolution of the evaporation process during the experiments.
During stage 1, the decay of the water content at 8 cm, is steepest compared to all other water content curves for which the corresponding TDR probes detect the drying of the soil mainly in stage 2. Even small flux changes, as the peak at day 15, can be perceived in the soil water content curves. The sand runs dry at 16 cm) around day 10. At first, the decrease is rather linear, but around day 12 it becomes flatter, even though it is not as

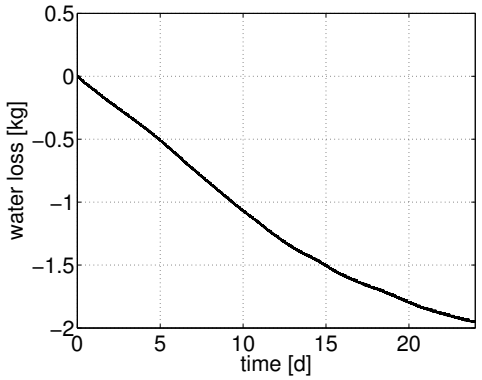

(a) Water loss calculated from the balance data.

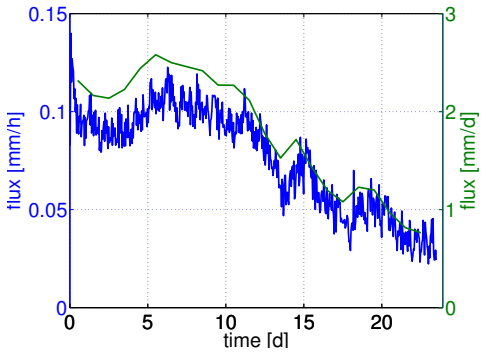

(b) Hourly and daily mean evaporation flux calculated from the balance data.

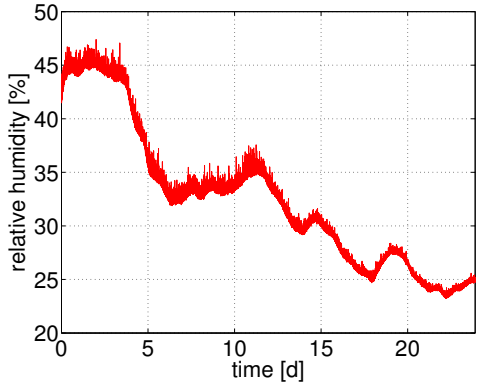

(c) Relative humidity.

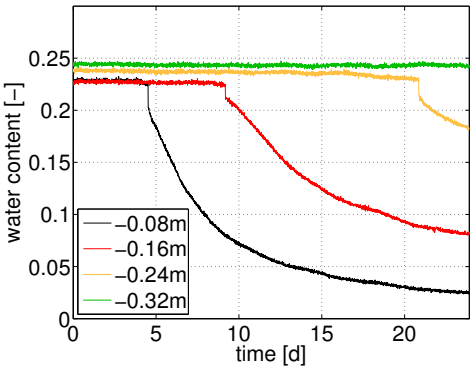

(d) Soil water content.

Figure 4.23: Further system variables measured during the evaporation experiment with constant air temperature.

dry as the first TDR at day 8 when the same effect was observed there. A simultaneous decrease of the evaporation flux at that time is shown in Figure 4.23(b) which indicates the transition to stage 2 evaporation. This characterizes the increasing displacement of the evaporation front from the surface into the soil.

Co-relations with evaporation flux Further insight in the coupling between the evaporation flux and significant state variables is provided by Figure 4.24. The main structure of the flux correlates with the water vapor pressure in air and is reflected in the surface temperature. However, additional features indicate that identifying as key control is not sufficient. For example, the relative humidity is close to constant between day 5 and 10, while the evaporation flux shows a decreasing trend. Yet, an increase in the surface temperature can be observed. In contrast, the surface temperature reflects no longer the increasing flux around day 15 and 20, as the system already shifted to stage 2 evaporation. This is evident, since stage 2 evaporation by definition means that water evaporates within the soil, not from the surface. Therefore, the surface temperature will no longer

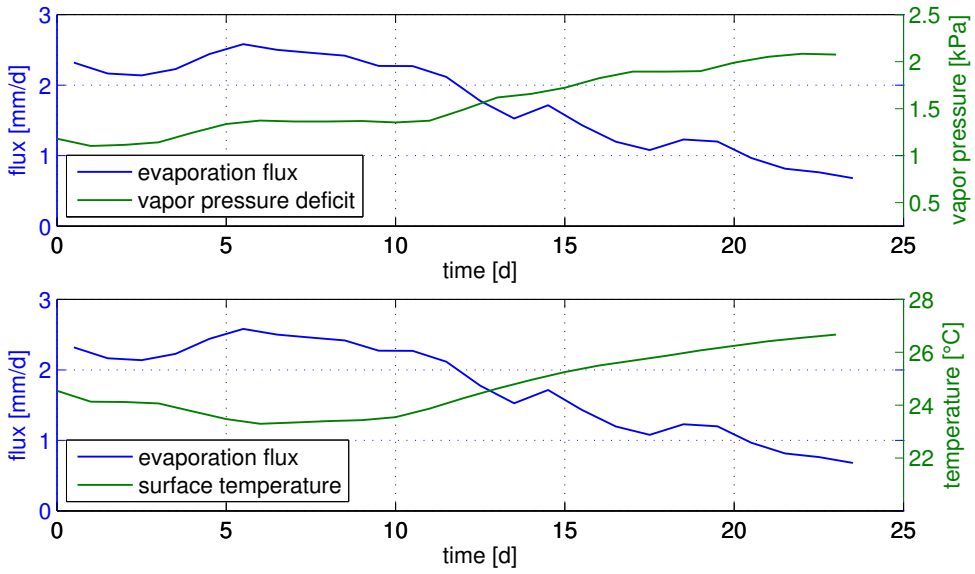

Figure 4.24: Co-relation of evaporation flux with water vapor pressure in air and the surface temperature for the evaporation experiment with constant air temperature.

indicate all flux details
Altogether, the main shape of the evaporation flux and the surface temperature is determined by the underlying soil water dynamics, but the dips and peaks in between are reversely correlated with changes in the relative humidity. Therefore, both humidity and surface temperature, have to be considered to get a reliable representation of the coupling processes at the surface for both evaporation stages. Eventually, the water vapor pressure deficit $e_\mathrm{a}(rh_\mathrm{a}, T_\mathrm{a}) - e_\mathrm{surf}(\psi_\mathrm{m}, T_\mathrm{surf})$ is the key control of the complete evaporation process. The first term accounts for the state of the atmosphere, defined by the relative humidity rh_a and the air temperature T_a (Eq. (2.43)), while the second reflects that of the soil, determined by the matric potential ψ_m and the surface temperature T_surf through Kelvin's equation (2.22).

Periodic Air Temperature Forcing

In the second evaporation experiment, the air temperature was again periodically modulated, while the soil column was completely water saturated at the beginning and the soil water was free to evaporate from the surface. The only applied modification was the depth of the soil profile. The sand column was only 37 cm high, hence the upper TDR was removed and the top four pt100 temperature probes measured an air temperature profile. Due to the reduced profile depth, the penetration depth of the temperature signal was decreased through an increase in frequencies superposed for the air temperature regulation. Its resultant frequency decomposition (Fig. 4.25) shows two main cycles with

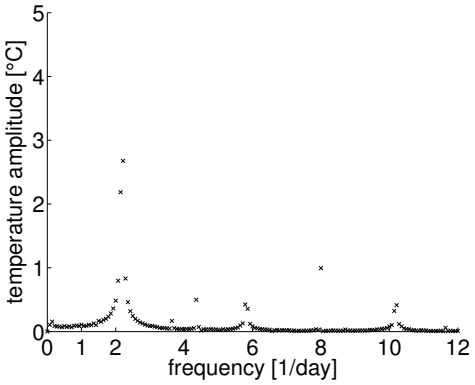

Figure 4.25: Frequency decomposition of air temperature for evaporation experiment with periodic air temperature forcing.

an amplitude of 3.2 °C for the 11 h- and of 1.3 °C for the 3 h-period. Furthermore, the first harmonics can be seen. The mean air temperature was finally 19.8 °C.

In total, the experiment took nearly 40 days. Again, we start to analyze the experiment from a thermal perspective. The resultant soil temperature profiles are partly shown in Figure 4.26. The experiment started from thermal equilibrium at 20 °C. In Figure 4.26(a), the corresponding air temperature forcing and its coupling to the surface and the soil is plotted from day 5 to day 15. The line plot highlights particularly the start of the evaporation in particular. During the cooling cycles, the surface temperature is below the top soil temperature measurement as it is linked closer to the air. When the air temperature increases above 20 °C, the surface temperature does not exceed the top soil temperature due to the energy sink at the soil surface.
The complete soil temperature profiles are well below 20 °C in the beginning of the experiment due to the strong evaporative cooling at the surface. The asymmetry of the temperature signal propagating in the soil in particular hints at the additional process during the warming periods. The cooling cycles are clearly represented, but the warming cycles seem to be skipped. The soil temperatures rise hardly above 19 °C, even when the outside temperature approaches 30 °C. Most of the thermal energy is removed by the evaporation process, and hence cannot warm the underlying soil. Thus, the mean surface and soil temperature is considerably below the mean air temperature and soil temperatures are nearly constant during the warming cycles.

During this evaporation experiment, the weight measurements failed. The balance device was not able to compensate the air temperature variations and hence to stabilize the measurement signal. This is the reason why we miss a quantitative measure for the evaporation flux and its changes during the experiment.
However, as we have already seen in the experiment before, the relative humidity and water availability control changes of the evaporation flux reflected in changes of the surface temperature. For example, the slightly higher surface temperature around day 10

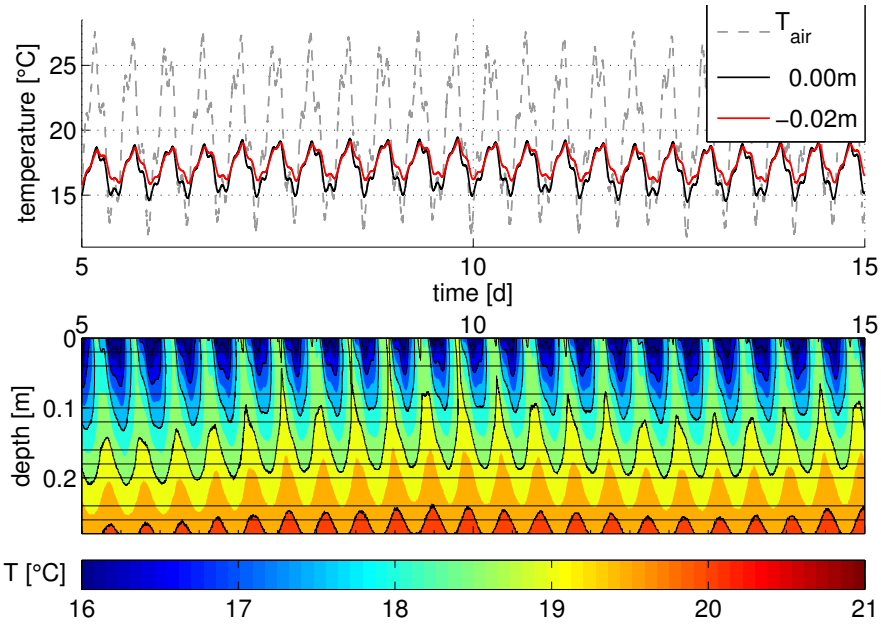

(a) Stage 1 evaporation.

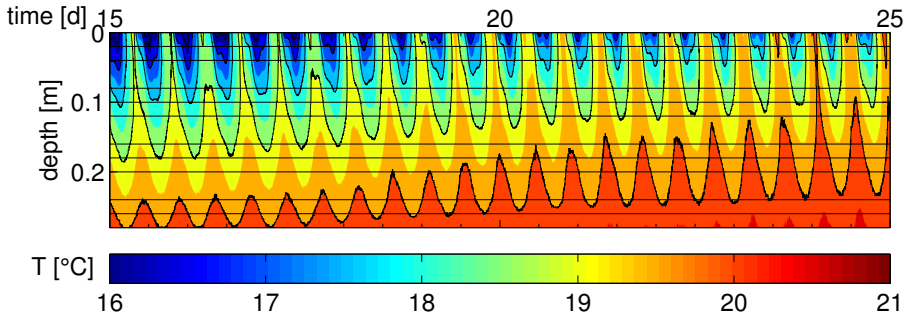

(b) Transition to stage 2 evaporation.

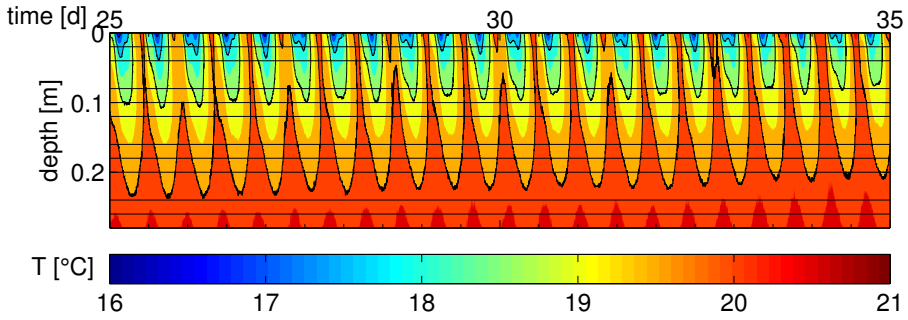

(c) Stage 2 evaporation.

Figure 4.26: Temperature data of evaporation experiment with periodic air temperature forcing. *top:* Air temperature forcing and upper two soil temperature measurements; *bottom:* Soil temperature profiles. Evaporation consumes almost all energy at the surface during the warming cycles.

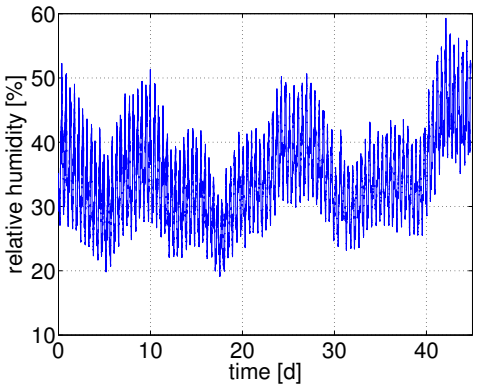

(a) Relative humidity.

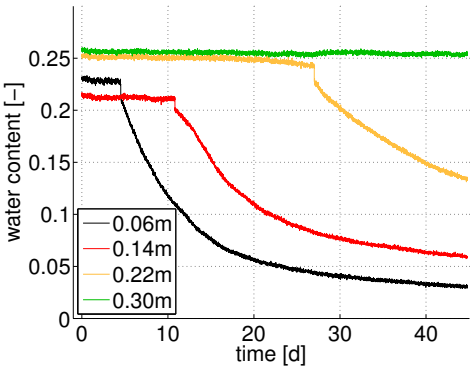

(b) Soil water content.

Figure 4.27: Water content and relative humidity data of evaporation experiment with periodic air temperature forcing.

corresponds to an increased relative humidity at that time (Fig. 4.27(a)), the most likely cause of a reduction of the evaporation flux during that time.

At day 15 (Fig. 4.26(b)), the evaporation flux seems to change. The slow rise in surface temperature indicates a decreasing energy removal at surface level. We would expect the surface water again to get limited at some point in the experiment, when the water table is too deep down in the column and hence the capillary forces can no longer bring the water up to the surface. Beginning with the large pores, evaporation happens more and more within the soil and the water vapor is not directly delivered to the free air. It has to be transported by the gas phase through the pores towards the surface. Therefore, the evaporation process is slowed down and less energy is removed from the system. Hence, the surface and consequently the soil temperatures rise.
The increase in surface temperature corresponds further with a change in the slope of the water content curve of the second TDR (Fig. 4.27(b)). As it is located 2 cm higher as in the experiment before, the drying at this sensor depth has already started during stage 1. Therefore, a kink of the curve at day 15 hints at a change in the water flux and indicates the start of the transition to stage 2.

In the third phase of the experiment, starting around day 25 (Fig. 4.26(c)), the system finally adapted to stage 2 evaporation. In this period, the evaporation flux is mainly determined by the vapor transport within the soil. Looking from the bottom, the mean temperature of the sand column fits the mean air temperature. An additional process can be observed during the warming periods. The temperature profile is close to constant for these phases, but the removed energy is significantly lower than in stage 1. Temperatures below 18 °C are now restricted to the upper 10 cm and the surface temperature rises for the first time above 20 °C.

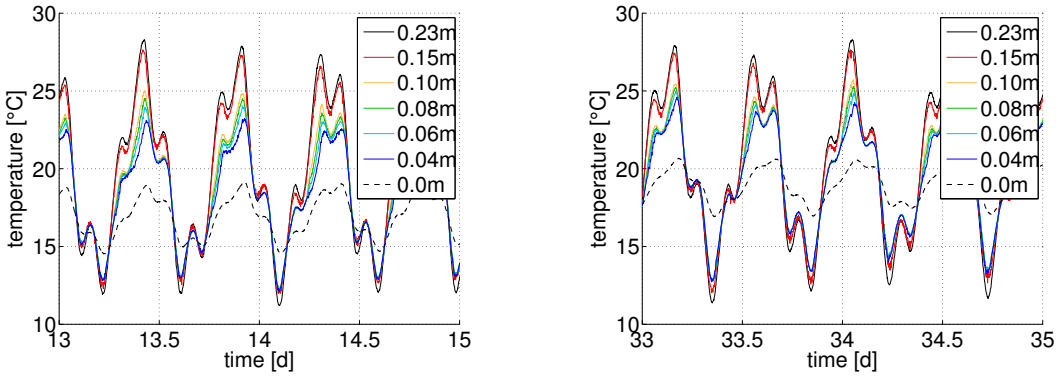

(a) Stage 1 evaporation.

(b) Stage 2 evaporation.

Figure 4.28: Influence of evaporation process on near surface air temperature profile.

Influence of surface evaporation on air temperature In Figure 4.28, two-day sections of the air temperature profiles are shown, one for stage 1, another one for stage 2 evaporation. Obviously, the evaporation process at the soil surface has an impact on these profiles. The air temperatures are following simultaneously the forcing during the cooling cycles, when only a slight sensor offset is detected. While air temperature rises, there is a spreading between the measurements at different heights. When the outside temperature exceeds 16 °C, the sensors closer to the surface detect temperatures below the forcing of the climate chamber. This effect is particularly strong for the high evaporation fluxes during stage 1, however it is still visible to a smaller degree during stage 2. This indicates the coupling of the surface temperature towards both compartments. As the diffusivity of air is at least one order of magnitude larger than that of soil, the damping and phase shift is obviously weaker and cannot be resolved for pure heat conduction during the cooling cycles. Yet, the presence of an additional energy sink at the surface due to evaporation influences the air profile from the bottom and releases a considerable footprint in the data under the present laboratory conditions.

4.3.2 Soil-Atmosphere Coupling

In this section, we will elaborate the temperature profiles in the soil and the air above. The temperature profiles at different times during the experimental progress reveal more details about fluxes and the overall energy partitioning at the surface. Hence, we will infer a deeper understanding of the coupling processes between the two compartments across the soil surface.

Evaporation for Constant Air Temperature

Figure 4.29 highlights the evolution of the temperature profiles with time. The air temperature is within an accuracy of 0.5 °C constant, but the temperatures close to the surface increase with time. In the beginning, the surface is more than 4 °C cooler than the air, as the evaporation removes much energy from the surrounding environment. Between day 5 and day 10, we already saw an increase in the evaporation flux due to the decreasing relative humidity. After day 12, the system moves towards stage 2 evaporation, because water close the surface gets limited. The profiles, especially in the upper

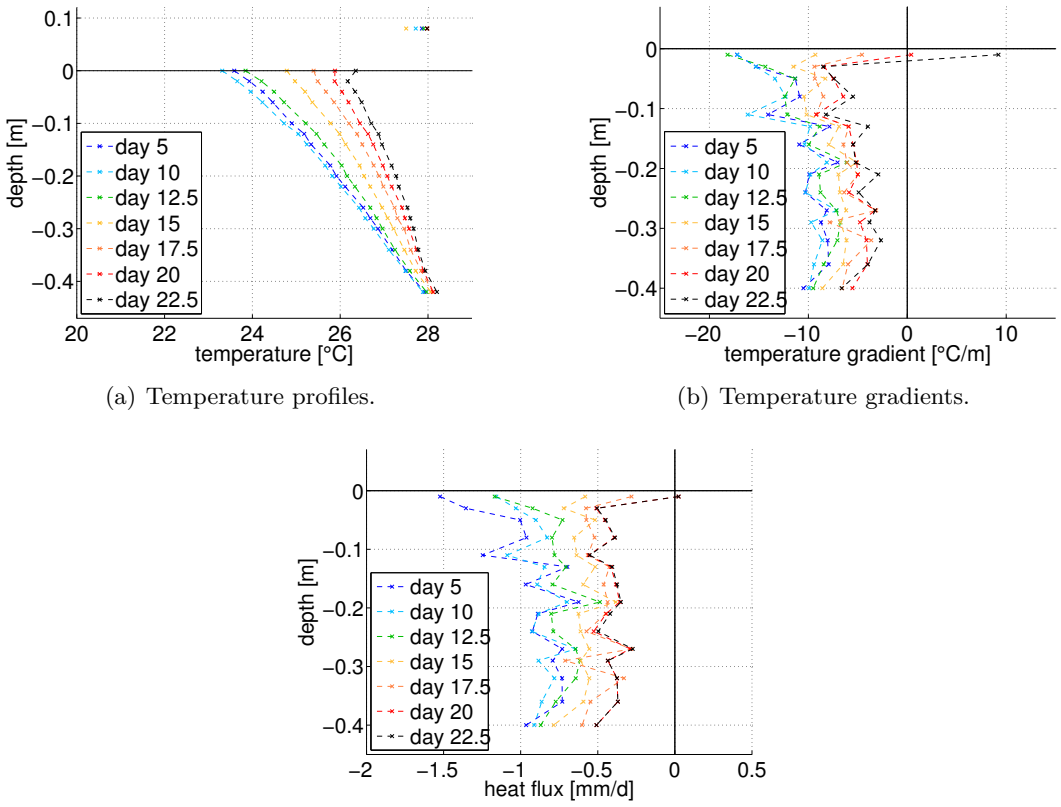

(a) Temperature profiles.

(b) Temperature gradients.

(c) Estimated soil heat flux.

Figure 4.29: Profiles of soil temperature, temperature gradients, and heat flux estimates for evaporation experiment with constant air temperature.

part of Figure 4.29(a) in the beginning of the experiment, are not linearly increasing with depth. Hence, the temperature gradients in Figure 4.29(b) are not constant over depth, as we would expect from theory (Eq. (2.17)) for a stationary system, where the flux is constant. The sign-convention is chosen following *Foken* (2008): negative gradients indicate a flux towards the surface, while positive ones point to fluxes that transport energy away from it. Besides the structure in the residuals of the numeric simulations in section 4.2.3, this hints on addition heat input from the sides. The horizontal heat flux was shown to be proportional to the difference between the inner and outer temperature (Eq. 4.8). Therefore, the upper part of the profile, where evaporation causes the largest decrease in temperature, is less influenced by side fluxes. The vertical heat flux is larger towards the surface. Directly at the surface, the steepest gradients can be recognized, as the phase change of the water occurs there. After day 12, water becomes spare and the evaporation flux decreased which reduces the soil heat flux and hence the gradients towards the surface in the subsequent days. Furthermore, the temperature gradients are increasingly higher within the soil than close to the surface for the transition to stage 2 evaporation. The temperature gradients at day 20 and 22.5 finally indicate a heat entry at the surface into the soil, while the ones below are still negative. This observation suggests a displacement of the evaporation front into the soil. Additionally, a reduction in the evaporation flux caused the temperature gradients to decrease. We should also keep in mind that thermal properties are related to the soil water content. Due to the drying, the soil thermal conductivity will decrease as well and therefore smaller gradients will result in an even smaller soil heat flux.

Quantitative analysis of the coupling processes in steady state The data-set of the first evaporation experiment with constant air temperature is the most complete, as we had measured the water loss over time with the balance, and hence the evaporation flux. All other state variables are also known. During stage 1, the fluxes are close to constant and the coupling between the water and the energy cycle can be quantified for the approximately steady state system. In the process, the thermal and hydraulic properties are roughly estimated.

Figure 4.29(c) shows the quantitative estimates for the soil heat flux calculated from the temperature gradients in different depths via the flux formula

$$j_{\mathrm{h,\,soil}} = -D_{\mathrm{h}} C_{\mathrm{h}}(\theta) \frac{\triangle T}{\triangle z} \tag{4.9}$$

where the diffusivity D_{h} is set constant and equal to the estimated value of $9.6 \times 10^{-7}\,\mathrm{m^2/s}$ for the wet sand to compensate best for the additional heat input through the insulation. This suffices for a rough estimate, as only the upper 15 cm of the soil became drier during the first 20 days of the experiment. Nevertheless, the heat capacity C_{h} was adapted for the changing water contents with the according data following equation (2.16). The porosity was set to 0.25 with respect to the water content measurements for saturation at the beginning of the experiment. The corresponding values for the specific heat capacities and the mass densities of the constituents are taken from *Roth* (2006), Table 7.1. The

underlying sign-convention indicates energy transport towards the surface as negative and a removal away from it as positive.
If we compare the fluxes at the bottom of the sand column with the surface evaporation flux of $2.5\,\mathrm{mm/d} \approx 71\,\mathrm{W/m^2}$ measured by the balance in the beginning of the experiment, we recognize that only about one third of the energy seems to be provided by the soil. The flux entering the system from the heating unit at the bottom is negative throughout the whole experiment, thus indicating a net energy entry up to 1 mm/d. For the part of the soil profile below $-0.2\,\mathrm{m}$, the assumption of complete saturation is valid. Hence, the assumed values for diffusivity and heat capacity are deemed reliable and consequently the estimated soil heat fluxes.

In the following, we will to investigate the detailed understanding of the system by applying the theoretical basis from section 2.3 to the soil-atmosphere coupling for the nearly stationary system during stage 1. All further calculations in this paragraph refer to the temperature profiles of day 5. The remaining system variables are given in table 4.1.
Calculating the mean of the deepest four flux estimates of the profile at day 5 in Figure 4.29(c) yields a lower bound of the net soil heat flux of 0.8 mm/d towards the surface. Thus, the soil heat flux contributes only about one third of the energy for the phase change at the surface. This shows that two third (1.7 mm/d) are supplied from the air above the soil. We would not expect this under conditions outside the laboratory, where the radiation from the sun provides most energy at the surface and hence is the main driving force for evaporation, not the sensible heat flux in air. Yet, for the laboratory conditions, radiation is excluded and the energy transport towards the surface is dominated by the air flux. Altogether, this flux can be described by an effective diffusion process. The appropriate diffusion coefficient will be larger than that in the soil ($\sim 10^{-6}\,\mathrm{m^2/s}$) and even larger than that of molecular diffusion in free air ($\sim 10^{-5}\,\mathrm{m^2/s}$), but smaller as that describing the effective eddy diffusion in the free atmosphere ($\sim 1\,\mathrm{m^2/s}$). To get the magnitude right for a heat flux of 1.7 mm/d in air, the diffusivity for the climate chamber experiment is approximately in the range of $10^{-3}\,\mathrm{m^2/s}$, since we measured a temperature difference of about 5 °C between the air and the soil surface.

Table 4.1: System variables to estimate the soil-atmosphere coupling quantitatively for the evaporation experiment with constant air temperature. Data is chosen exemplary for day 5.

relative humidity	40 %
T_{air}	28 °C
$T_{\mathrm{soil,bottom}}$	28 °C
T_{surface}	22.7 °C
j_{evap}	$2.5\,\mathrm{mm/d} = 70\,\mathrm{W/m^2}$
$D_{\mathrm{h,soil}}$	$9.56 \times 10^{-7}\,\mathrm{m^2/s}$

The dimension of the diffusivity in air reveals even more details about the type of transport process observed. As it is two orders of magnitude above the value for pure molecular diffusion, the temperature difference seems to be large enough that the stratification of the air gets unstable and convective cells are built above the surface. Hence, the heat is primarily transported convectively which is considerably more efficient than typical pure diffusion. This is further confirmed by the corresponding Rayleigh number (Eq. 2.27) which indicates the dynamical state of a fluid (*Niemela et al.*, 2000). It can be viewed as ratio of the convective forces and the product of thermal and momentum diffusivities. For this experiment, the characteristic length of the system is given by the height of the air column above the soil surface. For simplicity, we set it to 1 m which yields a lower estimate for the Rayleigh number of $> 10^6$, while an estimation of the critical Rayleigh number (Eq. 2.28) would yield $Ra_{\text{crit}} = 779$. Therefore, it is appropriate to expect convective transport for the large temperature difference between soil surface and air. The resultant flux could be described by an effective diffusivity orders of magnitude larger than that for molecular diffusion. Furthermore, this implies by definition that the transport of momentum, heat and vapor in air is characterized by the same parameter. Thus, we do not have to distinguish the transport parameters of those quantities in the further analysis. Their transport behavior differs only on a molecular scale, not in a macroscopic, convective dominated regime.

The final step in the quantitative investigation of the system is to link the water and the energy cycle at the surface. The exemplary data was again taken from day 5, hence the system is still in stage 1 and water evaporates directly from the surface. Therefore, the vapor flux in air (Eq. (2.42)) equals the water flux in the soil given by equation (2.2). As the measurement of relative humidity might be the one with the largest uncertainty (>2%), we calculate the water vapor pressure at day 5 from equation (2.43) as

$$e_{\text{air}}(rh_{\text{air}}, T_{\text{air}}) = 1.512 \pm 0.075\,\text{kPa}. \tag{4.10}$$

With that, we can deduce from equation (2.42) a thermal diffusivity of $1.505 \times 10^{-3}\,\text{m}^2/\text{s}$ in air for the measured evaporation flux. This yields a water vapor pressure of 2.759 kPa at the surface which in turn corresponds to a surface matric potential of -2.85 m. Increasing $D_{\text{h,air}}$ only by $\times 10^{-6}\,\text{m}^2/\text{s}$ changes the water vapor pressure by 0.004 kPa. This value is well below the resolution of the measurement, but it changes the corresponding matric potential by a factor of ten. Thus, the system is highly sensitive at the link and cannot be better determined within the measurement accuracy. Especially, any automatic optimization routine failed to approximate the parameters in the system and the manual tuning was the best we could achieve.

From the soil side, a hydraulic forward model solving Richards equation (Eq. 2.8) was implemented in the *COMSOL* (2008) multiphysics framework. The Brooks-Corey parameterization (Eq. 2.1.1) was chosen, since the slope of the water content curves (Fig. 4.23(d) and 4.27(b)) suggested an abrupt decay, not a smooth transition from saturation to drier states. Therefore, the hydraulic properties estimated for the Mualem-van Genuchten parametrization from a multi-step outflow experiment (*Bergmann*, 2010) were

transformed by relation (2.12).
For the adaptation of the parameters to the steady-state stage 1 scenario of this evaporation experiment, this yields an air entry value of 0.26 m. For stability reasons, we assumed the water table in the sand column at this height, since the Brooks-Corey parameterization is not continuous at the transition between saturated and unsaturated conditions in the soil. Yet, this implies continuous regions of film flow from the water table up to the surface and hence is consistent with the definition of stage 1 evaporation (*Lehmann et al.*, 2008). The total height of the sand column was set analogous to the experimental set-up to 0.47 m. A constant evaporation flux of 2.5 mm/d results for the stationary system in a surface matric potential of −0.21 m. Increasing the air entry value to −0.192 m yields a surface matric potential of −1.94 m. The system is highly sensitive to this parameter, as a further enlargement less than a millimeter causes numerical instabilities. However, we have observed that the so estimated air entry value corresponds to the depth of the water table at about 0.16 m at the end of stage 1.
As a side note, another possibility to approach the estimated matric potential from the air side would be to enlarge the λ-value in the parametrization. This highlights that the system has more than one degree of freedom to fit the matric potential deduced from the atmospheric water vapor flux and the soil measurements during the experiment.

Altogether, we saw that our process understanding of the coupling at the soil surface is correct. By fine tuning the system's parameters, we were able to quantitatively fit the model to the measurements. As the link between the two compartments, the soil and the atmosphere, is highly nonlinear, the coupling is extremely sensitive to the parameters. As measurement uncertainties, especially of relative humidity, are large, we stop the manual adaptation of the parameters after the matric potentials at the surface from soil's and atmospheric perspective were less than one meter apart from each other. Yet, an automatic optimization procedure did not function at all, since the soil hydraulic model easily gets unstable and the thermal diffusivity in air had to be adapted beyond the range of the measurement resolution. But even though, the rough estimates evince that our understanding includes all significant processes and fits within the right dimensions.

Evaporation for Periodic Air Temperature Forcing

For the evaporation experiment with periodically varying air temperature, the interpretation of temperature profiles is more complicated. In addition, the before estimated parameters are not the same. Especially the effective diffusivity for air will be different, because some sand was removed from the column before the experiment. Hence, the lower 20 cm of the air were located within the plastic tube. This might result in a less free flow of the air close to the surface compared to the experiments before and therefore in a smaller effective diffusivity. As in addition the evaporation flux was not measured directly due to technical failures of the balance, a similar quantitative estimation, as for the experiment before, is not possible in this case.

To characterize the differences between the two evaporation stages, we will analyze in a first step four temperature profiles an the corresponding temperature gradients, char-

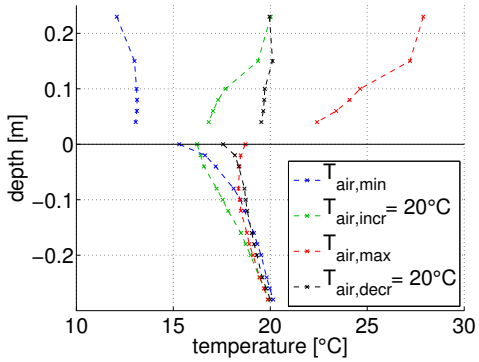

(a) Temperature profiles during stage 1 evaporation (day 4).

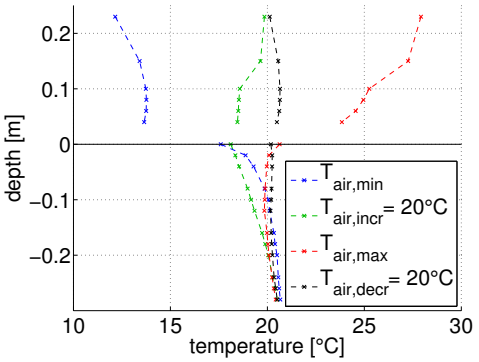

(b) Temperature profiles during stage 2 evaporation (day 35).

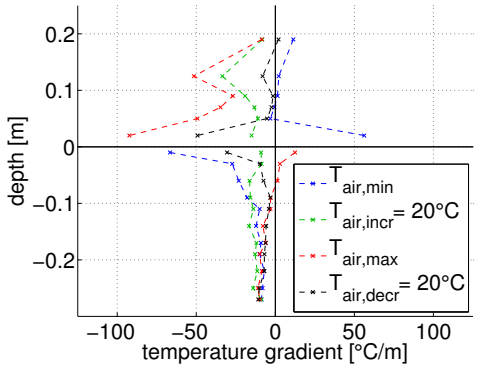

(c) Temperature gradients during stage 1 evaporation (day 4).

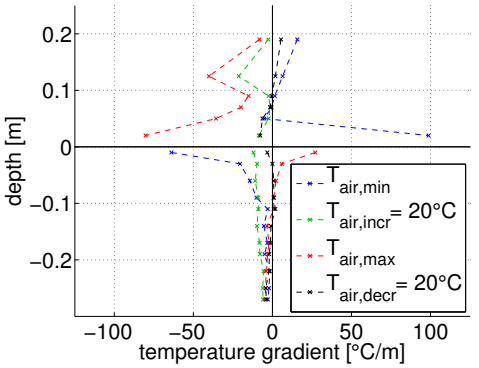

(d) Temperature gradients during stage 2 evaporation (day 35).

Figure 4.30: Temperature and temperature gradient profiles for evaporation experiment with periodic air temperature forcing.

acteristic for the air temperature cycles during both stages (Fig. 4.30). The profiles are chosen for minimal and maximal air temperature. In between, two additional times are taken, when the air temperature was at 20 °C, one for the rise and one for the decrease in temperature. The lower 15 cm of the soil profile seem to be uninfluenced by the air temperature variation. For these sensors, the measured soil temperatures remain almost at the same level over time and the corresponding temperature gradients are close to constant. For stage 1 evaporation, Figure 4.30(a) exhibits the energy sink at the surface. Its strength lead to temperatures considerably below the mean air temperature of about 20 °C, even when the air temperature is maximal. Furthermore, the temperature profiles reveal a hysteretic behavior. With the same air temperature (green and black profiles), the surface temperature is significantly lower for the rising temperatures due to the increasing evaporation flux. Although, the diffusivity in air is much higher than in soil, the surface temperature has a noticeable influence on the lower part of the air temperatures which causes a delay in the adaption to the overall temperature forcing at the top of the plastic tube. This lag is larger for the high evaporation flux in the first phase of the

experiment, as the surface temperature is lower. For stage 2 evaporation (Fig. 4.30(b)), these characteristics remain the same, but the soil and surface temperatures trace closer the trend of the air temperature outside the column. As a result, the air temperature profiles themselves are more homogeneous. In general, the blue profiles in air for stage 1 and stage 2 are nearly the same for minimum air temperature. Hence, evaporation is almost negligible in this state. On the other hand, the green soil temperature profiles, even for stage 2, point clearly to an energy sink at the surface during the warming cycles, as soil temperatures are minimal down to a depth of 20 cm.

The heat flux in the soil are proportional to the temperature gradient (Eq. 2.17). Even without knowing the true thermal properties, they indicate at least the qualitative processes in the systems and will therefore be analyzed next to enhance the observations from the temperature profiles. The sign convention of the temperature gradients in Figure 4.30(c) and 4.30(d) follows still the same raster: negative gradients indicate energy fluxes towards the surface and positive refer to an energy transport away from it. Again, the (blue) profiles for minimal outside temperature seem to be unaffected by the stage of the evaporation process. Heat is transported from within the soil towards the surface and is taken up by colder air. This is likewise true in the reversed direction for maximal air temperature. The warm air provides heat at the soil surface which is in parts absorbed by the soil resulting in a ground heat flux into the soil. In general, the difference between the sensible heat in air and the soil is removed by the evaporation of water. As gradients within the soil deviate between stage 1 and stage 2, there seems to be an change in the energy sink during the experiment. The profiles related to mean air temperature vary to a greater extend with the evaporation stage. Figure 4.30(c) shows a supply of energy from soil and air towards the surface for increasing and decreasing temperatures during stage 1. Even if the values next to the surface might be slightly biased by the accuracy of surface temperature measurement, the gradients suggest a significant energy flux from the soil towards the surface for the warming cycle which we would not expect without evaporation (compare the profiles in the pure heat conduction experiment Fig. 4.7). In particular, this indicates the start of the evaporation, when the air temperature rises above the mean of 20 °C. Finally, a comparison of the gradients at the bottom for stage 1 and stage 2 confirms a larger net energy entry from the heat plate for the higher evaporation fluxes in the beginning of the experiment compared to the lower fluxes in stage 2.

In the plots of Figure 4.30, we did not extrapolate the temperature or gradient profiles in air and soil across the surface. Therefore, we need to emphasize that both compartments influence each other and are linked at the surface, but the coupling processes are way to complex to estimate the resultant state variables, here temperature, in a simple linear way by extrapolating our knowledge about one part towards and above the boundary layer. This leads us to question the applicability and performance of the projection method for this data-set where the assumption of pure heat conduction is obviously not valid and an additional process is detected within the data. This phenomenon is discussed in the following section.

Estimation of the Evaporation Flux from Temperature Profiles

For first, we will propose an estimation procedure for the evaporation flux only from temperature profiles, since the direct measurement failed during this experiment. The concept is based on the assumption that the air temperature gradients are directly linked to those in the soil, if the energy at the soil surface is supplied only by sensible heat fluxes and not e. g. in addition by radiation. This is still true during the evaporation of water, as long as all energy is transported to and away from the surface by conduction.

To demonstrate the principle, these assumptions are tested at first for the evaporation experiment with constant air temperature. A comparison of the surface temperature gradients and the evaporation flux is shown in Figure 4.31. It confirms the suggested linear relation between the surface gradients in air and into the ground, at least for stage 1 (Fig. 4.32(b) and Fig. 4.32(c)). Furthermore, we already saw in the calculations before that soil and atmosphere provide comparable amounts of energy during the evaporation experiment with constant air temperature. Assuming the system to be close to stable during stage 1 evaporation (the first ten days) and the thermal properties to be approximately constant in that period allows to linearly fit the mean temperature profile (Fig. 4.32(a)) to get an estimate for the mean temperature gradient. Based on equation (4.9), this yields an approximation of the mean soil heat flux contribution to the surface evaporation. In terms of water loss during stage 1, this results in 0.33 l. From the water content profiles, the total amount of water evaporated during stage 1 can be estimated as 0.76 l. This suggests once more an overall larger energy contribution from the air and therefore is consistent with the estimations earlier in this section by equation 4.9. This mathematical calculus illustrates the stationary behavior of the system during stage 1. Yet more important, it confirms the first order or linear correlation between the air and corresponding soil temperature gradient by or even despite of the evaporation process (Fig. 4.32(b)).

Based on this pre-calculations, we propose an approach to estimate the evaporation flux

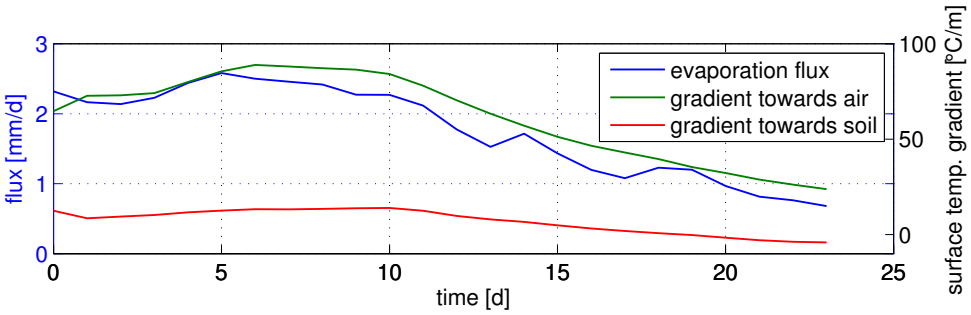

Figure 4.31: Correlation of evaporation flux with temperature gradients at the surface towards the soil and the air for evaporation experiment with constant air temperature.

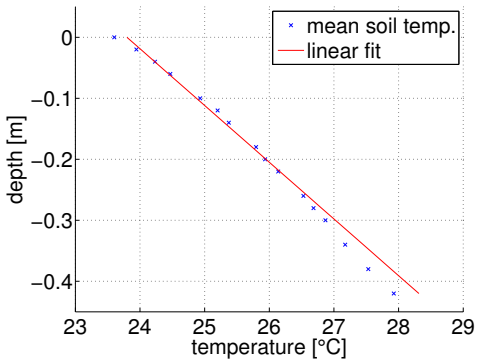

(a) Weighted linear fit of mean soil temperatures.

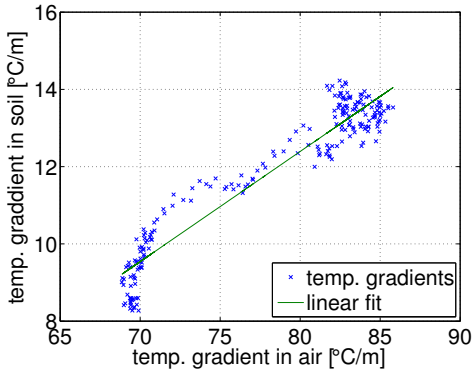

(b) Linear fit of surface temperature gradients in soil and air.

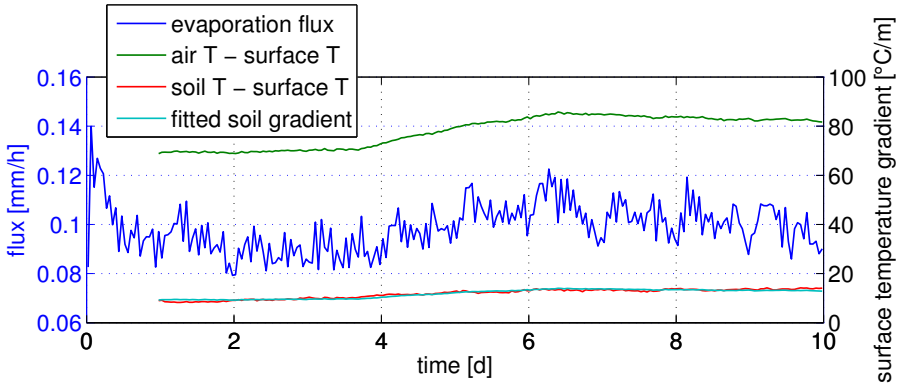

(c) Comparison of air and soil surface temperature gradients and the evaporation flux.

Figure 4.32: Analysis of temperature gradients towards the surface for evaporation experiment with constant air temperature.

for the experiment with periodic air temperature forcing from the asymmetry in the soil temperature variation due to the heat consumption of the evaporation during warming cycles. From the difference between an estimated hypothetical and the actually measured soil temperature gradients the small scale contributions of the actual temperature forcing to the overall evaporation flux can be calculated.

We would again assume the mean system to be stationary during stage 1. Thus, we can again calculate the main evaporation component from the linear regression results of the mean temperature profile shown in Figure 4.33(b) and equation (4.9). This yields 0.47 l compared to a total loss of water of 0.84 l detected by the TDRs within the first 14 days.
In addition, we have to consider minor contributions from the periodic temperature forcing. These can be estimated using the co-relation between temperature gradients in air and in soil towards the surface. Again, we have to assume constant thermal properties in both compartments and furthermore that an air temperature gradient always

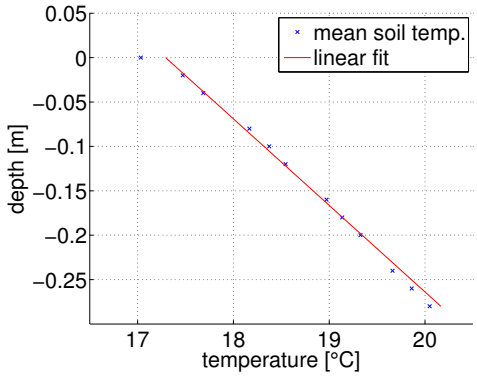

(a) Weighted linear fit of mean soil temperatures.

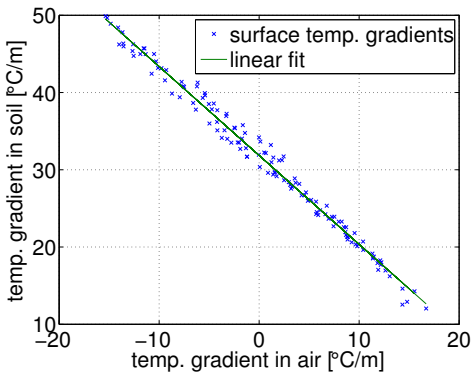

(b) Linear fit of surface temperature gradients in soil and air.

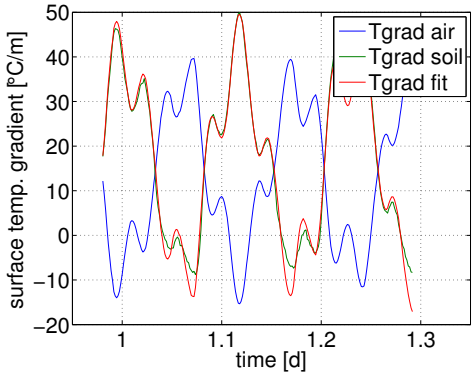

(c) Sketch of measured and estimated temperature gradients close to the surface.

Figure 4.33: Analysis of soil and air temperature gradients towards the surface for evaporation experiment with periodic air temperature forcing.

induces a corresponding soil temperature gradient, independent of the direction of the flux. Hence, analyzing this relation for the cooling cycles yields an approximately linear relation between the forcing in the air and the response in the soil (Fig. 4.33(b)). Since this dependency should hold for the warming and cooling cycles, we can estimate the hypothetical soil temperature gradients for the warming cycle in absence of the evaporation process at the surface. Summing up the additional soil heat flux components corresponding to the differences between the estimated and measured soil temperature gradients suggests a further water loss of approximately 0.1 l.

Finally, the estimated amount of energy provided by the soil during this experiment would be significantly higher compared to the heat flux component of the air side. Yet, the geometry of the experimental set-up at the soil surface has changed and the soil surface is no longer at the upper end of the plastic tube. Hence, the atmospheric diffusivity will probably be smaller compared to experimental set-up before and the energy transport in air might be less effective. This would explain a larger soil heat flux. But at this

point, we miss a definite verification, since direct measurements from the balance are not available here.
Altogether, we demonstrated an estimation procedure only based on measured temperature profiles to infer the evaporation and sensible heat fluxes in soil and the air above for stage 1 evaporation at the surface. Therewith, all energy components at the soil surface are determined and the surface energy balance is closed for these laboratory conditions.

Two concluding remarks concerning the general applicability of this approach. For stage 2 evaporation, the energy ratio provided by the soil is even higher. This suggests a water loss of 0.3 l purely from the mean soil heat flux component compared to an overall water loss of 0.4 l for the period of 14 days after day 25. Yet by definition, the evaporation front is within the soil and the air provides energy for the phase change only indirectly which penetrates as a soil heat flux from the top into the soil towards the evaporation front. In addition, the link between the temperature gradients in air and the soil at the surface is no longer usable for an estimation of the variational contributions and would result in an overestimation of the total amount of evaporated water.
Therefore, an estimation of the evaporation flux from the asymmetric temperature changes between the warming and cooling is only appropriate for stage 1 evaporation directly from the surface, when both compartments detect its thermal signature in the respective gradients. Furthermore, this relation is decoupled by additional, in particular non-constant heat entries at the soil surface, e. g. the net radiation under field conditions. Yet, defining a period for which the system is stationary in the mean might not be possible at all and altogether the surface coupling between the soil and the atmosphere is too complicated for simple first-order estimations as demonstrated above.

4.3.3 Soil Temperature Projection

To finish the analysis of the laboratory experiments, we will apply the soil temperature projection method to the evaporation experiment with periodic air temperature forcing. It will be used to analyze the performance of the reconstruction procedure in the presence of an additional surface process which is not explicitly described by the underlying heat conduction model.

Estimation of the Soil Thermal Diffusivity

The results of the linear regression is illustrated in Figure 4.34. Low frequency components ($f < f_{\text{cut-off}} = 9.2 \times 10^{-6}\,\text{Hz}$) are skipped, as they are not significantly modulated until the bottom of the soil profile and hence provide no valuable information about the projection factor.
For the analysis of the experiment, we distinguish two characteristic intervals in the dataset, one referring to stage 1 and one to stage 2 evaporation. Thus, we take the first 14 days for the stage 1 analysis and the period from day 25 to day 39 as the data basis for stage 2. The time span in-between is not considered in the context of the surface temperature reconstruction, as the smooth transition introduces low frequency noise components which bias the Fourier method and the further analysis steps.

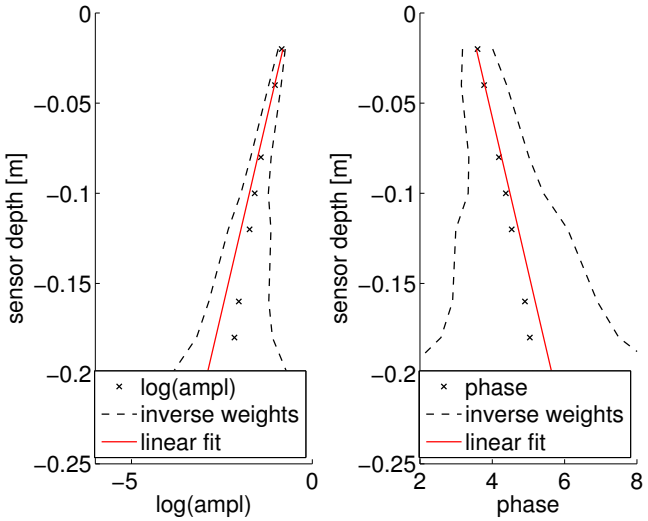

(a) Stage 1 evaporation.

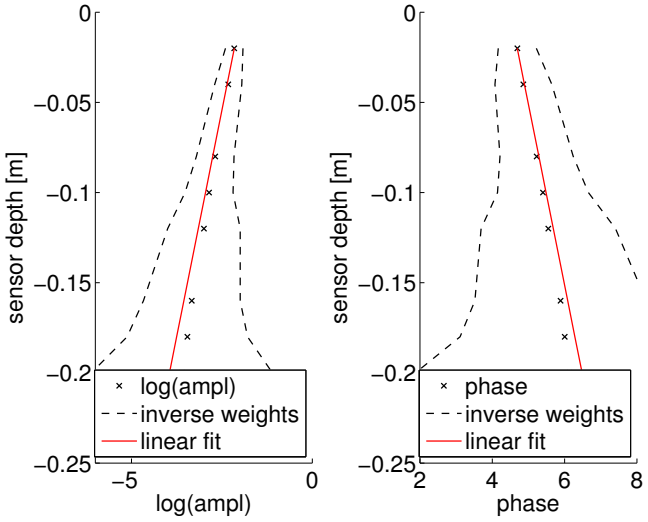

(b) Stage 2 evaporation.

Figure 4.34: Estimation of thermal diffusivity from soil temperature profiles of evaporation experiment. Fit results are shown exemplary for profile information of the 11 h-cycle. *left:* Linear fit (*red*) of log-amplitude data (*crosses*). *right:* Linear fit (*red*) of phase profile data (*crosses*). *Dashed lines* indicate inverse weights used within regression procedure, reflecting information loss with depth.

The linear fit seems to provide better results for this data-set than the heat conduction experiments. It is well within the uncertainty bounds and traces the data points. This time, we are no longer looking at the exemplary daily cycle, but take the main frequency of the air temperature forcing into consideration, which is $f_1 = (11\,\mathrm{h})^{-1}$. In addition, the quality of the fit might be slightly misleading at first, since we have to keep in mind that the depth of the sand column in this experiment is less deep.

The linear regression yields for the stage 1 data-set a thermal diffusivity of $6.0 \times 10^{-7}\,\mathrm{m^2/s}$ and for stage 2 a slightly higher value of $8.4 \times 10^{-7}\,\mathrm{m^2/s}$. This estimation from stage 1 is in good agreement with the estimated value for the wet sand. We would have expected this, since the water content has only decreased above the second TDR at 14 cm until day 10. The fit in the middle and lower part of the profile suggests a higher value, but we would assume the same artifact due to heat fluxes through the insulation from the side boundary. In addition, the changes in water content during stage 1 evaporation might serve as an explanation for the changing slope in the phase and amplitude profiles and likewise suggest a difference in the thermal diffusivity. Yet, we force the regression with the weights in the fit procedure to focus on the upper part which is more important in the context of the surface temperature reconstruction.
At day 30, even the third TDR probe at 22 cm detects the drying front and almost the whole profile is significantly drier compared to stage 1. Thus, we have no physical facts to explain why the thermal diffusivity is higher for stage 2. We could merely tentatively argue that the evaporation front within the soil might enlarge the side fluxes. The energy sink during stage 2 is mainly compensated by the soil heat flux, since the air is no longer facing it directly. However, at the same time, the evaporation flux is lower which queries an overall enlargement of the soil heat flux compared to stage 1.

Surface Temperature Reconstruction

The reconstructed surface temperature signal with the corresponding measurement is plotted in Figure 4.35 for a noise level in the order of the resolution of the PT100 temperature sensors of 0.2 °C. Besides a shift towards 0.5 °C, the residual reveals a lot of high frequency noise which hints at too many high frequency components projected towards the surface. Increasing the noise level comes along with a reduction of these oscillation. A noise level of 1 °C finally yields the best reconstruction for this experiment (Fig. 4.36(a)), while a further rise causes structural artifacts indicating missing significant frequency components in the reconstructed signal. The remaining structure in the residual has, as the pure heat conduction experiments discussed before, the same frequency decomposition as the corresponding air temperature forcing. This shows that we have again heat fluxes from the side resulting in an overestimated D_h, since they influence the soil temperatures by amplifying the horizontal heat flow. Consequently, the projection factor is too small, as it is proportional to the inverse of the thermal diffusivity, while surface temperature amplitudes are underestimated.
The same effect is even larger for the stage 2 reconstruction in Figure 4.35, as the thermal diffusivity estimated is larger.

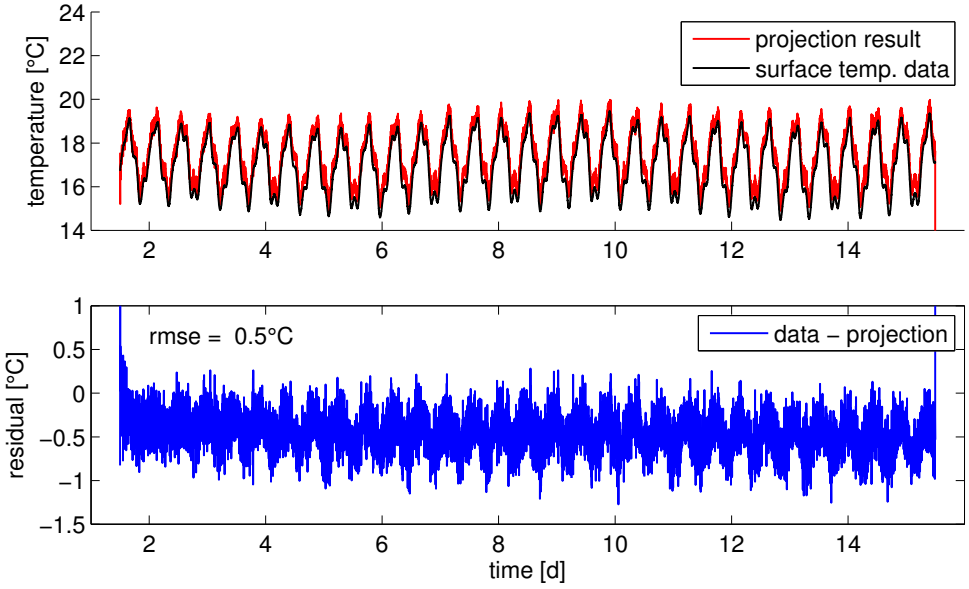

Figure 4.35: Projection results for stage 1 in the evaporation experiment. Noise level was set to 0.2 °C. *top:* Reconstructed (red) and measured (black) surface temperature. *bottom:* Residual: difference between data and projection.

Yet, the residual for the stage 1 reconstruction and stage 2 reconstruction have another characteristic feature in common. Both evince a negative offset which we did not observe for the pure heat conduction data-sets, synthetic and measured. In addition, we notice that the offset is smaller in the stage 2 data interval than in stage 1. This confirms a scaling of the shift with the evaporation flux.

By looking at the mean soil temperatures in different depth (Fig. 4.37), the origin of the offset becomes apparent. The soil temperature reconstruction is based on a Fourier analysis of the soil temperatures in different depth. Assuming temperature changes due to pure heat conduction allowed us to evaluate the centered temperature signals, since changes occur relative to a constant mean temperature level over depth. Therefore, the first step in the temperature projection procedure is to center the temperature data-set in each depth. The further analysis of amplitude damping and phase shifts with depth are performed on that revised time-series. After the extrapolation of all Fourier components towards the surface, the inverse Fourier transform yields a centered surface temperature signal which is shifted to the mean level of the first soil temperature sensor in the last step of the procedure. A constant mean soil temperature for all depths does not hold true during evaporation. As the mean soil temperatures reveal a net temperature gradient and thus a net heat flux towards the surface, this gradient comprises information about the mean soil heat flux. Shifting the centered temperature signal at the end of the projection procedure by the measured mean surface temperature almost balances the offset of the

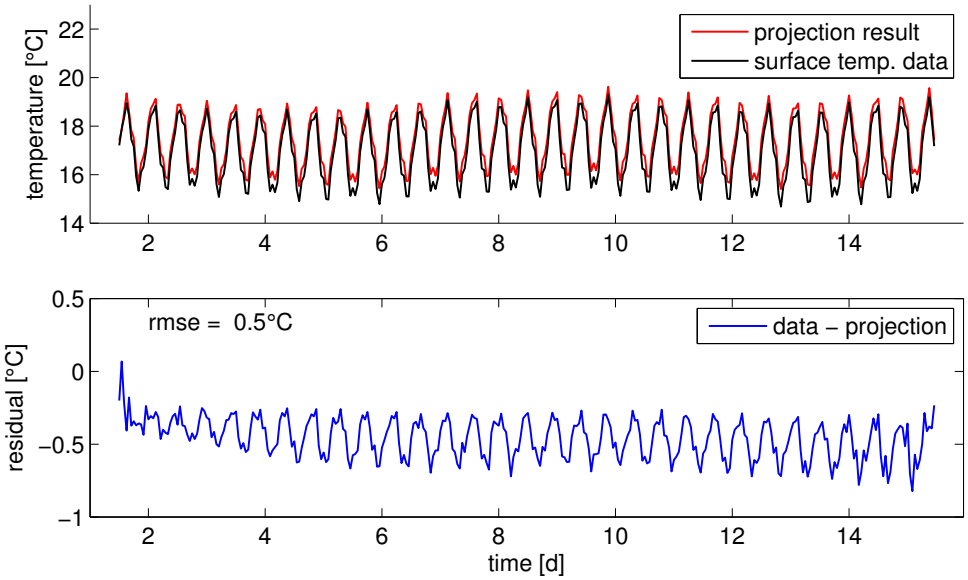

(a) Stage 1 evaporation.

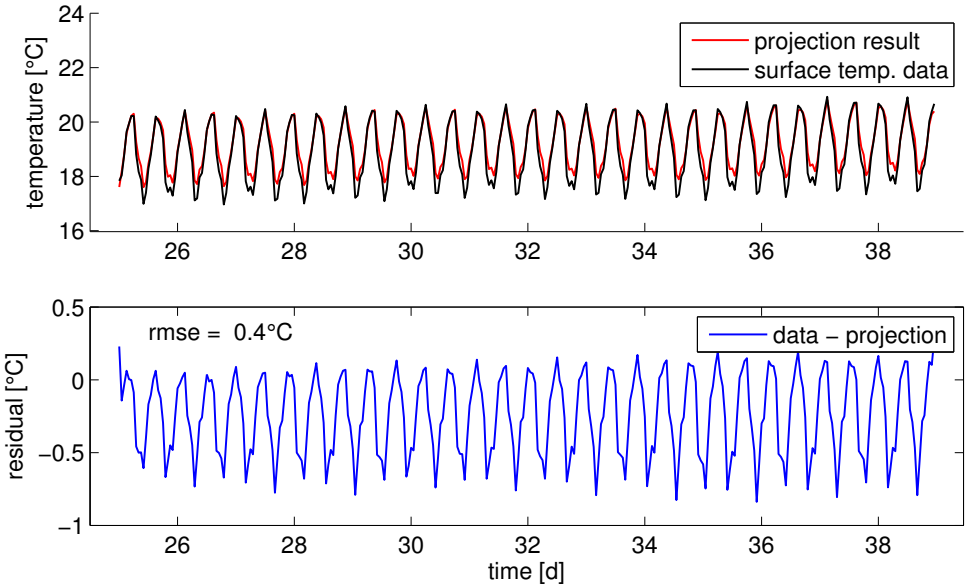

(b) Stage 2 evaporation.

Figure 4.36: Projection results for the evaporation experiment. Noise level was set to 1.0 °C. *top:* Reconstructed (red) and measured (black) surface temperature. *bottom:* Residual: difference between data and projection.

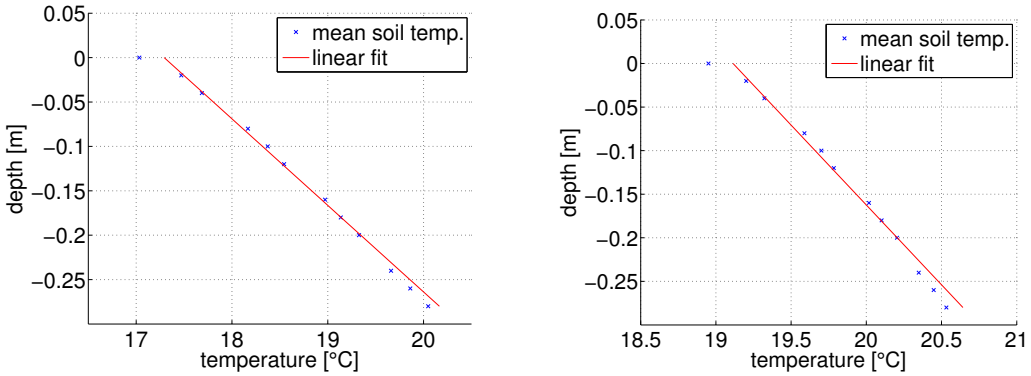

(a) Stage 1 evaporation.

(b) Stage 2 evaporation.

Figure 4.37: Linear Fit of mean soil temperature profile during evaporation experiment.

residual as shown by Figure 4.38 for the residual during stage 1 evaporation.

Usually, we lack the information about the surface temperature, however, we can assume the investigated systems here to be stationary in the mean. With this assumption, mean soil temperature gradient would be constant as well as the mean evaporation flux. Performing a linear fit on the mean soil temperature profile yields an estimate of the mean surface temperature. As Figure 4.37 illustrates, this leads to a slight underestimation of the surface mean of 0.2 °C for stage 1 and even less for stage 2 evaporation. Therefore, we can reconstruct the surface temperature in the presence of non-conductive heat transport, only from our knowledge gained from within the soil.
In the last section, it was already discussed how this surface, soil and air temperature information can be used to estimate energy fluxes towards the surface from within the soil and the air.

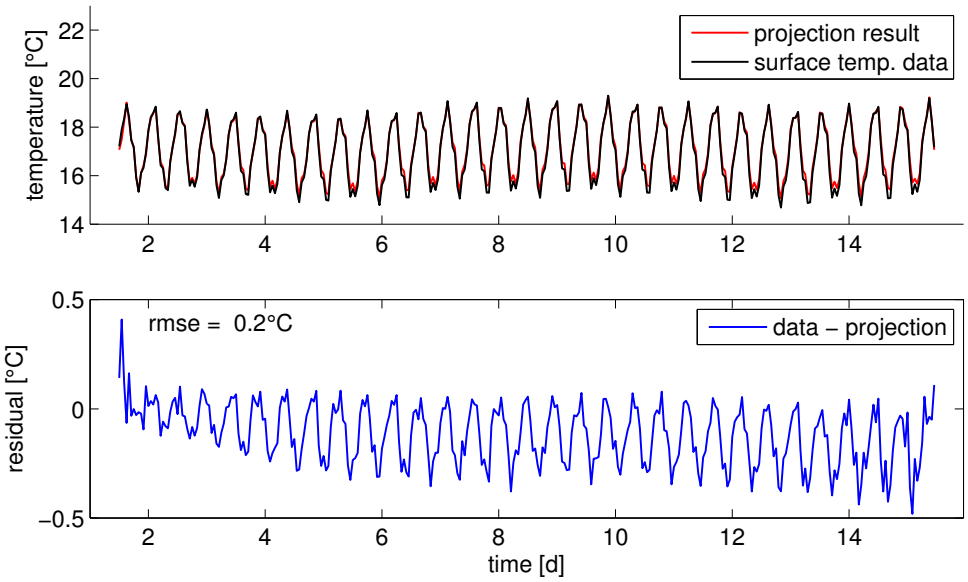

Figure 4.38: Projection results with correct mean surface temperature for stage 1 in laboratory evaporation experiment. Noise level was set to 1.0 °C. *top:* Reconstructed (red) and measured (black) surface temperature. *bottom:* Residual: difference between data and projection.

5 Coupling of Water and Energy Fluxes at the Field Scale

This chapter discusses the field experiment which was set up in 2009 and conducted over the last two years. Compared to the laboratory experiment, the system is much more complex, not only due to the natural layering of the soil. In the field, the forcing at the surface is a superposition of the radiation from the sun and turbulent fluxes of momentum, heat and water vapor in the atmosphere and the influence of the vegetation cover. Furthermore, two types of surface cover are considered. One surface is kept bare during the whole time of the experiment and the other profile is installed under grass. Therefrom, we can extract the influence of the plants and their transpiration on the water and energy budget close to the soil surface. Altogether, we will investigate how far our simplified model assumptions and process descriptions sustain for real field conditions.

5.1 Grenzhof Field Site

The Grenzhof field site, its instrumentation and experimental set-up will be introduced in the following. The measurements are installed on a $15 \times 200\,\mathrm{m}^2$ field stripe close to Heidelberg, Germany. Before the first weather station was built in 2004, the area was part of an agricultural field that was tilled and managed with different crops. For the last seven years, grass is growing on top which is regularly mown to a mean height of 10 cm.

5.1.1 Experimental Set-Up

The field site, looking from the South, is shown in Figure 5.1(a). In the foreground, the weather station can be seen with different meteorological sensors to measure the wind speed and direction (Windmonitor 05103, Campbell Scientific, Logan, UT), the incoming and outgoing long- and short-wave radiation (CNR1 Kipp & Zonen Net Radiometer, Campbell Scientific, Logan, UT), the relative humidity and air temperature (MP100A, Campbell Scientific, Logan, UT) and precipitation (Tipping Bucket Raingauge 52202,Campbell Scientific, Logan, UT). Below the surface, PT100 temperature sensors and TDR probes with a rod length of 20 cm are installed at different depths to measure soil temperature and soil water content respectively. Both sensor types are calibrated and evaluated analogous to the laboratory experiment (Sec. 4.1.2). The station was installed in 2004 and since that time, all weather sensors are automatically logged every 10 min by a CR10X Data Logger (Campbell Scientific, Logan, UT). In the back, the position of the newest experiments with different surface cover can be seen. Figure 5.1(b) provides a closer look at that set-up which is in the main focus of this work. The two separated experimental areas span $5 \times 5\,\mathrm{m}^2$. Soil temperature and water content are measured in

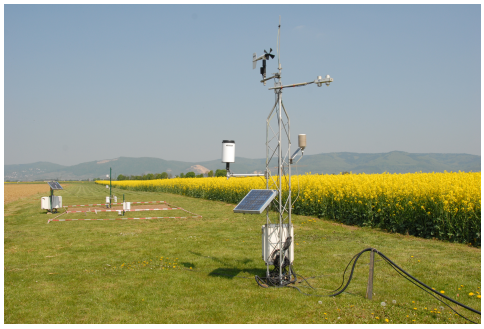

(a) Weather station at Grenzhof field site. Devices from the top: wind monitor, radiation sensor, shielded air temperature and relative humidity sensor, rain gauge, solar panel, and white box with data logger.

(b) Field experiment under grass and a bare surface. The stakes mark the position of the soil profiles. Relative humidity, air and surface temperature are measured directly above the corresponding surface cover.

Figure 5.1: Grenzhof field site close to Heidelberg, Germany. All sensors are connected to the data loggers in the white boxes.

profiles below the stacks. In the middle of the stretch, the surface temperature (IR120 Infra-red Remote Temperature Sensor, Campbell Scientific, Logan, UT), air temperature and relative humidity (Vaisala HMP45C, Campbell Scientific, Logan, UT) are measured at 0.4 m height. The infrared sensors have a field of view of 20 ° (half angle) and the corresponding surface cut-out is shown in Figure 5.2. In addition, the net radiation is measured over the bare surface via an NR-LITE Net Radiometer (Campbell Scientific, Logan, UT) and additional air temperature sensors are measuring at 0.1 m, 0.4 m, 1 m, and 1.5 m. All sensors are read out in 10 min intervals, except for the water content measurements which are recorded hourly. In the following sections, the data of one complete year, starting in June 2010, is presented and analyzed in detail.

(a) Bare surface.

(b) Grass surface.

Figure 5.2: Field of view of infrared sensors over both surface covers.

5.1.2 Soil Profile Characterization

The soil textural profile was already described by *Wollschläger et al.* (2009) who inverted the soil hydraulic properties of the soil profile using water content time-series from various depths just a few meters apart from the new experiment. As we found a comparable layering during the installation, the results of the textural analysis performed in the context of their work will be transfered to the profiles here. Based on Figure 5.3, we will only briefly outline the main textural characteristics.

The soil profile under the bare surface is shown exemplary for the complete test field. According to the USDA-Soil Taxonomy, the overall soil texture of the whole test site can be classified as sandy loam. The humous plough horizon classified as sandy loam reaches down to a depth of 35 to 38 cm. The field was agriculturally cropped in earlier times and grass was sowed when it finally became a scientific test field in 2004. Thus, the first layer exhibits a high content of organic matter. The second layer can be denoted as nearly homogeneous loamy sand. In the profile covered with grass, we still find root channels all over this layer. At a depth of 0.7 m, the third layer can be distinguished

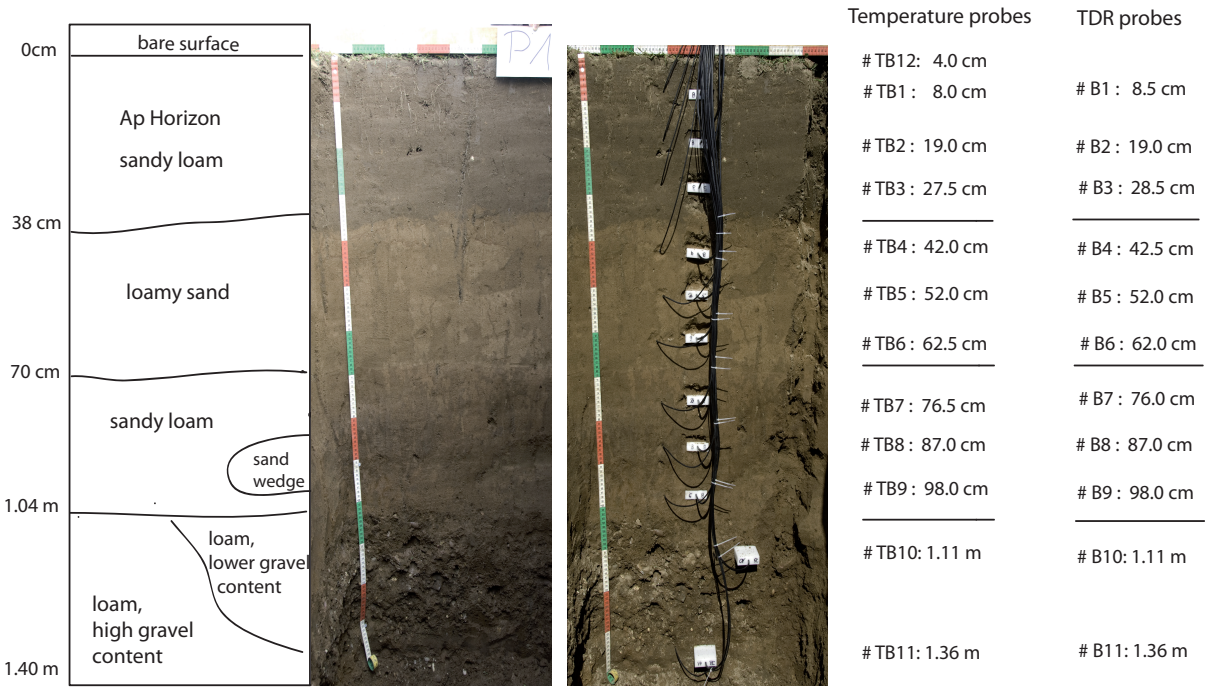

Figure 5.3: Soil profile under the bare surface. Mainly four layers can be distinguished, each instrumented with three TDR probes and three temperature sensors. Installations in the lowest layer were difficult due to the high gravel content.

in darker brown in Figure 5.3. Loam is the dominant constituent there and the soil is in general more dense. Besides a still high sand content all over that layer, there is an additional separated sand wedge on the right border of the profile. Gravel embedded in a loamy matrix constitutes the lowest layer. In general, we inserted several sensors in one layer in intervals of about 10 cm, but at least 4 cm apart from the layer boundaries. In addition, the temperature sensors are directly located next to the TDR probes, as we need the temperature information to calculate the water content from the TDR signals (Sec. 4.1.2).
The installation of the sensors was more difficult below 1.04 m in the fourth layer. Due to the high gravel content, contact between soil and sensor had to be ensured to get reliable data afterwards. That is the reason why we could not keep to the structure of installing three sensors for soil temperature and water content in this layer. We have furthermore installed an additional temperature probe at 4 cm below the surface to increase the resolution there, because in the following we are interested in the coupling between the soil and the atmosphere.

5.2 Experimental Results

The following section introduces the field data above and below the soil surface which were recorded by the weather stations. The soil sensors were already measuring since June 2009. Humidity and air temperature measurements close to the surface were added in June 2010 and we will focus in this work on the data interval since then until June 2011.

5.2.1 Bare Soil Data-Set

For simplicity, we will firstly have a look at the data-set corresponding to the bare surface area and later on focus on the influence of the vegetation cover and transpiration by plants on the soil temperature and water content profiles.

Weather Data

An overview of the meteorological data during the year of interest is given in Figure 5.4. The net radiation is the difference between the incoming long- and short-wave radiation and outgoing long- and shortwave radiation reflected at and emitted from the soil surface. Following equation (2.44), parts of the surface energy will be used to evaporate water, if available. The rest is partitioned between the soil and the air, resulting in sensible heat fluxes which in turn cause temperature to change in the corresponding compartment. Hence, the energy cycle is predominantly forced by the radiation from the sun and coupled to the water cycle via the evaporation process at or close to the soil surface. The key controls of the water flux are precipitation and relative humidity or the related water vapor potential. For the moment, we focus on the meteorological quantities measured in air, but we have to keep in mind that the corresponding water potential of the soil is at least of the same importance for analyzing the response of the coupled soil-atmosphere

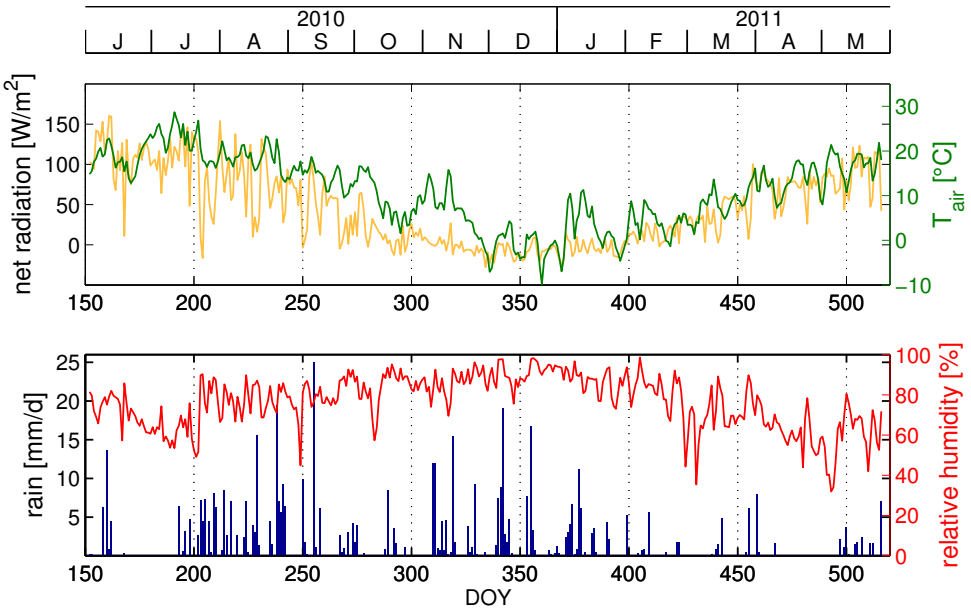

Figure 5.4: Meteorological data over the bare surface starting June 1st, 2010 (DOY 152): *top*: net radiation [W/m^2] and air temperature [°C]; *bottom*: rain [mm/d] and relative humidity [%]. Daily mean values and the daily sum of the rain are plotted, respectively.

system to some rain event.

In general, the air temperature traces the seasonal trend in the net radiation, as it responds to the energy entry that is provided at the surface. Furthermore, we can state that the during rainy days or directly during rain events the atmosphere is nearly saturated with water vapor which results in a relative humidity of nearly 100 %. For clear sky conditions, especially in spring and summer when the net radiation is high, the relative humidity decreases and the air can potentially take up water vapor which evaporates from the soil surface. Of course, the final evaporation flux is controlled by the interplay of various factors, but the most important one might be the soil water or soil matric potential close to the surface which determines the water availability from the soil.

Soil Water Content

As already mentioned, the soil water content is not only a resultant quantity of the net water flux at the surface, but a key control of the flux directly at the surface itself. It is linked to the soil matric potential and thus the water vapor pressure in the pore space of the soil via the soil water characteristic (Eq. (2.11)) and Kelvin's equation (Eq. (2.22)). Therefore, the matric potential indicates, if water is available and how much energy is needed for a phase change. The water content distribution in the soil profile for the

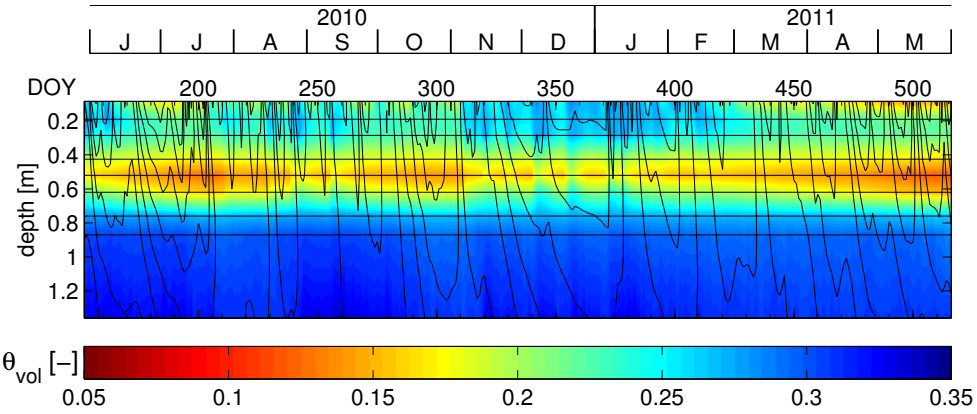

Figure 5.5: Water content profile under the bare surface. *Horizontal black lines* indicate sensor positions. *Contour lines* refer to the corresponding soil temperatures (Fig. 5.7). The three main textural layers are distinguishable by differences in water content. Mainly the top 0.3 m are influenced by surface water fluxes.

considered year is shown in Figure 5.5. It is the result of the infiltration of the rain and the evaporation at the bare ground surface. Down to a depth of about 0.3 m, the water content varies during the year. In June 2010, the top layer is almost saturated. Then a warm weather period with low relative humidity and high net radiation causes the upper 0.2 m (detected by the upper two TDR probes) to dry out until mid of July (day 200). Afterwards, the summer was dominated by many rain events until middle of September (day 260). During autumn, there was only little precipitation until the beginning of November (day 310). That caused another drying of the topmost layer. During both dry weather periods in summer and autumn, it is remarkable that water contents are not falling below 0.2. To finish the yearly cycle, we note that the water contents in the profile are around field capacity close to the surface during winter time (until day 420). Afterwards, the net energy entry from the sun and hence temperatures rise again causing soil water to evaporate from the surface and the soil profile to become drier again.Therefore, the following May is very dry.

Within the water content profile, we can clearly distinguish the three main textural layers, as the water content exhibits sharp jumps at the corresponding depths of 0.3 m and 0.7 m. As a consequence of the different soil-water characteristics of the different layers (Eq. (2.22)), the water content is not the continuous state variable related to the water flux, but the matric potential or the pressure head in the water phase. Therefore, the change in water content with depth can directly be linked to the soil texture and the corresponding hydraulic properties. This results in sharp jumps in water content of up to 0.15 between layer 2 and its surrounding layers, as it contains a higher sand content which results in a lower water content and hence the driest layer of the complete profile over the whole year and that in addition is less affected by the processes at the surface.

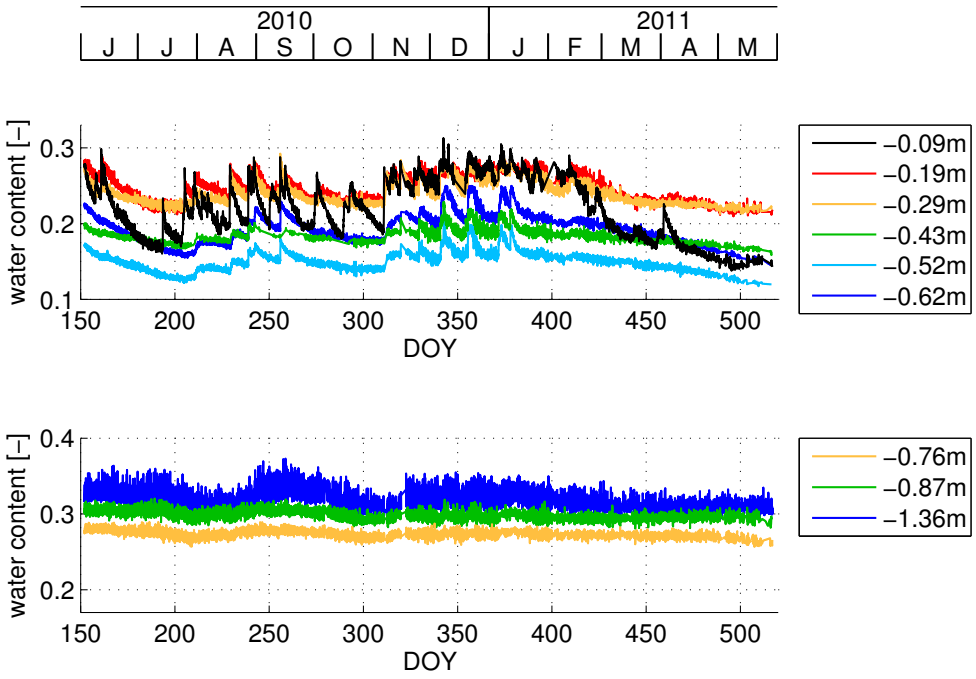

Figure 5.6: Water contents under the bare surface corresponding to the contours in Figure 5.5. The steep increase in the beginning of a rain event and the smooth decay afterwards are characteristic for the nonlinear soil water dynamics.

Deeper down, where loam is the main soil constituent, the related hydraulic properties become dominant and the soil is much wetter all over the year.

To take an even closer look at the water content changes due to single rain events, Figure 5.6 shows the corresponding line plots to the contours in Figure 5.5. It reveals, especially close to the surface, the nonlinear character of the soil hydraulic system. Each rain event is detected within the soil as a steep peak in the water content. Close to the surface, these jumps can exceed a change of 0.05, depending on the amount of rain and the initial water content of the soil at that time. The steep increase is followed by a smooth decay of the water content afterwards which accompanies the redistribution of the infiltrated water to deeper layers as well as evaporation. Mainly the precipitation in winter infiltrates water into deeper soil layers and increasing water contents are detected by the fourth to the sixth TDR sensor placed in the second layer. In summer and spring, from March to July, only the topmost TDR probe shows an increase in water content after a rain. This highlights that evaporation is high enough during these times and the water is removed from the surface, before it can infiltrate deeper into the soil. In addition, Figure 5.6 emphasizes that the upper part of layer 1 acts like a capillary barrier. Only soil at the top TDR probe dries out below 0.2, whereas the second and third TDR probe, placed in the same textural layer, stay wet. This suggests a very dry crust at the top

of the soil profile with an extremely negative matric potential which prevents a capillary rise of water from pores deeper down in the profile up to the surface and hence stops the soil water evaporation, independent of the atmospheric forcing from above.

Besides the details about the surface processes, the accuracy of the measurement is obvious from the bottom part of Figure 5.6. Altogether, the water contents measured at the lower probes show hardly no trend throughout the year. Only slight decreases are noticeable at the beginning in June and July, the drying period in October and again in spring of the following year. But as the water contents are continuously very high, we might simply not detect a water flux down there, since the hydraulic conductivity is also high under these conditions and the discharge of water is not limited by the hydraulic properties of that layer. But in addition, the oscillation in the measurements reveal its resolution which can therefrom be estimated as 0.01. The situation seems to be different for the deepest probe at 1.36 m. As already mentioned in the profile characterization of the previous section, the deepest layer is composed of gravel embedded in a loamy matrix and installation of the sensors emerged to be difficult. The larger fluctuations of the data points might indicate a higher uncertainty in the evaluation of the TDR signal. Due to a higher clay content in the loamy matrix of this layer, the electrical conductivity is larger and therewith the damping of the reflected electromagnetic pulse. This yields finally to an increased uncertainty in the measured water contents of up to 0.05.

Soil Temperature

The soil temperature profile for the bare soil profile is shown in Figure 5.7. The dry and warm summer period until day 200 results in the maximum temperatures during the year. The rain period at the end of July causes an abrupt cooling of around 10 °C, because

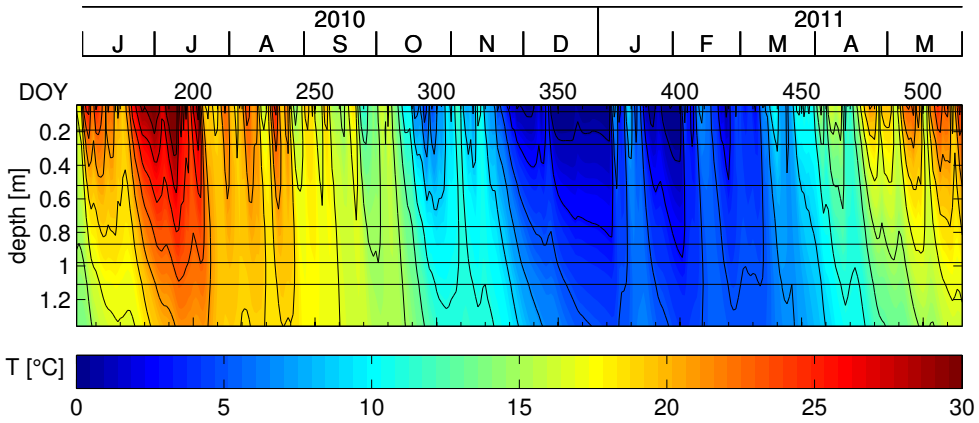

Figure 5.7: Time series of soil temperatures under the bare surface. *Horizontal black lines* indicate sensor positions. *Contour lines* are plotted in 2 °C intervals. Rain events results in sharp temperature changes due to convective heat transport.

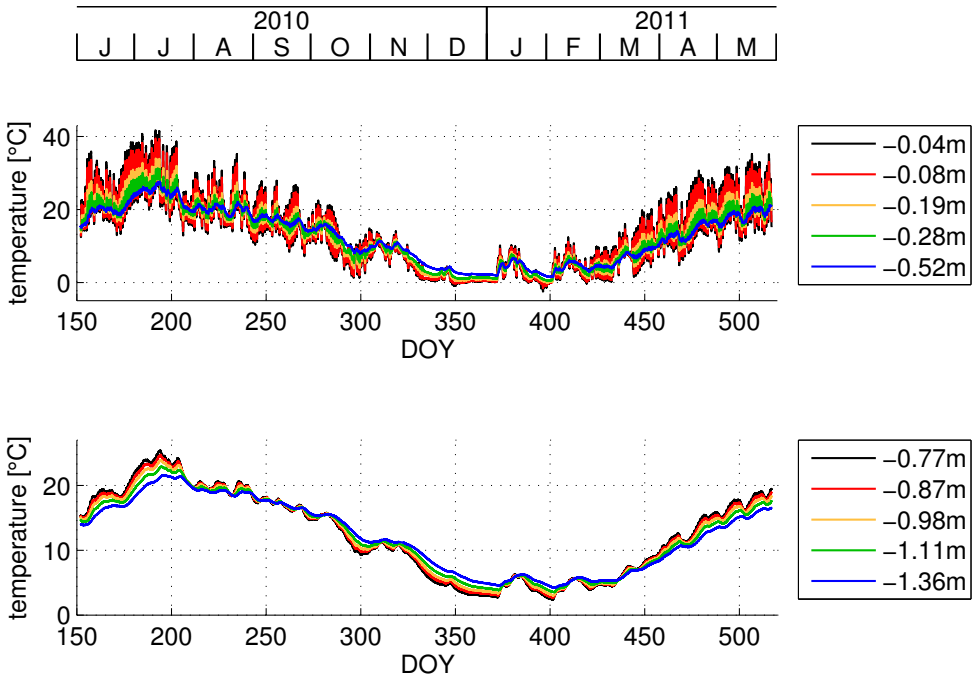

Figure 5.8: Soil temperatures under the bare surface. The high frequency variations and larger amplitudes close to the surface become more obvious compared to the contours in Figure 5.7.

the infiltrating water is of approximately the temperature of the cooler air. As the soil water content is high over the whole profile and hence the hydraulic conductivity is high at that time, the soil is cooled down nearly down to the bottom by the convective heat flow due to the infiltrating and redistributed water. During the days without rain events, the soil heats again quickly (day 200 to day 270) as the energy entry at the surface is still high during summer. A further example for the convective heat transport in winter is the rain around day 370, because the rain occurs in a phase of warmer air temperatures. As a consequence, the water flux causes a warm spike in the cool soil. So altogether we can conclude that rain events are accompanied by abrupt temperature changes at least in parts of the soil profile, if the water can infiltrate and the thermal state of the soil differs significantly from the thermal state of the atmosphere during the rain event.

In general, seasonal temperature trends penetrate predominantly by heat conduction and exhibit a phase shift and amplitude damping with depth as predicted for conduction dominated heat transfer (*Carslaw and Jaeger*, 1959). As expected, we find the largest amplitudes for all frequencies, daily to yearly cycle, close to the surface which results in temperature changes of more than 40 °C over the year and more than 10 °C between day and night (Fig. 5.8). Furthermore, all the extreme values and high frequency fluctuations are damped away in the upper 30 cm and at the bottom of the profile, soil temperatures

vary only due to seasonal trends and finally not more than 15 °C over the year. This again allows in a later step the analysis of the frequency information with depth and from this further conclusions about the surface temperature and fluxes.

A final remark on soil freezing: The mean air temperature falls from time to time below 0 °C between end of November and end of January. The topmost soil temperature probes are located at 4 cm and 8 cm. A temperature plateau recorded by the upper temperature sensors (Fig. 5.8) points on two things: the covering of the surface with snow and besides that the soil might have started to freeze in December and might be frozen for a few days at End of January in the upper 10 cm. This has to be kept in mind as it is the other type of phase change occurring under field conditions. Yet, it is of minor interest in this work, but might have to be considered when interpreting model results.

5.2.2 Influence of Vegetation Cover

The observations change at some points for an enhanced system complexity, when analyzing the data-sets of the soil profile under grass. We will be able to extract the influence of the vegetation by comparing the soil temperature and water content data-sets below both surface covers. The direct and quantitative comparison between the two profiles is possible, as they are located less than two meters apart from each other.

The potential evapotranspiration rate for a well-watered reference grassland (*Allen et al.*, 2006) for the weather conditions at our test site during the one year period is shown in Figure 5.9. The calculation is based on the meteorological measurements in the atmosphere using the FAO Penman-Monteith equation (2.48). Besides, the partitioning in potential evaporation and transpiration following *Campbell and Norman* (1998) is presented to gain an even deeper insight in the influence of the grass. Of course, this is only a rough estimate and a handle for the upper limit of possible evapotranspiration flux

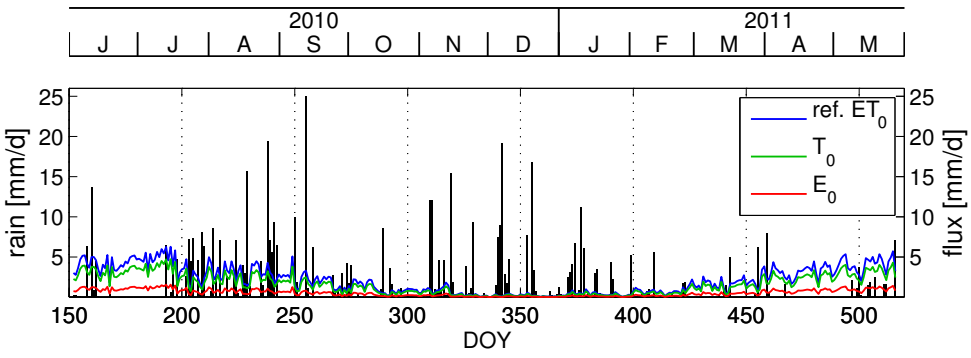

Figure 5.9: Potential evaportranspiration for reference grass (*Allen et al.*, 2006) and its partitioning in evaporation and transpiration following *Campbell and Norman* (1998) for the weather conditions at the Grenzhof field site (Fig. 5.4).

assuming unlimited water availability in the soil. At low soil water contents, the transpiration rate may be significantly lower as estimated in this simple calculation. But it illuminates the impact of the plants qualitatively and will help to explain in the following the differences in water content and soil temperature between both profiles.

Comparing qualitatively the potential evaporation from the soil with the potential transpiration by the plants (Fig. 5.9) reveals that the main water loss at the soil surface, particularly in spring and summer, is due to the plants. Evaporation will always be involved, but in comparison transpiration removes considerably more water close to the soil surface and the layers below. Besides, most of the rain is directly removed by the evapotranspiration during the warm seasons and only heavy rain events provide enough water to infiltrate even into deeper soil layers. The rainy August however suggests as well an increasingly wet soil layer close to the surface with an also increasing hydraulic conductivity which enables with time larger water fluxes into the soil. But as soon as the weather conditions change towards warm and sunny days, the flux will also change its direction and water is again removed by evaporation and mainly transpiration from the plant leaves. Altogether, a water recharge to deeper soil layer will predominantly occur in autumn and winter, when the surface vegetation is less active and the atmospheric conditions provide less energy for the phase change, indicated by negligible estimates for the potential evapotranspiration.

Soil Water Content under Grass

Assuming the precipitation to be homogeneous over the whole field site, the impact of the plants can be clearly seen in the water content profiles under the grass surface (Fig. 5.10). During the warm and dry period end of June to end of July, the profile is significantly drier. Under the bare surface, only the upper 0.2 m are influenced by the evaporation, but under the grass the upper two soil layers, until a depth of 0.7 m, are completely dried out. As the texture of the profiles is comparable and root channels and organic matter were found down to the bottom of the second layer during the profile installations, this emphasizes more efficient water removal due to root water uptake and transpiration by the grass. This data-set gives evidence that the roots will take up all the water close to the surface and even the deep soil layers will be dried out by them. They furthermore circumvent the capillary barrier that the soil might build at the surface in form of a completely dry crust. Hence, the water loss due to evaporation might still be the same, maybe even less due to the shielding of the plant leafs, but Figure 5.9 already exhibits that the main water loss in the soil profile will be due to transpiration. The same can be seen in spring of the following year. Already March and April were very warm and dry. Thus, the drying front enters the soil already in April due to the weather conditions and the plant growth which results in an increased transpiration. By the end of May, all rain events are below the potential evapotranspiration rate and hence could not significantly re-wet the soil, as the water was most probably directly evaporated from the surface and transpirated by the plant leaves. From end of July until March 2011, the precipitation exceeds the potential evapotranspiration and the profile can be wetted. We will have a closer look on that coupling for a few exemplary scenarios in section 5.3.

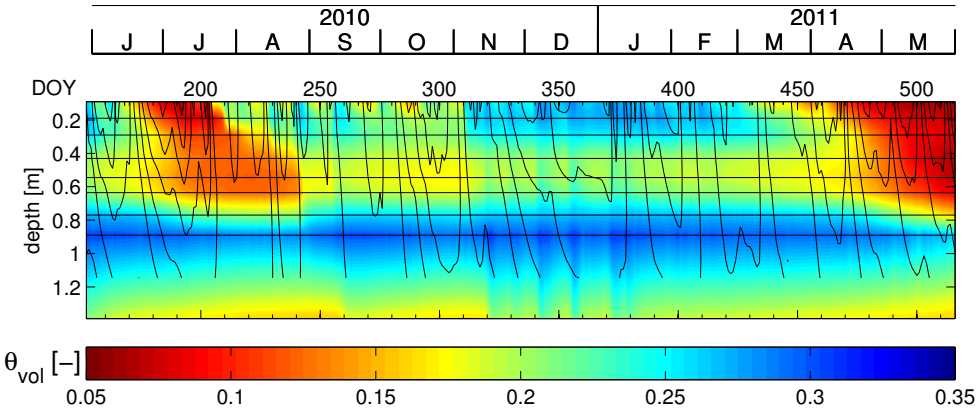

Figure 5.10: Water content profile under grass. *Horizontal black lines* indicate sensor positions. *Contour lines* refer to the corresponding soil temperatures (Fig. B.1). During spring and summer, the upper two soil layers dry out due to the root water uptake and transpiration of the grass.

Besides the impact of plants, we can again distinguish the different textural layers. Especially in winter, when the influence of the plants is negligible, the higher sand content in layer 2 results in systematically lower water contents as in the layers above and below. In addition, the lowest layer or at least the area around the lowest TDR probe under grass differs significantly from its surrounding. The soil water content is lower which again hints at sand as the dominant constituent. This is consistent with what we already found during installation. The soil matrix around the gravel at the bottom of the profile was described to be more sandy compared to the predominantly loamy matrix for the profile under the bare surface. Besides the textural difference, the water contents at the bottom of the profile might indicate a drying from below due to a varying groundwater table. Under the bare surface, the loamy soil matrix was almost saturated during the whole year. Yet, the more sand bottom layer reveals water content changes up to 0.1 during the year. (The corresponding line plot for further details can be found in Figure B.3 in the appendix.) During summer 2010 and spring 2011, the decreasing water contents at the bottom of the profile correlate with the drying at the surface. However, drying can also be observed in autumn and winter independent of water fluxes at the soil surface. This points to additional drainage of the profile at its bottom caused by a lower groundwater table, but definite data is not available to confirm this correlation.

Soil Temperature and Water Content Differences between Both Profiles

To focus on the influence of the surface cover on soil temperature and water content, the difference between the bare soil and grass data-sets are shown as profiles in Figure 5.11. The layer boundaries and the sensors in both profiles are located in less than 2 cm different depths. Thus, we assume both data-sets to be directly comparable in a sense that

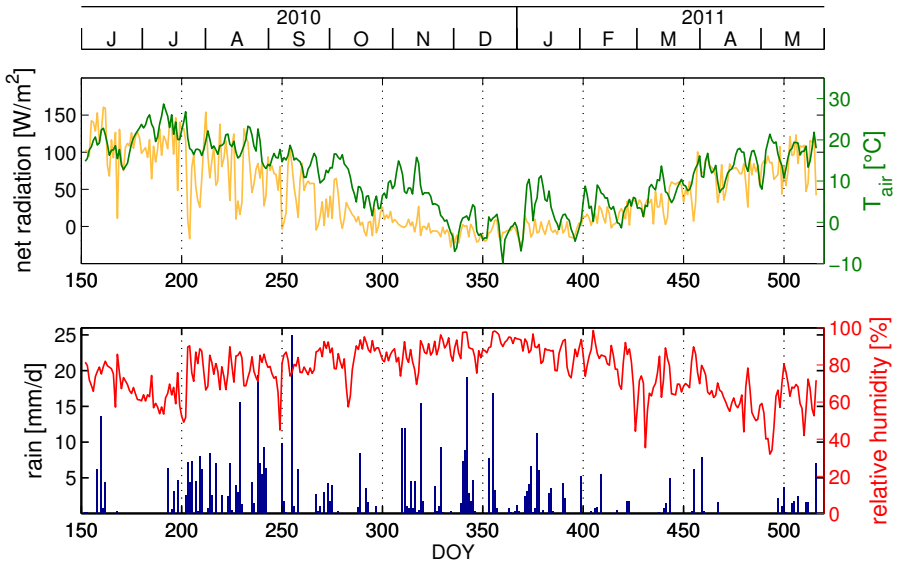

(a) Weather data corresponding to the analyzed year.

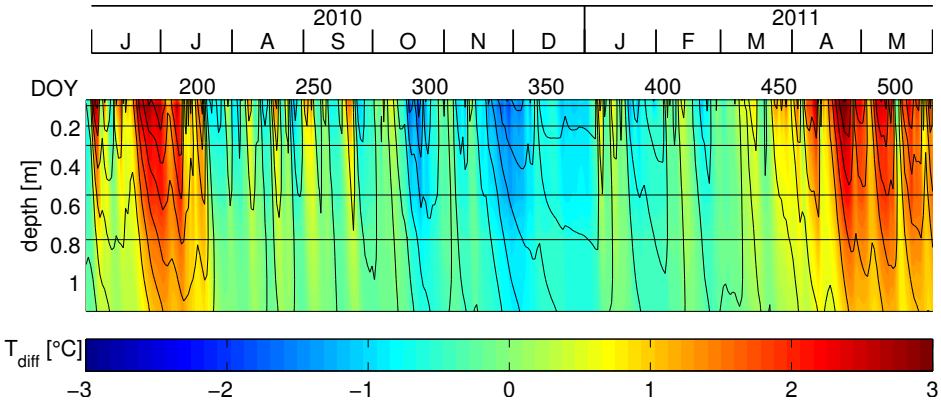

(b) Difference in soil temperature: bare data - grass data.

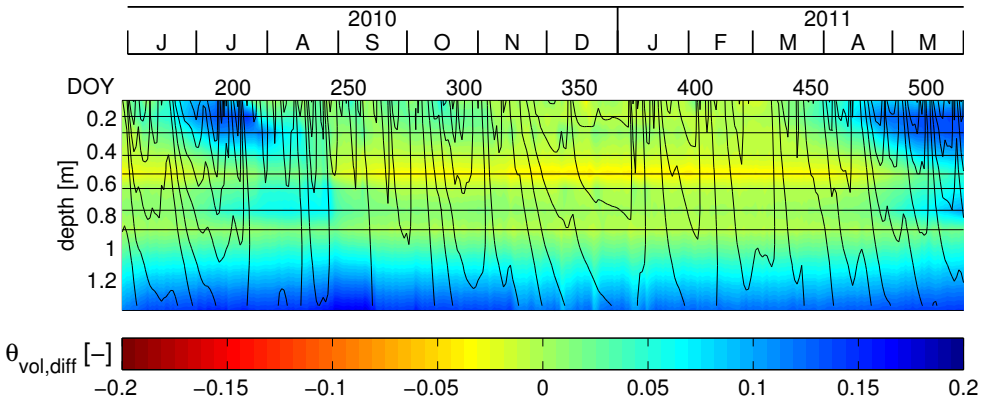

(c) Difference in water content: bare data - grass data.

Figure 5.11: Difference plot of soil temperature and water content profiles between both types of surface cover. *Horizontal black lines* indicate the sensor positions. *Contour lines* refer to the soil temperatures under the bare surface.

we can explicitly calculate the difference between corresponding sensors. If a sensor was completely failing in one of the profiles, the whole depth is excluded from the respective difference plot. But altogether, deviations due to the exact sensor positioning have to be considered throughout the following comparison.

Again, the corresponding weather data for the one-year period is presented in Figure 5.11(a), as it allows a direct comparison between the atmospheric state variables and the structure in the difference plots. The differences in soil temperature are shown in Figure 5.11(b) and the analog for the water contents directly below (Fig. 5.11(c)).
The difference in soil temperature indicate warmer temperatures in spring and summer and colder temperatures in winter under the bare surface and therewith overall larger annual amplitudes in the soil temperature signal in the whole profile. Thus, the vegetation cover works as a kind of insulation or boundary layer which thermally shields the soil from the atmosphere. In addition, the temperature differences penetrate down to the bottom of the profile which hints at an overall higher effective thermal diffusivity for the bare soil profile due to the higher water contents. But even for a similar value for D_{h}, we would expect this structure as the damping of the temperature signal at the surface is less without vegetation cover.
The summer rain period between day 200 and 250 exposes again a change in the heat transport regime under the bare surface. If it pertains for both surface covers, the difference plot should not exhibit a structure at that point. We have already discussed the conductive heat transport during and after rain events within the soil profile under the bare surface. This is now further affirmed by this difference plot, as there is an abrupt change in the sign of the soil temperature difference around day 200. Before, the bare soil was warmer, but due to the rain the temperature difference flips and afterwards the bare soil profile is equally tempered or cooler until the next dry period. This flip is caused by the water flux in the profile, since the precipitation has the temperature of the air above the soil which is in summer cooler during the rain events compared to the heated soil. Under the grass, the water flux infiltrates not as deep due to the water uptake by the plants and an overall lower soil hydraulic conductivity due to the lower water contents in the upper soil layers. Again, we can see the same phenomenon vice versa in January, when the air is warmer compared to the soil during the precipitation period and the infiltrating water warms the soil. Here, the effect is not due to a difference in water contents. But, as the vegetation cover acts as an insulation, the temperature difference between the cooler bare soil profile and the warmer air during the rain event is larger and the temperature change caused by the infiltrating water is less under grass.

The resultant differences in water content are shown in Figure 5.11(c). In particular, the impact of the plants through root water uptake and transpiration is obvious in summer 2010 and spring 2011. The upper 30 cm of the soil profile are significantly wetter under the bare surface. Even from the generally drier second layer, the roots take up water down to a depth of 70 cm which results in overall higher water contents for the bare soil profile.
In comparison, water contents in both profiles are similar in the first and third layer during autumn and winter. There is almost no difference, except for the rain events

beginning of October, when air temperatures are still high and the bare soil profile is wetter after this rain period. Since the potential evapotranspiration rate during this time (Fig. 5.9) indicates an increase, the grass seems to be still active. This again points to transpiration and root water uptake by the plants and hence they directly remove parts of the rain water close to the surface.
During the winter season, we can see that the TDR probe at 0.5 m, in the middle of the second layer, detects lower water contents under the bare surface than under grass. This might be a hint at a higher sand content in this layer and hence at an overall textural difference between the two profiles. Yet, this TDR is systematically below those 10 cm above and below. Therefore, the interpolation in the contour plot might overemphasize the deviation between both profiles in this depth and it might mainly be due to heterogeneity within the second soil layer.
The second significant difference in water content are the higher ones in the loamy soil matrix of the lowest soil layer. Here, we have already observed a textural difference during the installation, as under grass the layer with high gravel content (1.1-1.4 m) was distinguished in two parts at a depth of approximately 1.3 m. In general, the soil layer will be drier due to the gravel content. Yet, the matrix embedding the gravel becomes more sandy at the lower end of the grass profile and we were only able to install the last TDR sensor therein, as above it was not possible due to the gravel configuration.

The mentioned differences in water content become more quantitative by Figure 5.12. During winter, from November until end of February, all sensors in both profiles detect almost constant water contents. For the deepest sensor at 1.36 m and that at 0.52 m, the main difference between both profiles can be noticed from their constant offset. Again, for the bottom part of the profiles, we would state a textural difference between the corresponding layers, as already suggested during installation. The deviations in the middle could also hint at an overall textural difference of the whole second layer. Yet, the surrounding sensors are in good agreement between the two profiles during winter and deviate only due to the impact of the plants in spring and summer. Thus, deviations in 0.52 m might result from a more sandy surrounding of this specific sensor under the bare surface. Layer boundaries in the profiles were determined by eye during the installation and sand wedges or other heterogeneities were not observed within this layer. It is well known that the reliability of water content measurements by TDR probes depend crucially on the homogeneity of the surrounding material. But of course, we cannot control this assumption for the soil further behind the front of the profile without destroying the soil structure where the TDR probes was stuck into. Therefore, we can only state a textural difference between both profile in the surrounding of the sensors at 0.52 m which need not be mandatory for an overall difference in this layer.
In December and January, similar changes in all depths were detected correlating with rain events at the surface and therefore indicating the redistribution of rain water through the complete grass profile. For the bare profile, a drier layer 2 might act as a second capillary barrier to prevent deep soil water to be moved up and evaporated close to the surface. In June and July 2010, the difference in water content between both profiles is up to 0.15 due to the root water uptake and transpiration by the grass. In addition, even the lower layers under grass get drier during August. The impact of the plants in spring 2011 is

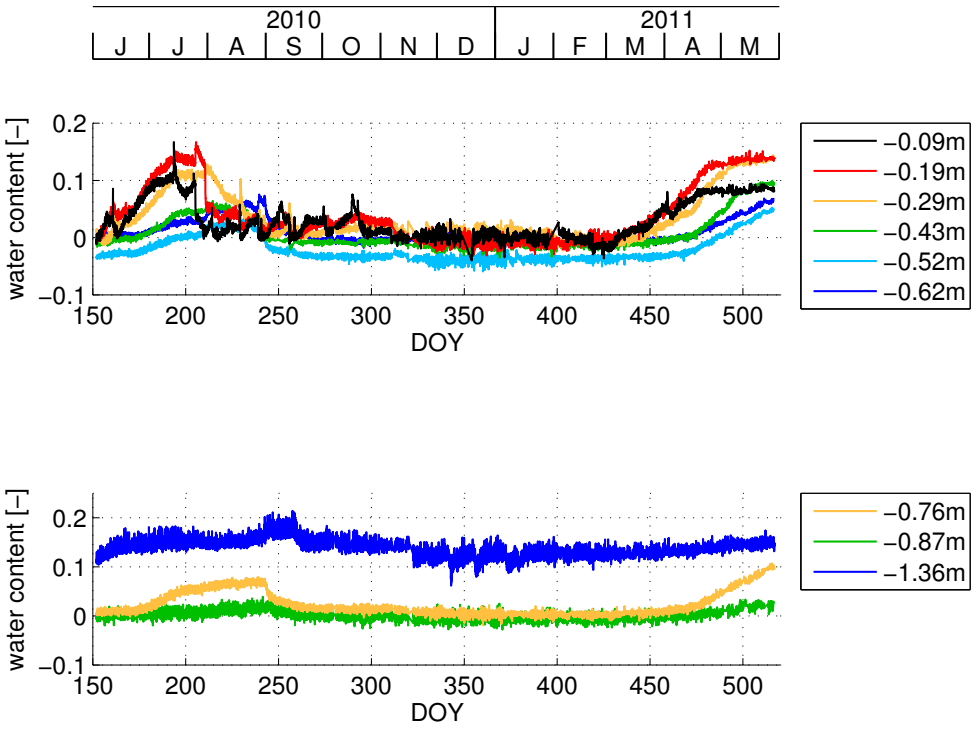

Figure 5.12: Water content difference between both surface covers: bare surface data - data under grass. Offsets during winter time indicate textural differences. Deviations in spring and summer refer predominantly to root water uptake and transpiration by plants.

even stronger and deeper in the grass profile. At that time, the grass starts to grow and hence takes up large amounts of water. This is further affirmed by a nearly constant potential evaporation rate compared to an increasing potential transpiration during that time (Fig. 5.9). Even the sensor in 76 cm records a decrease in water content up to 0.1 and also the sensors below follow the trend at least slightly.

Altogether, the differences in water content and soil temperature throughout the profile highlight the strong impact of the vegetation. Due to root water uptake and transpiration, the profile under grass is nearly completely dried out in the upper two soil layers. Furthermore, the leaves shield the soil surface, so that the overall temperature changes are damped below the grass covered surface.
The coupling processes between soil and atmosphere will now be analyzed in detail based on four examples of characteristic rain events throughout the year.

5.3 Soil-Atmosphere Coupling

The focus of this section is on the interaction between soil and atmosphere at the field scale. The fluxes in air are highly turbulent and eddies due to convective buoyancy exhibit scaled structures. In addition, solar radiation is changing the thermal and hydraulic state of the atmosphere and therefore controls water and energy transport from and towards the surface. The characterization of fluxes in the atmosphere via flux-gradient similarities is not simply possible, as the stratification of the atmosphere is not stable for many weather conditions and most of the time only during the nights. Altogether, the coupling between soil and atmosphere is much more complex compared to the laboratory conditions discussed in the chapter before. That is why we will focus in the following on four exemplary scenarios of rain events during different seasons of the year to extract details about the coupling of the water and energy cycle and the differences resulting from the two types of surface cover.

Four nine-day scenarios were chosen to work out the thermal and hydraulic coupling of the soil and the atmosphere at the soil surface. Therewith, the change in the coupled system will be characterized from an initial state before the rain, continuing with the change of the system during the rain and ending with the beginning of the equilibration phase afterwards.

The first two are pointing out the system's behavior for wet soil conditions: one in mid of October representative for autumn and one in spring beginning at and of March. Thus, the hydraulic state is similar, but the thermal state is completely different. From the comparison of the two profiles, we can extract the difference due to the vegetation cover and an increase in the net energy entry at the surface.
The third and fourth scenario were chosen to highlight the complex interaction caused by the rain events, while the potential evapotranspiration is high. In late spring (mid of May) and the middle of the summer (end of July), both soil profiles are rather dry, particularly close to the surface, but the thermal regime is completely different.

5.3.1 Comparison of Two Rain Events in Autumn and Spring

In the following, two rain events are discussed which are characteristic for the differences between the seasons. We will start with a nine-day period in autumn when the net energy input from the sun is already decreasing compared to the summer before. Afterwards, the complexity is increased by considering the analogous scenario in spring, when evapotranspiration becomes more and more dominant.

Autumn

Our analysis starts with the temperature and water content profiles of a nine-day period in mid of October (starting day 287). The corresponding profiles are shown in Figure 5.13. A comparison of air temperatures at 0.3 m and 1.0 m showed that they are rather similar most of the times due to the turbulent mixing of atmosphere. Hence, temperature

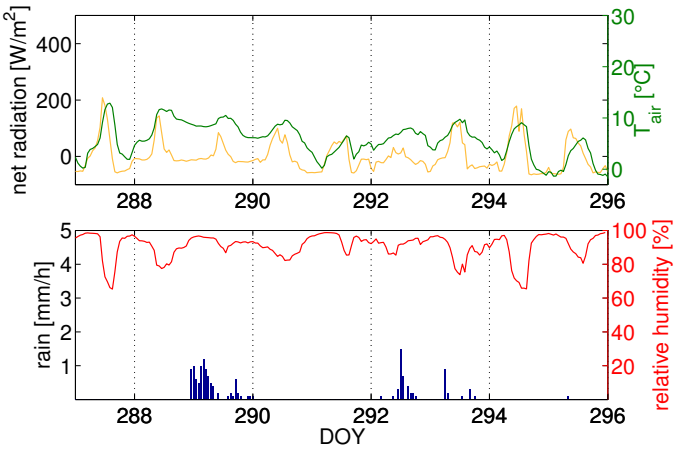

(a) Weather data, October 14th to 23rd, 2010.

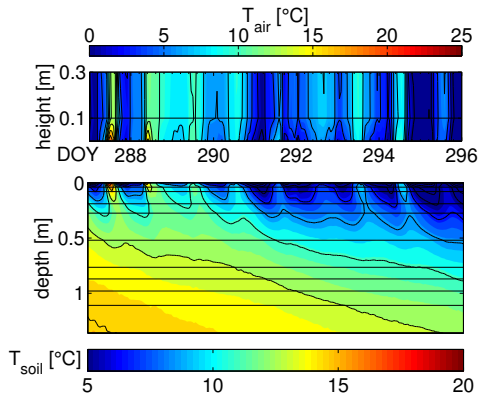

(b) Temperature profile at the bare surface.

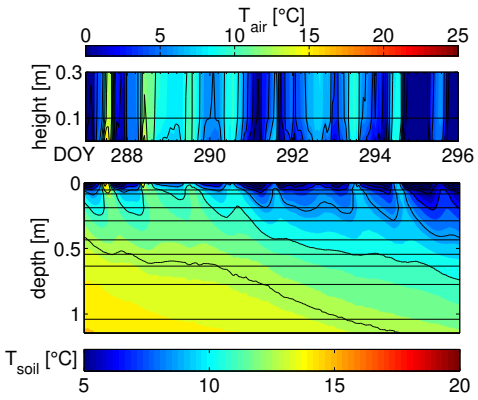

(c) Temperature profile at the grass surface.

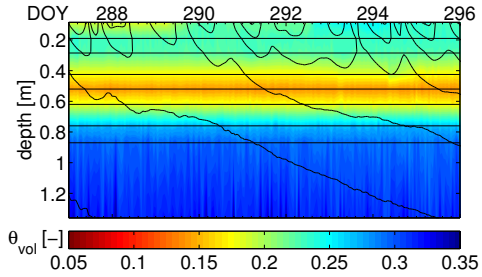

(d) Water content profile under the bare surface.

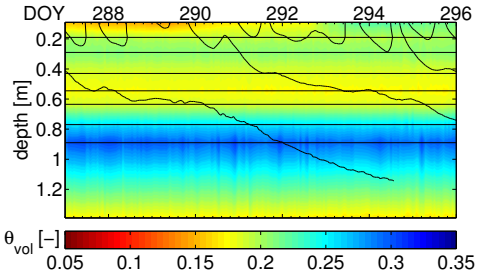

(e) Water content profile under the grass surface.

Figure 5.13: Soil temperature and water content profiles in autumn. Plotted are hourly means of the data measured between October 14th and 23rd, 2010. Rain events come along with an increase in relative humidity and a damping of the daily amplitudes in net radiation and temperature. After the summer, the bare soil profile is warmer than the one covered by grass. Yet, the cooling is slower under grass, since the plants act as an insulation layer at the top. For warm periods, the plants are still active and the soil water loss due to evapotranspiration is larger under grass.

profiles in air were not plotted above 0.3 m for this analysis.
After a rainy summer until mid of September, the temperature and water content distributions are a consequence of a month with hardly any precipitation. From the air temperature, the insulation effects of the cloud cover can be recognized which dampens the daily amplitudes to a great extent. Both profiles are rather wet exhibiting water contents between 0.15 and 0.33. The lower water contents are recorded by the TDR probes between 30 and 70 cm which corresponds to the second textural layer. Due to the higher sand content in this layer, this is characteristic for the textural differences between the different layers in the profile. As in the bare soil profile, the sensor directly at 52 cm reveals the lowest values, this might furthermore hint on textural heterogeneity within the layer itself. Close to the surface, both profiles exhibit water contents below 0.2 due to evaporation and the enduring influence of plants over the last days and weeks. Yet, the net energy entry in September is not as high as during summer time, even for clear sky conditions only about a half of the high values during summer. Thus, all temperatures in the system unveil already a decreasing trend and this will most probably pursue to the evapotranspiration rates (rise before day 300 in Fig. 5.9). Even the total water loss is no longer as large as during summer, it changes the water content noticeably close to the surface. The contour line corresponding to the cooling in the night 289 shows a steep right edge in the bare soil profile. This again indicates the convective heat transport by the water flux entering the system at the top and transporting the temperature information of the air into the soil. In the progress, the cooling of the bare soil profile occurs faster than under the grass, as the plants again act as an insulation for the soil below. Under the grass, we find only the upper TDR probe detecting increasing water contents at day 289 and 293. As the grass is still active to some extent, some rain will immediately be taken up by the roots which explains a deeper infiltration of the water front in the bare profile.

Spring

The rain events at the end of March (day 455 and 459) were the first significant precipitation after the last snow fall in winter (Fig. 5.14). Net radiation increases due to the elongation of the days. As a consequence, temperatures are continuously rising during that time. The mean air temperature is well above 0 °C and the night frost is over. Soil temperatures are still low and the warming cycles during the days have not yet reached the deeper soil layers and are damped away in the upper 0.3 m due to the cold soil layers deeper down. The first considered rain event starts in the night before day 455. From the net radiation and the corresponding air temperature, we can see that the clouds at the sky prevent the air to cool down and thus the complete system has a nearly constant mean temperature during this time. The daily amplitudes of the air temperature and furthermore in the soil temperature are almost damped away until day 456. But for that first scattered rain showers, the soil water content, even close to the surface, stayed almost the same. As the air temperature laid above 10 °C, most of the water might be directly evaporated from the surface or taken up by the grass. This is emphasized by the potential evapotranspiration rates which are already up to 5 mm/d and therewith nearly compensate the total 6 mm of precipitation during that day. The three days in-between

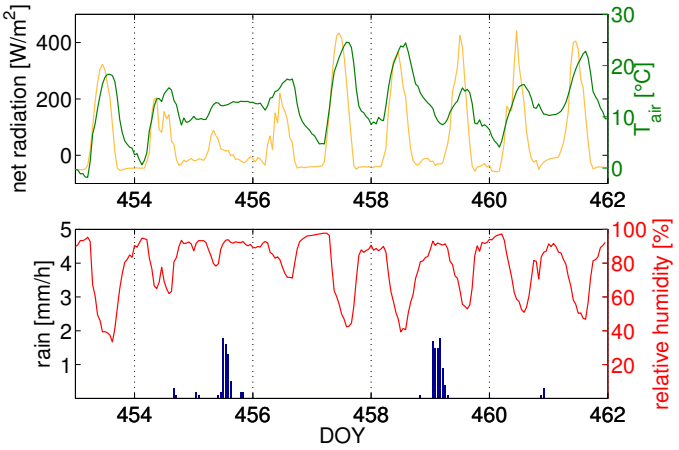

(a) Weather data, March 29th to April 7th, 2011.

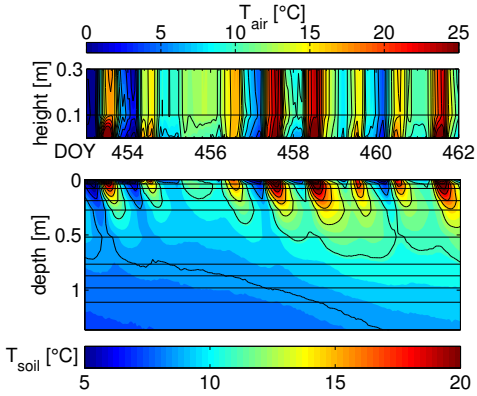

(b) Temperature profiles at the bare surface.

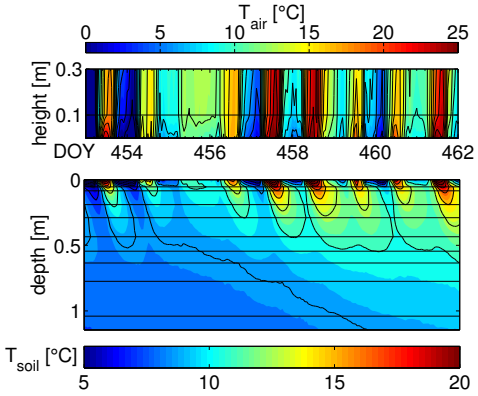

(c) Temperature profile at the grass surface.

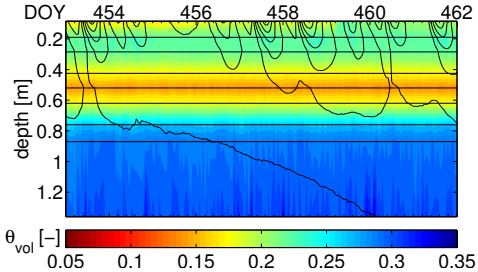

(d) Water content profile under the bare surface.

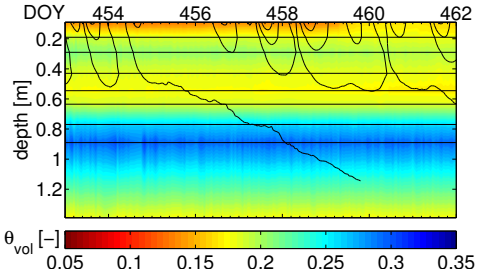

(e) Water content profile under grass.

Figure 5.14: Soil temperature and water content profiles after winter. Plotted are hourly means of the data measured between March 29th and April 7th, 2011. Rain events come along with an increase in relative humidity, a damping of the daily amplitudes in net radiation and temperature and an increase in soil water content close to the surface.

were predominantly sunny and dry. Hence, the daily temperature cycle penetrates deeper and deeper into the soil and yields temperatures to rise until a depth of 0.7 m. The bare soil is already warmer than the profile under grass which is a result of a larger energy entry at the surface during the day. The relative humidity decreases to 50 % during these sunny days. During the nights, it is always increasing due to the temperature dependence of the saturated water vapor pressure (Eq. (2.23)). Therefore, the humidity data evinces daily fluctuations as well as the temperature data.

As the second rain event occurs in the night before and the early morning of day 459, the relative humidity as well as the net radiation are nearly unaffected this time. But again, a slight delay in the decrease of the air temperature during that night reveals the presence of low clouds that shield the lower atmosphere from cooling and which were obviously carrying the rain. As the rain has approximately the temperature of the cold air at night, the surface and the upper part of the soil are additionally cooled down. Despite the fact that the net radiation on the following day reaches nearly the same level as the days before, the air temperature and as well the soil surface and the upper soil layers are cooler which indicates that they received a lower energy entry as the days before. One reason for the behavior of the soil can be attributed to be the increased heat capacity due to the added 8 mm of rain water which is slightly indicated by the higher water contents close to the surface. Another could be that the rain has the temperature of the air and as it falls during the colder nighttime, this temperature penetrates via convective transport into the soil and yields an additional cooling component. But the main reason for this energy sink at the two days after that rain event will most probably be the evaporation of the surface water. We already saw in the laboratory evaporation experiments that the energy removal due to the evaporation causes an asymmetry between the propagation of the warming and cooling cycles into the soil. This effect can be noticed as well in the warming cycles of day 460 and 461. Even the external forcing seems to be comparable to that two days before and the one afterwards, the temperature amplitude during these days is damped which hints on a loss of energy due to phase change.

A final remark on the shape of the temperature contour lines also plotted in both water content profiles. The steepness of the edges at the sides is related to the soil thermal properties, as they illustrate the phase shift and amplitude damping with depth. It is apparent that the slope will change, if the temperature contours approach a layer with different water content, for example the warming cycle of day 457 in the bare soil profile or the warming of day 459 and 461 under the grass. For the bare surface profile, the change in water content between layer 1 and 2 is large and rather sharp. As the grass profile is already drier within the first 30 cm, the layer boundary is not as dominant there. But again, the water content at the TDR probes in 52 cm depth is minimal in both profiles compared to their surrounding. Thus, it influences the penetration of the temperature signal, because a change in water content is always related with a change in the thermal properties of the soil. For example, a 0.1 smaller water content corresponds for a loamy sand to a by a factor two smaller thermal diffusivity and results in an about 5 cm smaller penetration depth of the daily cycle. (Estimation is based on values for heat capacities and thermal conductivities given in *Roth* (2006), Sec. 7.2 and an assumed

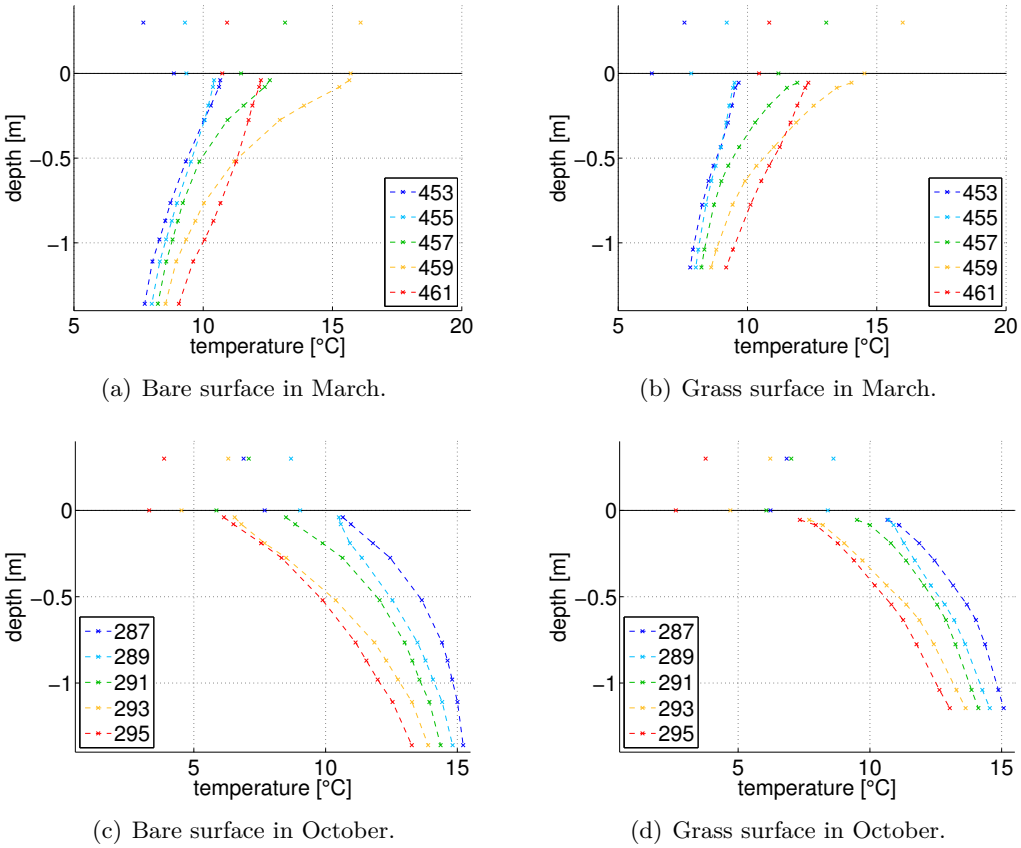

(a) Bare surface in March.

(b) Grass surface in March.

(c) Bare surface in October.

(d) Grass surface in October.

Figure 5.15: Daily mean temperature profiles in spring and autumn. Underlying data intervals: October 14th to 23rd, 2010 and March 29th to April 7th, 2011.

porosity of 0.35).

Surface Coupling Analyzed from Daily Mean Temperatures

The main seasonal difference in the temperature regime is illustrated by the daily mean temperature profiles for the spring and autumn scenario plotted in Figure 5.15. During winters, even the deeper soil layers cool down below 10 °C. The elongated days and the increasing net energy entry in spring starts to warm up the profiles from the top. In the daily mean, the air temperature in the considered nine-day interval end of March is below the soil temperatures in the upper 20 cm, as the nights are still cold even the maximal daily temperature rises already above 20 °C, except for the clear sky conditions between day 457 and 459. Furthermore, the surface temperature are also below those within the soil which points on evapotranspiration, in particular since both, the soil and the air above seem to be considerably warmer. The infiltrating water after the rain event during day 455 results in a slight cooling of the upper 50 cm of the soil. The second precipitation at day 459 occurs after two warm and sunny days. Thus, the water entering the soil transports heat via convection to deeper soil layers. The redistribution of the water and

thus the introduced heat can be clearly seen by the strong increase in temperature in the last profile at day 461.
Compared to the bare surface the profiles under grass reveal the same structure. But, the grass acts like an insulation layer and therefore the absolute soil temperatures are still lower and the warming front as well as the redistribution of the infiltrating water reaches not as deep due to the lower water content in that profile and transpiration.

The temperature conditions in autumn are nearly the other way round (Fig. 5.15(c) and 5.15(d)). The deeper soil is still heated up from the summer and cooling start now from the top. Daily mean air temperatures are well below the temperatures within the soil, as its heat capacity makes it a better heat storage than the air above. The cloudy sky during the rain on day 289 hinders the air to cool down during the night. Thus, it stays warmer and the infiltrating water again leads to an additional heat entry into the soil and temperatures rise close to the surface. In the following days, soil temperatures close to the soil surface decrease more rapidly under the bare surface, as again the grass damp the temperature change induced from the air temperature.

The temperature profiles allow to calculate the corresponding temperature gradients in the soil and close to the soil surface (Fig. 5.16). They indicate at least the direction of the resultant fluxes, even we lack the corresponding thermal properties of the atmosphere for further quantitative flux estimates and surface energy balance considerations.
Negative gradients refer to energy fluxes towards the surface and positive ones indicate a heat removal away from it. The main difference between spring and autumn are the soil temperature gradients at the bottom of the profiles. As we would have expected, the positive sign of the gradients indicate a net heat flux into the ground in spring to heat up the cold layers at the bottom of the profiles. In autumn, the gradient points in the opposite direction, as heat is released from the warm soil towards the atmosphere. The heat stored during summer is slowly removed from the deep layers by the heat flux towards the atmosphere.
At the surface, the temperature gradients are largest, independent of the season. But we know that the soil thermal diffusivity might change with depth due to the changes in water content. Thus, the resultant flux, especially under the grass, might even be smaller compared to the bare soil profile. The gradients close to the grass surface are larger, but the corresponding temperature change was smaller which would be consistent with lower water contents and hence a lower D_h in the upper 10 to 30 cm.
Furthermore, the sign of the near surface gradients is switched from positive to negative in spring compared to the deeper parts in the profile. This hints at the evapotranspiration process which might as well be the reason for systematically lower surface temperatures compared to the soil and air temperature close to it. But, we should keep in mind that the uncertainty of the infra-red sensors is considerably higher as the respective PT100 resistivity probes in the soil. Therefore, the values should be interpreted carefully, although the trend seems to be clear, however.
Altogether, the sunny days around day 457 and the rain event at day 459 result in the largest heat input for the spring profiles, especially close to the surface. The gradients deeper in the soil are nearly constant, indicating a constant heat flux at the bottom of

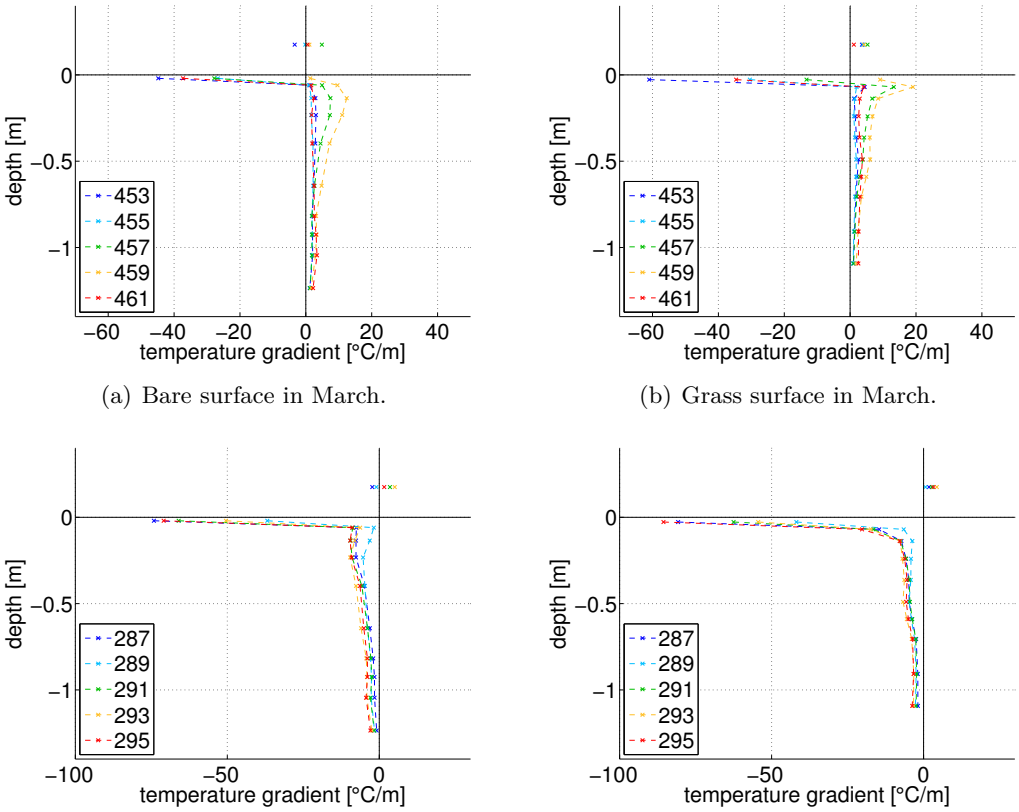

(a) Bare surface in March.

(b) Grass surface in March.

(c) Bare surface in October.

(d) Grass surface in October.

Figure 5.16: Daily mean temperature gradients in spring and autumn. Underlying data intervals: October 14th to 23rd, 2010 and March 29th to April 7th, 2011.

the profile. Only, the water redistribution after the second rain event in the night before day 459 leads to an increased heat flux even from the bottom of the profile.

In autumn, the net energy entry from the sun is only about a half of that in spring. The soil heat flux is now generally directed towards the surface and especially the gradients close to the surface are steeper compared to spring. Therefore, more energy will be provided at the surface from within the soil as in spring. Again, the impact of the rainy days 289 and 292 are apparent due to characteristic changes in the gradient profile indicating an additional flux component. As temperature rises due to the infiltrating warm water, the heat flux from the bottom is nearly equalized at that time close to the surface and the gradients are smaller.

Concerning the mean air temperature, the gradients reveal no systematic picture of the corresponding fluxes for both seasons. For the grass surface, the gradients indicate in spring and autumn a net energy removal from the air, independent of the distinct weather conditions. For the bare surface, the mean gradients, at least of these exemplary

periods, show no systematic correlation. But this may be caused by the low heat capacity of the air and thus the short memory of the atmospheric quantities. In combination with the turbulent character of the fluxes and the dominant impact of the daily cycle which causes fluctuations in net radiation, air temperature and relative humidity, a daily mean value balances probably out most of the characteristic features from the process scale. A detailed analysis at that point would have to resolve turbulent structures and would therefore have to be done with the respective equipment, e. g. eddy-covariance measurements, on shorter time scales. With the set-up used here, the link between the both compartments could not be resolved better than on a daily mean basis due to the type of atmospheric measurements and hence only seasonal features can be derived for the atmosphere.

5.3.2 Comparison of Two Rain Events in Late Spring and Summer

In the second set of rain events, the effect high evapotranspiration rates will be analyzed based on two scenarios in late spring and in the middle of the summer. In the upper 10 cm below the surface, both profiles are rather dry, but deeper down significant differences in soil water content and temperature dominate the processes in the profiles.

Late Spring

Approximately one month after the scenario end of March, especially the hydraulic state under grass has changed crucially (Fig. 5.17, bottom). While the bare soil is only at the upper TDR probe in 9 cm depth and is still wet in the deeper part of the first layer, the drying front under the grass reaches down to the third layer in 70 cm. For the bare soil, the upper few centimeters of the soil built most likely a dry crust that operates as a capillary barrier to prevent deeper soil water to be moved up and to evaporate at the surface. Even the temperatures at the surface and in the soil are higher than those under grass, the water loss under grass was considerably larger. Firstly, the plant leaves shield the soil surface at least partly. Hence, a crust could not develop that fast and strong. As a consequence, the capillary barrier will not work that effectively and wetter soil patches will transport water upwards which then evaporates from the soil surface. But most dominantly, the profile is dried out by the root water uptake and the transpiration of the plants. Even if there is a crust at the surface comparable to the bare surface, the roots could circumvent a potential capillary barrier. Down to a depth of some 20 cm the root density is considerably high. This was already observed during the installation of the profile. Thus, the upper part of the soil is dried out directly by the root water uptake. But even below the first textural layer, sporadic root channels were found down to a depth of 70 cm. Hence, the plants will also take up water from deeper down in the soil. A redistribution of the water phase around the roots results in water fluxes preferentially directed towards them and by that mechanism, the complete upper two layers are finally dried out. The net energy entry at the surface and a low relative humidity in the air result in a potential evapotranspiration rate which is higher than the amount of rain (Fig. 5.9). Therefore, all the precipitation during that period at the end of May is directly removed by evapotranspiration and no changes in water content were detected by the upper TDR

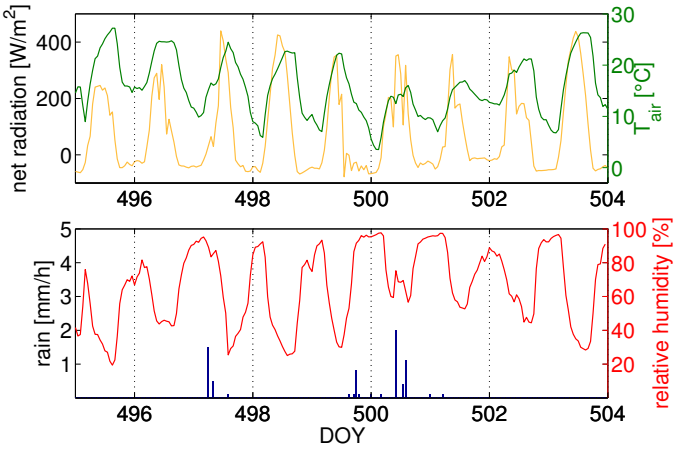

(a) Weather data, May 15th to 24th, 2011.

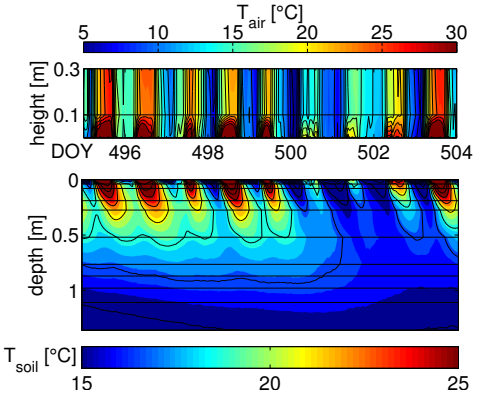

(b) Temperature profile at the bare surface.

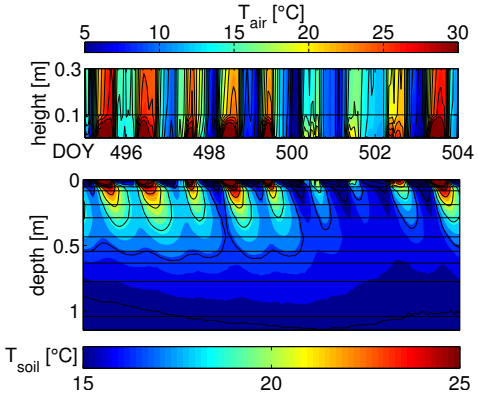

(c) Temperature profile at the grass surface.

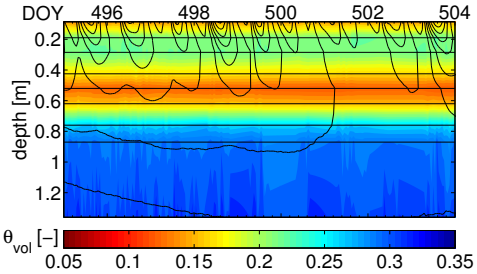

(d) Water content profile under the bare surface.

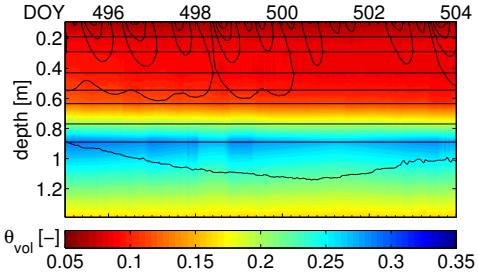

(e) Water content profile under grass.

Figure 5.17: Soil temperature and water content profiles in late spring. Plotted are hourly means of the data measured between May 15th and 24th, 2011. Rain events come along with an increase in relative humidity and a damping of the daily amplitudes in net radiation and temperature. But due to evapotranspiration, there is no net increase in soil water content of both profiles.

probes in both profiles.

In the soil temperature data, we notice once more a deeper penetration depth of the warming cycle under the bare surface. This again hints at larger temperature amplitudes at the soil surface as there is no shielding by the plants. In addition, the large discrepancy between the water contents of both profiles suggests a higher thermal diffusivity for the bare soil profile. But as the influence of the dry crust and furthermore its thermal properties might play a crucial role, we should be careful with conclusions at that point. Besides, it can be seen that the rain events are again followed by less pronounced daily temperature variations in the air and in the soil. But as the amount of rain is less compared to the scenario discussed before, the damping is as well smaller, especially for day 497. The rain clouds influence the air temperature and net radiation stronger for the precipitation around day 500. Thus, the overall heat entry at the surface is reduced during those days which retards the warming of the soil. For both rain events, the 4 mm of rain water do not notably enter both profiles down to the first TDR probe at 9 cm. Therefore, an increased heat capacity cannot be the reason for the cooling or reduced warming cycles following the rain at day 500.
In the whole period, the heat transport in the soil seems to be purely conductive, without any convective component. Furthermore. the only reasonable explanation for the energy sink in that case is evaporation and transpiration. And hence, this scenario enables the most direct insight into the thermal signature of surface evaporation in this field data-set.

Summer

The final scenario (Fig. 5.18) requires a small shift in the time line, as it refers to the summer of the year before. But from the perspective of the hydraulic and thermal state of the system, it is a follow-up of the scenarios discussed before.
The summer period at the end of July 2010 was the end of a hot and dry month without any precipitation. This resulted in maximum soil temperatures of about 25 °C to a depth of 50 cm and low water contents close to the surface. Again, the grass profile is much drier compared to the bare one, as the roots took up nearly all the waterfrom the upper two soil layers. The bare surface itself might be similarly dry, but below 10 cm the profile stayed wetter. The reason could again be a dry crust at the top which operates as a capillary barrier and stops at some point the surface evaporation. This results finally in higher water contents in the upper part of the profile. The rain events between day 203 and day 205 are heavier than those discussed in the scenario before and in total nearly 20 mm reached the soil surface. But despite the air temperature is now also higher, the potential evapotranspiration has not significantly increased compared to the conditions in spring caused by a high relative humidity during these events which reduces the potential of the air to take up water. Hence, not all the precipitation was directly removed from the soil surface, but it partly infiltrated and re-wetted the upper soil layer. Altogether, the upper TDR probes detect an increase in water content. For the grass, this was only the case for the topmost one. Assuming a similar evaporation flux for both profiles, the reason for the smaller water flux into the soil is most probably the root water uptake and the transpiration. And Figure 5.9 reveals again that the transpiration exceeds the pure

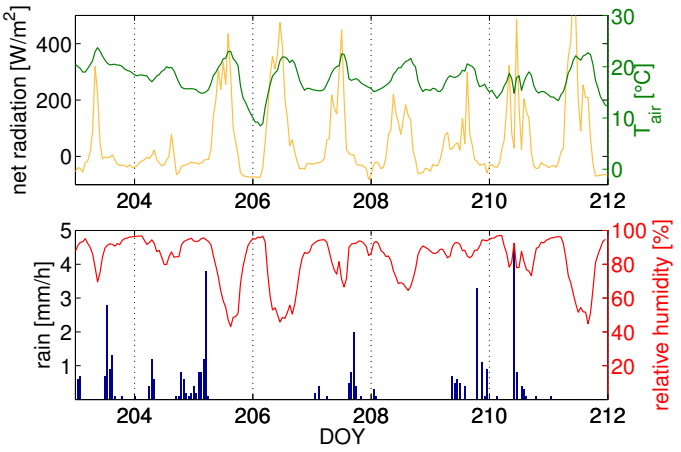

(a) Weather data, July 22nd to 31st, 2010.

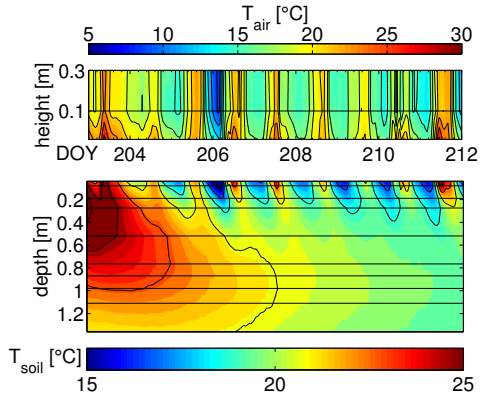

(b) Temperature profile at the bare surface.

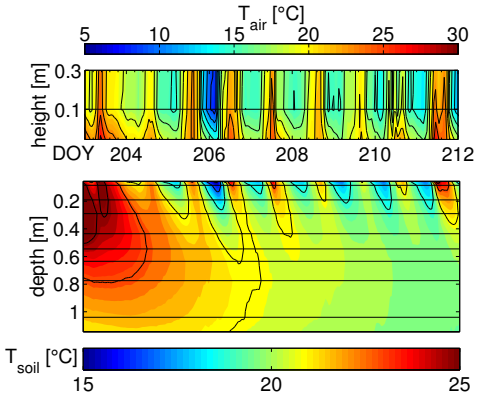

(c) Temperature profile at the grass surface.

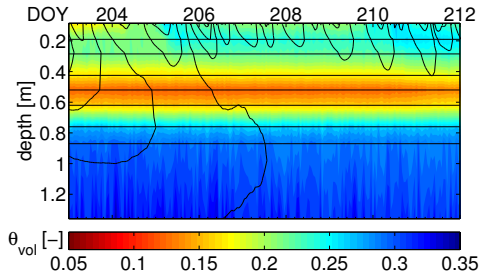

(d) Water content profile under the bare surface.

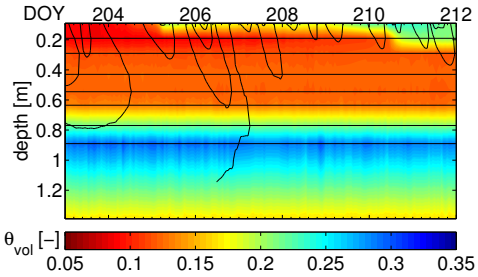

(e) Water content profile under grass.

Figure 5.18: Soil temperature and water content profiles in summer. Plotted are hourly means of the data measured between July 22nd and 31st, 2010. Direct surface temperature measurements are not yet available. Hence, the air temperature profile is interpolated towards the upper soil temperature measurement. Rain events come along with an increase in relative humidity and a damping of the daily amplitude in net radiation and temperature. Temperature regimes are different under grass and the bare surface due to stronger evaporative cooling for the wetter bare soil. Furthermore, lower water contents result in a smaller thermal diffusivity in the upper soil layer under grass and hence a different penetration depth of the temperature cycles.

evaporation flux considerably. The amount of water during all the rain showers was significant (more than 40 mm). Under the presumption that the textural composition of the first layer is the same for both profiles and due to the fact that the hydraulic conductivity is a function of the water content (Eq. (2.14)), the more than 0.1 cm^3/cm^3 lower water content at the top of the grass profile initially results in a considerably lower hydraulic conductivity and thus a significantly reduced water flux from the top. As a consequence, we notice that the rain before day 206 infiltrates in the bare soil profile down to the third TDR sensor and the water content increases over the complete first layer which was by far not the case under the grass.

A further effect of the higher water content under the bare surface can be identified by the shape of the contour lines following the heavy rain events on day 205 and 210. As already mentioned, contour lines evince a certain steepness related to the phase shift and amplitude damping of the temperature signal with depth. Thus, their shape depends on the thermal diffusivity. At or shortly after those rain events, the contours get steeper around a depth of 0.2 m. This points again on convective heat transport in the bare profile which decouples the fixed phase and amplitude signal in depth and causes a nearly instantaneous adaptation of the temperatures in the upper 30 cm.

Looking at the air temperature profile during that period might lead to the conclusion that, over grass, it is warmer close to the surface for both, day and night time. First we have to remark that the infra-red sensor was not yet available for this period, so that the air temperature profile is extrapolated over the surface towards the top soil temperature probe at about 5 cm depth. This might cause optical interpolation artifacts compared to the previous air temperature profiles which could be miss-leading for interpretation. But even comparing only the air temperatures measured above the soil, we might come to that conclusion. During nighttimes, an explanation could be given by the shielding of the leaves which prevent a larger heat loss. However, during the day an explanation could not easily be found. But in general, a lower energy sink at the surface would correlate with smaller evapotranspiration fluxes, which would be confirmed by the lower water content under the grass surface. In combination with an overall lower thermal diffusivity of the leaves, compared to the soil below, this could be a reasonable explanation for the overall warmer surface.

Finally, we want to focus on the extremely cold night at day 206. One might have expected that the cooling front under the bare surface would penetrate deeper compared to that in the profile under grass due to the different surface cover. However, the corresponding contour line under grass reaches down to almost the same depth. This can be explained by the fact that the bare soil profile is warmer in the beginning of this data section. The amount of heat stored deeper down in the bare profile is larger than that in the grass profile. Therefore, the warmer soil counteracts stronger the cooling front penetrating from the top in this night compared to the profile under grass. The larger penetration depth of the warming cycle below the grass the day afterwards could be explained by the smaller evaporation flux at the surface. The upper part of the grass profile is just dry and an energy sink caused due to evapotranspiration will be smaller.

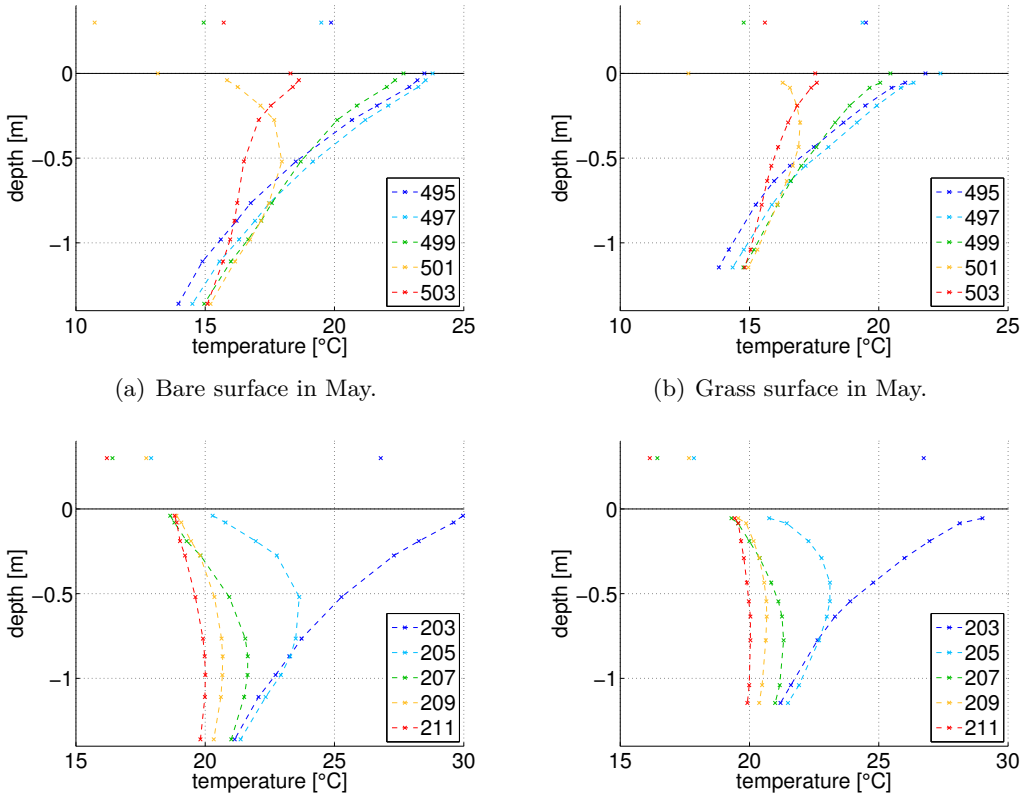

(a) Bare surface in May.

(b) Grass surface in May.

(c) Bare surface in July.

(d) Grass surface in July.

Figure 5.19: Daily mean temperature profiles in late spring and summer. Underlying data intervals: May 15th to 24th, 2010 and July 22nd to 31st, 2011.

After the summer period, the cooling of the soil will proceed and due to rain events that come along with autumn, the soil profiles will be further re-wetted. Thus, it is only a matter of time until the system is back in the state from which we started this analysis of the soil-atmosphere coupling and we can close the circle at that point.

Surface Coupling Analyzed from Daily Mean Temperatures

The overall analysis of the soil-atmosphere coupling will be completed by the discussion of the mean temperature and gradient evolution for the warm scenarios, in May and late July. The corresponding profiles under both types of surface cover are summarized in Figure 5.19.

The temperatures in May are up to 5 °C below those in July. Even the energy entry at the soil surface is comparable, the soil and air temperatures do not reach the same level as two months later. The reason for this is on the one hand the bottom temperature of the soil profile which is significantly cooler in May. On the other hand, the evapotranspiration at the soil surface which might be different, even if the weather conditions are

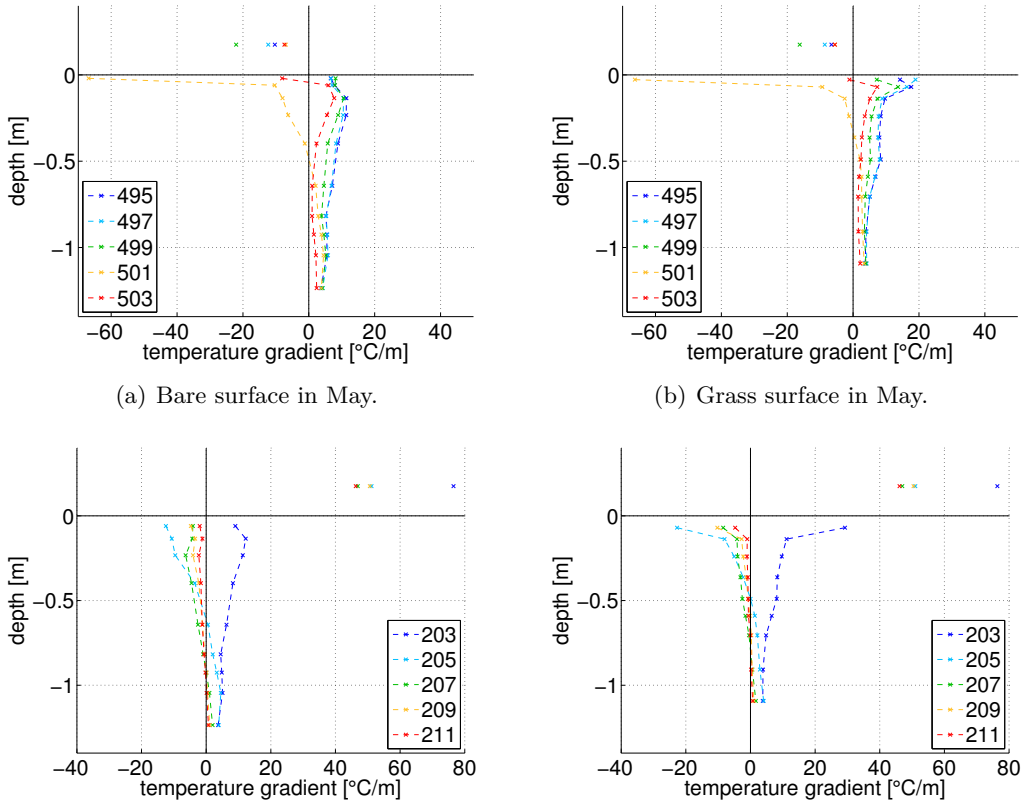

(a) Bare surface in May.

(b) Grass surface in May.

(c) Bare surface in July.

(d) Grass surface in July.

Figure 5.20: Daily mean temperature gradients in late spring and summer. Underlying data intervals: May 15th to 24th, 2010 and July 22nd to 31st, 2011.

similar. In May, the rather cold rain water infiltrates into the soil and cools the upper part of the soil profile around day 501. Hence, the amount of water itself increases the heat capacity and thus the energy required for a further temperature rise. As the bare soil profile is the warmer and wetter one, the temperature change corresponding to the rain event is larger compared to the profile under grass. But as the bare soil is directly exposed to the radiative forcing of the sun, the re-heating occurs also much faster. From the lower mean surface temperature after the precipitation at day 501 and due to the fact that no changes in water content could be detected confirms this assumption that surface evaporation is the most probable reason for the energy sink.
For the period in late July, the infra-red surface temperature sensor was not yet installed. Hence, we lack this information for further conclusions concerning the explicit thermal footprint of the evaporation flux. Nevertheless, the infiltration of the cool rain water can be seen from the soil profiles in Figure and 5.19(c) and 5.19(d). The water flux fastens the cooling within the soil by convective transport of the temperature information. The redistribution of the water within the soil causes a further temperature decrease close to the surface of more than 10 °C within the eight-day period considered here. The fact that the change in the corresponding mean air temperature is smaller hints in addition to the

non-conductive character of the transport process in the soil at that point.

Looking at the corresponding temperature gradients in Figure 5.20 exhibits that the rain events in May cause only a change in the overall heating of the soil close to the surface. Especially around the rainy day 501, energy is provided at the surface to enable the evaporation of the rain water. The gradients in air temperature reveal the same surface heating trend, but for the complete period. As the profile under grass is already rather dry, the evaporation phase from the bare profile seems to last longer. This is pronounced by the already smaller temperature gradient under grass at day 503.
The rain events at end of July stand for the beginning of a different weather period as the heat flux changes direction down to a depth of 70 cm after the first rain at day 204. The resultant temperatures are not returning towards the profile from the beginning during those eight days. In general, the soil heat flux changes from transporting energy into the soil and further increasing temperatures to providing energy at the surface to evaporate water and to compensate for the cooling from the atmosphere.

This time the temperature gradients in air provide a consistent image about the heat flux situation. After spring, the air supplies energy at the soil surface to heat up the underlying profile and later in summer, the flux changes direction. The soil is already heated up and acts as a heat storage that counteracts the temperature fluctuations in the daily cycle and longterm cooling trends in the atmosphere.
Again, the data-set reveals well traced processes in the soil, but on a daily mean scale the atmospheric quantities render only long-term trends, as small-scale turbulent processes occur at several Hz and are balanced out even by the weather measurements in 10 min intervals. Finally, the near surface measurements within the soil still yield a deeper insight in the coupling towards the atmosphere. Information about the water and energy cycle can be extracted even on a daily-mean scale, despite of its damping and due to the longterm memory of both, soil temperature and water content. Therewith, the corresponding fluxes from the soil can be estimated to some extent for known thermal and hydraulic properties. Only for the final closure of the surface energy balance, especially on scales below the daily means, temporally high resolution measurements within the atmosphere are indispensable.

5.4 Soil Temperature Projection

This section discusses the application and performance of the soil temperature projection method for the field data-sets. At first, we take a closer look on the frequency decomposition of the soil temperature profiles. From this, the thermal diffusivity will be estimated. Finally, the reconstructed surface temperature information is compared with that measured by the infrared sensor.

As we are now working with profile data of sensors buried in the field, we would assume that lateral fluxes, as detected in the laboratory experiments, are negligible in this system. Yet in the context of this work, we are analyzing natural and undisturbed soil profiles for the first time. (As the installation of the sensors was more than a year before the data-set used in this work, we assume that the current data is undisturbed.) Furthermore, the soil temperature forcing under field conditions is diverse. It is a superposition of various factors and not only a modulated air temperature signal. Compared to the laboratory conditions, the level of complexity for testing our method has thus significantly increased and this allows to analyze limits of the underlying model assumptions for describing a natural field system.

Frequency Information Comprised in Soil Temperature Profiles

An impression of the variety of frequencies comprised in the field measured data-set is given in Figure 5.21. To gain deeper insight into the underlying temperature signals, take a look at the line plots of the soil temperature data (under the bare surface: Fig. 5.8; under grass: Fig. B.2 in the appendix). The measurement depths in both profiles are not completely identical, but comparable. However, the lowest sensor under grass broke shortly after the installation and hence this profile is 20 cm less deep.
The amplitudes next to the y-axis corresponds to the yearly cycle. As we would have expected, the daily and yearly cycle with their first harmonics are the most dominant

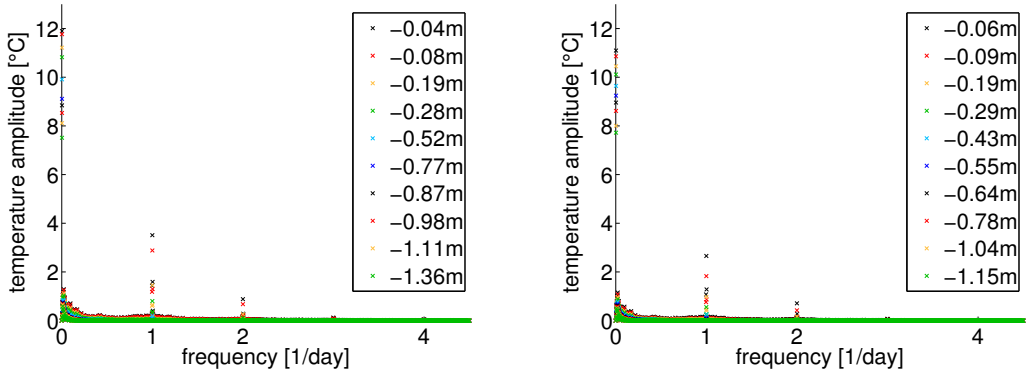

(a) Data set under bare surface.

(b) Data set under grass.

Figure 5.21: Amplitude spectra of both field measured soil temperature data-sets.

entries in the frequency spectra, independent of the surface cover. The fact, that the grass on top of the soil profile serves as an insulation layer, is affirmed by up to 1 °C lower amplitudes for both dominant frequencies under grass. This deviation cannot be explained by a difference in measurement depth of $\Delta z = 2\,\mathrm{cm}$ for the upper temperature sensors. The damping ratio for the daily cycle ($f_d = 1/86400\,\mathrm{Hz}$) can be estimated via

$$\exp(-kz) = \exp(-\sqrt{\frac{\pi f_d}{D_{\mathrm{t,s}}}}\Delta z) \approx 0.9 \tag{5.1}$$

with $D_{\mathrm{t,s}} = 1.0 \times 10^{-6}\,\mathrm{m^2/s}$ for a typical soil. If the only difference in temperature would result from the difference in sensor position, the temperature amplitude of 3.6 °C under the bare surface would correspond to an amplitude of 3.2 °C under the grass surface. The actually measured one was 2.7 °C which confirms the insulation effect of the vegetation cover and therewith explains the different amplitudes of the soil temperature signals measured within the two profiles.

As the forcing at the soil surface is not purely harmonic, various frequency components are introduced by weather events shorter than the seasons or the daily radiative forcing by the sun. Rain events or other changes of the weather caused due to changing high- or low-pressure conditions leave a thermal signature in the corresponding temperature data. These influences are captured by the Fourier analysis resulting in a variety of frequency entries ranging between the yearly and daily cycles with comparatively small amplitudes (Fig. 5.21). As we are finally interested in a reconstruction of the temperature right at the soil surface, we need to catch all significant structures from frequency space to get a good reconstruction. Hence, reducing the signal only to the known seasonal and daily components, many characteristic features in the temperature variation would get lost. Yet, at the same time, we need to skip all entries which would finally result in a destabilization of our projection procedure and we have to come up again with an appropriate noise level criterion.

5.4.1 Estimation of the Thermal Diffusivity

Firstly, the soil profiles will be thermally characterized by the thermal diffusivity from the frequency information comprised in the soil temperature profiles. At the same time, this yields the projection factor k and the extrapolated Fourier coefficients for the surface temperature reconstruction afterwards.

From Soil Temperatures under the Bare Surface

From Figure 5.22(a), an underestimation of the amplitude damping and phase shift with depth can be noticed, if all frequency components are used within the weighted linear regression. This again hints at a bias due to low frequency components. Yet, only frequencies should be used in the regression procedure which are clearly resolved from the time-series and significantly modulated while penetrating into the ground. As a consequence, we will skip frequencies below $f_{\text{cut-off}} = 4.2 \times 10^{-7}\,\mathrm{Hz} = (27.5\,\mathrm{d})^{-1}$ (Eq. (4.6)) in the further analysis which seems to fulfill both requirements. The resultant fit is shown

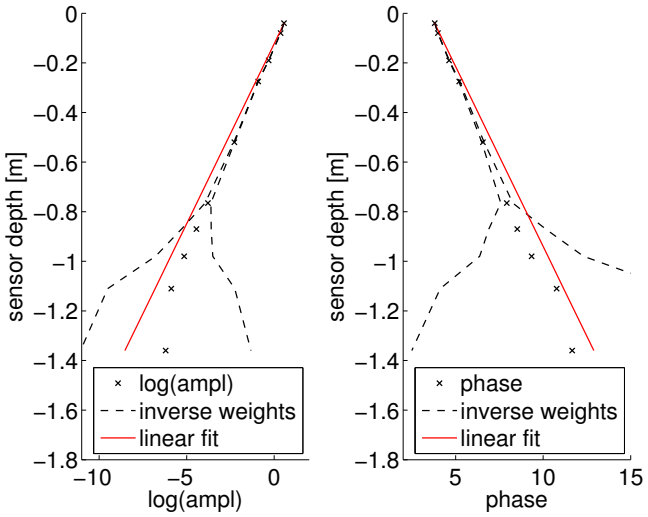

(a) Frequencies for linear fit chosen through noise level criterion.

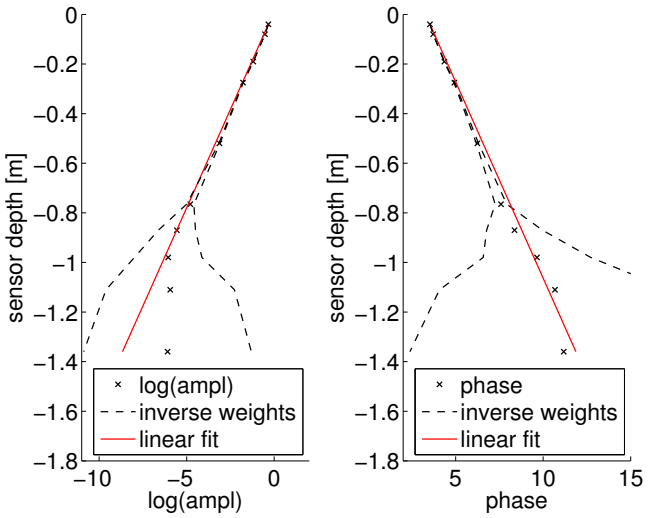

(b) Low frequency entries excluded from linear regression procedure.

Figure 5.22: Estimation of thermal diffusivity from field-measured soil temperature profile under the bare surface. Fit results are shown exemplary for profile information of the daily cycle. *left:* Linear fit (*red*) of log-amplitude data (*crosses*). *right:* Linear fit (*red*) of phase profile data (*crosses*). *Dashed lines* indicate inverse weights used within regression procedure, reflecting information loss with depth.

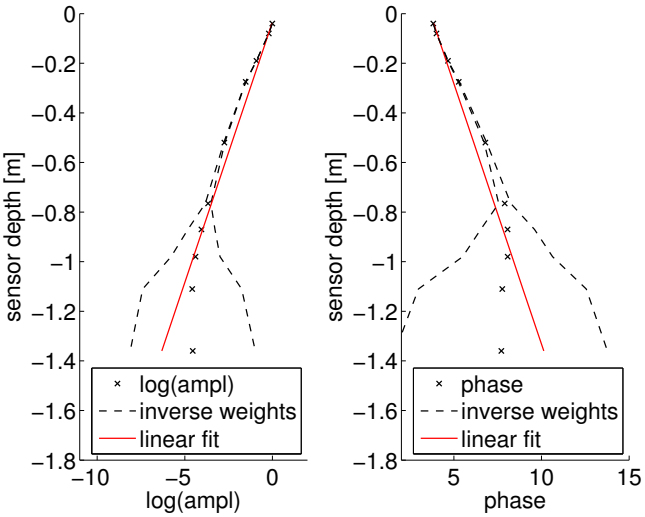

Figure 5.23: Estimation of the thermal diffusivity of field-measured soil temperature profiles under the bare surface for wet period, August 2010 to February 2011. Fit results are shown exemplary for profile information of the daily cycle. *left:* Linear fit (*red*) of log-amplitude data (*crosses*). *right:* Linear fit (*red*) of phase profile data (*crosses*). *Dashed lines* indicate inverse weights used within regression procedure, reflecting information loss with depth.

in Figure 5.22(b) which yields a final thermal diffusivity of $D_\mathrm{h} = 9.1 \times 10^{-7}\,\mathrm{m}^2/\mathrm{s}$ for the soil profile under the bare surface.

By looking at the amplitude and phase profiles for the daily cycle in Figure 5.22, two general observations can be made. Firstly, the signal to noise ratio for the daily cycle becomes considerably worse below 0.8 m, since the amplitude information from the lower two sensors is nearly constant. Hence, we detect mainly white noise for all frequencies higher than the daily cycle at the lower end of the profile.
The other feature of the profile is the slightly steeper decrease in amplitude and increase in phase suggested by the upper two sensors compared to the rest of the profile. Considering the influence of thermal layers (Sec. 3.5), the changing slope points to a change in the thermal diffusivity close to the surface. A linear fit of only the upper two temperature measurements indeed yields a higher estimate for $D_\mathrm{h} = 1.6 \times 10^{-6}\,\mathrm{m}^2/\mathrm{s}$. We have seen from the water content profiles (Fig. 5.5) that the second textural layer is much drier than the soil above. Hence, water contents differ up to 0.1 within the profile and results, as already discussed in the previous section, in an up to a factor two higher thermal diffusivity and thus a factor $\sqrt{1/2}$ smaller projection factor. However, the effect is not that obvious in the profiles and in addition, the first layer reaches down to a depth of 30 cm, but only the upper two sensors placed in that layer exhibit this trend. Furthermore, the drying during summer occurs only at the topmost TDR probe at 10 cm and the upper two temperature sensors which suggests a lower D_h and hence contradicts a generally

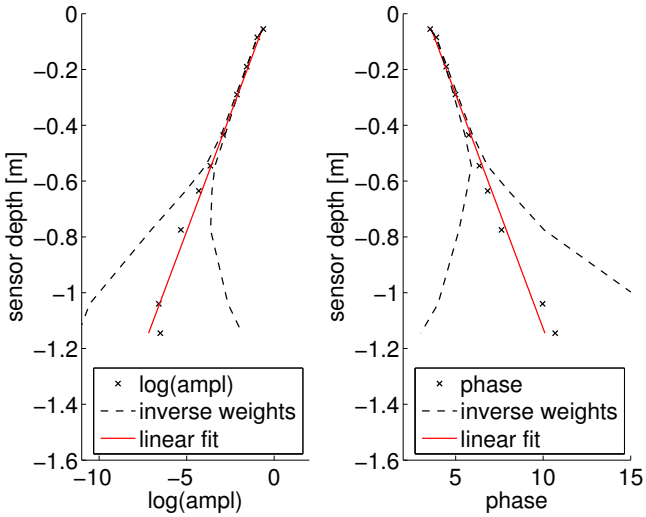

Figure 5.24: Estimation of the thermal diffusivity for field-measured soil temperature profiles under grass. Fit results exemplary for profile information of the daily cycle. *left:* Linear fit (*red*) of log-amplitude data (*crosses*). *right:* Linear fit (*red*) of phase profile data (*crosses*). *Dashed lines* indicate inverse weights used within regression procedure, reflecting information loss with depth.

higher value close to the surface. Yet, water contents in the surface layer are only lower during warm and dry periods, otherwise the second textural layer with its higher sand content is drier compared to the one above and below.
Analyzing only temperature profiles for wet soil conditions, August 2010 to February 2011, reveals indeed a change in the slope of the amplitude and phase profiles that agrees well with the textural layer boundary in 0.3 m (Fig. 5.23). Due to the weights, the focus of the fit is on the steeper part at the top of the profile resulting again in an estimated D_h of $1.6 \times 10^{-6}\,\mathrm{m^2/s}$. The impact of seasonal changes in water content is hardly recognizable analyzing the complete data-set of one year. Furthermore, textural differences between the upper two layers are not dominant during spring and summer due to the overall lower water contents close to the surface.

From Soil Temperatures under Grass

The linear fit of phase and amplitude information with depth for the soil temperature data under grass is shown in Figure 5.24. Frequency entries below $f_\text{cut-off} = (27.5\,\mathrm{d})^{-1}$ are neglected. This yields an estimated thermal diffusivity of $D_\mathrm{h} = 1.0 \times 10^{-6}\,\mathrm{m^2/s}$. Therefore, the overall effective thermal properties of the two profiles are similar analyzing the temperature profiles of the whole year.

In contrast to the bare surface, the situation at the top of the grass profile is different. A decoupling of the phase and amplitude relation between the upper 10 cm and the lower

part of the profile can be clearly noticed. Yet, the effect points to the opposite direction compared to the trend in the profiles under the bare surface. The changing slope in the amplitude and phase relation suggests a smaller thermal diffusivity close to the surface than below. It is remarkable that this affects again not the complete upper 30 cm and hence the complete upper textural layer. The impact is strongest within the top 10 cm, the range between the upper two temperature sensors. *Wollschläger et al.* (2009) found a root parameter of 8 cm for this field site which is consistent with the thickness of the layer we found analyzing the frequency spectra. In this upper few centimeters, the root net is most dense and active resulting in a lower D_h for several reasons. Firstly, the soil is less compact due to the root channels which reduces the thermal conductivity and hence the thermal diffusivity (Eq. (2.18)). On the other hand, the D_h of the organic matter itself is low with a value of about $1.3 \times 10^{-7}\,\mathrm{m^2/s}$ (*Tabil et al.*, 2003). And finally, water contents are lowest close to the surface. All these factors point on a decreased thermal diffusivity in the root zone at the top of the grass rofile. Analyzing only the two temperature time-series in the upper 10 cm below the surface yields indeed a considerably lower thermal diffusivity of $2.5 \times 10^{-7}\,\mathrm{m^2/s}$.

Altogether, we conclude for the field data-sets that changes in water content between different textural layers alone are not noticeable as distinct values for D_h from the analysis of soil temperatures of one year. Focusing on periods of certain hydraulic conditions reveals different thermal diffusivities under the bare surface highlighting a time- or water-content-dependency of the parameter. To explain the strong change in the spectral profiles under grass, various impact factors due to the plant roots have to be considered. Lower water contents alone are not sufficient, since the effect can also be observed during autumn and winter when water contents in the whole profile are high. Hence, we found an effective thermal diffusivity for the lower soil profile independent of textural differences and related changes in water content. For both profiles, the upper part indicates a certain type of decoupling of the phase and amplitude relation compared to the deeper soil part. This layering will be further analyzed by numerical simulations in the following section.

5.4.2 Surface Temperature Reconstruction

The results of the temperature projection will be discussed in comparison with surface temperatures measured by thermal infrared sensors (Sec. 4.1.2). From previous works (*Ehrmann* (2011) and *Bauser* (2011)), we know that there are several uncertainties comprised in the final temperature values. For example, we assume the soil to be almost a black-body with an emissivity of 0.96 ± 0.04 (*Geiger et al.*, 1995). In addition, corrections due to a lower emissivity consider the air temperature measured at 2 m height. Yet more precisely, we would have to account for the thermal radiation of the "sky" which is reflected at the soil surface towards the sensor. The temperature of the atmosphere above 1 km is increasingly colder and considerably below that of the soil. In particular for clear-sky conditions, the reflected radiation from the upper atmosphere will introduce a bias up to $2 - 3\,^\circ\mathrm{C}$ in the measured surface temperatures due to the unknown emissivity of the respective surface (*Bauser*, 2011). However, for cloudy weather conditions, the effect is almost negligible and a correction using the measured air temperature sufficed,

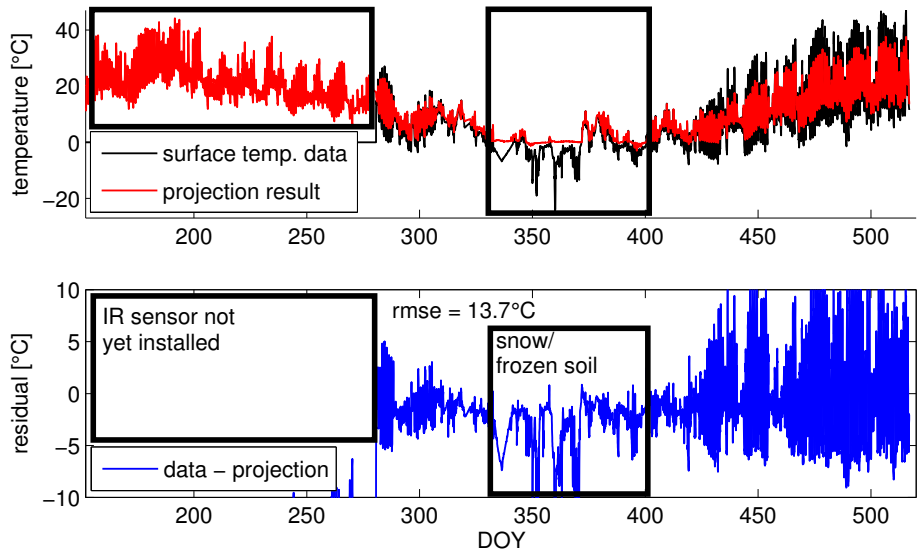

Figure 5.25: Projection results for soil temperatures under bare surface. The thermal diffusivity was estimated only from upper two time-series. Noise level was set to 0.5 °C. *top:* Reconstructed (red) and measured (black) surface temperature. *bottom:* Residual between measured and projected surface temperature.

since clouds have a similar temperature as the surrounding air. Yet, we lack the correct sky temperature and the actual emissivity of both types of surface cover to calculate the appropriate correction for the measured time-series. Hence, we have to keep this uncertainty related with the infrared measurements in mind when comparing the reconstructed and measured surface temperatures in the end.

From Soil Temperatures under the Bare Surface

The result of the temperature reconstruction at the bare surface using the projection factor estimated from the complete profile information is shown in Figure 5.25. The overall residual suggests that the estimated thermal diffusivity is too large, as the projection factor is proportional to the diffusivity's squared inverse and the amplitude of the whole reconstruction is too small. By evaluating only the upper two time-series of the profile or only the wet period during autumn and winter, the estimated value of D_h was even larger. As a consequence, the projection result would become even worse by reducing the data basis. Therefore, we conclude from the discrepancy of the reconstruction that the soil profile with the bare surface seems to be decoupled from the remote temperature measurements from above the surface. And this is not only the case for the warm period in spring and summer when we would assume a dry crust to dominate the surface properties, but also during the rest of the year. For example, also soil freezing in winter

(a) Bare surface.

(b) Grass surface.

Figure 5.26: Both types of surface cover from the perspective of the infrared sensors.

has an impact on the the soil structure. Altogether, the upper few millimeter or the first centimeters of the soil profile might have considerably changed, since the soil surface has been kept bare. The structure of the bare surface itself suggests this with its crumbs and cracks (Fig. 5.26(a)). As a consequence, this boundary layer exhibits material properties different from those below, but the soil temperature measurements are not close enough to the surface to resolve this in the data-sets from within the soil.

From Soil Temperatures under Grass

The reconstructed and measured surface temperatures for the grass surface are show in Figure 5.27. The lower thermal diffusivity estimated from the upper two temperature sensors was used within the projection. However, comparing the residual between autumn or winter 2010 and spring 2011 reveals a time-dependency in the misfit between the reconstruction and the measured surface temperatures. For warm and dry periods, it points to a still overestimated D_h and hence an underestimated projection factor. Since spectral information from Fourier analysis lacks a temporal resolution, this could not be observed from the phase and amplitude profiles used in the estimation procedure for D_h. Yet, the effect is clearly visible in the projection results. Since the amplitudes are exponentially increased towards the surface, a difference in D_h up to a factor two results in a significantly different surface temperature signal. Thus, the influence of changing water contents close to the surface might be hard to resolve from the soil temperature data, but are not negligible for a correct projection.

Analyzing the reconstruction results for October 2010 in more detail, a different structure can be found in Figure 5.28(b). A systematic offset between the projection result and the measured surface temperature is recognized which seems to be representative for the complete autumn and winter period. The missing correction of the infrared measurements with the actual emissivity of the surface cover and the sky-temperature could explain this. The measured surface temperatures are too low which points to surface reflections of thermal radiation from the upper atmosphere. Furthermore, the effect is

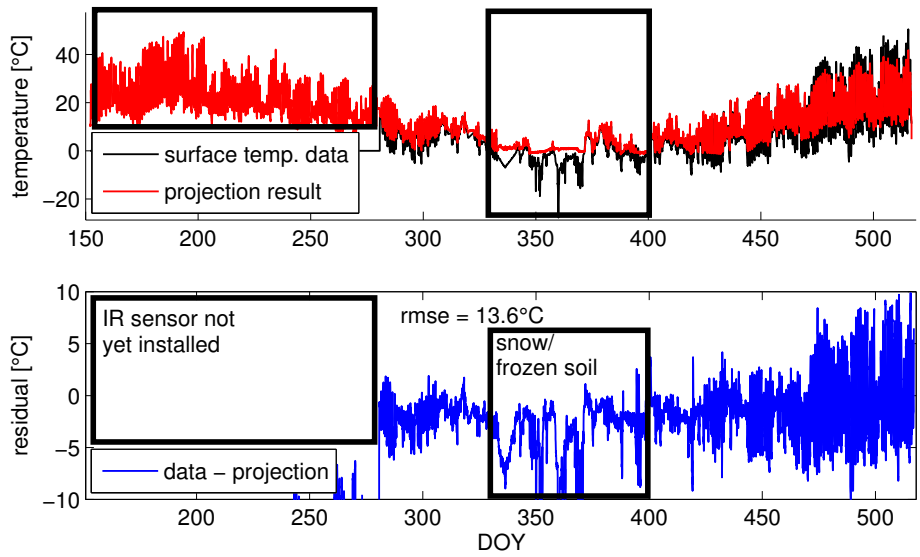

Figure 5.27: Projection results for soil temperatures under grass. The thermal diffusivity was estimated only from upper two time-series. Noise level was set to 0.5 °C. *top:* Reconstructed (red) and measured (black) surface temperature. *bottom:* Residual between measured and projected surface temperature.

less for cloudy or rainy days, e. g. around day 290 (Fig. 5.28(a)). Altogether, the offset due to the missing correction could be in the range of the systematic shift of the residual in this period.

Considering the sensor's field of view (Fig. 5.2), the remaining daily fluctuations in the residual of the reconstruction might be be explained by the remaining radiative contributions from the soil surface comprised in the infrared measured temperatures. As already mentioned, the infrared sensors detect a mean surface temperature emitted from the grass itself and the soil patches in between (*Ehrmann*, 2011). The heat capacity of the plant leaves is lower than that of soil. Therefore, the different thermal properties will cause different temperature variations at the leaves than at the soil patches in between. Hence, a reconstruction of the surface temperature from within the soil will always result in temperatures different from those measured by looking from above. Depending on the overall intention, one or the other information would be the more reliable. For example, the reconstructed surface temperatures should be appropriate for ground heat flux calculations. While for the sensible heat flux in air, the conclusion would exactly be in the opposite direction. We would not expect the information extracted from within the soil to be representative for calculating temperature gradients at the lower boundary of the atmosphere, if the surface is covered by some vegetation. An flux estimate based on this information would also be biased.

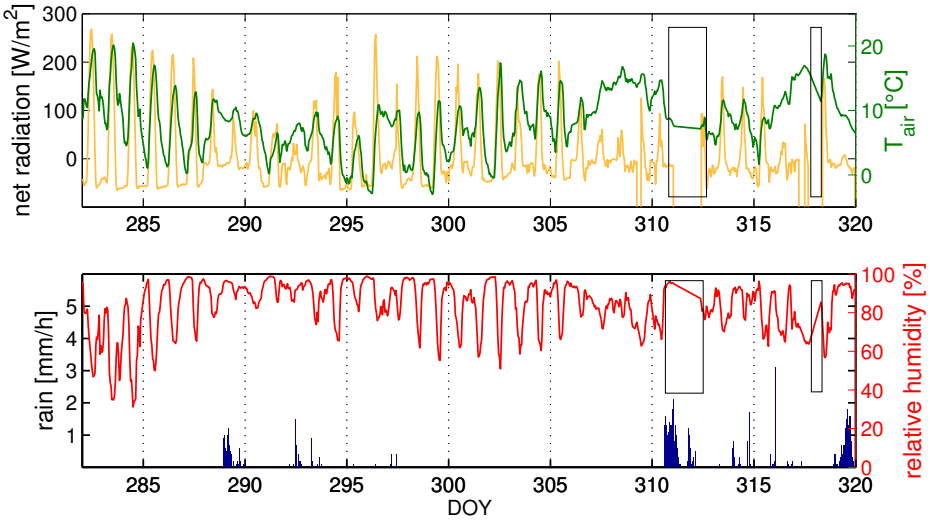

(a) Weather conditions during October 2010. *Black boxes* indicate interpolated data points due to technical failures of some sensors.

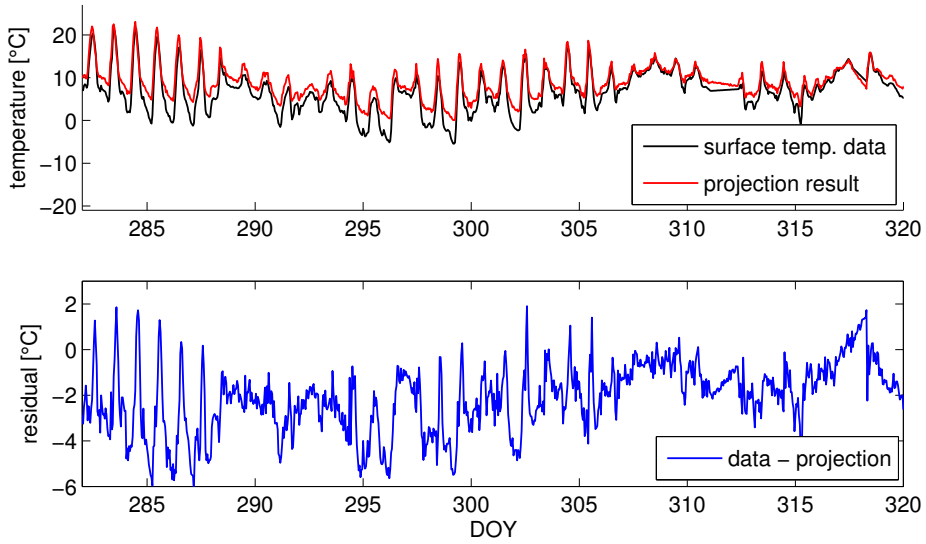

(b) Projection results under grass for October 2010. The thermal diffusivity was estimated only from upper two soil temperature measurements. *top:* Reconstructed (red) and measured (black) surface temperature. *bottom:* Residual between measured and projected surface temperature.

Figure 5.28: Zoom in projection results under grass for October 2010.

Therewith, both type of surface covers hint at a decoupled boundary layer or transition zone with distinct thermal properties. For the vegetated one, the plants and the air in between prevent an extrapolation of the information from the soil surface towards the atmosphere as well as in the opposite direction. This is obviously a limitation of our method and furthermore has implications for the larger context of the soil-atmosphere coupling.
Furthermore, looking from within the soil towards the surface highlights in addition the crucial role of the boundary layer for closing the energy balance. Without an explicit or at least effective representation of this zone, an estimation of surface energy fluxes seems to be biased, independent from which compartment the surface is approached. But at the same time, measurements which allow a reliable characterization of its thermal and hydraulic properties are hardly possible. This clearly shows the dilemma for describing the water and energy exchange between the soil and the atmosphere.

5.5 Numerical Inversion to Estimate the Thermal Diffusivity

During the surface temperature reconstruction in the previous section, challenges of the thermal characterization of field soil profiles became obvious. Textural layering and natural forcing at the soil surface as well as resulting changes in water content and the influence of the vegetation cover, all exhibit a considerable influence on the effective soil thermal properties.
In this section, we will compare parameters obtained during the surface temperature projection before with estimates from nonlinear regression based on a numerical heat diffusion model. This additionally allows to estimate thermal properties when assuming a layered soil profile.

The analysis of profile information of phase shift and amplitude damping with depth suggested a layering in both soil profiles with a layer boundary at or within the upper textural layer (Sec. 5.4.1). Nevertheless, we will analyze in a first step the estimates from numerical inversion on the unprejudiced assumption of a homogeneous soil profile. Afterwards, the data basis will be adapted and the model complexity will be enhanced according to the encountered deviations.

5.5.1 Soil Profile under the Bare Surface

Neglecting all prior information from former analysis, we now first use the whole soil temperature profile in the objective function for the nonlinear regression based on a numerical heat diffusion model. This yields an effective thermal diffusivity of $1.0 \times 10^{-6}\,\mathrm{m^2/s}$ for the bare soil profile which compares well with the estimate from the linear fit of the amplitude and phase information of the whole profile. Deviations between measured and simulated soil temperatures are illustrated in Figure 5.29(a). Especially during the wet season, August to March, simulated temperatures are in good agreement with the data and vertical deviations in the profile can be correlated with heavy rain events. During these events, heat is transported not purely diffusive, but also by convection due to the water flux. Since this process is not represented in the underlying models, we would

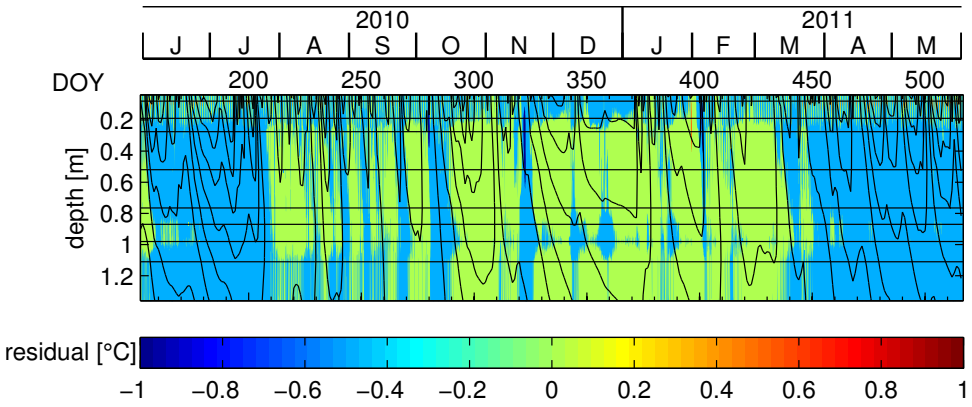

(a) Inversion based on complete data-set.

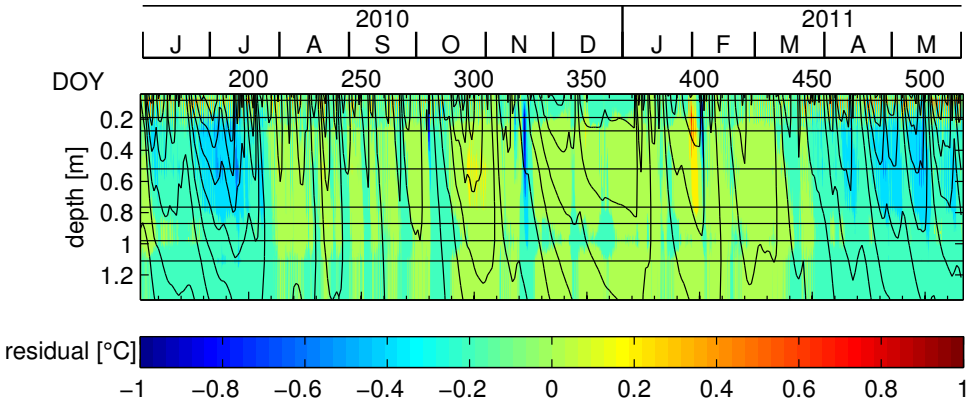

(b) Inversion based on dry Periods: June, July, and March to May.

Figure 5.29: Residual (data-model) for bare soil temperature profile with D_h estimated from numerical inversion. The inversion procedure based on the complete data-set exhibits a time-dependency of the thermal diffusivity. Considering only dry periods in summer 2010 and spring 2011 improves the fit for these periods and reveals in addition a thermal layering corresponding to the textural layer boundaries at 30 and 70 cm.

expect that residuals clearly indicate its impact.

In addition, the residual suggests once more a temporal change in thermal diffusivity due to differences in water content between wet and dry seasons. Analyzing only the wet period, autumn and winter, results indeed in a higher D_h of $1.2 \times 10^{-6}\,\mathrm{m}^2/\mathrm{s}$ which is smaller than the estimate from the weighted linear regression in frequency space. Furthermore, this value does not significantly improve the simulation result for that period, as deviations are mainly caused by non-diffusive processes which are unrepresented in the underlying model.
Considering only soil temperature profiles during spring and summer in the inversion, when the soil profile is rather dry, yields a 20 % lower D_h of $0.98 \times 10^{-6}\,\mathrm{m}^2/\mathrm{s}$. This reduces deviations between data and model for dry soil conditions by a factor two (Fig. 5.29(b)), while the fit during winter is not significantly worse compared to the estimates before. Two more features are now obvious in the residual. The rain event in October which was already analyzed in detail in section 5.3.1 and the rain during the warm period in January after the snow. Both indicate convective heat fluxes in the upper two soil layers which is not described by the purely diffusive heat transport model.

The accuracy of the temperature sensors is assumed as 0.5 °C. Hence, the estimated effective diffusivity fits the data-set well, even without considering thermal layers in the soil profile under the bare surface. Besides, introducing a thermal layer at 30 cm, as slightly indicated by the residual, does neither change the value of D_h considerably, nor improve the fit. Yet, deviations are caused predominantly by processes as convection or seasonal changes in water content which are not represented in the model. Textural layering and smaller changes in water content with depth seem to be secondary and their effect cannot be clearly extracted by both optimization procedures.

Altogether, optimizing the thermal diffusivity for the complete soil temperature data-set yields already a system representation by the model within the measurement accuracy of the temperature probes. Restricting the data basis on the dry periods, as suggested by the structure in the overall residual, yields a lower D_h which is consistent with a lower heat capacity due to the lower water contents. Therewith, the residual for these periods could be halved. The final residual suggests now a layer boundary at 30 cm, but an inversion based on a layered soil profile did neither significantly change the estimate for D_h nor further improve the residual.

5.5.2 Soil Profile under Grass

Assuming a Homogeneous Soil Profile

Firstly, the effective parameter for the soil profile under grass is estimated by an unweighted nonlinear regression using the complete soil temperature time-series. This yields for D_h $7.2 \times 10^{-7}\,\mathrm{m}^2/\mathrm{s}$. The deviations between data and model are shown in Figure 5.30(a). Weighting the information close to the surface yields a value of $3.7 \times 10^{-7}\,\mathrm{m}^2/\mathrm{s}$ which is by a factor two lower. These weights are chosen as the factor describing the

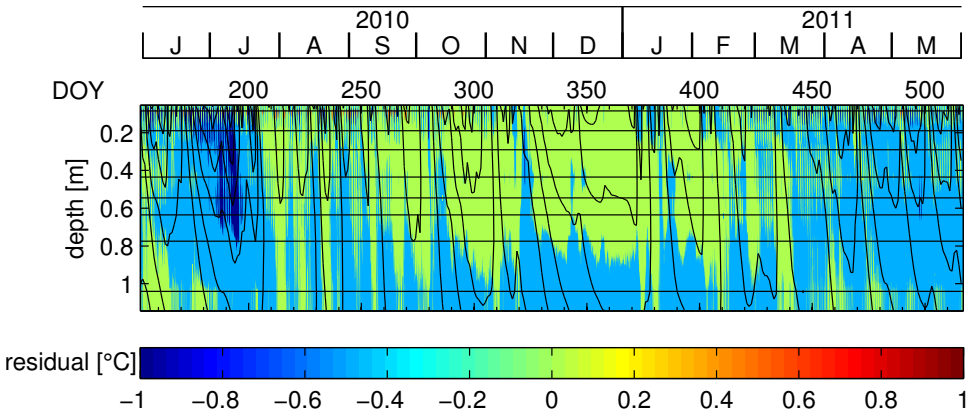

(a) Unweighted inversion of complete data-set.

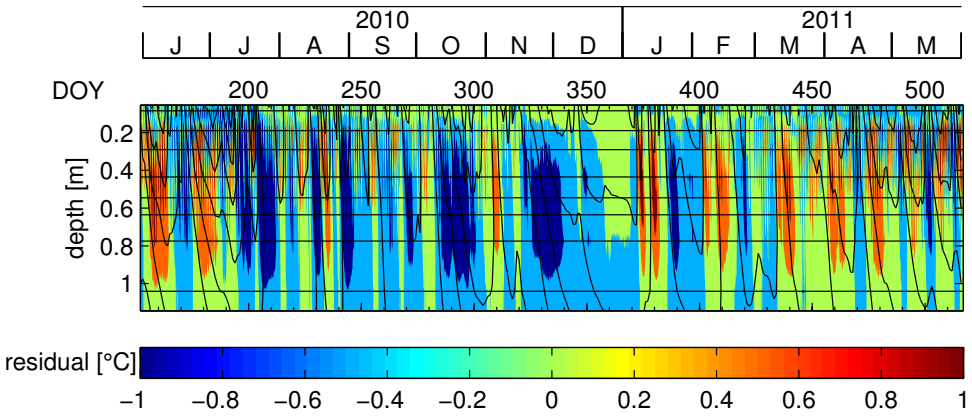

(b) Weighted inversion of complete data-set.

Figure 5.30: Residual (data-model) of soil temperature profile under grass with D_h estimated from numerical inversion. The unweighted inversion yields a D_h which is about a factor two larger than the estimation from a weighted inversion procedure.

exponential amplitude damping in the analytic solution. They were calculated for the daily cycle analogous to those used in the linear regression within the surface temperature reconstruction procedure. The resultant residual is illustrated in Figure 5.30(b).
Again, the overall fit of the thermal diffusivity estimated by the unweighted inversion is reasonable. In particular, during autumn and winter, the upper part of the profile is represented well and deviations are below the sensor accuracy of 0.5 °C. Larger deviations occur in spring and summer and hence seem to correlate with low soil water contents, especially close to the surface. Employing weights, the focus of the fit within the inversion procedure is shifted towards the upper part of the profile. Therefore, the simulation fits the data better in the upper 20 cm, except for the driest periods and the lower D_h represents the upper soil part well. In contrast, this thermal diffusivity seems to be completely off for the soil profile deeper down, since the residual shows an overestimation during dry

months and an underestimation of soil temperatures during cool or rainy periods.

The frequency analysis of the upper two temperature sensors (Sec. 5.4.1) already suggested a difference in D_h close to the surface and hence thermal layering in the soil profile under grass. Furthermore, the proposed order of magnitude for the change in D_h is consistent with the estimates here. Yet, a layering would not be evident only from the structure in the residual of the unweighted inversion results. In contrast, this could be clearly seen from the frequency analysis by the changing slope in the phase and amplitude relation with depth. Hence, this is a clear advantage of that method compared to numerical simulations. Even more, a definite implementation of useful weights is directly suggested by the analytic model which would not become obvious from any numerical consideration.
However, a seasonal change in the parameters cannot be deduced from frequency analysis. Analyzing soil temperatures in frequency space, temporal changes in D_h could also only be observed when comparing the final projection results with corresponding measurement data. Due to the underlying Fourier method with its continuous base functions, the analysis in frequency space lacks the temporal resolution. Using shorter data sets or several sections would however counteract the nature of the Fourier analysis. This is one of the disadvantages compared to numerical investigations or the transfer function approach proposed by *Jury and Roth* (1990).

For the bare soil profile, we noticed a clear seasonal trend in the residual (Fig. 5.29). Under grass, a similar characteristic can be recognized in the deviations between data and model (Fig. 5.30). Independent of the usage of weights, the residuals exhibit changing features between dry and wet periods. Therefore, a seasonality of D_h is suggested by both data-sets that seems to correlate with seasonal changes in water content. In the soil profile under grass, this change occurs within the soil and is resolved by the measurements, as the root water uptake mainly forces the drying. For the bare surface, a capillary barrier close to the surface is suggested that prevents the soil profile to dry out below a depth of 10 cm. Hence, this results also in a surface layer with distinct thermal parameters. Yet, this became not directly obvious from measurements within the soil, but only after projecting this information towards the surface and comparing the result with the surface temperature measured from above.

Assuming Thermal Layers

For further investigations, we set up a model with two layers to estimate distinct thermal diffusivities for the upper and lower parts of the soil profile. From spectral analysis and the structure in the numerical residual so far, the layer boundary is assumed at 10 cm. Since the soil temperature time-series measured at 6 cm is used as upper boundary condition, the temperature probe at 9 cm is the only one placed in the upper thermal layer and hence the one on which the optimization of the parameter in this layer is based. Weights are not considered during this inversion, since the surface layer is no longer of particular interest and the fit should optimize the parameters of both layers equally.

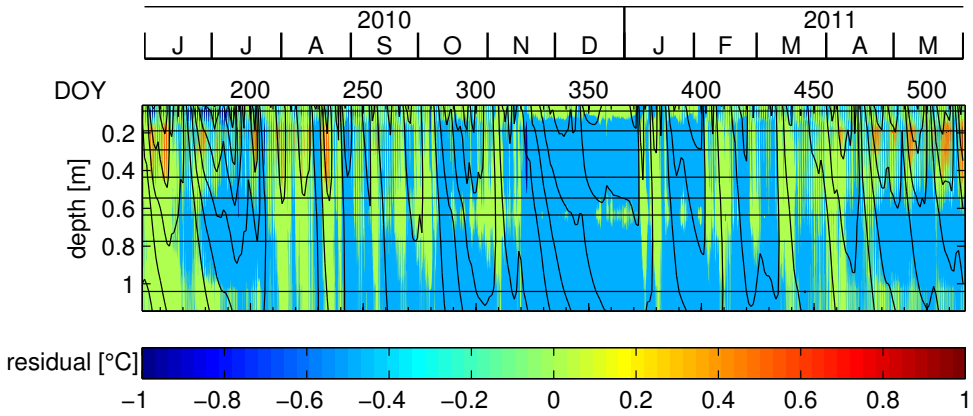

Figure 5.31: Residual (data-model) for soil temperature profile under grass assuming two layers in the heat diffusion model. The estimated diffusivities of both layers differ by a factor two.

For the wet season, the simulation before, assuming a homogeneous profile, fits already reasonable well the measured soil temperature profile, at least close to the surface (Fig. 5.30(b)). Therefore, considering thermal layers should mainly improve the model results during the dry months, when the upper part of the soil profile under grass is rather dry. The residual using the data of summer 2010 and spring 2011 in the optimization is shown in Figure 5.31. As expected, the estimated thermal diffusivities between the two layers vary considerable. For the upper 10 cm, the main root zone of grass, the estimation yields a D_h of $0.53 \times 10^{-6}\,\mathrm{m}^2/\mathrm{s}$. Meanwhile, a value of $1.0 \times 10^{-6}\,\mathrm{m}^2/\mathrm{s}$ is estimated for the lower soil profile. The overall residual during June and July as well as March to May, improved not significantly. However, this calculation reveals a further characteristic, which was hidden or covered by the overall misfit before. Between the considered root zone and the first textural boundary at 30 cm, the model occasionally underestimates actual soil temperatures, while an overestimation is more dominant below. Due to textural differences, this correlates with the water content distribution in the profile.

Again, almost all deviations between model and data were in the order of the sensor's accuracy, independent of the usage of weights or the consideration of thermal layers. Yet, extending step-by-step the model's complexity completes our system understanding more and more. In particular, the weighted regression revealed additional system properties such as thermal layers in the soil profiles. However, knowledge about the analytic solution of the heat diffusion equation was a prerequisite to implement the weights appropriately. Altogether, the interplay between analytic and numerical model and the stepwise extension of the model structure turned out to provide a deeper understanding of the system's characteristics not only for this field experiment, but already for the laboratory experiments discussed in the chapter before.

6 Summary and Outlook

This work consists of three parts: (i) the first one, develop a method to reconstruct the surface temperature from measured soil temperature profiles, (ii) the second constitutes laboratory experiments to verify the method and investigate the soil-air interaction under controlled conditions, and (iii) the third one describes a field experiment with different types of surface cover to extract their impact and to analyze the applicability and limitations of simplified model assumptions under natural conditions.

The information directly at the soil surface is of specific importance for the understanding of the coupling processes between soil and atmosphere. Surface processes influence considerably the temperatures in both compartments close to the ground surface. We analyzed temperature profiles within the soil, the atmosphere and directly at the soil surface. In general, we proceeded from simple model assumptions to study systems with increasing complexity. This step-by-step procedure unveiled additional processes necessary for an extended system conception. Finally, this led to a well-founded and deeper understanding of the soil-atmosphere coupling.

The following paragraphs summarize the major results of the main parts of this thesis and point out conclusions and implications for the larger research context.

Surface Temperature Reconstruction

So far, the analytic solution of the heat diffusion equation for periodic surface forcing (Eq. (3.3)) has always been fitted directly to measured soil temperature time-series, e. g. *Horton et al.* (1983), *Passerat de Silans et al.* (1996), resulting in a bias in the estimated thermal diffusivity which scales the amplitude damping and phase shift with depth. Since this signal modulation is frequency dependent, the new approach of this study analyzes soil temperature profiles in Fourier space and estimates the thermal diffusivity from the spectral information and hence considers the contribution of each frequency component comprised in the signal separately.
Amplitude and phase information of at least two depths allow to reconstruct the original surface temperature. Projecting the diffusion process back in time or space is a well-known, mathematically ill-posed problem, e. g. *Skaggs and Kabala* (1994). It can be solved through a weighted linear regression on the relative signal modulation between two depths. This yields an extrapolation of the frequency components towards the surface. Finally, all components above a presumed noise level are transformed back to time domain. Through this procedure, a stable and reliable reconstruction of the temperature signal at the soil surface is yielded.

Thermal layers in the profile result in a decoupling of the phase and amplitude relation approaching the layer boundary. The changing thermal properties are reflected in a change of the amplitude scaling and the ratio of the phase shift. Yet, this cannot be considered within this projection approach. For a thermal characterization of one soil layer, at least time-series at two depths are required within the linear regression. In case of thermal soil layers, a distinct projection kernel would be needed which includes this type of heterogeneity and would be based on further extended analytical solutions (*Lettau*, 1954). This is also a crucial point for projections in the opposite direction, from the surface deeper into the ground.

For synthetic data, we recognized limitations for finite, and not strictly periodic time-series which are already inherent in the Fourier method. These emerge in particular for different temperatures in the beginning and the end of the data interval and in a linear trend comprised in the temperature signals which cannot be represented by Fourier series. Therefore, the method is most efficient and reliable for long time-series and periodic signals due to characteristics of the underlying Fourier method. Sharp changes, jumps or other discontinuities will result in a biased frequency spectrum and a projection kernel with a distinct type of basis function would be required to allow for a more localized signal analysis. Possible starting points in this direction are the transfer function approach proposed by *Jury and Roth* (1990) or wavelets.

Altogether, the proposed Fourier approach allows a stable back-projection of the heat diffusion in soils within a homogeneous soil layer. The surface temperature information can be reconstructed from time-series of soil temperature profiles of at least two measurement depths, if the characteristics of the corresponding temperature signals can be represented by a Fourier series. In parallel, the thermal diffusivity of the underlying soil is estimated.

Heat Transport at the Laboratory Scale

Laboratory heat conduction and evaporation experiments were performed in a sand column under controlled conditions in a climate chamber. The proposed method to reconstruct the surface temperature from time-series of soil temperature profiles was validated for both types of experiments. All necessary information about the surface temperature could be extracted from the measured soil temperatures to get a reconstruction that fits the measurements within the accuracy of the temperature sensors, for the non-conductive evaporation process at the surface likewise.
Non-ideal experimental representations of the model assumptions needed restrictions on the data basis from the profile measurements. The presence of a mean net heat flux, e. g. due to evaporation at the soil surface is reflected by differences in the mean temperature level at each depth. Assuming that the mean soil system is stationary and hence the corresponding temperature gradient constant, its extrapolation towards the surface balances the systematic shift between measurement and reconstruction.

In general, systematic deviations between simplified model assumptions in 1D and

measured temperature profiles showed the two-dimensional character of the processes influencing the laboratory data-set. This was not only the case for the projection method, but could also be observed in numerical forward simulations with a pure heat conduction module.
Therefore, we concluded that the insulation around the soil column does not completely prevent lateral heat entries and that their influence is particularly high approaching the temperature-stabilized bottom of the soil column. Numerical heat conduction simulations were conducted in 2D to validate the qualitative structure of the deviations for a one- and two-dimensional representation of the system. However, measurements were only conducted in a vertical profile in the soil and hence the data basis is not sufficient to run an inversion explicitly based on the 2D model.

Finally, the laboratory investigations verified our process understanding about heat transfer in soils and about the soil-atmosphere coupling at the surface in the presence of evaporation. Since surface heat fluxes and the energy sink due to the evaporation of water influence the temperatures in the system, their "thermal signature" could be decoded and furthermore, the water and energy fluxes at the surface were quantified. Yet, the system's state at the surface depends crucially on the thermal and hydraulic properties of both compartments and the adaptation of the respective parameters is highly sensitive. An automatic optimization procedure was therefore not able to succeed. In particular, the water vapor pressure in air deduced from relative humidity measurements turned out to be too inaccurate and hence the estimated parameters were not unique within the accuracy of the measurements.

Coupling of the Water and Energy Fluxes at the Field Scale

Two soil profiles were instrumented with soil temperature and water content sensors positioned at various depths, one under a bare surface and one under grass. Due to similar textural layering, the definite influence of plants could be extracted from the profile measurements. During the wet seasons, autumn and winter, both profiles exhibited similar water contents. Yet, in spring and summer, the soil profile under grass was much drier due to root water uptake and transpiration compared to that under the bare surface. In addition, this surface seemed to build a dry crust during warm and dry periods which acted as a capillary barrier at the top of the soil profile and prevents soil water to evaporate further.

The evolution of the soil temperature profiles is also influenced by the surface cover. The grass leaves act as an additional insulation layer which shields the respective soil profile. Hence, soil temperature amplitudes under the bare surface were larger during the year. Furthermore, convective heat transport was observed during and as a consequence of rain events, if water contents were high in the upper part of the soil profile.

The interaction between soil and atmosphere was further investigated for both profiles by analyzing four distinct rain events from different seasons during the year. Soil temperature and water content profiles under both surface covers showed a distinct behavior,

in particular during times when the grass was active. Furthermore, an analysis on a daily mean basis yielded that the main thermal and hydraulic surface processes can be traced in the ground. The daily means of atmospheric quantities, however, exhibited only seasonal trends, since their memory is shorter due to lower capacities and the turbulent nature of the transport processes.

Again, deviations between simplified model assumptions and measured data gave a deeper insight in the type of neglected processes. In the field, the thermal properties vary in space and time because of the seasonal water dynamics and different textural layers in the natural soil profiles. Neglecting these effects led to deviations up to 1 °C between measured and simulated soil temperatures.

The surface temperature projection under field conditions displayed thermal layers in both profiles, especially for the root zone under grass. Comparing the reconstructed with the infrared measured surface temperatures, a decoupling of the measurements above the surface and the underlying soil profile was observed. For the bare soil, the projection deviated systematically from the measured value which hints not only at a dry crust covering the profile during dry periods, but an apparently decoupled surface layer throughout the whole year. On top of the grass, mainly the leaf temperature is measured by the thermal infrared sensor. In spring, systematic deviations were also observed which indicate distinct thermal properties for the boundary layer between the soil itself and the lower atmosphere. However, under well-watered conditions in autumn and winter, the residual of the projection revealed a specific offset which points to a bias in the measured temperatures due to the unknown, actual emissivity of the soil surface.
Altogether, surface temperatures measured from above the soil and reconstructed from measurements within the soil seem to be decoupled due to a boundary layer with distinct thermal properties for both surface covers. However, they could not be determined by the experimental set-up used in this work.

Implications and Outlook

In general, potential and limitations of first order model assumptions in the context of the soil-atmosphere coupling were studied to describe the water and energy fluxes at and close to the soil surface. We developed a method to project back the diffusive heat transport in soils which yields an effective thermal characterization of the investigated soil profile and a reconstruction of the soil surface temperature. This information can be used to calculate the ground heat flux and can contribute to the closure of the surface energy balance. Furthermore, we found that the reconstruction of the surface temperature from within the soil seems, under field conditions and independent of the surface cover, to be decoupled from the infrared temperatures measured from above the soil surface.
This raises the question how to link observations from one compartment to the other. Our findings suggest a boundary layer with specific material properties. A similar layer was already proposed by *Schneider-Zapp et al.* (2010) for laboratory evaporation experiments. For the laboratory experiments in this work, this was not necessary for their quantitative description, since an effective description of the water and energy fluxes at the soil sur-

face could be found that fitted the measurements and did not necessitate to distinguish this layer at top of the soil profile. However, the more complicated surface interaction under field conditions revealed that this layer is crucial and furthermore has considerably different thermal properties. Thus, an adequate conception of the soil-atmosphere system might need to represent it explicitly.
With respect to this finding, we do furthermore not expect that remote surface temperature observations, e. g. from satellites, can be easily linked to the sub-surface thermal regime of the soil without further specification of this linking layer. *Vereecken et al.* (2008) already presumed this for the hydraulic regime and in addition it is consistent with the findings of, e. g. *Walker et al.* (2002) and *de Lannoy et al.* (2007), for the retrieval of soil moisture profiles from remotely measured surface soil moisture.

From an operational perspective, this project highlights the potential of temperature profile measurements. They are particularly valuable close to the surface where information about the surface energy fluxes can be extracted from temperature measurements. With the experimental set-up of this work, further analysis is restricted by the spatial and temporal resolution of the measurements and the unknown emissivity of the different surface covers. Therefore, I consider it worthwhile to extend the experiments, so that, especially close to the surface, the exchange processes can be better traced within temperature data.
In addition, the actual measurements cannot resolve the thermal properties of the boundary layer at the soil surface. Therefore, one approach might be to increase the resolution of the measurements, yet another could make use of the reconstructed information from within the soil. Relying finally on both, the correctly measured and the reconstructed surface temperatures, yields the possibility to invert for the thermal properties of the boundary layer assuming that it is homogeneous and therefore that the heat transfer can be described as an effective diffusion process.

From a modeling perspective, the experimental set-up suggests to use a coupled water and energy transport model to describe the corresponding surface exchange processes. So far, most of these models consider one of the compartments, soil or atmosphere, e. g. *Saito et al.* (2006) or *Bittelli et al.* (2008). The challenge is to approximate the coupling towards the other. Yet, we found the surface boundary to be crucial. This highlights the need of coupled soil-atmosphere models, with a resolution according to the underlying data basis to calculate the involved processes on adequate scales.
Altogether, the challenge from a modeling perspective is to parameterize the process model in an appropriate way and, from an operational point of view, to adapt the experimental set-up in a way that the data basis allows a reliable characterization of the system.

The water content profiles measured in the field have been neglected during the quantitative analysis so far. Performing an optimization of the hydraulic parameters from the water dynamics in the profile would allow further flux calculations in the system. Compared to the study of *Wollschläger et al.* (2009) who utilized one water content sensor per layer, several TDR probes measure water contents in each layer of the profiles analyzed in this work. Thus, the results could prove to be more reliable and would be a first step

to parameterize the hydraulic regime. We would use this information as a starting point to parameterize the above mentioned fully coupled models.
Yet, the critical point remains the representation of the water flux at the upper boundary. It highlights the importance of an adequate representation of the surface coupling. Consecutive analysis could then investigate the uniqueness or equifinality of the hydraulic parameters. In addition, further details about the coupling processes at the soil surface can be inferred on the basis of the pre-estimated thermal and hydraulic properties of the soil by analyzing the consistency of the surface flux estimates from both regimes.

Finally, the time- and space dependency of the thermal parameters suggests a complementary direction for further analysis. For the simplified models used in a first step, the capability of data assimilation schemes can be analyzed to adapt these imperfect system representations to the measured soil temperature profile. This is a complementary option to gradually extending the model. Hence, the simple underlying model conception would be retained, yet used in a framework, that handles the related uncertainties. For example, direct insertion or a Kalman filter trace the model along the data-set with the help of selective measurement information and hence these approaches would account for the model's incompleteness.

Appendix

A Theoretical Completions

A.1 Heat Conduction Equation in Cylindrical Coordinates

Following *Carslaw and Jaeger* (1959), the heat conduction equation (2.19) can be expressed in cylindrical coordinates

$$x = r \cdot \cos\phi \,, \tag{A.1}$$
$$y = r \cdot \sin\phi \,, \tag{A.2}$$
$$z = z \,, \tag{A.3}$$

as

$$C_\mathrm{h} \frac{\partial T}{\partial t} = \frac{1}{r} \frac{\partial}{\partial r} \left(K_\mathrm{h} r \frac{\partial T}{\partial r} \right) + \frac{1}{r^2} \frac{\partial}{\partial \phi} \left(K_\mathrm{h} \frac{\partial T}{\partial \phi} \right) + \frac{\partial}{\partial z} \left(K_\mathrm{h} \frac{\partial T}{\partial z} \right) \tag{A.4}$$

with the heat capacity C_h and the heat conductivity K_h.

For rotational symmetry, meaning no dependence on the angle, this can be further simplified as

$$C_\mathrm{h} \frac{\partial T}{\partial t} = \frac{1}{r} \frac{\partial}{\partial r} \left(K_\mathrm{h} r \frac{\partial T}{\partial r} \right) + \frac{\partial}{\partial z} \left(K_\mathrm{h} \frac{\partial T}{\partial z} \right) \,. \tag{A.5}$$

A.2 Derivation of the Penman-Monteith Equation

Extending *Snyder and Paw U* (2002), a derivation of the Penman-Monteith equation (2.48) will be given in the following to highlight the underlying assumptions which determine limitations of its applicability.

Flux-Gradient Derivation

Starting point is the latent heat flux

$$\lambda E_0 = \frac{\rho_\mathrm{a} c_\mathrm{p,a}}{r_\mathrm{E}} \frac{e_0(T_0) - e_\mathrm{a}}{\gamma} \tag{A.6}$$

with the air density ρ_a, the specific heat capacity of air $c_\mathrm{p,a}$, the aerodynamic resistance for vapor transport r_E, and the water vapor pressure e_a [kPa] in air. γ [kPa/°C] is the *psychrometric constant* that relates the water vapor pressure in air to the air temperature. $e_0(T_0)$ [kPa] denotes the saturated water vapor pressure at the soil surface which depends on the surface temperater T_0 [°C] and is given by the Magnus' formula (Eq. (2.23)). At this point, the soil surface is assumed to be saturated and not the actual water vapor

pressure at the soil surface is considered.

The sensible heat flux is given by

$$H = -\frac{\rho_{\mathrm{a}} c_{\mathrm{p,a}}}{r_{\mathrm{H}}}(T_{\mathrm{a}} - T_0) \tag{A.7}$$

with the aerodynamic resistance for sensible heat transfer r_{H} and the air and soil surface temperature T_{a} and T_0, respectively.

To deduce the Penman-Monteith equation (2.48), we make use of the relation between the transport parameters r_{E} and r_{H}

$$\gamma^* = \gamma \frac{r_{\mathrm{E}}}{r_{\mathrm{H}}} \; . \tag{A.8}$$

This yields

$$\lambda E_0 = \frac{\rho_{\mathrm{a}} c_{\mathrm{p,a}}}{r_{\mathrm{H}}} \frac{e_0(T_0) - e_{\mathrm{a}}}{\gamma^*} \; . \tag{A.9}$$

However, we do not know the surface temperature T_0, but the air temperature T_{a}. Therefore, assuming the soil surface to be water saturated, the surface temperature can be approximated by the *wet bulb temperature* T_{w}. This denotes the minimum temperature that can be achieved by pure evaporative cooling of a water-wetted surface. In addition, the slope Δ of the saturated water vapor pressure curve (Eq. (2.23)) can be approximated in first-order around the air temperature by

$$\Delta \approx \frac{e_0(T_{\mathrm{a}}) - e_0(T_{\mathrm{w}})}{T_{\mathrm{a}} - T_{\mathrm{w}}} \; . \tag{A.10}$$

With $T_0 \approx T_{\mathrm{w}}$, this yields

$$e_0(T_0) = e_0(T_{\mathrm{a}}) - \Delta(T_{\mathrm{a}} - T_0) \tag{A.11}$$

and $e_0(T_0)$ can be substituted in equation (A.9)

$$\lambda E_0 = \left[\frac{\rho_{\mathrm{a}} c_{\mathrm{p,a}}}{\gamma^* r_{\mathrm{H}}}\right] \left[e_0(T_{\mathrm{a}}) - \Delta(T_{\mathrm{a}} - T_0) - e_{\mathrm{a}}\right] \; . \tag{A.12}$$

Rearranging equation (A.7), we can express the temperature difference $T_{\mathrm{a}} - T_0$ by

$$T_{\mathrm{a}} - T_0 = \frac{-H r_{\mathrm{H}}}{\rho_{\mathrm{a}} c_{\mathrm{p,a}}} \; . \tag{A.13}$$

Substituting this in equation (A.12) leads to

$$\lambda E_0 = \left[\frac{\rho_{\mathrm{a}} c_{\mathrm{p,a}}}{\gamma^* r_{\mathrm{H}}}\right] \left[e_0(T_{\mathrm{a}}) - \Delta \frac{-H r_{\mathrm{H}}}{\rho_{\mathrm{a}} c_{\mathrm{p,a}}} - e_{\mathrm{a}}\right] \; , \tag{A.14}$$

which can further be simplified as

$$\lambda E_0 = \left[\frac{\rho_{\mathrm{a}} c_{\mathrm{p,a}}}{\gamma^* r_{\mathrm{H}}}\right] \left[e_0(T_{\mathrm{a}}) - e_{\mathrm{a}}\right] + \frac{\Delta}{\gamma^*} H \; . \tag{A.15}$$

For a non-adiabatic process, the sensible heat flux can be expressed by $H = Q_\mathrm{n} - \lambda E$ with the net external energy flux Q_n. For a plant canopy, this external energy source is given by $Q_\mathrm{n} = R_\mathrm{n} - G$ and from this, we get

$$\lambda E_0 = \left[\frac{\rho_\mathrm{a} c_\mathrm{p,a}}{\gamma^* r_\mathrm{H}}\right] [e_0(T_\mathrm{a}) - e_\mathrm{a}] + \frac{\Delta}{\gamma^*}(Q_\mathrm{n} - \lambda E) \; . \tag{A.16}$$

Separating λE on one side yields

$$\left[1 + \frac{\Delta}{\gamma^*}\right] \lambda E_0 = \left[\frac{\rho_\mathrm{a} c_\mathrm{p,a}}{\gamma^* r_\mathrm{H}}\right] [e_0(T_\mathrm{a}) - e_\mathrm{a}] + \frac{\Delta}{\gamma^*} Q_\mathrm{n} \; . \tag{A.17}$$

Using

$$\left[1 + \frac{\Delta}{\gamma^*}\right] \lambda E_0 = \left[\frac{\gamma^* + \Delta}{\gamma^*}\right] \lambda E_0 \; , \tag{A.18}$$

we end up with

$$\lambda E_0 = \frac{\Delta Q_\mathrm{n} + \rho_\mathrm{a} c_\mathrm{p,a} \, [e_0(T_\mathrm{a}) - e_\mathrm{a}] \, r_\mathrm{H}^{-1}}{\Delta + \gamma^*} \tag{A.19}$$

which corresponds to the Penman-Monteith equation (2.48).

B Completion of Field Data-Set

To complete the data-set from the field experiments, the measurements not discussed in section 5 are presented below.

Soil Temperature Profiles under Grass

The soil temperature profiles under grass are shown as contours in Figure B.1. Due to technical failures of the deepest sensors, the profile is 20 cm less deep compared to that under the bare surface. Furthermore, the temperature amplitudes are smaller, since the grass on top shields the underlying soil profile in summer and in winter.

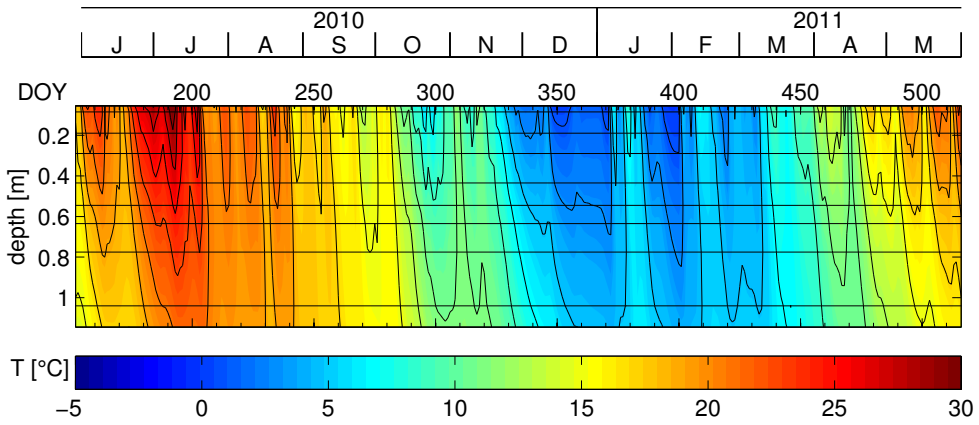

Figure B.1: Time series of soil temperatures under bare surface. *Horizontal black lines* indicate sensor positions. *Contour lines* are plotted in 2 °C intervals. Rain events results in sharp temperature changes due to convective heat transport.

To get a more detailed insight on the temperature variations and the frequencies comprised in the temperature signal, the soil temperatures under grass are additionally illustrated in a line plot in Figure B.2.

Soil Water Content Data under Grass

The water contents under the grass surface are shown in Figure B.3. They correspond to the contours (Fig. 5.10) discussed in section 5.2.2. During summer the upper two soil layers under the grass surface are dried out due to root water uptake and transpiration by the plants. Hence, the bare soil is wetter, although the net energy entry at the soil surface is larger.

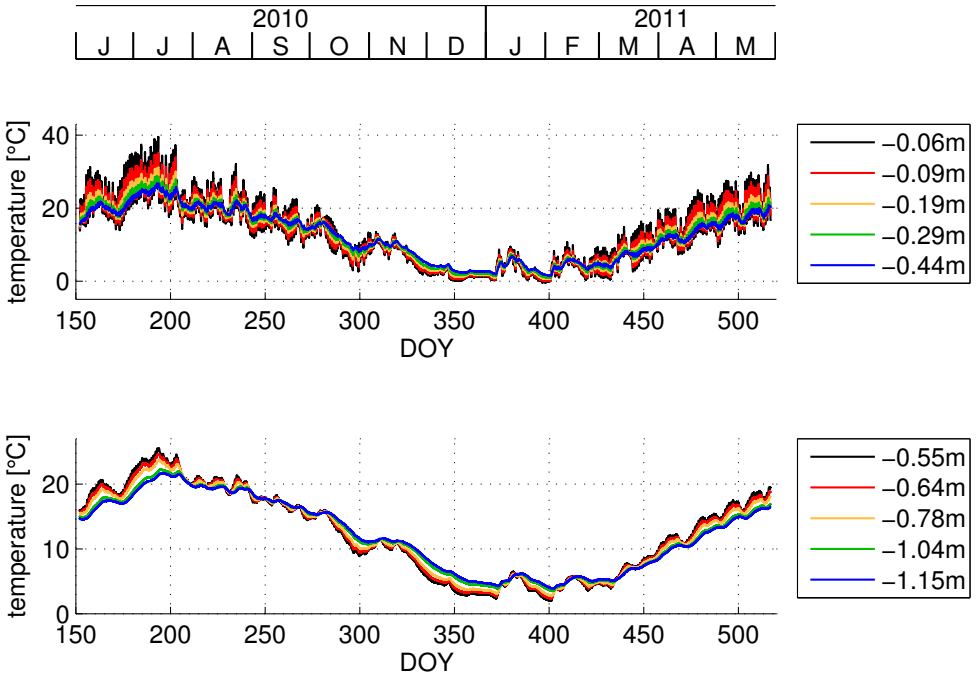

Figure B.2: Field measured soil temperatures of one year under grass cover. In the line plot, the high frequency fluctuations and their stronger damping close to the surface become obvious.

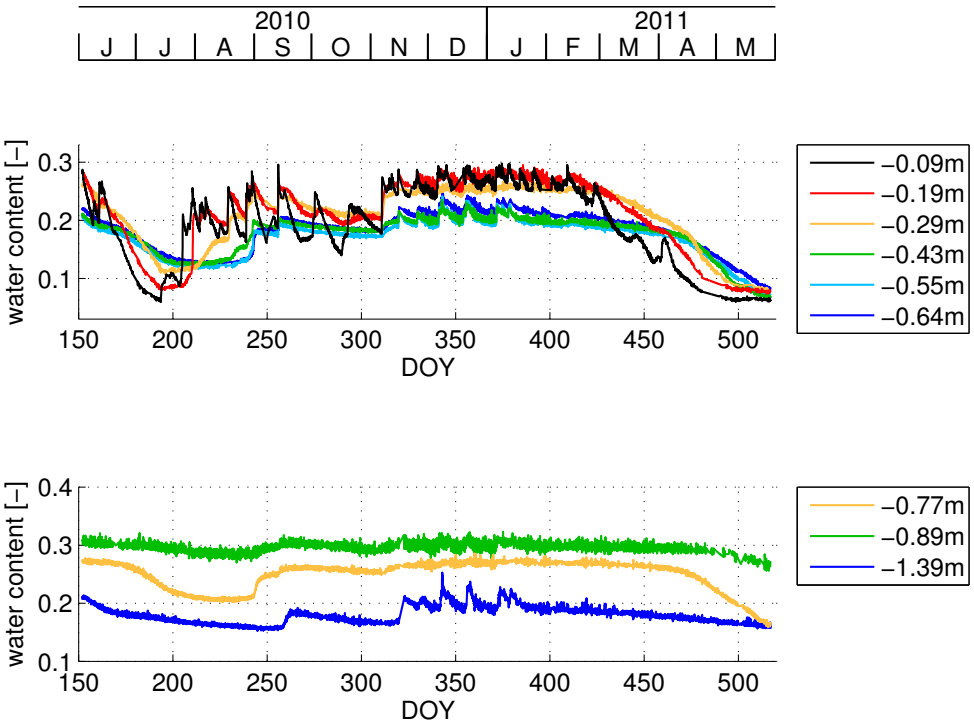

Figure B.3: Water contents under grass corresponding to the contours in Figure 5.10. During spring and summer, the drying due to root water uptake and transpiration is detected even by the lowest sensors.

C Acknowledgements

In the last years, many people contributed to realize this research project and I would like to thank the most important ones in the following:

This work was founded by the Helmholtz Gemeinschaft within the project JICG42 “Inverse Modelling of Terrestrial Systems”.

I would like to express my sincere thanks to Prof. Kurt Roth who gave me the opportunity to work on this project and left me a large degree of freedom designing its final direction and details. Thanks a lot for all inspiring discussions - about and besides science. These years included a wide spectrum of challenges which made them an enriching experience beyond science likewise.

Thanks to Prof. Hans-Georg Bock and the HGS MathComp which were an exciting environment to gain insights in the field of optimization and parameter estimation.

In the context of field work, I benefited from the huge experience and knowledge of Dr. Ute Wollschläger. Thanks for your patient introducing me to the practical side of soil physics and lifting my theoretical knowledge to the field-scale.

During both, the daily work in the lab and at the field site, the help of Angelika Gassama was irreplaceable. Thanks for your steady and reliable commitment - collecting data, mowing grass, picking the bare surface that it deserves this name, ... But furthermore, for all the encouraging chats and finally just being a friend - no matter if things worked out or didn’t - in the institute and beyond.

Most of the laboratory work was done together with Paul Bergmann and Florian Ehrmann. Without the two of you, the climate chamber would have been much more trite, but instead it finally was a lot of fun building and conducting experiments, grumbling at computers, and just laughing a lot.

Thanks to all the proof-readers of parts of this thesis: Ute, Jens, Steffen, Patrick, Ulrike, Miri, Edel. It improved a lot through your challenging questions and valuable comments!

Finally thanks to all Bophys and IUPler which made this time such a pleasure: Steffen, Jens B. Cornelius, Ute, Ulrike, Felix H. , Patrick, Pan, Philipp, Klaus, Paul, Florian, Anne, Hannes, Jens T. , Michi, Claudi, Pascal, Felix V. ... Thanks for relaxing and inspiring chats and coffee breaks that made me enjoy the work at this institute even more!

Last, but not least: thanks to my family who shared all ups and downs. Who invested time and energy to keep me on the track, helped me to overcome all crisis, the smaller and the larger ones, and had imperturbable faith in me.
In particular, I would like to thank Werner, my husband, who encouraged me unremittingly and was optimistic no matter how I felt. You have a large share on this work and one of the two letters is yours!

D Bibliography

Allen, R. G., L. S. Pereira, D. Raes, and M. Smith: *FAO Irrigation and Drainage Paper No. 56: Crop Evapotranspiration*, FAO Water Resources Development and Management Service, 2006.

Bauser, H.: Messung von Struktur und Dynamic der Oberflächentemperaturen eines Testfeldes, Bachelor thesis, Heidelberg University, 2011.

Bergmann, P.: Aufbau und Durchführung eines Experiments zur Untersuchung der Verdunstung aus Böden, Staatsexamensarbeit, Heidelberg University, 2010.

Bittelli, M., F. Ventura, G. S. Campbell, R. L. Snyder, F. Gallegati, and P. Rossi Pisa: Coupling of heat, water vapor, and liquid water fluxes to compute evaporation in bare soils, *Journal of Hydrology* **362**, 191–205, 2008.

Boike, J., K. Roth, and O. Ippisch: Seasonal snow cover on frozen ground: Energy balance calculations of a permafrost site near Ny-Alesund, Spitsbergen, *Journal of Geophysical Research* **108**, 2003.

Boll, M.: Tau- und Gefrierprozesse in Permafrostböden, Diploma thesis, Heidelberg University, 2009.

Brooks, R. H., and A. T. Corey: Properties of porous media affecting fluid flow, *Journal of Irrigation and Drainage Division, Proc. Am. Soc Civil Eng. (IR2)* **92**, 61–88, 1966.

Buck, A. L.: New Equations for Computing Vapor Pressure and Enhancement Factor, *Journal of Applied Meteorology* **20**, 1527–1532, 1981.

Burykin, A. A., and A. M. Denisov: Determination of the unknown sources in the heat-conduction equation, *Computational Mathematics and Modeling* **8**, 309–313, 1997.

Camillo, P. J., R. J. Gurney, and T. Schmugge: A Soil and Atmospheric Boundary Layer Model for Evaporation and Soil Moisture Studies, *Water Resources Research* **19**, 371–380, 1983.

Campbell, G. S., and J. M. Norman: *An introduction to environmental biophysics*, 2nd ed., Springer, New York, 1998.

Cannon, J. R., and S. P. Esteva: An inverse problem for the heat equation, *Inverse Problems* **2**, 395–403, 1986.

Carslaw, H. S., and J. C. Jaeger: *Conduction of Heat in Solids*, Oxford Science Publications, 1959.

COMSOL: Multiphysics, Version 3.5a, Finite element modeling and simulation software, http://www.comsol.de, 2008.

Crank, J.: *The Mathematics of Diffusion*, Oxford Science Publications, 1975.

Dahl-Jensen, D., K. Mosegaard, N. Gundestrup, G. D. Clow, J. S. Johnsen, A. W. Hansen, and N. Balling: Past Temperatures Directly from Greenland Ice Sheet, *Science* **282**, 268–271, 1998.

de Lannoy, G. J. M., P. R. Houser, V. R. N. Pauwels, and N. E. C. Verhoest: State and bias estimation for soil moisture profiles by an ensemble Kalman filter: Effect of assimilation depth and frequency, *Water Resources Research* **43**, 2007.

de Vries, J. J., and I. Simmers: Groundwater recharge: an overview of processes and challenges, *Hydrogeology Journal* **10**, 5–17, 2002.

Ehrmann, F.: Experimentelle Untersuchung des Zusammenhangs zwischen Bodenoberflächentemperatur und Verdunstung, Staatsexamensarbeit, Heidelberg University, 2011.

Entekhabi, D., H. Nakamura, and E. G. Njoku: Solving the inverse problem for soil moisture and temperature profiles by sequential assimilation of multifrequency remotely sensed observations, *IEEE Trans Geoscience Remote Sensing* **32**, 438–448, 1994.

Foken, T.: 50 years of Monin-Obukhov similarity theory, *Boundary-Layer Meteorology* **119**, 431–447, 2006.

Foken, T.: *Micrometeorology*, Springer Verlag, 2008.

Francois, C.: The potential of directional radiometric temperatures for monitoring soil and leaf temperature and soil moisture status, *Remote Sensing of Environment* **80**, 122–133, 2002.

Franks, S. W., K. J. Beven, P. F. Quinn, and I. R. Wright: On the sensitivity of soil-vegetation-atmosphere transfer (SVAT) schemes: equifinality and the problem of robust calibration, *Agricultural and Forest Meteorology* **86**, 63–75, 1997.

Gardner, W. R., and F. J. Miklich: Unsaturated Conductivity and Diffusivity Measurements by a Constant Flux Method, *Soil Science* **93**, 271–274, 1962.

Geiger, R., R. H. Aron, and P. Todhunter: *The climate near the ground*, Friedr. Vieweg & Sohn Verlagsges. mbH, Braunschweig, Wiesbaden, 1995.

Gergely, M.: Dynamics of a Salty Permafrost, Diploma thesis, Heidelberg University, 2007.

Hadamard, J.: Sur les problèmes aux dérivées partielles et leur signification physique, *Princeton University Bulletin* pp. 49–52, 1902.

Hellstrom, J.: U-Th dating of speleothems with high initial 230Th using stratigraphical constraint, *Quaternary Geochronology* **1**, 289–295, 2006.

Horton, R., and P. J. Wierenga: Estimating the Soil Heat Flux from Observations of Soil Temperature near the Surface, *Soil Science Society of America Journal* **47**, 14–20, 1983.

Horton, R., W. P. J., and D. R. Nielsen: Evaluation of Methods for Determining the Apparent Thermal Diffusivity of Soil Near the Surface, *Soil Science Society of America Journal* **47**, 25–32, 1983.

IPCC: Le Treut, H., R. Somerville, U. Cubasch, Y. Ding, C. Mauritzen, A. Mokssit, T. Peterson, and M. Prather: *Historical Overview of Climate Change. In: Climate Change 2007: The Physical Science Basis. Contribution of Working Group I to the Fourth Assessment Report of the Intergovernmental Panel on Climate Change*, Cambrigde University Press, United Kingdom and New York, NY, USA, 2007.

Jimenez, C., et al.: Global intercomparison of 12 land surface heat flux estimates, *Journal of Geophysical Research* **116**, 2011.

Jury, W. A., and K. Roth: *Transfer Functions and Solute Movement Through Soil*, Birkhauser Verlag, Boston, Mass., 1990.

Kalman, R. E.: A new approach to linear filtering and prediction problems, *Transactions of the ASME - Journal of Basic Engineering* **82**, 35–45, 1960.

Katul, G. G., and M. B. Parlange: Estimation of bare soil evaporation using skin temperature measurements, *Journal of Hydrology* **132**, 91–106, 1992.

Lehmann, P., and D. Or: Evaporation and capillary coupling across vertical textural contrasts in porous media, *Physical Review E* **80**, 2009.

Lehmann, P., S. Assouline, and D. Or: Characteristic lengths affecting evaporative drying of porous media, *Physical Review E* **77**, 2008.

Lettau, H. H.: Improved Models of Diffusion in the Soil, *Trans. American Geophysical Union* **35**, 121–132, 1954.

Liebethal, C., and T. Foken: Evaluation of six parameterization approaches for the ground heat flux, *Theoretical and Applied Climatology* **88**, 43–56, 2007.

Ling, L., M. Yamamoto, Y. C. Hon, and T. Takeuchi: Identification of source locations in two-dimensional heat equations, *Inverse Problems* **22**, 1289–1305, 2006.

Lowry, C. S., J. F. Walker, H. J. Randall, and M. P. Anderson: Identifiying spatial variability of groundwater discharge in a wetland stream using a distributed temperature sensor, *Water Resources Research* **43**, 2007.

Ludin, A. R.: Permafrost Temperature Analysis and Projection from Samoylov Island in the Lena River Delta, Siberia, Diploma thesis, Heidelberg University, 2010.

Lüers, J., and J. Bareiss: The effect of misleading surface temperature estimations on the sensible heat fluxes at a high Arctic site - the Arctic Turbulence Experiment 2006 on Svalbard (ARKTEX-2006), *Atmospheric Chemistry and Physics* **10**, 157–168, 2010.

Marquardt, D. W.: An Algorithm for Least-Squares Estimation of Nonlinear Parameters, *Journal of the Society for Industrial and Applied Mathematics* **11**, 431–441, 1963.

Menzel, L.: *Modellierung der Evapotranspiration im System Boden-Pflanze-Atmosphäre*, vol. 67, Geographischen Institut ETH Zuerich, 1997.

Miralles, D. G., R. A. M. De Jeu, J. H. Gash, T. R. H. Holmes, and A. J. Dolman: Magnitude and variability of land evaporation and its components at the global scale, *Hydrology and Earth System Science* **15**, 967–981, 2011.

Monin, A. S., and A. M. Obukhov: Osnovnye zakonomernosti turbulentnogo peremesivanija v prizemnom sloe atmosfery (Basic laws of turbulent mixing in the atmosphere near the ground), *Trudy geofiz inst AN SSSR* **24**, 163–187, 1954.

Monteith, J. L.: Evaporation and surface temperature, *Quarterly Journal of the Royal Meteorological Society* **107**, 1–27, 1981.

Moran, M. S., A. F. Rahman, J. C. Washburne, D. C. Goodrich, M. A. Weltz, and W. P. Kustas: Combining the Penman-Monteith equation with measurements of surface temperature and reflectance to estimate evaporation rates of semiarid grassland, *Agricultural and Forest Meteorology* **80**, 87–109, 1996.

Mualem, Y.: A New model for Predicting the Hydraulic Conductivity of Unsaturated Porous Media, *Water Resources Research* **12**, 513–522, 1976.

Nassar, I. N., and R. Horton: Determination of the apparent thermal diffusivity of a nonuniform soil, *Soil Science* **147**, 238–244, 1989.

Nassar, I. N., and R. Horton: Determination of soil apparent thermal diffusivity from multiharmonic temperature analysis for nonuniform soil, *Soil Science* **149**, 125–130, 1990.

Niemela, J. J., L. Skrbek, K. R. Sreenivasan, and R. J. Donnelly: Turbulent convection at very high Rayleigh numbers, *Nature* **404**, 837–840, 2000.

Norman, J. M., W. P. Kustas, and K. S. Humes: Source approach for estimating soil and vegetation energy fluxes in observations of directional radiometric surface temperature, *Agricultural and Forest Meteorology* **77**, 263–293, 1995.

Passerat de Silans, A. M. B., B. A. Monteny, and J. P. Lhomme: Apparent soil thermal diffusivity, a case study: HAPEX-Sahel experiment, *Agricultural and Forest Meteorology* **81**, 201–216, 1996.

Pielke Sr., R. A., J. O. Adegoke, T. N. Chase, C. H. Marshall, T. Matsui, and D. Niyogi: A new paradigm for assessing the role of agriculture in the climate system and in climate change, *Agricultural and Forest Meteorology* **142**, 234–254, 2007.

Qian, A., and Y. Li: Optimal error bound and generalized Tikhonov regularization for identifying an unknown source in the heat equation, *Journal of Mathematical Chemistry* **49**, 765–775, 2011.

Qiu, G. Y., and M. Zhao: Remotely monitoring evaporation rate and soil water status using thermal imaging and "three-temperatures model (3T Model)" under field-scale conditions, *Journal of Environmental Monitoring* **12**, 716–723, 2010.

Qiu, G. Y., T. Yano, and K. Momii: An improved methodology to measure evaporation from bare soil based on comparison of surface temperature with a dry soil surface, *Journal of Hydrology* **210**, 93–105, 1998.

Richtmeyer, R. D., and K. W. Morton: *Difference methods for initial-value problems*, Interscience Publisher, New York, 1967.

Ritchie, J. T.: Model for predicting evaporation from a row crop with incomplete cover, *Water Resources Research* **8**, 1204–1213, 1972.

Roth, K.: *Soil Physics - Lecture Notes*, Institut of Environmental Physics, Heidelberg University, 2006.

Roth, K., and J. Boike: Quantifying the thermal dynamics of a permafrost site near Ny-Alesund, Svalbard, *Water Resources Research* **37**, 2901–2914, 2001.

Roth, K., R. Schulin, H. Flühler, and W. Attinger: Calibration of time domain reflectometry for water content measurement using a composite dielectric approach, *Water Resources Research* **26**, 2267–2273, 1990.

Saffman, P. G., and G. Taylor: The Penetration of a Fluid into a Porous Medium or Hele-Shaw Cell Containing a More Viscous Liquid, *Proceedings of the Royal Society A: Mathematical, Physical and Engineering Sciences* **245**, 312–329, 1958.

Saito, H., J. Simunek, and B. P. Mohanty: Numerical Analysis of Coupled Water, Vapor, and Heat Transport in the Vadose Zone, *Vadose Zone Journal* **5**, 784–800, 2006.

Schelde, K., A. Thomsen, T. Heidmann, P. Schjonning, and J. P.-E.: Diurnal fluctuations of water and heat flow in bare soil, *Water Resources Research* **34**, 2919–2929, 1998.

Schelle, H., S. C. Iden, and W. Durner: Hydraulic Properties in a Wide Pressure Head Range, *Soil Science Society of America Journal* **75**, 5, 2010.

Scherer, G. W.: Theory of Drying, *Journal of American Ceramic Society* **73**, 3–14, 1990.

Schneider, K., O. Ippisch, and K. Roth: Novel evaporation experiment to determine soil hydraulic properties, *Hydrology and Earth System Science* **10**, 817–827, 2006.

Schneider-Zapp, K., O. Ippisch, and K. Roth: Numerical study of the evaporation process and parameter estimation analysis of an evaporation experiment, *Hydrology and Earth System Science* **14**, 765–781, 2010.

Selker, J. S., et al.: Distributed fibre-optic temperature sensing for hydrologic systems, *Water Resources Research* **42**, W12,202, 2006.

Sepaskhah, A. R., and L. Boersma: Thermal conductivity of soils as a function of temperature and water content, *Soil Science Society of America Journal* **43**, 439–444, 1979.

Shahraeeni, E., and D. Or: Thermo-evaporative fluxes from heterogeneous porous surfaces resolved by infrared thermography, *Water Resources Research* **46**, 2010.

Shokri, N., P. Lehmann, and D. Or: Evaporation from layered porous media, *Journal of Geophysical Research* **115**, 2010.

Skaggs, T. H., and Z. J. Kabala: Recovering the history of a groundwater contaminant, *Water Resources Research* **30**, 71–79, 1994.

Skaggs, T. H., and Z. J. Kabala: Limitations in recovering the history of a groundwater contaminant plume, *Journal of Contaminant Hydrology* **33**, 347–359, 1998.

Snodgrass, M. F., and P. K. Kitanidis: A geostatistical approach to contaminant source identification, *Water Resources Research* **33**, 537–546, 1997.

Sorooshian, S., J. Li, K.-I. Hsu, and X. Gao: How significant is the impact of irrigation on the local hydroclimate in California's Central Valley? Comparison of model results with ground and remote-sensing data, *Journal of Geophysical Research* **116**, D06,102, 2011.

Tabil, L. G., M. V. Eliason, and H. Qi: Thermal Properties of Sugarbeet Roots, *Journal of Sugar Beet Research* **40**, 209–228, 2003.

Tikhonov, A. N., and V. Y. Arsenin: *Solution of Ill-Posed Problems*, Winston and Sons, New York, 1977.

van Dam, J. C., J. N. M. Stricker, and P. Droogers: Inverse method to determine soil hydraulic functions from multistep outflow experiments, *Soil Science Society of America Journal* **38**, 647–652, 1994.

van Genuchten, M. T.: A Closed-form Equation for Predicting the Hydraulic Conductivity of Unsaturated Soils, *Soil Science Society of America Journal* **44**, 892–898, 1980.

Vereecken, H., J. A. Huisman, H. Bogena, J. Vanderborght, J. A. Vrugt, and J. W. Hopmans: On the value of soil moisture measurements in vadose zone hydrology: A review, *Water Resources Research* **44**, 2008.

Walker, J. P., G. R. Willgoose, and J. D. Kalman: One-dimensional soil moisture retrieval by assimilation of near-surface observations: a comparison of retrieval algorithms, *Water Resources Research* **24**, 631–650, 2001.

Walker, J. P., G. R. Willgoose, and J. D. Kalman: Three-dimensional soil moisture retrieval by assimilation of near-surface measurements: A simplified Kalman filter covariance forecasting and field application, *Water Resources Research* **38**, 37–1 – 37–13, 2002.

Wendroth, O., W. Ehlers, H. Kage, J. W. Hopmans, J. Halbertsma, and J. H. M. Wösten: Determining Hydraulic Functions in Unsaturated Soils, *Soil Science Society of America Journal* **57**, 1436–1443, 1993.

Westermann, S., J. Lüers, M. Langer, K. Piel, and J. Boike: The annual surface energy budget of a high-arctic permafrost site on Svalbard, Norway, *The Cryosphere* **3**, 245–263, 2009.

Wollschläger, U., T. Pfaff, and K. Roth: Field-scale apparent hydraulic parameterisation obtained from TDR time series and inverse modelling, *Hydrology and Earth System Science* **13**, 1953–1966, 2009.

Woodbury, A., and T. J. Ulrych: Minimum relative entropy inversion: Theory and application to recovering the release history of a groundwater contaminant, *Water Resources Research* **32**, 2671–2681, 1996.

Woodbury, A., E. Sudicky, T. J. Ulrych, and R. Ludwig: Three-dimensional plume source reconstruction using minimum relative entropy inversion, *Journal of Contaminant Hydrology* **32**, 131–158, 1998.

Yiotis, A. G., A. G. Boudouvis, A. K. Stubos, I. N. Tsimpanogiannis, and Y. C. Yortsos: Effect of Liquid Films on the Drying of Porous Media, *American Institute of Chemical Engineers AIChE Journal* **50**, 2721–2737, 2004.

Zdunkowski, W. G., J. Paegle, and J. P. Reilly: The effect of soil moisture upon the atmospheric and soil temperature near the air-soil interface, *Meteorology and Atmospheric Physics* **24**, 245–268, 1975.

Zhang, S., H. Li, W. Zhang, C. Qiu, and X. Li: Estimating the Soil Moisture Profile by Assimilating Near-Surface Observations with the Ensemble Kalman Filter (EnKF), *Advances in Atmospheric Sciences* **22**, 936–945, 2006.